



UNIVERSITÀ
DEGLI STUDI
DI PADOVA

Sede Amministrativa: Università degli Studi di Padova

Dipartimento di COSTRUZIONI E TRASPORTI

SCUOLA DI DOTTORATO DI RICERCA IN: SCIENZE DELL'INGEGNERIA CIVILE ED
AMBIENTALE
CICLO XXII°

**IMPLEMENTATION AND VALIDATION OF ADVANCED
CONSTITUTIVE MODELS FOR THE ANALYSIS OF
HYDRO-THERMO-MECHANICAL INTERACTIONS
IN GEO-ENVIRONMENTAL ENGINEERING PROBLEMS**

Direttore della Scuola: Ch.mo Prof. Stefano Lanzoni

Supervisor: Ch.mo Prof. Bernhard Schrefler

Dr. Lorenzo Sanavia

Dottorando: Loris Luison

ABSTRACT

In recent years increasing interest in thermo-hydro-mechanical analysis of multiphase porous materials, i.e. saturated and partially saturated porous materials, is observed, because of a wide spectrum of their engineering applications. An area of particular interest is Environmental Geomechanics, where some challenging problems are of interest. Examples are subsidence above gas reservoirs, injection of fluids into deep or superficial aquifers, long-term storage of carbon dioxide, onset of flowslides and catastrophic landslides, nuclear and other hazardous waste disposal and stability of salt marshes.

In all the aforementioned situations, the soil or rock need to be considered as multiphase porous medium in isothermal or non-isothermal conditions, made of a solid phase and voids containing one or more fluids, in which the interaction between all the components of the material cannot be neglected. In case of liquid and gaseous fluids, capillary effects cannot be a priori neglected and also phase change for liquid water and its vapour can play a role.

This thesis aims to contribute to develop a general framework for the computational analysis of geo-environmental engineering problems analysed as coupled multi-physics processes.

To this end, advanced constitutive models for isothermal and non-isothermal water saturated or unsaturated soils have been implemented and numerically validated in the finite element code COMES-GEO.

In this THM model the porous medium is assumed to be a multiphase system where interstitial voids of the deforming solid matrix may be filled with liquid water, water vapour and dry air or other gas. To handle this multiphase system, an analytical multi-scale approach has been used by the general frame of averaging theories in deriving the governing balance equations. These equations have been discretized in space and time by means of the finite element method for a numerical solution.

These following advanced constitutive models for soil have been implemented:

1. ACMEG-T for water saturated clays in non isothermal condition;
2. ACMEG-TS for water saturated and partially saturated clays in non isothermal condition;
3. Pastor-Zienkiewicz for water saturated sands in isothermal condition;
4. Bolzon-Schrefler-Zienkiewicz for partially saturated sands in isothermal condition;
5. Bolzon-Schrefler for partially saturated sands in non isothermal condition.

Validation of the implemented models was performed by comparison between the F.E.M. results and the results obtained by experimental tests or by the model driver. Three different tests were simulated: isotropic compression test, oedometric compression test and triaxial compression test in different conditions of confining pressure, temperature and suction and for different kind of soils. This comparison was done in cooperation with the research group of Prof. Lyesse Laloui (EPFL of Lausanne) and the research group of the Prof. Manolo Pastor (UPM of Madrid).

Preliminary results concerning typical geo-environmental problems such as the thermo-hydro-mechanical behaviour of deep nuclear waste disposal in a geological clay formation and the simulation of the subsidence above gas reservoirs due to gas production close this present work, pointing out that with a sufficiently general thermo-hydro-mechanical model the main couplings occurring in soils may be reproduced in a relevant manner and that very different situations can be modelled without special assumptions.

SOMMARIO

Negli ultimi anni è aumentato notevolmente l'interesse per le analisi termo-idro-meccaniche sui mezzi porosi multifase, che possono essere ad esempio analisi rivolte allo studio del comportamento dei terreni in parziale o totale saturazione, per via della vasta gamma di applicazioni ingegneristiche che è possibile investigare. In particolare un'area di grande interesse è rappresentata dai problemi di Geomeccanica Ambientale, dove si incontrano fenomeni di considerevole importanza per la salvaguardia della società.

Alcuni esempi sono la subsidenza dovuta all'estrazione di gas dal sottosuolo, iniezione di fluidi dentro acquiferi profondi o superficiali, stoccaggio a lungo termine di biossido di carbonio per la mitigazione del riscaldamento globale, innesco di frane, stoccaggio di scorie nucleari o pericolose e la stabilità delle barene marine.

In tutte le situazioni menzionate, il terreno deve essere considerato come un mezzo poroso multifase, in condizioni anche non isoterme, costituito da uno scheletro solido e da vuoti riempiti da uno o più fluidi dove le interazioni fra tutti i costituenti non possono essere trascurate. In particolare nel caso di fluidi liquidi e gassosi, l'effetto delle pressioni capillari non può essere tralasciato a priori, come anche il cambiamento di fase dell'acqua liquida e del vapor acqueo.

Lo scopo di questa tesi di dottorato è quello di contribuire a sviluppare uno strumento di carattere generale per l'analisi computazionale di problemi ingegneristici di geomeccanica ambientale e questo è stato fatto mediante l'implementazione e la validazione numerica di due modelli costitutivi avanzati nel codice agli elementi finiti COMES-GEO.

Considerando il mezzo poroso multifase costituito da uno scheletro solido deformabile dove i vuoti possono essere riempiti da acqua, vapore e aria secca (o un altro gas), tramite un approccio multiscala basato sulla teoria ibrida delle miscele, con opportune procedure di media sono state derivate le equazioni di bilancio del modello. Queste equazioni sono state poi discretizzate nello spazio e nel tempo per poter ottenere una soluzione numerica col metodo degli elementi finiti.

I modelli costitutivi implementati sono i seguenti:

1. ACMEG-T per argille sature in condizioni non isoterme;
2. ACMEG-TS per argille parzialmente sature in condizioni non isoterme;
3. Pastor-Zienkiewicz per sabbie sature in condizioni isoterme;
4. Bolzon-Schrefler-Zienkiewicz per sabbie parzialmente sature in condizioni isoterme;
5. Bolzon-Schrefler per sabbie parzialmente sature in condizioni non isoterme.

La validazione dell'implementazione numerica dei modelli costitutivi è stata fatta tramite il confronto fra i risultati F.E.M. e risultati sperimentali od ottenuti con il driver del modello. Le prove simulate sono di tre tipi: compressione isotropa, compressione edometrica e compressione triassiale eseguite in differenti condizioni di pressione di confinamento, temperatura e grado di saturazione per diversi tipi di materiale. Il lavoro di validazione è stato svolto in collaborazione col gruppo di ricerca del Prof. Lesse Laloui (EPFL di Losanna) e quello del Prof. Manolo Pastor (UPM di Madrid).

Infine vengono mostrati alcuni risultati preliminari riguardanti due tipici problemi di Geomeccanica Ambientale, quali lo stoccaggio di scorie nucleari e la subsidenza, per dimostrare come con un modello termo-idro-meccanico di carattere sufficientemente generale, senza particolari assunzioni, sia possibile studiare un numero rilevante di problematiche inerenti i problemi di accoppiamento nei terreni.

RINGRAZIAMENTI

Un ringraziamento particolare va al Dr. Lorenzo Sanavia prima per avermi proposto il dottorato e poi per avermi indirizzato nel mondo della ricerca scientifica tramite varie vie. Non tralascio di ringraziarlo per l'attento e preciso controllo fatto al presente lavoro.

Ringrazio Prof. Schrefler, senza il quale questo lavoro non sarebbe mai potuto essere stato fatto.

Parte di questo lavoro devo dividerlo anche con Mareva Passarotto per le analisi svolte assieme nella validazione e per aver letto con pazienza le pagine successive.

Un ringraziamento anche a Raffaella Santagiuliana e Roberto Bortolotto per il contributo datomi nelle simulazioni.

Un aiuto fondamentale per poter completare questo lavoro è giunto dal Prof. Lyesse Laloui e dal Dr. Bertrand Francois di Losanna con i quali il rapporto di cooperazione è iniziato già prima del dottorato.

Un grazie anche al Prof. Manolo Pastor e al Dr. Pablo Mira per il materiale che mi hanno fornito e senza il quale non avrei potuto ottenere il risultato finale.

Volgo un ringraziamento particolare al Controrelatore di questa tesi, la Prof. Cristina Jommi di Milano, la quale, dopo aver controllato con pazienza e profonda competenza il mio lavoro, ne ha dato un giudizio che mi ha infuso maggiore sicurezza e consapevolezza.

Oltre che per il materiale fornitomi, ringrazio di cuore il Prof. Claudio Tamagnini per la disponibilità dimostratami e per la compagnia offertami nelle occasioni in cui ci siamo incontrati.

Un ringraziamento infine va a tutto quello che ha rappresentato il dottorato in questi tre anni, alle persone incontrate nei vari convegni e alle scuole di dottorato, a questo periodo della mia vita che ricorderò sempre con immenso piacere, per gli infiniti stimoli che il mondo della ricerca ha saputo darmi e per le grandi persone che ne fanno parte e che ho potuto conoscere o solo apprezzare.

Il mio ultimo pensiero infine va al mondo che sta al di fuori di quello che ho ringraziato finora, che indirettamente mi ha permesso di fare tutto ciò con serenità e convinzione: Mareva, famiglia, amici.

CONTENTS

1	INTRODUCTION	3
2	MATHEMATICAL MODEL	11
2.1	INTRODUCTION	11
2.2	AVERAGING PRINCIPLES	11
2.2.1	AVERAGING PROCESS	12
2.2.2	MICROSCOPIC BALANCE EQUATIONS	15
2.2.3	MACROSCOPIC BALANCE EQUATIONS	15
2.3	MACROSCOPIC BALANCE EQUATIONS FOR A NON ISOTHERMAL PARTIALLY SATURATED POROUS MATERIAL	17
2.3.1	KINEMATIC EQUATIONS	18
2.3.2	MASS BALANCE EQUATIONS	20
2.3.3	LINEAR MOMENTUM BALANCE EQUATION	23
2.3.4	ANGULAR MOMENTUM BALANCE EQUATION	23
2.3.5	BALANCE OF ENERGY EQUATION	23
2.3.6	ENTROPY INEQUALITY	24
2.4	CONSTITUTIVE EQUATIONS	25
2.4.1	STRESS TENSOR IN THE FLUID PHASES	25
2.4.2	GASEOUS MIXTURE OF DRY AIR AND WATER VAPOUR	26
2.4.3	SORPTION EQUILIBRIUM	26
2.4.4	CLAUSIUS-CLAPEYRON EQUATION	27
2.4.5	PORE SIZE DISTRIBUTION	27
2.4.6	EQUATION OF STATE FOR WATER	28
2.4.7	DARCY'S LAW	28
2.4.8	FICK'S LAW	29
2.4.9	STRESS TENSOR IN THE SOLID PHASE AND TOTAL STRESS	30
2.4.10	SOLID DENSITY	31
2.4.11	FOURIER'S LAW	31
2.5	GENERAL FIELD EQUATIONS	32
2.5.1	MASS BALANCE EQUATION	32
2.5.2	LINEAR MOMENTUM BALANCE EQUATION	35
2.5.3	ENERGY BALANCE EQUATION	35
2.6	PHYSICAL APPROACH: EXTENDED BIOT'S THEORY	36
2.6.1	THE PHYSICAL MODEL	36
2.6.2	CONSTITUTIVE EQUATIONS	40

2.6.3	GOVERNING EQUATIONS	42
2.7	QUASI STATIC CASE.....	45
2.8	BOUNDARY AND INITIAL CONDITIONS	46
3	FEM MODEL	51
3.1	THE CODE COMES-GEO	51
3.1.1	INTRODUCTION	51
3.1.2	FINITE ELEMENT METHOD	52
3.1.3	FINITE ELEMENT LIBRARY	55
3.1.4	NUMERICAL INTEGRATION	57
3.1.5	MATRIX SOLUTION PROCEDURE	58
3.1.6	CONVERGENCE AND ERROR ANALYSIS	59
3.2	PLASTICITY IN SOILS	60
3.2.1	CLASSICAL ELASTOPLASTICITY	61
3.2.2	MOHR-COULOMB YIELD SURFACE.....	64
3.2.3	CRITICAL STATE MODEL.....	67
3.2.4	CORNERS OF YIELD AND POTENTIAL SURFACES.....	73
3.2.5	ADVANCED CONSTITUTIVE MODEL.....	74
3.3	SIMULATION METHOD.....	74
3.3.1	INTRODUCTION	74
3.3.2	FINITE ELEMENTS USED FOR THE NUMERICAL VALIDATION.....	74
3.3.3	TYPES OF TESTS.....	75
3.3.4	REMARKS ON THE F.E.M. MODELLING APPROACH	79
4	THE THERMO-ELASTO-PLASTIC CONSTITUTIVE MODEL ACMEG-T.....	87
4.1	TEMPERATURE EFFECTS IN SOILS.....	87
4.1.1	THERMAL PROBLEM IN SOILS	87
4.1.2	THERMO-MECHANICAL BEHAVIOUR OF SOILS	87
4.1.3	TEMPERATURE EFFECT ON PRECONSOLIDATION PRESSURE.....	91
4.1.4	TEMPERATURE EFFECTS ON SHEARING BEHAVIOUR.....	92
4.2	ACMEG-T MODEL	93
4.2.1	INTRODUCTION	93
4.2.2	ACMEG MODEL	94
4.3	ACMEG-T MODEL.....	101
4.3.1	THERMO ELASTICITY	101
4.3.2	THERMO PLASTICITY	102

4.4	VALIDATION OF THE IMPLEMENTATION OF ACMEG-T MODEL IN COMES-GEO F.E. CODE	105
4.4.1	INTRODUCTION	105
4.4.2	ELASTIC ISOTROPIC COMPRESSION IN NON-ISOTHERMAL CONDITION	105
4.4.3	ELASTOPLASTIC ISOTROPIC COMPRESSION IN ISOTHERMAL CONDITION	115
4.4.4	ELASTOPLASTIC TRIAXIAL COMPRESSION IN ISOTHERMAL CONDITION	119
4.4.5	ELASTOPLASTIC ISOTROPIC COMPRESSION IN NON-ISOTHERMAL CONDITION	120
4.5	A NON ISOTHERMAL CONSOLIDATION EXAMPLE	123
5	THE THERMO-HYDRO-ELASTO-PLASTIC CONSTITUTIVE MODEL ACMEG-TS.....	131
5.1	PARTIAL SATURATION IN SOIL	131
5.1.1	MECHANICAL BEHAVIOUR	132
5.1.2	CONCLUSION.....	135
5.2	ACMEG-TS MODEL.....	136
5.2.1	ISOTROPIC PLASTIC MECHANISM.....	136
5.2.2	DEVIATORIC PLASTIC MECHANISM.....	137
5.2.3	COUPLING BETWEEN THE TWO PLASTIC MECHANISMS.....	137
5.3	WATER RETENTION CONSTITUTIVE PART	140
5.3.1	BROOKS AND COREY	141
5.3.2	SAFAI AND PINDER	143
5.3.3	ACMEG-HYDRO	144
5.3.4	COMPARISON	146
5.4	VALIDATION OF THE IMPLEMENTATION OF ACMEG-TS MODEL IN COMES-GEO F.E. CODE.....	147
5.4.1	TRIAXIAL COMPRESSION TEST	147
5.4.2	OEDOMETRIC COMPRESSION TESTS	153
6	THE GENERALIZED PLASTICITY MODEL FOR WATER SATURATED SANDS	165
6.1	GENERALIZED PLASTICITY	165
6.2	PASTOR-ZIENKIEWICZ MODEL FOR SAND.....	168
6.2.1	PZ IN LOADING CONDITIONS	171
6.2.2	PZ IN UNLOADING CONDITIONS	177
6.2.3	LIQUEFACTION AND CYCLIC MOBILITY PHENOMENA.....	177
6.3	VALIDATION OF THE IMPLEMENTATION OF PZ MODEL IN COMES-GEO	179
6.3.1	BANDING SAND.....	179
6.3.2	ADIGE SAND	183
6.3.3	DENSE SAND	187

7 THE GENERALIZED PLASTICITY MODEL FOR UNSATURATED SANDS	191
7.1 INTRODUCTION	191
7.2 BSZ MODEL.....	192
7.3 BS MODEL	194
7.3.1 BS MODEL FOR SATURATED SOILS	195
7.3.2 BS MODEL FOR PARTIALLY SATURATED SOILS.....	196
7.4 VALIDATION OF THE IMPLEMENTATION OF THE BSZ MODEL IN THE F.E. CODE COMES-GEO.....	198
7.5 REMARKS.....	203
8 APPLICATION TO GEO-ENVIRONMENTAL ENGINEERING PROBLEMS	207
8.1 DEEP NUCLEAR WASTE DISPOSAL	207
8.1.1 INTRODUCTION	207
8.1.2 SOURCE OF TEMPERATURE	208
8.1.3 MATERIAL PARAMETERS.....	210
8.1.4 INITIAL AND BOUNDARY CONDITIONS	211
8.1.5 MESH.....	213
8.1.6 SIMULATIONS.....	213
8.1.7 RESULTS.....	214
8.1.8 FAILURE CONDITIONS	219
8.2 SUBSIDENCE DUE TO GAS PRODUCTION.....	220
8.2.1 INTRODUCTION	220
8.2.2 IDENTIFICATION OF PARAMETERS.....	220
8.2.3 RESERVOIR ANALYSIS	225
9 CONCLUSIONS AND FUTURE DEVELOPMENTS.....	231

1 INTRODUCTION

In recent years, increasing interest in thermo-hydro-mechanical analysis of multiphase porous materials, i.e. saturated and partially saturated porous materials, is observed, because of a wide spectrum of their engineering applications. An area of particular interest is Environmental Geomechanics [Vul02], [Sch01] and [S&D10], where some challenging problems are of interest. Examples are subsidence above gas reservoirs with possible water injection to maintain pressure (Figure 1.1), injection of other fluids into deep or superficial aquifers, long-term storage of carbon dioxide for the mitigation of global warming, problems linked with soil failure such as the onset of flowslides and catastrophic landslides (Figure 1.2), problems connected with nuclear and other hazardous waste disposal (Figure 1.3 and Figure 1.4), or groundwater, saturation response and stability of salt marshes subjected to both tide fluctuation and flooding (Figure 1.5).

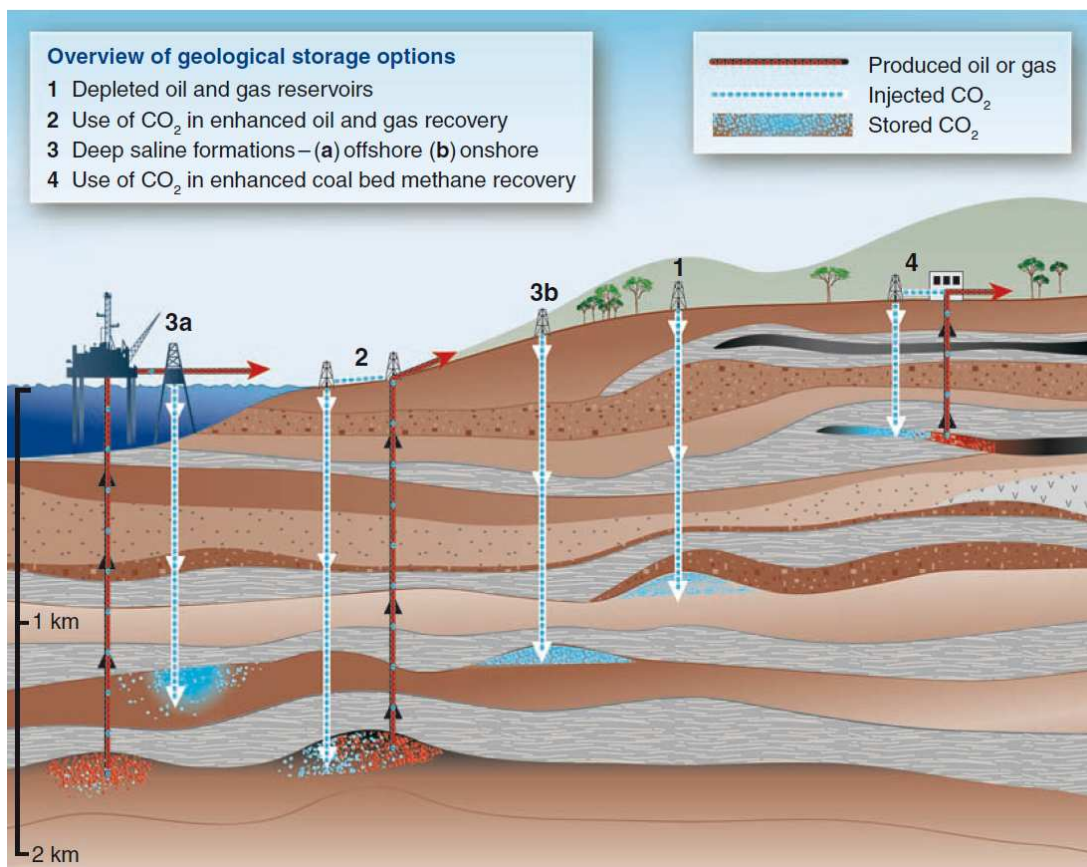


Figure 1.1: Scheme of extraction of gas and injection of CO₂ [Sci09]

In all the aforementioned situations, the soil or rock need to be considered as multiphase porous medium in isothermal or non-isothermal conditions, made of a solid phase and voids containing one or more fluids, in which the interaction between all the components of the material cannot be neglected. In case of liquid and gaseous fluids, capillary effects cannot be a priori neglected, and also phase change for liquid water and its vapour can play a role.

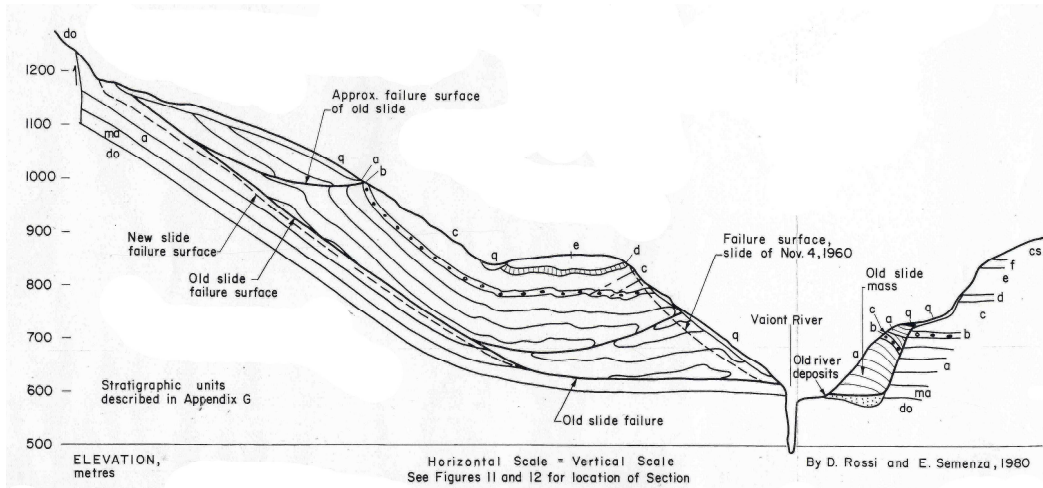


FIGURE 15
Geologic Section 2, Vaiont Slide
Before October 9, 1963

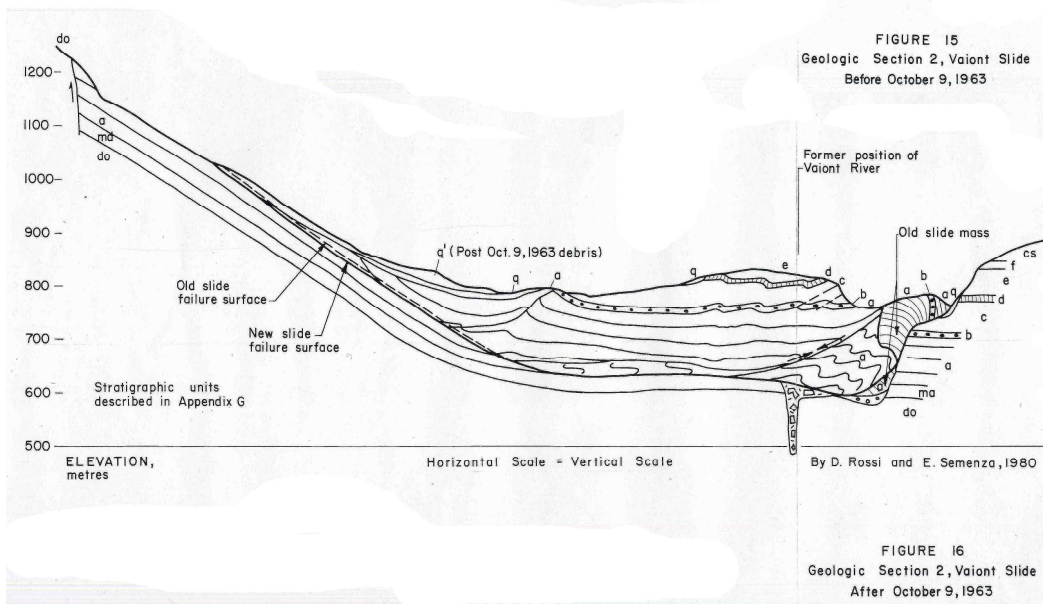


FIGURE 16
Geologic Section 2, Vaiont Slide
After October 9, 1963

Figure 1.2: Geologic section of Vajont slide before and after 9 October 1963 [R&S65] and [H&P85]

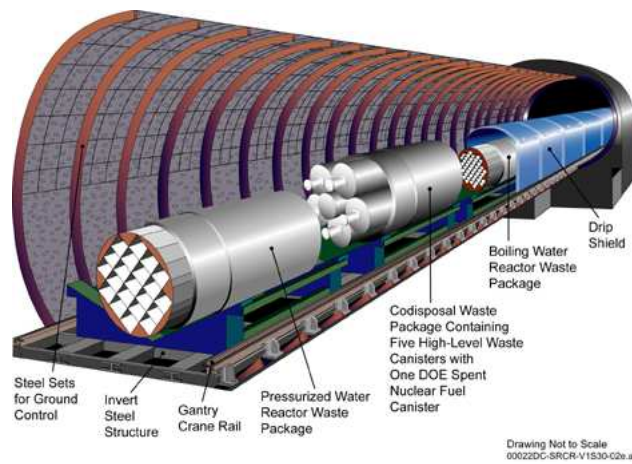


Figure 1.3: Repository tunnel with used fuel containers (Yucca tunnel, USA. NAI)

For enabling significant predictive simulations to be carried out, in particular for the long term behaviour, suitable physical and mathematical models have to be developed and based on robust science; then, powerful and well validated

software is necessary. To this end, coupled Thermo-Hydro-Mechanical (THM) finite element codes are of paramount importance for simulation and analysis of geo-environmental engineering problems.

There are no general purpose codes available which handle all the above mentioned situations. There exist only a few specialized codes which need however improvement.

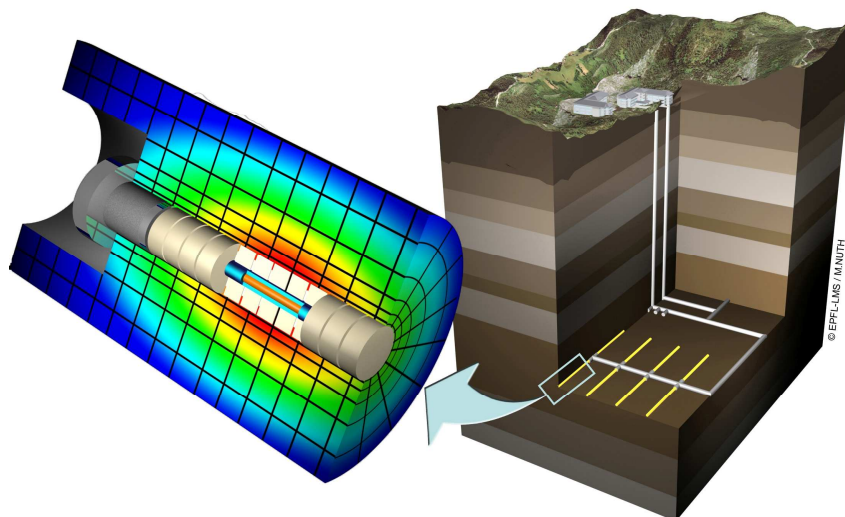


Figure 1.4: Geological disposal of nuclear waste (M. Nuth, EPFL)



Figure 1.5: View of Venice lagoon marshes and view of a marsh border [Col08]

This thesis aims to contribute to develop a general framework for the computational analysis of geo-environmental engineering problems analysed as coupled multi-physics processes.

To this end, advanced constitutive models for isothermal and non-isothermal water saturated or unsaturated soils have been implemented and numerically validated in the finite element code COMES-GEO [G&S96], [L&S98], [S&P04], [San06], [G&S09]. This code is based on an existing fully coupled Thermo-Hydro-Mechanical (THM) model developed during years at the University of Padua [G&S96], [L&S98], [Sch02], [G&S09].

In this THM model the porous medium is assumed to be a multiphase system where interstitial voids of the deforming solid matrix may be filled with liquid water, water vapour and dry air [L&S98] or other gas such as methane. To handle

this multiphase system, an analytical multi-scale approach has been used by the general frame of averaging theories in deriving the governing balance equations, [H&G79/1] and [H&G79/2]. These equations have been discretized in space and time by means of the finite element method for a numerical solution [L&S98] and [Zie99].

In particular, the following advanced constitutive models for soil have been implemented:

1. ACMEG-T (Advanced Constitutive Model for Environmental Geomechanics – Thermal effects) for water saturated clays in non isothermal condition, [M&L97] and [L&C08];
2. ACMEG-TS (Advanced Constitutive Model for Environmental Geomechanics – Thermal and Suction effects) for water saturated and partially saturated clays in non isothermal condition [Fra08];
3. Pastor-Zienkiewicz for water saturated sands in isothermal condition, [Pas90] and [Zie99];
4. Bolzon-Schrefler-Zienkiewicz for partially saturated sands in isothermal condition [Bol96];
5. Bolzon-Schrefler for partially saturated sands in non isothermal condition [B&S05].

The first two models are based on the multi-mechanism elastoplasticity theory integrated by the bounding surface theory, while the other three are based on the Generalized Plasticity theory.

The computational formulation of the elastoplastic algorithms developed for this thesis is of explicit type (Euler Forward Method); for the tangent operator of the linearized system of equations [3.12] elastoplastic continuum tangent operator has been computed.

Validation of the implemented models was performed by comparison between the F.E.M. results and the results obtained by experimental tests or by the model driver. Three different tests were simulated: isotropic compression test, oedometric compression test and triaxial compression test in different conditions of confining pressure, temperature and suction and for different kind of soils.

This comparison was done in cooperation with:

1. the research group of Prof. Lyesse Laloui (EPFL of Lausanne) and in particular with the Dr. Bertrand Francois for the ACMEG models;
2. the research group of the Prof. Manolo Pastor (UPM of Madrid) and in particular with the Dr. Pablo Mira for the PZ model.

Validation of the implementation of BS model will be performed in the near future.

As further numerical validation a linear thermo elastic consolidation in fully saturated condition proposed originally by Aboustit et al. [Abo85] and then by Lewis and Schrefler [L&S98] was analyzed. Then this case was extended to non liner elasticity and [San08].

Preliminary results concerning typical geo-environmental problems such as the thermo-hydro-mechanical behaviour of deep nuclear waste disposal in a geological clay formation and the simulation of the subsidence above gas reservoirs due to gas production close this present work, pointing out that with a sufficiently general thermo-hydro-mechanical

model the main couplings occurring in soils may be reproduced in a relevant manner and that very different situations can be modelled without special assumptions.

This thesis is organized as follows:

After the introduction, CHAPTER 2 presents the governing equations of the T-H-M model following [L&S98].

Then CHAPTER 3 describes the space and time discretization of the mathematical model, a brief summary of the elastoplasticity in soils and the F.E.M. modelling approach need in this work.

CHAPTER 4 to 7 present the constitutive models implemented in the finite element code COMES-GEO and the main results concerning the validation of their FEM implementation.

CHAPTER 8 shows the preliminary results of the thermo-hydro-mechanical behaviour of deep nuclear waste disposal in a geological clay formation and the simulation of the subsidence above gas reservoirs due to gas production.

References

- [Abo85] Aboustit B.L., Advani S.H. and Lee J.K. (1985). Variational principles and finite element simulations for thermo-elastic consolidation. *International Journal for Numerical and Analytical Methods in Geomechanics*, 9: 49-69.
- [B&S05] G. Bolzon, B.A. Schrefler. Thermal effects in partially saturated soils: a constitutive model. *International Journal for Numerical and Analytical Methods in Geomechanics*, Vol. 29, pp. 861-877, 2005.
- [Col08] Cola S., L. Sanavia, P. Simonini, B.A. Schrefler (2008) Coupled thermo-hydro-mechanical analysis of Venice lagoon marshes. *Water Resources Research*, 44, W00C05. DOI:10.1029/2007WR006570.
- [Fra08] François B. (2008). Thermo-Plasticity of Fine-Grained Soils at Various Saturation States: Application to Nuclear Waste Disposal. PhD Thesis. École Polytechnique Fédérale De Lausanne. Suisse.
- [G&S09] Gawin D., and L. Sanavia, (2009 – online first), Simulation of cavitation in water saturated porous media considering effects of dissolved air, *Transport in porous media*. DOI: 10.1007/s11242-009-9391-4.
- [G&S96] Gawin, D., and B.A. Schrefler, (1996), Thermo- hydro- mechanical analysis of partially saturated porous materials, *Engineering Computations*, 13(7), 113-143.
- [H&G79/1] Hassanizadeh, M. and Gray W.G., General conservation equations for multiphase systems: 1 Averaging procedure, *Adv. Water Resources*, 2 (1979), 131-144.
- [H&G79/2] Hassanizadeh, M. and Gray W.G., General conservation equations for multiphase systems: 2. Mass, momenta, energy and entropy equations, *Adv. Water Resources*, 2(1979), 191-203.
- [H&P85] Hendron, A.J. Patton, F.D.: The Vaiont slide, a geotechnical analysis based on new geologic observations of the failure surface, Technical Report GL-85-5. Washington DC, Department of the Army US Corps of Engineers vol. I, 1985.
- [L&C08] Laloui L. and Cekerevac C. (2008). Non-isothermal plasticity model for cyclic behaviour of soils. *International Journal for Numerical and Analytical Methods in Geomechanics*, 32(5): 437-460.
- [L&S98] Lewis R.W. and Schrefler B.A. *The Finite Element Method in the Static and Dynamic Deformation and Consolidation of Porous Media*. J. Wiley, Chichester 1998.
- [M&L97] Modaressi H. and Laloui L. (1997). A thermo-viscoplastic constitutive model for clays. *International Journal for Numerical and Analytical Methods in Geomechanics*, 21(5): 313–315.
- [R&S65] Rossi D., Semenza E., Carte geologiche del versante settentrionale del Monte Toc e zone limitrofe, prima e dopo il fenomeno di scivolamento del 9 ottobre 1963, Istituto di Geologia dell'Università di Padova, 1965.
- [S&D10] B.A.Schrefler and Pierre Delage. *Environmental Geomechanics*. ISTE-Wiley, 2010.
- [S&P04] Schrefler BA, F. Pesavento, Multiphase flow in deforming porous material., *Computers and Geotechnics*, 31 (2004), 237-250.
- [San06] Sanavia, L., F. Pesavento, and B.A. Schrefler, (2006), Finite element analysis of non-isothermal multiphase geomaterials with application to strain localization simulation, *Computational Mechanics*, 37(4), 331-348.
- [San08] Sanavia L., François B., Bortolotto R., Luison L., Laloui L. (2008). Finite element modelling of thermo-elasto-plastic water saturated porous materials. *Journal of Theoretical and Applied Mechanics*, 38, 1-2, pp 7-34.

-
- [Sch01] B.A. Schrefler. Environmental Geomechanics. CISM Courses and Lectures No 417, Springer Verlag Wien, New York, 2001.
- [Sch02] Schrefler, B.A., (2002), Mechanics and Thermodynamics of Saturated-Unsaturated Porous Materials and Quantitative Solutions, Applied Mechanics Review, 55(4), 351-388.
- [Sci09] Science. 25 september 2009 vol 325, issue 5948, pages 1585-1740
- [Vul02] L. Vulliet, L. Laloui, B.A. Schrefler. Environmental Geomechanics – Monte Verità. EPFL Press, Lausanne, 2002.
- [Zie99] Zienkiewicz, O.C., A. Chan, M. Pastor, B.A. Schrefler, and T. Shiomi, (1999) Computational Geomechanics with special Reference to Earthquake Engineering. John Wiley & Sons, Chichester.

2 MATHEMATICAL MODEL *

2.1 INTRODUCTION

In this chapter the governing equations for the full dynamic behaviour of a partially saturated porous medium are developed. In particular, we consider here the voids filled with water and air. Today the description of multiphase systems made of interpenetrating continuous bodies, such as porous media, is based either on the mixture theory integrated by the concept of volume fractions, or on averaging theories and from a classical point of view on Biot's theory. Since the averaging theories offer the possibilities of a better understanding of the microscopic situation and its relation to the macroscopic one, which is, however, the natural domain of all continuum mechanical models, we use in the following the averaging theory based on spatial averaging operators. Within this theory we make use of macroscopic variables which correspond to real measurable quantities directly linked to laboratory practice, e.g. in soil mechanics. It has to be pointed out that, under appropriate assumptions, the averaging theory yields the same equations as the classical mixture theory, as shown in [deB91]. Care has to be taken, however, in the linear momentum balance equation as explained in section 2.3.3.

For the reader mainly interested in the resulting governing equations and their numerical solution we derive these equations again in section 2.6 using Biot's theory. This also permits us to establish a link between the classical, phenomenological approach and the description of the real microscopic composition of the multiphase system. Furthermore, it shows the essential correctness of Biot's findings.

Tensorial notation is used throughout this chapter.

2.2 AVERAGING PRINCIPLES

Here only a short summary of the principles necessary for the development of the governing equations is given. For a full account of the averaging theories the reader is referred to References [deB91] and [B&D83]. Sections 2.2 and 2.3 follow, in particular, the work by Hassanizadeh and Gray [H&G79/1] and [Has86/2] and by de Boer et al. [deB91].

We introduce the following definitions:

1. **microscopic level:** we consider the real nonhomogeneous structure of the porous medium domain (Figure 2.1). The scale of inhomogeneity is of the order of magnitude of the dimensions of a pore or a grain, say d . Attention is focussed on what happens at a mathematical point within a single phase and the field variables describing the status of a phase are defined only at the points occupied by that phase. For the practical

* From *Chapter 2: Mechanics of saturated and partially saturated porous media* of: "Lewis R.W. and Schrefler B.A. The Finite Element Method in the Static and Dynamic Deformation and Consolidation of Porous Media. J. Wiley, Chichester 1998".

description of the processes taking place in a porous medium, this level is not useful since microscopic quantities are generally not measurable. Only their average values are measurable.

2. **macroscopic level:** the real multiphase system that occupies the porous medium domain is replaced by a model in which each phase is assumed to fill up the entire domain. This means that at every point all phases are supposed present at the same time (overlapping continua). This is the level of interest of continuum mechanics, where we investigate the continuous distribution of the constituents through a macroscopic control space. At this level, we usually deal with homogeneous media, but nonhomogeneities may still be present, e.g. strata. Their scale is of the order of magnitude comparable with the order of magnitude of the entire domain, say L .
3. **megascopic level:** at this level the conditions are similar to those of the previously defined level. The difference depends on the fact that some macroscopic inhomogeneities are eliminated by averaging and/or on the fact that the mathematical model is stated in a domain which has less dimensions than the real domain, e.g. 2-D problem with field values averaged over the thickness [B&C81] and [S&S89]. Typical applications of this level are found in the simulation of land subsidence problems of regional scale.

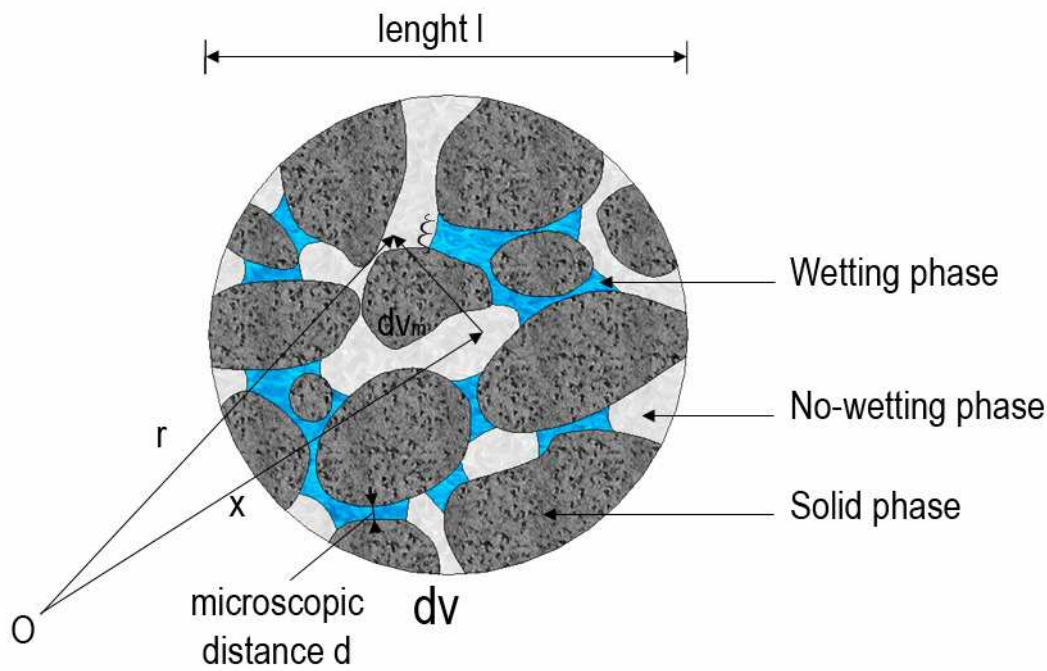


Figure 2.1: Typical averaging volume dv of a porous media consisting of three constituents

2.2.1 Averaging process

We consider here a multiphase system occupying a total volume, V , and bounded by surface, A . The constituents $\pi=1,2,\dots,k$ have the partial volumes V^π . Each point of the total volume, V , is considered to be the centroid of a representative elementary volume (R.E.V.) or average volume element, dv . The position of the centre of an R.E.V. in a global coordinate system is described by position vector x while r indicates the position of a microscopic volume

element, dv_m , see Figure 2.1. The volume of constituent π within an R.E.V, called average volume element dv^π , is obtained by defining a phase distribution function, γ^π

$$\gamma^\pi(\mathbf{r}, t) = \begin{cases} 1 & \text{for } \mathbf{r} \in dv^\pi \\ 0 & \text{for } \mathbf{r} \in dv^\alpha \quad \pi \neq \alpha \end{cases} \quad [2.1]$$

where $\mathbf{r} = \mathbf{x} + \boldsymbol{\xi}$

and the integration refers to the microscopic local coordinate system with its origin in \mathbf{x} (Figure 2.1).

Similarly we write for the part of area da^π of the R.E.V., occupied by constituent π

$$da^\pi(\mathbf{x}, t) = \int_{da} \gamma^\pi(\mathbf{r}, t) da_m \quad [2.2]$$

where da_m is the microscopic area element

The knowledge of dv^π enables the introduction of the concept of volume fraction, η^π , which is of paramount importance in multiphase systems

$$\eta^\pi(\mathbf{x}, t) = \frac{dv^\pi}{dv} = \frac{1}{dv} \int_{dv} \gamma^\pi(\mathbf{r}, t) dv_m \quad [2.3]$$

with

$$\sum_{\pi=1}^{A_c} \eta^\pi = 1 \quad [2.4]$$

In fact, as indicated under the heading "macroscopic level" in paragraph 2.2, substitute continua fill the entire domain simultaneously, instead of the real fluids and the solid which each fill only part of it. These substitute continua have a reduced density which is obtained through the volume fractions.

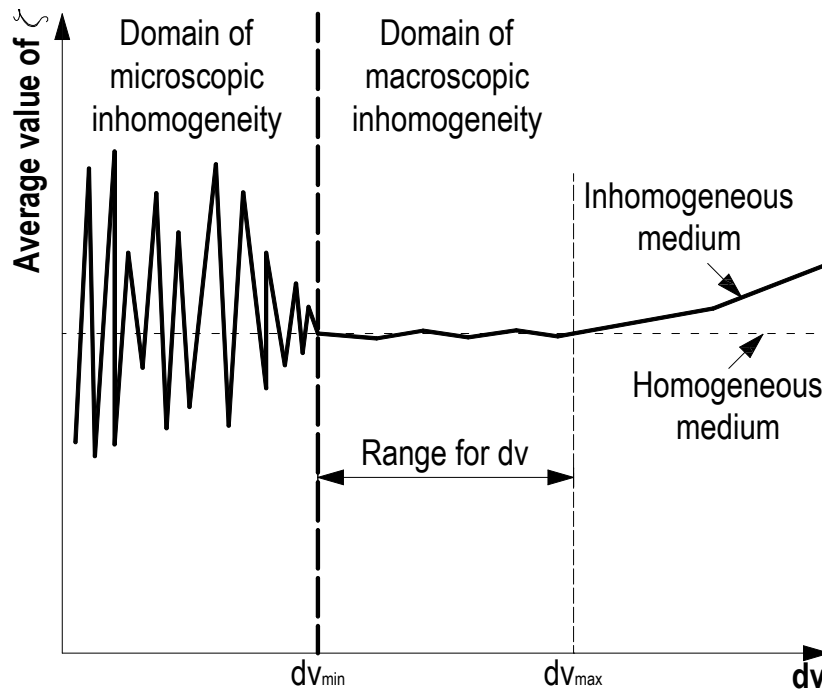


Figure 2.2: Averaged value ζ versus size of the average volume dv

In the following, averaged quantities are obtained by integrating (averaging) a microscopic quantity over the volume, dv , or the area, da , of an R.E.V. A field of macroscopic variables results from this, where the average volume, dv , and the average area, da , is associated with material points.

The importance in the choice of size of an R.E.V. is self evident. Average quantities have to be independent of the size of the average volume and continuous in space and time. Thus an R.E.V. has to fulfil the following requirements:

- dv has to be small enough to be considered as infinitesimal, i.e. the partial derivatives appearing in the governing equations must make sense and
- dv must be large enough, with respect to the heterogeneities of the material to give average quantities without fluctuations depending on the size of the R.E.V., Figure 2.2.

To obtain meaningful average values, the characteristic length, l , of the average volume must satisfy the inequality

$$d \ll l \ll L \quad [2.5]$$

where l is dependent on the specific material which constitutes the medium.

Some typical values of l are given in [L&C88]

	l [mm]
metals	0.5
plastics	1.0
wood	10.0

Table 2.1: characteristic length l for some materials

The following average operators are now defined and applied to a function, ζ , which is a microscopic field variable.

Volume average operators

phase average

$$\langle \zeta \rangle_{\pi}(\mathbf{x}, t) = \frac{1}{dv} \int_{dv} \zeta(\mathbf{r}, t) \gamma^{\pi}(\mathbf{r}, t) dv_m \quad [2.6]$$

intrinsic phase average

$$\langle \zeta \rangle_{\pi}^{\pi}(\mathbf{x}, t) = \frac{1}{dv^{\pi}} \int_{dv} \zeta(\mathbf{r}, t) \gamma^{\pi}(\mathbf{r}, t) dv_m \quad [2.7]$$

From the definition of volume fraction [2.3] it follows that

$$\langle \zeta \rangle_{\pi}(\mathbf{x}, t) = \eta^{\pi}(\mathbf{x}, t) \langle \zeta \rangle_{\pi}^{\pi}(\mathbf{x}, t) \quad [2.8]$$

Mass average operator, with $\rho(\mathbf{r}, t)$ microscopic mass density as weighting function

$$\overline{\zeta}^{\pi}(\mathbf{x}, t) = \frac{\int_{dv} \rho(\mathbf{r}, t) \zeta(\mathbf{r}, t) \gamma^{\pi}(\mathbf{r}, t) dv_m}{\int_{dv} \rho(\mathbf{r}, t) \gamma^{\pi}(\mathbf{r}, t) dv_m} \quad [2.9]$$

with constant microscopic mass density the following equation holds

$$\frac{1}{\gamma^\pi(\mathbf{x}, t)} \langle \zeta^\epsilon \rangle_\pi(\mathbf{x}, t) = \overline{\zeta^\pi}(\mathbf{x}, t) \quad [2.10]$$

Area average operator

$$\overline{\zeta^\pi}(\mathbf{x}, t) = \frac{1}{da} \int_{da} \zeta^\epsilon(\mathbf{r}, t) \cdot \mathbf{n} \gamma^\pi(\mathbf{r}, t) da_m \quad [2.11]$$

with \mathbf{n} the outward normal unit vector of an area element da_m and ζ has a tensorial nature.

In the following, averages of velocity, external body force, internal energy, external supply of heat, internal entropy, external supply of entropy and total production of entropy are obtained through the mass average operator [H&G79/1].

2.2.2 Microscopic balance equations

We now consider the classical balance equations of continuum mechanics which are used to describe the microscopic situation of any π phase. At the interfaces with other constituents, the material properties and thermodynamic quantities may present step discontinuities.

For a generic conserved variable, ψ , the conservation equation within the π phase may be written as

$$\frac{\partial(\rho\psi)}{\partial t} + \text{div}(\rho\psi\dot{\mathbf{r}}) - \text{div} \mathbf{i} - \rho\mathbf{b} = \rho\mathbf{G} \quad [2.12]$$

where $\dot{\mathbf{r}}$ is the local value of the velocity field of the phase in a fixed point in space

\mathbf{i} is the flux vector associated with ψ

\mathbf{b} is the external supply of ψ

\mathbf{G} is the net production of ψ

At the interface between two constituents π and α , the jump condition holds

$$[\rho\psi(\mathbf{w} - \dot{\mathbf{r}}) + \mathbf{i}]|_\pi \cdot \mathbf{n}^{\pi\alpha} + [\rho\psi(\mathbf{w} - \dot{\mathbf{r}}) + \mathbf{i}]|_\alpha \cdot \mathbf{n}^{\alpha\pi} = 0 \quad [2.13]$$

where \mathbf{w} is the velocity of the interface

$\mathbf{n}^{\pi\alpha}$ is the unit normal vector pointing out of the π phase and into the α phase, with

$$\mathbf{n}^{\pi\alpha} = -\mathbf{n}^{\alpha\pi} \quad [2.14]$$

and $|_\pi$ indicates that the preceding term [...] must be evaluated with respect to the π phase

No thermomechanical properties are attributed to these interfaces. This assumption does not exclude the possibility of exchange of mass, momentum or energy between the constituents.

Moreover the local thermodynamic equilibrium hypothesis is assumed to hold because the time scale of the modelled phenomena is substantially larger than the relaxation time required to reach equilibrium locally.

2.2.3 Macroscopic balance equations

Instead of deriving the macroscopic balance equation separately for each quantity to which the conservation law applies, we derive it for the generic quantity, ψ , as in [deB91] and [B&D83] and specialise the law afterwards for specific

quantities: mass, linear momentum, angular momentum and energy. Note that the balance equations are written in a material free manner. The constitutive equations are introduced successively.

A general, average macroscopic balance equation is obtained from the microscopic balance equation [2.12] by multiplying it with the distribution function $\gamma^\pi(\mathbf{r}, t)$ and by integrating this product over the volume element, dv , and over the total volume, V . In this elaboration of the balance equations, macroscopic quantities are obtained through the previously defined averaging operators.

This averaging procedure yields that ([deB91] and [B&D83])

$$\begin{aligned}
 & \int_V \left[\frac{1}{dv} \int_{dv} \frac{\partial(\rho(\mathbf{r}, t)\psi(\mathbf{r}, t))}{\partial t} \gamma^\pi(\mathbf{r}, t) dv_m \right] dV \\
 & + \int_V \left[\frac{1}{dv} \int_{dv} \text{div}(\rho(\mathbf{r}, t)\dot{\mathbf{r}}(\mathbf{r}, t)\psi(\mathbf{r}, t)) \gamma^\pi(\mathbf{r}, t) dv_m \right] dV \\
 & - \int_V \left[\frac{1}{dv} \int_{dv} \text{div} \mathbf{i}(\mathbf{r}, t) \gamma^\pi(\mathbf{r}, t) dv_m \right] dV \tag{2.15} \\
 & - \int_V \left[\frac{1}{dv} \int_{dv} \text{div} \mathbf{i}(\mathbf{r}, t) \gamma^\pi(\mathbf{r}, t) dv_m \right] dV \\
 & - \int_V \left[\frac{1}{dv} \int_{dv} \rho(\mathbf{r}, t) \mathbf{b}(\mathbf{r}, t) \gamma^\pi(\mathbf{r}, t) \right] dV \\
 & = \int_V \left[\frac{1}{dv} \int_{dv} \rho(\mathbf{r}, t) \mathbf{G}(\mathbf{r}, t) \gamma^\pi(\mathbf{r}, t) dv_m \right] dV
 \end{aligned}$$

As suggested in References [H&G79/1], [H&G79/2], [H&G80/3] and [deB91], it is possible obtain the following form of the general balance equation for the macroscopic thermodynamic property, $\bar{\psi}^\pi$, associated with the phase

$$\begin{aligned}
 & \int_V \left\{ \frac{\partial}{\partial t} [\langle \rho \rangle_\pi(\mathbf{x}, t) \bar{\psi}^\pi(\mathbf{x}, t)] + \text{div} [\langle \rho \rangle_\pi(\mathbf{x}, t) \bar{\mathbf{v}}^\pi(\mathbf{x}, t) \bar{\psi}^\pi(\mathbf{x}, t)] \right\} dV \\
 & - \int_V \left\{ \frac{1}{dv} \sum_{\alpha \neq \pi}^k \int_{da^{\pi\alpha}} \rho(\mathbf{r}, t) \psi(\mathbf{r}, t) [\mathbf{w}(\mathbf{r}, t) - \dot{\mathbf{r}}(\mathbf{r}, t)] \cdot \mathbf{n}^{\pi\alpha}(\mathbf{r}, t) da_m \right\} dV \\
 & - \int_V \left[\frac{1}{dv} \sum_{\alpha \neq \pi}^k \int_{da^{\pi\alpha}} \mathbf{i}(\mathbf{r}, t) \cdot \mathbf{n}^{\pi\alpha}(\mathbf{r}, t) da_m \right] dV \tag{2.16} \\
 & - \int_A \left\{ \frac{1}{da} \int_{da} [\mathbf{i}(\mathbf{r}, t) - \rho(\mathbf{r}, t) \tilde{\psi}^\pi(\mathbf{x}, \xi, t) \tilde{\mathbf{r}}^\pi] \cdot \mathbf{n}(\mathbf{r}, t) \gamma^\pi da_m \right\} dA \\
 & - \int_V \langle \rho \rangle_\pi(\mathbf{x}, t) \bar{\mathbf{b}}^\pi(\mathbf{x}, t) dV = \int_V \langle \rho \rangle_\pi(\mathbf{x}, t) \bar{\mathbf{G}}^\pi(\mathbf{x}, t) dV
 \end{aligned}$$

or in more concise form

$$\left[\int_V \left[\frac{\partial}{\partial t} (\langle \rho \rangle_\pi \bar{\psi}^\pi) + \text{div} (\langle \rho \rangle_\pi \bar{\psi}^\pi \bar{\mathbf{v}}^\pi) - \text{div} \mathbf{i}^\pi \right. \right.$$

$$-\langle \rho \rangle_{\pi} \left[\bar{\mathbf{b}}^{\pi} + \mathbf{e}^{\pi}(\rho\psi) + \mathbf{I}^{\pi} \right] dV = \int_V \rho_{\pi} \bar{\mathbf{G}}^{\pi} dv \quad [2.17]$$

where \mathbf{i}^{π} is the flux vector associated with $\bar{\psi}^{\pi}$

$\bar{\mathbf{b}}^{\pi}$ is the external supply of $\bar{\psi}^{\pi}$

$\langle \rho \rangle_{\pi}$ is the volume average value of mass density

This last balance equation contains two further interaction terms, which describe chemical and physical exchanges.

Exchange of due to mechanical interactions between the constituents is given by

$$\mathbf{I}^{\pi} = \frac{1}{\langle \rho \rangle_{\pi}} \sum_{\alpha \neq \pi} \int_{da^{\pi\alpha}} \mathbf{n}^{\pi\alpha} \cdot \mathbf{i} \, da_m \quad [2.18]$$

Phase change of a constituent or possible mass exchange between the constituent π and the other constituents α is given by

$$\mathbf{e}^{\pi}(\rho\psi) = \frac{1}{\langle \rho \rangle_{\pi}} \sum_{\alpha \neq \pi} \int_{da^{\pi\alpha}} \rho\psi (\mathbf{w} - \mathbf{i}) \cdot \mathbf{n}^{\pi\alpha} \, da_m \quad [2.19]$$

2.3 MACROSCOPIC BALANCE EQUATIONS FOR A NON ISOTHERMAL PARTIALLY SATURATED POROUS MATERIAL

In this section, the macroscopic balance equations for mass, linear momentum, angular momentum and energy (enthalpy) are obtained and then specialised for a deforming porous material where heat transfer and flow of water (liquid and vapour) and of dry air is taking place. The starting points are the microscopic balance equations [2.12], where, for each constituent, the generic thermodynamic variable, ζ , is replaced by appropriate microscopic quantities, suitable for a microscopic non polar material.

For the proper description of the nonisothermal unsaturated porous medium we need to take into account not only heat conduction and vapour diffusion, but also heat convection, liquid water flow due to pressure gradients or capillary effects and latent heat transfer due to water phase change (evaporation and condensation) inside the pores. Furthermore the solid is deformable, resulting in coupling of the fluid, the solid and the thermal fields. All fluid phases are in contact with the solid phase.

The constituents are assumed to be immiscible except for dry air and vapour, and chemically non reacting. Because of the local thermodynamic equilibrium hypothesis, the temperatures of each constituent at a point in the multiphase medium are taken to be equal. This does not mean that the temperature is uniform throughout the medium but only that at each point one temperature is sufficient to characterize the state.

Momentum exchanges due to mechanical interaction are independent of the temperature gradient.

In the following, the stress is defined as tension positive for the solid phase, while pore pressure is defined as compressive positive for the fluids.

It should be noticed that in this section the formulation is still material free, i.e. no specific assumptions for the material behaviour have been introduced so far, except for the quite general ones, indicated above. For the development of the macroscopic balance equations in the following sections, we still need to specify kinematics.

2.3.1 Kinematic Equations

As indicated in section 2.2, a multiphase medium can be described as the superposition of all π phases, whose material points, X^n , can be thought of as occupying simultaneously each spatial point x in the actual configuration. The state of motion of each phase is, however, described independently. Based on these assumptions, the kinematics of a multiphase medium is dealt with next.

In a Lagrangian or material description of motion, the position of each material point, x^π , at time, t , is function of its placement in a chosen reference configuration, and of the current time, t

$$\mathbf{x}^\pi = \mathbf{x}^\pi(\mathbf{X}^\pi, t) = x_i^\pi(X_1, X_2, X_3, t) = \varphi_i(\mathbf{X}^\pi) = \varphi(\mathbf{X}^\pi, t) \quad i = 1, 2, 3 \quad [2.20]$$

To have this mapping continuous and bijective at all times, the Jacobian, J , of this transformation must be non zero and strictly positive, since it is equal to the determinant of the deformation gradient tensor,

$$\mathbf{F}^\pi = \mathbf{Grad} \mathbf{x}^\pi \quad (\mathbf{F}^\pi)^{-1} = \mathbf{grad} \mathbf{X}^\pi \quad [2.21]$$

Because of the non-singularity of the Lagrangian relationship [2.20], its inverse can be written and the Eulerian or spatial description of motion follows

$$\mathbf{X}^\pi = \mathbf{X}^\pi(\mathbf{x}^\pi, t) \quad [2.22]$$

It is also assumed that functions which describe the motion have continuous derivatives. If the path of the particle of the π -phase is known, its velocity and acceleration are, in the material description

$$\mathbf{v}^\pi = \frac{\partial \mathbf{x}^\pi(\mathbf{X}^\pi, t)}{\partial t} \quad [2.23]$$

$$\mathbf{a}^\pi = \frac{\partial^2 \mathbf{x}^\pi(\mathbf{X}^\pi, t)}{\partial t^2} \quad [2.24]$$

The corresponding spatial expression can be obtained by introducing equation [2.22] into the above two equations. But, if only the spatial description is given for the velocity field in the form

$$\mathbf{v}^\pi = \mathbf{v}^\pi(\mathbf{x}^\pi, t) \quad [2.25]$$

to evaluate its time derivative with material coordinates held constant, we introduce the description of motion of equation [2.20] into the last equation. By applying the chain rule of differentiation, it follows

$$\mathbf{a}^\pi = \frac{\partial \mathbf{v}^\pi}{\partial t} + \mathbf{grad} \mathbf{v}^\pi \cdot \mathbf{v}^\pi \quad [2.26]$$

The material time derivative of any differentiable function, $f^\pi(\mathbf{x}, t)$, given in its spatial description and referring to a moving particle of the phase is

$$\frac{Df^\pi}{Dt} = \frac{\partial f^\pi}{\partial t} + \mathbf{grad} f^\pi \cdot \mathbf{v}^\pi \quad [2.27]$$

If superscript α is used for the operator $\frac{D}{Dt}$

$$\frac{Df^\pi}{Dt} = \frac{\partial f^\pi}{\partial t} + \mathit{grad} f^\pi \cdot \mathbf{v}^\alpha \quad [2.28]$$

the time derivative is taken moving with the α -phase.

Subtraction of equation [2.27] from equation [2.28] yields the following relation

$$\frac{Df^\pi}{Dt} = \frac{Df^\pi}{Dt} + \mathit{grad} f^\pi \cdot \mathbf{v}^{\alpha\pi} \quad [2.29]$$

where

$$\mathbf{v}^{\alpha\pi} = \mathbf{v}^\alpha - \mathbf{v}^\pi \quad [2.30]$$

is the velocity of the α phase with respect to the π phase. This velocity is called the diffusion velocity [H&G80/3].

The operator $\frac{D}{Dt}$ is a scalar operator and may be applied either to a vector quantity or a scalar quantity. If \mathbf{f}^π is a vector property per unit volume referring to the π phase, the total time derivative of its integral over a volume, V , is given by

$$\frac{d}{dt} \int_V \mathbf{f}^\pi dV = \int_V \left(\frac{\partial \mathbf{f}^\pi}{\partial t} + \mathit{grad} \mathbf{f}^\pi \cdot \mathbf{v}^\pi + \mathbf{f}^\pi \mathit{div} \mathbf{v}^\pi \right) dV = \int_V \left[\frac{\partial \mathbf{f}^\pi}{\partial t} + \mathit{div}(\mathbf{f}^\pi \otimes \mathbf{v}^\pi) \right] dV \quad [2.31]$$

For a scalar property, f^π

$$\frac{d}{dt} \int_V f^\pi dV = \int_V \left(\frac{\partial f^\pi}{\partial t} + \mathit{div}(f^\pi \mathbf{v}^\pi) \right) dV \quad [2.32]$$

In the above equations, velocities and accelerations of the π phase are considered as mass averaged quantities since these are the quantities usually measured in a field situation or in laboratory practice. In porous media theory it is customary to describe the motion of the fluid phases in terms of mass averaged velocities relative to the moving solid. Their motion is described with reference to the actual configuration assumed by the solid skeleton. The velocities and accelerations of each fluid particle can then be written with reference to the ones of corresponding solid points, once the relative velocities are introduced. We specify the superscripts π now as s for soil, w for the liquid phase and g for the gas phase (dry air plus vapour) and write for the relative velocities of water and gas phase respectively,

$$\mathbf{v}^{ws} = \mathbf{v}^w - \mathbf{v}^s \quad [2.33]$$

$$\mathbf{v}^{gs} = \mathbf{v}^g - \mathbf{v}^s \quad [2.34]$$

Water and gas acceleration are given from [2.26], [2.28], [2.33] and [2.34] as

$$\mathbf{a}^w = \mathbf{a}^s + \frac{D\mathbf{v}^{ws}}{Dt} + \mathit{grad}(\mathbf{v}^s + \mathbf{v}^{ws}) \cdot \mathbf{v}^{ws} \quad [2.35]$$

$$\mathbf{a}^g = \mathbf{a}^s + \frac{D\mathbf{v}^{gs}}{Dt} + \mathit{grad}(\mathbf{v}^s + \mathbf{v}^{gs}) \cdot \mathbf{v}^{gs} \quad [2.36]$$

The deformation process of the solid skeleton can be described by the velocity gradient tensor, \mathbf{L}^s , which, referred to spatial co-ordinates, is given by [C&T92] and [Mol86]:

$$\mathbf{L}^s \equiv \text{grad } \mathbf{v}^s = \mathbf{D}^s + \mathbf{W}^s \quad [2.37]$$

Its symmetric part \mathbf{D}^s , is called the eulerian strain rate tensor, being related to pure straining while its skew-symmetric component \mathbf{W}^s is the spin tensor.

2.3.2 Mass balance equations

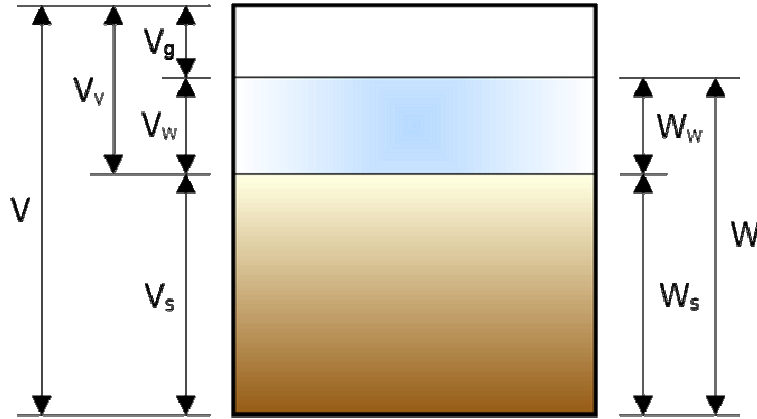


Figure 2.3: Schematic composition of soil

In the following, we identify the volume fractions, η^π , of the constituents as

solid phase

$$\eta^s = 1 - n \quad [2.38]$$

where $n = \frac{dv^w + dv^g}{dv}$ is the porosity

water

$$\eta^w = n \cdot S_w \quad [2.39]$$

where $S_w = \frac{dv^w}{dv^w + dv^g}$ is the degree of water saturation

gas

$$\eta^g = n \cdot S_g \quad [2.40]$$

where $S_g = \frac{dv^g}{dv^w + dv^g}$ is the degree of gas saturation

It follows immediately that

$$S_w + S_g = 1 \quad [2.41]$$

2.3.2.1 Solid phase

In the microscopic situation, the variables for solid in equation [2.12] assume the following values

$$\psi = \mathbf{1}, \mathbf{i} = \mathbf{0}, \mathbf{b} = \mathbf{0}, \mathbf{G} = \mathbf{0} \quad [2.42]$$

and the microscopic mass balance equation results in

$$\frac{\partial \rho}{\partial t} + \mathit{div}(\rho \dot{\mathbf{r}}) = 0 \quad [2.43]$$

The averaged macroscopic solid mass balance equation is

$$\frac{\partial \rho_s}{\partial t} + \mathit{div}(\rho_s \bar{\mathbf{v}}^s) = \rho_s \mathbf{e}^s(\rho) \quad [2.44]$$

Where ρ_s stands simply for $\langle \rho \rangle_\pi$, the phase averaged solid density and $\bar{\mathbf{v}}^s$ is the mass averaged solid velocity. The same simplified notation will be used for the other constituents, once π is accordingly specified.

From [2.27] we have

$$\frac{\overset{s}{D} \rho_s}{Dt} = \frac{\partial \rho_s}{\partial t} + \mathit{grad} \rho_s \cdot \bar{\mathbf{v}}^s \quad [2.45]$$

By introducing the latest in the previous equation we obtain

$$\frac{\overset{s}{D} \rho_s}{Dt} + \rho_s \mathit{div} \bar{\mathbf{v}}^s = 0 \quad [2.46]$$

By introducing intrinsic phase averaged densities through equation [2.8] we have finally

$$\frac{\overset{s}{D}(1-n)\rho^s}{Dt} + \rho^s(1-n)\mathit{div} \bar{\mathbf{v}}^s = 0 \quad [2.47]$$

where the shorthand $\rho_s = \langle \rho \rangle_s^s$ has been introduced for the intrinsic phase averaged density.

2.3.2.2 Liquid phase: water

As for the solid phase we have:

$$\frac{\partial \rho_w}{\partial t} + \mathit{div}(\rho_w \bar{\mathbf{v}}^w) = \rho_w \mathbf{e}^w(\rho) \quad [2.48]$$

$$\frac{\overset{w}{D} \rho_w}{Dt} + \rho_w \mathit{div} \bar{\mathbf{v}}^w = \rho_w \mathbf{e}^w(\rho) \quad [2.49]$$

$$\rho_w \mathbf{e}^w(\rho) = -\dot{m} \quad [2.50]$$

Is the quantity of water per unit time and volume, lost through evaporation.

2.3.2.3 Gaseous phases: dry air and vapour

The gaseous phase here is a multi-component material, composed of two different species: dry air and vapour. These species are miscible. We first write the mass balance equations for both species.

Their microscopic mass balance equations are again given by equation [2.43] if we neglect net production of mass of each species, due to chemical reactions with the other species [Has86/2].

The macroscopic mass balance equation for dry air is given by equation [2.44] with appropriate super/subscripts and with exchange term zero. We introduce intrinsic phase averaged densities and use super/subscript ga to indicate dry air. Because the two species, dry air and vapour, are miscible, they have the same volume fraction nS_g

$$\frac{\partial}{\partial t} (n S_g \rho^{ga}) + \text{div} (n S_g \rho^{ga} \bar{\mathbf{v}}^{ga}) = 0 \quad [2.51]$$

Similarly we write for vapour, using super/subscript

$$\frac{\partial}{\partial t} (n S_g \rho^{gw}) + \text{div} (n S_g \rho^{gw} \bar{\mathbf{v}}^{gw}) = n S_g \rho^{gw} e^{gw}(\rho) = \dot{m} \quad [2.52]$$

We now derive the mass balance equation for the whole gaseous phase. This is obtained by summing the macroscopic balance equations of the two species and using appropriate definitions for bulk properties of the gaseous phase [Has86/2].

$$\frac{\partial}{\partial t} (n S_g \rho^g) + \text{div} (n S_g \rho^g \bar{\mathbf{v}}^g) = \dot{m} \quad [2.53]$$

with

$$\rho^g = \rho^{ga} + \rho^{gw} \quad [2.54]$$

and

$$\bar{\mathbf{v}}^g = \frac{1}{\rho^g} (\rho^{ga} \bar{\mathbf{v}}^{ga} + \rho^{gw} \bar{\mathbf{v}}^{gw}) = \mathbf{c}^{ga} \bar{\mathbf{v}}^{ga} + \mathbf{c}^{gw} \bar{\mathbf{v}}^{gw} \quad [2.55]$$

where $\mathbf{c}^\pi = \rho^\pi / \rho^g$ is the mass fraction of component π , subject to

$$\sum_{\pi} \mathbf{c}^\pi = 1, \quad \pi = gw, ga \quad [2.56]$$

We introduce further the macroscopic diffusive dispersive velocity, $\mathbf{u}^\pi, \pi = ga, gw$ defined as [Has86/1]

$$\mathbf{u}^\pi = \bar{\mathbf{v}}^{\pi g} = \bar{\mathbf{v}}^\pi - \bar{\mathbf{v}}^g \quad [2.57]$$

and subject to

$$\rho^{ga} \mathbf{u}^{ga} + \rho^{gw} \mathbf{u}^{gw} = \rho^g \sum_{\pi} \mathbf{c}^\pi \mathbf{u}^\pi = 0 \quad [2.58]$$

Transformation of [2.53] as in the case of the mass balance equation for the solid phase yields for gas

$$\frac{g}{Dt} (n S_g \rho^g) + n S_g \rho^g \text{div} \bar{\mathbf{v}}^g = \dot{m} \quad [2.59]$$

With a proceedings similar to the earlier we obtained the following form of the mass balance equation for vapour

$$\frac{g}{Dt} (n S_g \rho^{gw}) + \text{div} (n S_g \rho^{gw} \mathbf{u}^{gw}) + n S_g \rho^{gw} \text{div} \bar{\mathbf{v}}^g = \dot{m} \quad [2.60]$$

We introduce now the diffusive-dispersive mass flux of component gw as [E&S64]

$$\mathbf{J}_g^{gw} = n S_g \rho^{gw} \mathbf{u}^{gw} \quad [2.61]$$

and now we can write

$$\frac{g}{Dt} (n S_g \rho^{gw}) + \text{div } \mathbf{J}_g^{gw} + n S_g \rho^{gw} \text{div } \bar{\mathbf{v}}^g = \dot{m} \quad [2.62]$$

2.3.3 Linear momentum balance equation

Solid phase

$$\text{div } \mathbf{t}^s + \rho_s (\bar{\mathbf{g}}^s - \bar{\mathbf{a}}^s) + \rho_s \hat{\mathbf{t}}^s = \mathbf{0} \quad [2.63]$$

Liquid phase

$$\text{div } \mathbf{t}^\pi + \rho_\pi (\bar{\mathbf{g}}^\pi - \bar{\mathbf{a}}^\pi) + \rho_\pi [\mathbf{e}^\pi (\rho \dot{\mathbf{r}}) + \hat{\mathbf{t}}^\pi] = \mathbf{0} \quad [2.64]$$

where $\bar{\mathbf{g}}^\pi = \frac{1}{\rho_\pi} \int_{dv} \rho \mathbf{g} \gamma^\pi dv_m$ is the external momentum supply, which we assume to be related to gravitational effects

$$\bar{\mathbf{a}}^\pi = \dot{\bar{\mathbf{v}}^\pi} = \frac{\partial \bar{\mathbf{v}}^\pi}{\partial t} + \text{grad } \bar{\mathbf{v}}^\pi \cdot \bar{\mathbf{v}}^\pi \text{ is the } \pi\text{-phase acceleration}$$

The term

$$\mathbf{I}^\pi = \hat{\mathbf{t}}^\pi = \frac{1}{\rho_\pi} \int_{dv} \sum_{\alpha \neq \pi} \int_{da^{\pi\alpha}} \mathbf{t}_m \cdot \mathbf{n}^{\pi\alpha} da_m \quad [2.65]$$

accounts for the exchange of momentum due to mechanical interaction of π -phase with the other α -phases.

2.3.4 Angular momentum balance equation

As indicated in section 2.3, all phases of the semi-saturated porous medium are considered microscopically non-polar. The following microscopic variables are necessary for the balance equation [2.12] when angular momentum balance is considered

$$\boldsymbol{\psi} = \mathbf{r} \times \dot{\mathbf{r}}$$

$$\mathbf{i} = \mathbf{r} \times \mathbf{t}_m$$

$$\mathbf{b} = \mathbf{r} \times \mathbf{g}$$

$$\mathbf{G} = \mathbf{0}$$

[2.66]

With a proceedings similar to the earlier balance equation, or with an appropriate method chosen for the development of the average angular momentum equation [deB91] and [H&G79/2], that for non-polar media, also at macroscopic level, it can be shown that the partial stress tensor is symmetric

$$\mathbf{t}^\pi = (\mathbf{t}^\pi)^T \quad [2.67]$$

and that the sum of the coupling vectors of angular momentum between the phases vanishes.

2.3.5 Balance of energy equation

For the energy balance, the following components must be taken into account in the generic microscopic balance equation [2.12]:

$$\begin{aligned}
 \psi &= E + \frac{1}{2} \dot{\mathbf{r}} \cdot \dot{\mathbf{r}} \\
 \mathbf{i} &= \mathbf{t}_m \dot{\mathbf{r}} - \mathbf{q} \\
 \mathbf{b} &= \mathbf{g} \cdot \dot{\mathbf{r}} + h \\
 \mathbf{G} &= 0
 \end{aligned}
 \tag{2.68}$$

where $E(\mathbf{r}, t)$ is the specific intrinsic energy

$\rho(\mathbf{r}, t)$ is the heat flux vector

$h(\mathbf{r}, t)$ is the intrinsic heat source

The energy balance equation can be written as follows

$$\rho_\pi \frac{D \bar{E}^\pi}{Dt} = \mathbf{t}^\pi : \mathbf{D}^\pi + \rho_\pi h^\pi - \text{div} \tilde{\mathbf{q}}^\pi + \rho_\pi R^\pi
 \tag{2.69}$$

where $\rho_\pi R^\pi = \rho_\pi \left[\mathbf{e}^\pi(\rho \hat{\mathbf{E}}) - \mathbf{e}^\pi(\rho) \bar{E}^\pi + Q^\pi \right]$

The equilibrium between all the phases can be write

$$\sum_\pi \rho_\pi \left[\mathbf{e}^\pi(\rho \hat{\mathbf{E}}) + \mathbf{e}^\pi(\rho \tilde{\mathbf{r}}) \cdot \bar{\mathbf{v}}^\pi + \frac{1}{2} \mathbf{e}^\pi(\rho) \bar{\mathbf{v}}^\pi \cdot \bar{\mathbf{v}}^\pi + \hat{\mathbf{t}}^\pi \cdot \bar{\mathbf{v}}^\pi + Q^\pi \right] = 0
 \tag{2.70}$$

and physically means that the total balance of energy exchange between all the phases is zero.

2.3.6 Entropy inequality

Exploitation of entropy inequality is a tool for developing constitutive equations in a systematic manner, leading to a consistent thermodynamic description of the material behaviour at macroscale. The use of entropy inequality further assures that the second law of thermodynamics is not violated. The procedure was proposed by Coleman and Noll [C&N63]. It is, for instance, exploited in [S&W79], and by Gray and Hassanizadeh [G&H91/1] for the development of constitutive equations for unsaturated flow in dry or partially saturated soil, including interfacial phenomena.

The variables in the microscopic balance equation [2.12] are now

$$\begin{aligned}
 \psi &= \lambda \\
 \mathbf{i} &= \emptyset \\
 \mathbf{b} &= \mathbf{s} \\
 \mathbf{G} &= \varphi
 \end{aligned}
 \tag{2.71}$$

where λ is the specific entropy

\emptyset is the entropy flux vector

\mathbf{s} is an intrinsic entropy source

The net production φ denotes an increase of entropy. The balance equation becomes then

$$\frac{\partial}{\partial t}(\rho \lambda) + \text{div}(\rho \lambda \dot{\mathbf{r}}) - \text{div} \emptyset - \rho \mathbf{s} = \rho
 \tag{2.72}$$

Starting from this last equation, λ^π , the averaged specific entropy of constituent π , and the entropy supply due to mass exchange are determined for obtain the entropy inequality for the mixture

$$\sum_{\pi} \left[\rho_{\pi} \frac{D\bar{\lambda}^{\pi}}{Dt} + \rho_{\pi} \mathbf{e}^{\pi}(\rho) \bar{\lambda}^{\pi} + \operatorname{div} \left(\frac{1}{\Theta^{\pi}} \mathbf{q}^{\pi} \right) - \frac{1}{\Theta^{\pi}} \rho_{\pi} h^{\pi} \right] \geq 0 \quad [2.73]$$

where $\bar{\lambda}^{\pi} = \frac{1}{\rho_{\pi}} \int_{dv} \rho \lambda \gamma^{\pi} dv_m$

\mathbf{q}^{π} the flux of entropy for unit of temperature

$\frac{h^{\pi}}{\Theta^{\pi}}$ is the source of entropy for each phase

Again, this corresponds to the form used in the mixture theory as shown in [deB91].

Before further transformations of the macroscopic balance equations are made, we introduce the constitutive equations for the constituents.

2.4 CONSTITUTIVE EQUATIONS

To complete the description of the mechanical behaviour, we now need to specify the constitutive equations. The balance equations developed in the previous sections allows for the introduction of quite elaborate constitutive theories, especially if the balance equations presented in the previous sections for the bulk material are extended to the interfaces, as done by Gray and Hassanizadeh in [G&H91/1] and [G&H91/2] for the aspects concerning multiphase flow. For the solid phase, second-grade material theories are also possible, where the gradients of relevant thermodynamic properties, such as densities, are considered as independent variables [Ehl89]. However, since this book is application oriented, i.e. we aim for the quantitative solution of real engineering problems, we make a different choice.

We select constitutive models which are based on quantities currently measurable in laboratory or field experiments, and which have been extensively validated both with reference to known exact solutions and to experiments. Many of these constitutive models correspond to linearization of more complex arguments.

We deal first with the properties of the fluid phases, and only briefly mention the solid phase here, because this is the main aspect of this thesis and then this will be seen later.

2.4.1 Stress tensor in the fluid phases

By applying entropy inequality for the bulk material [H&G80/3] [G&H91/1], it can be shown that the stress tensor in the fluid phases, is

$$\mathbf{t}^{\pi} = -\eta^{\pi} p^{\pi} \mathbf{I} \quad [2.74]$$

where \mathbf{I} is the identity tensor

p^{π} is the macroscopic pressure of the π -phase

The volume fraction, η^{π} , appears in equation [2.74] because \mathbf{t}^{π} is the force exerted on the fluid-phase per unit area of multiphase medium. It should be noted that the stress vector in the fluid phase does not have any dissipating part. The

macroscopic effects of deviatoric stress components will be accounted for in linear momentum balance equations through momentum exchange terms.

2.4.2 Gaseous mixture of dry air and water vapour

The moist air in the pore system is usually assumed to be a perfect mixture of two ideal gases, i.e. dry air and water vapour. Hence the ideal gas law, relating the partial pressure, $p_{g\pi}$, of species π , the mass concentration, $\rho^{g\pi}$, of species π in the gas phase and the absolute temperature, Θ , is used.

The equations of state of a perfect gas, applied to dry air (ga), vapour (gw) and moist air (g) are

$$p^{ga} = \rho^{ga} \Theta R / M_a \quad [2.75]$$

$$p^{gw} = \rho^{gw} \Theta R / M_w$$

$$\rho^g = \rho^{ga} + \rho^{gw}$$

$$p^g = p^{ga} + p^{gw} \quad [2.76]$$

$$M_g = \left(\frac{\rho^{gw}}{\rho^g} \frac{1}{M_w} + \frac{\rho^{ga}}{\rho^g} \frac{1}{M_a} \right)^{-1}$$

where M_π is the molar mass of constituent π

R is the universal gas constant

The second of equations [2.76] expresses Dalton's law [M&S93]. For the averaging process it is reminded that dry air, vapour and moist air occupy the same volume fraction, nS_g .

2.4.3 Sorption equilibrium

If an oven-dry porous medium is exposed to moist air, the weight of such solid increases because the moisture is adsorbed on the inner surfaces of the pores starting with the finest ones. In the cases of interest here, the water is usually present as a condensed liquid that, because of the surface tension, is separated from its vapour by a concave meniscus (capillary water). There is then a relationship between the relative humidity, the water content (saturation) and the capillary pressure in the pores.

The capillary pressure is defined as the pressure difference between the gas phase and the liquid phase, by the capillary pressure equation

$$p^c = p^g - p^w \quad [2.77]$$

where p^w is the pressure of the liquid-phase (water).

In [G&H91/2], it is shown that $p^c = p^g - p^w$ is not just a definition, but a derived relationship between two independent quantities p^c and $p^g - p^w$, at equilibrium.

For the relationship between the relative humidity (R.H.) and the capillary pressure in the pores, Kelvin-Laplace law is assumed to be valid

$$R.H. = \frac{p^{gw}}{p^{gws}} = \exp \left(\frac{p^c M_w}{\rho^w R \Theta} \right) \quad [2.78]$$

The water vapour saturation pressure, p^{gws} , which is a function of the temperature only, can be obtained from the Clausius-Clapeyron equation indicated below, or from empirical formulas such as the one proposed by Hyland and Wexler [ASH93].

Assuming zero contact angle between the liquid phase and the solid phase, as is usually accepted for pore water, the capillary pressure can be obtained through the Laplace equation from the pore radius, r

$$p^c = \frac{2\sigma}{r} \quad [2.79]$$

where σ is the surface tension

These considerations are applicable if the water is present in the pores, as a condensed liquid (capillary region). When, instead, the water is present as one or more molecular layers adsorbed on the surface of a solid because of the Van der Waals and/or other interactions, the capillary pressure no longer has an obvious meaning, even if it can be retained, referring to the broader concept of water potential or moisture stress. In such a case, a direct relationship between the water content and the relative humidity is assumed to hold such as the BET equation. [ASH93].

2.4.4 Clausius-Clapeyron equation

As indicated above, this equation links the water vapour saturation pressure with temperature

$$p^{gws}(\Theta) = p^{gws0} \exp \left[-\frac{M_w \Delta H_{gw}}{R} \left(\frac{1}{\Theta} - \frac{1}{\Theta_0} \right) \right] \quad [2.80]$$

where Θ_0 is a reference temperature

p^{gws} is the water vapour saturation pressure at Θ

p^{gws0} is the water vapour saturation pressure at Θ_0

ΔH_{gw} is the specific enthalpy of evaporation

The equation is obtained from the second law of thermodynamics and is valid in the vicinity of Θ_0 .

In the following, we denote T as the temperature difference above a reference value such that

$$T = \Theta - \Theta_0 \quad [2.81]$$

2.4.5 Pore size distribution

As it turns out from equations [2.78] and [2.79], the problem is to know the pore size distribution of the considered porous medium, to relate the size of the largest pore filled (from which the capillary pressure depends) with the actual water content. This relationship is obtained through experimental tests, usually centrifuge tests, sorption isotherm measurements or mercury porosimetry.

The question is somewhat complex, because both the Laplace equation [2.79] and the Kelvin equation [2.78] are obtained from a force equilibrium, evaluated in a cylindrical capillary tube, and the porous medium is considered as a bundle of capillary tubes that do not intersect. The real porous media are more correctly represented as three-dimensional networks of sites (or bodies) interconnected by narrower bonds (or throats) and then intrusion, extrusion, adsorption and desorption are subjected to hysteresis. In this case, the actual value of capillary pressure can be only

interpreted as a measurable quantity describing complex adsorbed water-solid matrix interaction. The determination of pore size distribution from sorption isotherms, results of centrifuge tests and mercury porosimetry should then be done following the percolation theory approach, [B&S78].

The Rayleigh distribution or the log-normal distributions are often a good estimation of the pore size and often such distribution can be bi-modal or multi-modal.

For soils, we need the Kelvin-Laplace equation [2.78], the Clausius-Clapeyron equation [2.80] and the capillary pressure relationship

$$S_{\pi} = S_{\pi}(p^c, T) \quad [2.82]$$

which is directly obtained in laboratory.

In later chapters, where the constitutive models are introduced, will show different relationships for the pore size distribution and one of them gives

$$S_{\pi} = S_{\pi}(p^c, T, \varepsilon_v) \quad [2.83]$$

where ε_v is the volumetric strain

2.4.6 Equation of state for water

From the mass conservation in differential form

$$\frac{D^w(\rho^w V^w)}{Dt} = 0 \quad [2.84]$$

It can be possible to obtain

$$\frac{1}{\rho^{wo}} \frac{D^w \rho^w}{Dt} = \frac{1}{K_w} \frac{D^w p^w}{Dt} - \beta_w \frac{D^w T}{Dt} \quad [2.85]$$

where β_w is the thermal expansion coefficient

$$K_w = \frac{1}{C_w}$$

C_w is the compressibility coefficient

and where

$$\frac{1}{\rho^{wo}} \frac{\partial \rho^w}{\partial p^w} = \frac{1}{K_w} \quad [2.86]$$

$$\frac{1}{\rho^{wo}} \frac{\partial \rho^w}{\partial T} = -\beta_w \quad [2.87]$$

2.4.7 Darcy's law

Darcy's law, generalized to allow for relative permeability

$$\eta^{\pi} \bar{\mathbf{v}}^{\pi s} = \frac{\mathbf{k}^{r\pi} \mathbf{k}}{\mu^{\pi}} (-\text{grad } p^{\pi} + \rho^{\pi} \mathbf{g}) \quad [2.88]$$

where \mathbf{k} is the permeability of the medium

μ is the dynamic viscosity

$k^{r\pi}$ the relative permeability, a dimensionless parameter varying from zero to one

is assumed valid for the transport of both water and gas in slow phenomena.

For each particular porous medium, the relations $k^{r\pi}(S_w)$ are either predicted by models based on some more or less realistic capillary assumption or experimentally determined in laboratory as well as field conditions. For typical curves of relative permeabilities to water and air the reader is referred to Corey [Cor57].

The relative permeability goes to zero before the saturation reaches the value zero. The water saturation at which the relative permeability goes to zero is termed the residual water saturation or displacement residual water saturation.

Relationships used in the following are e.g. those by Brooks and Corey [B&C66]

$$k^{rw} = S_e^{\frac{(2+3\lambda)}{\lambda}} \quad [2.89]$$

$$p^c = \frac{p^b}{S_e^{\frac{1}{\lambda}}} \quad [2.90]$$

where $S_e = \frac{S_w - S_{wc}}{1 - S_{wc}}$ is the effective saturation

S_{wc} is the irreducible saturation

λ the pore size distribution index

p^b the bubbling pressure

2.4.8 Fick's law

Diffusive-dispersive mass flux is governed by Fick's law

$$\mathbf{J}_\alpha^\pi = -\rho^\alpha \mathbf{D}_\alpha^\pi \text{grad} \left(\frac{\rho^\pi}{\rho^\alpha} \right) \quad [2.91]$$

where \mathbf{D}_α^π is the effective dispersion tensor

π is diffusing phase

a is the phase in which diffusion takes place ($\alpha = w, g$)

\mathbf{D}_α^π is a function of the tortuosity factor, which accounts for the tortuous nature of the pathway in soil; because of mechanical dispersion, \mathbf{D}_α^π is also correlated with seepage velocity.

For dry air and water vapour (binary system) we have in particular, by the first of equations [2.76] and from the relation

$\rho^g = \rho^{ga} + \rho^{gw}$ that

$$\begin{aligned} \mathbf{J}_g^{ga} &= -\rho^g \frac{M_a M_w}{M_g^2} \mathbf{D}_g \text{grad} \left(\frac{p^{ga}}{\rho^g} \right) = \\ &= \rho^g \frac{M_a M_w}{M_g^2} \mathbf{D}_g \text{grad} \left(\frac{p^{gw}}{\rho^g} \right) = -\mathbf{J}_g^{gw} \end{aligned} \quad [2.92]$$

It is worthwhile to emphasise that gas diffusion can take place even in the absence of a gas pressure gradient, i.e. when its mass weighted velocity $\bar{\mathbf{v}}^g$ is zero.

2.4.9 Stress tensor in the solid phase and total stress

From the entropy inequality written in [G&H91/1] for unsaturated flow, including interfacial phenomena, it can be shown that the stress vector in the solid phase is

$$\mathbf{t}^s = (1 - n)(\mathbf{t}_e^s - \mathbf{l}p^s) \quad [2.93]$$

pressure in the solid phase is

$$p^s = p^w S_w + p^g S_g \quad [2.94]$$

and

$$\boldsymbol{\sigma}' = (1 - n)\mathbf{t}_e^s \quad [2.95]$$

is the effective stress tensor.

Introduction of [2.94] into [2.93] yields

$$\mathbf{t}^s = (1 - n)\left[\mathbf{t}_e^s - \mathbf{l}(S_w p^w + S_g p^g)\right] \quad [2.96]$$

The volume fraction (1-n) indicates that \mathbf{t}^s is the stress exerted on the solid phase per unit area of a multiphase medium. The sum of [2.96] and of [2.74] written for gas and for water gives the total stress, $\boldsymbol{\sigma}$, acting on a unit area of a multiphase medium

$$\boldsymbol{\sigma} = \mathbf{t}^s + \mathbf{t}^w + \mathbf{t}^g = (1 - n)\left[\mathbf{t}_e^s - \mathbf{l}(S_w p^w + S_g p^g)\right] - S_w n \mathbf{l} p^w - S_g n \mathbf{l} p^g = (1 - n)\mathbf{t}_e^s - \mathbf{l}(S_w p^w + S_g p^g) \quad [2.97]$$

This can be put in the usual soil mechanics form as

$$\boldsymbol{\sigma} = \boldsymbol{\sigma}' - \mathbf{l}(S_w p^w + S_g p^g) \quad [2.98]$$

or

$$\boldsymbol{\sigma}' = \boldsymbol{\sigma} + \mathbf{l}(S_w p^w + S_g p^g) \quad [2.99]$$

From this last equation, it follows that the relationship between effective stress and total stress, in partially saturated porous media, is no longer independent of the soil type because of the saturations, while in fully saturated soils, where $S_g=0$ and $S_w=1$, the effective stress principle is unique for all soil types.

An expression of the effective stress principle was obtained by Bishop and Blight [B&B63] using a phenomenological approach.

The effective stress is responsible for all major deformations in the skeleton and is linked to the strain rate tensor, \mathbf{D}^s , by means of a constitutive relationship

$$\frac{D\boldsymbol{\sigma}'}{Dt} = \mathbf{D}_T \left[(\mathbf{D}^s - \mathbf{D}_0^s) \right] \quad [2.100]$$

where

$$\mathbf{D}_T = \mathbf{D}_T(\mathbf{D}^s, \boldsymbol{\sigma}', p^c, T) \quad [2.101]$$

is a fourth order tensor and \mathbf{D}_0^s represents the increment of all other strains not directly associated with stress changes.

2.4.10 Solid density

When considering the solid phase as compressible, a relationship for the material time derivative of the solid density can be obtained from the mass conservation equation in differential form

$$\frac{\overset{s}{D}(\rho^s V^s)}{Dt} = 0 \quad [2.102]$$

By assuming that the solid density is a function of p^s , of temperature and of the first invariant of the effective stress, and defining the Biot's constant [B&W57] as

$$\alpha = 1 - \frac{K_T}{K_s} \quad [2.103]$$

we obtain

$$\frac{1}{\rho^s} \frac{\overset{s}{D}\rho^s}{Dt} = \frac{1}{1-n} \left[(\alpha - n) \frac{1}{K_s} \frac{\overset{s}{D}p^s}{Dt} - \beta_s (\alpha - n) \frac{\overset{s}{D}T}{Dt} - (1-\alpha) \text{div } \bar{\mathbf{v}}^s \right] \quad [2.104]$$

where K_T is the bulk modulus of the skeleton

K_s is the bulk modulus of the of the grain material

β_s is the thermal expansion coefficient for the solid

In soils volumetric strain is relatively insignificant and can be ignored ($\alpha=1$), but it is important in rock mechanics and in concrete, where the compressibility of the solid phase is comparable to that of the skeleton.

2.4.11 Fourier's Law

A constitutive assumption for the heat flux is the generalized Fourier's Law

$$\bar{\mathbf{q}} = -\chi_{\text{eff}} \text{grad } T \quad [2.105]$$

where χ_{eff} is the effective thermal conductivity tensor and is the heat flux of the multiphase medium

For isotropic media the generalized Fourier's Law becomes the well known empirical Fourier's Law

$$\mathbf{q} = -\chi_{\text{eff}} \text{grad } T \quad [2.106]$$

where χ_{eff} is the effective thermal conductivity

The effective thermal conductivity can be predicted theoretically as well as determined experimentally.

For porous building materials, for instance, the following linear relationship may be used, which represents with sufficient accuracy the data by Bomberg and Shirliffe [B&S78]

$$\chi_{\text{eff}} = \chi_{\text{dry}} \left(1 + 4 \frac{n S^w \rho^w}{(1-n) \rho^s} \right) \quad [2.107]$$

2.5 GENERAL FIELD EQUATIONS

The macroscopic balance laws are now transformed, and the constitutive equations introduced, to obtain the general field equations, which will be used in the subsequent chapters. The averaging symbol, overbar, will be omitted in the remainder of this book, because all quantities belong to the macroscopic situations.

2.5.1 Mass balance equation

2.5.1.1 Solid phase

The macroscopic mass balance equation for the solid phase [2.47], divided by ρ^s is

$$\frac{1-n}{\rho^s} \frac{\overset{s}{D}\rho^s}{Dt} - \frac{\overset{s}{D}n}{Dt} + (1-n) \operatorname{div} \mathbf{v}^s = 0 \quad [2.108]$$

2.5.1.2 Liquid phase

Upon introduction of the relative velocity [2.33] and the material time derivative with respect to the moving solid [2.29] equation [2.49] for liquid water becomes

$$\frac{\overset{s}{D}\rho_w}{Dt} + \mathbf{v}^{ws} \cdot \operatorname{grad} \rho_w + \rho_w \operatorname{div} (\mathbf{v}^s + \mathbf{v}^{ws}) = -\dot{m} \quad [2.109]$$

Introduction of intrinsic phase averaged densities with the appropriate volume fractions, use of vector identity written for water and division by $S_w \rho^w$ allows us to transform last equation into

$$\frac{\overset{s}{D}n}{Dt} + \frac{n}{\rho^w} \frac{\overset{s}{D}\rho^w}{Dt} + \frac{n}{S_w} \frac{\overset{s}{D}S_w}{Dt} + \frac{1}{S_w \rho^w} \operatorname{div} (n S_w \rho^w \mathbf{v}^{ws}) + n \operatorname{div} \mathbf{v}^s = -\frac{\dot{m}}{S_w \rho^w} \quad [2.110]$$

Summation with [2.108], to eliminate $\frac{\overset{s}{D}n}{Dt}$ gives

$$\frac{(1-n)}{\rho^s} \frac{\overset{s}{D}\rho^s}{Dt} + \operatorname{div} \mathbf{v}^s + \frac{n}{\rho^w} \frac{\overset{s}{D}\rho^w}{Dt} + \frac{n}{S_w} \frac{\overset{s}{D}S_w}{Dt} + \frac{1}{S_w \rho^w} \operatorname{div} (n S_w \rho^w \mathbf{v}^{ws}) = -\frac{1}{S_w \rho^w} \dot{m} \quad [2.111]$$

Introduction of [2.85] and [2.104] for the material derivatives of the solid and water densities and of [2.94] gives

$$\begin{aligned} & \frac{\alpha - n}{K_s} \frac{\overset{s}{D}}{Dt} (S^w p^w + S^g p^g) - \beta_s (\alpha - n) \frac{\overset{s}{D}T}{Dt} + \alpha \operatorname{div} \mathbf{v}^s + n \left(\frac{1}{K_w} \frac{\overset{s}{D}p^w}{Dt} - \beta_w \frac{\overset{s}{D}T}{Dt} \right) \\ & + \frac{n}{S_w} \frac{\overset{s}{D}S_w}{Dt} + \frac{1}{S_w \rho^w} \operatorname{div} (n S_w \rho^w \mathbf{v}^{ws}) = -\frac{1}{S_w \rho^w} \dot{m} \end{aligned} \quad [2.112]$$

where p^w , p^g and T are independent variables

$$\beta_{sw} = S_w [(\alpha - n)\beta_s + n\beta_w]$$

For incompressible grains ($\alpha = 1$ and $\frac{1}{K_s} = 0$) this equation may be simplified as follows

$$\frac{n S_w}{K_w} \frac{\overset{s}{D} p^w}{Dt} + S_w \operatorname{div} \mathbf{v}^s - \beta_{sw} \frac{\overset{s}{D} T}{Dt} + n \frac{\overset{s}{D} S_w}{Dt} + \frac{1}{\rho^w} \operatorname{div} (n S_w \rho^w \mathbf{v}^{ws}) = - \frac{\dot{m}}{\rho^w} \quad [2.113]$$

2.5.1.3 Gaseous phase

The mass balance equation for gas as a mixture of dry air and vapour is dealt with next.

In the same mode of the liquid phase, starting from [2.59] we obtain

$$\begin{aligned} & \frac{\alpha - n}{K_s} S_w S_g \frac{\overset{s}{D} p^w}{Dt} + \frac{\alpha - n}{K_s} S_g^2 \frac{\overset{s}{D} p^g}{Dt} + \alpha S_g \operatorname{div} \mathbf{v}^s + \frac{n S_g}{\rho^g} \frac{\overset{s}{D} \left[\frac{1}{\Theta R} (p^{ga} M_a + p^{gw} M_w) \right]}{Dt} + \\ & - \left(\frac{\alpha - n}{K_s} p^c S_g + n \right) \frac{\overset{s}{D} S_w}{Dt} + \frac{1}{\rho^g} \operatorname{div} (n S_g \rho^g \mathbf{v}^{gs}) - \beta_s (\alpha - n) S_g \frac{\overset{s}{D} T}{Dt} = \frac{1}{\rho^g} \dot{m} \end{aligned} \quad [2.114]$$

where p^w , p^g and T are independent variables

For incompressible grains ($\alpha = 1$ and $\frac{1}{K_s} = 0$) this equation may be simplified as follows

$$\begin{aligned} & - n \frac{\overset{s}{D} S_w}{Dt} - \beta_s (1 - n) S_g \frac{\overset{s}{D} T}{Dt} + S_g \operatorname{div} \mathbf{v}^s + \frac{n S_g}{\rho^g} \frac{\overset{s}{D} \left[\frac{1}{\Theta R} (p^{ga} M_a + p^{gw} M_w) \right]}{Dt} \\ & + \frac{1}{\rho^g} \operatorname{div} (n S_g \rho^g \mathbf{v}^{gs}) = \frac{\dot{m}}{\rho^g} \end{aligned} \quad [2.115]$$

For heat transfer analysis, in partially saturated porous media, it is more convenient to consider the mass balance equation for dry air separately from that of vapour [Bag93] [Gaw95] and to sum the mass balance equations for both water species, liquid water and water vapour. In this way, the mass rate of water evaporation, \dot{m} , disappears from the mass balance equations. An evolution equation needed and this will be given by the energy balance equation. Note that, in this way, no constitutive model for the mass rate of water evaporation is needed.

2.5.1.4 Gaseous phase: dry air

The mass balance equation for dry air is transformed in the following equation

$$\frac{\overset{g}{D} (n S_g \rho^{ga})}{Dt} + \operatorname{div} \mathbf{J}_g^{ga} + n S_g \rho^{ga} \operatorname{div} \mathbf{v}^g = 0 \quad [2.116]$$

The resulting equation is divided by $\rho^{ga} S_g$ and summed with [2.108] we obtained

$$\begin{aligned} & \frac{\alpha - n}{K_s} S_w S_g \frac{\overset{s}{D} p^w}{Dt} + \frac{\alpha - n}{K_s} S_g^2 \frac{\overset{s}{D} p^g}{Dt} + \alpha S_g \operatorname{div} \mathbf{v}^s + \frac{n S_g}{\rho^{ga}} \frac{\overset{s}{D} \rho^{ga}}{Dt} + \frac{1}{\rho^{ga}} \operatorname{div} \mathbf{J}_g^{ga} + \\ & - \left(\frac{\alpha - n}{K_s} p^c S_g + n \right) \frac{\overset{s}{D} S_w}{Dt} + \frac{1}{\rho^{ga}} \operatorname{div} (n S_g \rho^{ga} \mathbf{v}^{gs}) - \beta_s (\alpha - n) S_g \frac{\overset{s}{D} T}{Dt} = 0 \end{aligned} \quad [2.117]$$

For incompressible solid grains this equation is simplified as

$$\begin{aligned}
 & -n \frac{\overset{s}{D} S_w}{Dt} - \beta_s (1-n) S_g \frac{\overset{s}{D} T}{Dt} + S_g \operatorname{div} v^s + \frac{n S_g}{\rho^g} \frac{\overset{s}{D}}{Dt} \left[\frac{1}{\ominus R} (\rho^{ga} M_a + \rho^{gw} M_w) \right] \\
 & + \frac{1}{\rho^g} \operatorname{div} (n S_g \rho^g v^{gs}) = \frac{\dot{m}}{\rho^g}
 \end{aligned} \tag{2.118}$$

Introducing now the constitutive equations for ρ^{ga} and for \mathbf{J}_g^{ga} to obtain

$$\begin{aligned}
 & -n \frac{\overset{s}{D} S_w}{Dt} - \beta_s (1-n) S_g \frac{\overset{s}{D} T}{Dt} + S_g \operatorname{div} v^s + \frac{S_g n}{\rho^{ga}} \frac{\overset{s}{D}}{Dt} \left(\frac{M_a}{\ominus R} \rho^{ga} \right) \\
 & - \frac{1}{\rho^{ga}} \operatorname{div} \left[\rho^g \frac{M_a M_w}{M_g^2} D_g \operatorname{grad} \left(\frac{\rho^{ga}}{\rho^g} \right) \right] + \frac{1}{\rho^{ga}} \operatorname{div} (n S_g \rho^{ga} v^{gs}) = 0
 \end{aligned} \tag{2.119}$$

2.5.1.5 Gaseous phase: vapour

The way to derive the mass balance equation for vapour is identical to that of dry air and results, for the case of incompressible solid grains, in

$$\begin{aligned}
 & -n \frac{\overset{s}{D} S_w}{Dt} - \beta_s (1-n) S_g \frac{\overset{s}{D} T}{Dt} + S_g \operatorname{div} v^s + \frac{S_g n}{\rho^{gw}} \frac{\overset{s}{D}}{Dt} \left(\frac{M_w}{\ominus R} \rho^{gw} \right) \\
 & - \frac{1}{\rho^{gw}} \operatorname{div} \left[\rho^g \frac{M_a M_w}{M_g^2} D_g \operatorname{grad} \left(\frac{\rho^{gw}}{\rho^g} \right) \right] + \frac{1}{\rho^{gw}} \operatorname{div} (n S_g \rho^{gw} v^{gs}) = \frac{\dot{m}}{\rho^{gw}}
 \end{aligned} \tag{2.120}$$

This equation is now multiplied by ρ^{gw} and added to the mass balance equation of liquid water, in turn multiplied by ρ^w .

This sum gives the mass balance equation for the water species, liquid and vapour, without mass rate of water evaporation as

$$\begin{aligned}
 & n(\rho^w - \rho^{gw}) \frac{\overset{s}{D} S_w}{Dt} - \beta_{swg} \frac{\overset{s}{D} T}{Dt} + (\rho^{gw} S_g + \rho^w S_w) \operatorname{div} v^s \\
 & + \frac{n \rho^w S_w}{K_w} \frac{\overset{s}{D} \rho^w}{Dt} + S_g n \frac{\overset{s}{D}}{Dt} \left(\frac{M_w}{\ominus R} \rho^{gw} \right) - \operatorname{div} \left[\rho^g \frac{M_a M_w}{M_g^2} D_g \operatorname{grad} \left(\frac{\rho^{gw}}{\rho^g} \right) \right] \\
 & + \operatorname{div} (n S_g \rho^{gw} v^{gs}) + \operatorname{div} (n S_w \rho^w v^{ws}) = 0
 \end{aligned} \tag{2.121}$$

where

$$\beta_{swg} = \beta_s (1-n) (S_g \rho^{gw} + \rho^w S_w) + n \beta_w \rho^w S_w \tag{2.122}$$

In these equations Darcy's law for the fluid velocities relative to the solid has still to be introduced. This law was introduced in section Darcy's law 2.4.7 and will be derived again in its generalized form in the next section from the linear momentum balance equations.

2.5.2 Linear momentum balance equation

2.5.2.1 Fluids

A more suitable form for the linear momentum balance equation for the fluid-phases is now obtained by introducing kinematic equations and constitutive relationships.

Equations [2.35] and [2.36] allow us to write for acceleration, \mathbf{a}^π

$$\mathbf{a}^\pi = \mathbf{a}^s + \mathbf{a}^{\pi s} + \mathbf{v}^{\pi s} \cdot \text{grad } \mathbf{v}^\pi \quad [2.123]$$

where $\mathbf{a}^{\pi s}$ is the relative acceleration

$$\text{Introduction in [2.64] of [2.123], [2.64], the momentum exchange term and of the intrinsic phase averaged density yields} \\ -\eta^\pi \rho^\pi (\mathbf{a}^s + \mathbf{a}^{\pi s} + \mathbf{v}^{\pi s} \cdot \text{grad } \mathbf{v}^\pi) - \text{div}(\eta^\pi p^\pi \mathbf{I}) + \eta^\pi p^\pi \mathbf{e}^\pi(\rho \dot{\mathbf{r}}) + \eta^\pi p^\pi \mathbf{g} - \mathbf{R}^\pi \eta^\pi \mathbf{v}^{\pi s} = \mathbf{0} \quad [2.124]$$

By neglecting the term dependent on the gradient of the fluid velocity, the effects of phase change and by applying a vector identity, for the divergence of the stress tensor in the fluid-phase, we obtain the relative velocity of the fluid as

$$\eta^\pi \mathbf{v}^{\pi s} = (\mathbf{R}^\pi)^{-1} \eta^\pi [-\text{grad } p^\pi + \rho^\pi (\mathbf{g} - \mathbf{a}^s - \mathbf{a}^{\pi s})] \quad [2.125]$$

$$\eta^\pi \mathbf{v}^{\pi s} = \frac{\mathbf{k} k^{r\pi}}{\mu} [-\text{grad } p^\pi + \rho^\pi (\mathbf{g} - \mathbf{a}^s - \mathbf{a}^{\pi s})] \quad [2.126]$$

Finally, neglecting the soil acceleration and the relative acceleration terms, it yields Darcy's law in the form [2.88]

$$\eta^\pi \bar{\mathbf{v}}^{\pi s} = \frac{k^{r\pi} \mathbf{k}}{\mu^\pi} (-\text{grad } p^\pi + \rho^\pi \mathbf{g}) \quad [2.127]$$

Due to the simplifications introduced, this law is valid as a first approximation for slow flow of a macroscopically inviscid fluid through a porous medium with incompressible grains.

2.5.2.2 Solid-phase

Taking into account equations [2.93], [2.94], [2.95], the linear momentum balance equation for the solid-phase becomes

$$\text{div}[\boldsymbol{\sigma}' - \mathbf{I}(1-n)(S_w p^w + S_g p^g)] + (1-n)\rho^s \mathbf{g} - (1-n)\rho^s \mathbf{a}^s + \mathbf{R}^w \eta^w \mathbf{v}^{ws} + \mathbf{R}^g \eta^g \mathbf{v}^{wg} = \mathbf{0} \quad [2.128]$$

2.5.2.3 Multiphase medium

By summing the momentum balance equations, written for water and gas-phase respectively, with that of the solid phase [2.128], by taking into account the definition of total stress, assuming continuity of stress at the fluid-solid interfaces and by introducing the averaged density of the multiphase medium

$$\rho = (1-n)\rho^s + n S_w \rho^w + n S_g \rho^g \quad [2.129]$$

we obtain the linear momentum balance equation for the whole multiphase medium

$$-\rho \mathbf{a}^s - n S_w \rho^w [\mathbf{a}^{ws} + \mathbf{v}^{ws} \cdot \text{grad } \mathbf{v}^w] - n S_g \rho^g [\mathbf{a}^{gs} + \mathbf{v}^{gs} \cdot \text{grad } \mathbf{v}^g] + \text{div } \boldsymbol{\sigma} + \rho \mathbf{g} = \mathbf{0} \quad [2.130]$$

2.5.3 Energy balance equation

The energy balance equation for the single phase is

$$\rho_{\pi} \mathbf{C}_p^{\pi} \frac{D\Theta^{\pi}}{Dt} = \rho_{\pi} h^{\pi} - \text{div} \tilde{\mathbf{q}}^{\pi} + \rho_{\pi} R^{\pi} - \rho_{\pi} \mathbf{e}^{\pi}(\rho) H^{\pi} \quad [2.131]$$

where $H^{\pi} = H^{\pi}(\bar{p}^{\pi}, \Theta^{\pi})$ is the specific enthalpy of the phase π

$$\mathbf{C}_p^{\pi} = \left(\frac{\partial H^{\pi}}{\partial \Theta^{\pi}} \right)_{\bar{p}} \text{ is the specific heat at constant pressure}$$

For the continuum multiphase, with the impose of thermodynamic equilibrium, the energy balance equation is

$$(\rho \mathbf{C}_p)_{\text{eff}} \frac{\partial T}{\partial t} + (\rho_w \mathbf{C}_p^w \mathbf{v}^w + \rho_g \mathbf{C}_p^g \mathbf{v}^g) \cdot \text{grad} T - \text{div}(\chi_{\text{eff}} \text{grad} T) = -\dot{m} \Delta H_{\text{vap}} \quad [2.132]$$

where $(\rho \mathbf{C}_p)_{\text{eff}} = \rho_s \mathbf{C}_p^s + \rho_w \mathbf{C}_p^w + \rho_g \mathbf{C}_p^g$

$$\chi_{\text{eff}} = \chi^s + \chi^w + \chi^g$$

$$\Delta H_{\text{vap}} = H^{gw} - H^w$$

2.6 PHYSICAL APPROACH: EXTENDED BIOT'S THEORY

The governing equations, using Biot's theory [Bio41/1] [Bio41/2] [Bio55] [Bio56/1] [Bio56/2] [Bio63] are again derived but extended to the case of non-isothermal two-phase flow in deforming porous media. This extension was made in References [Sch95] [S&Z93] for the case of slow phenomena. Also, inertia forces are taken into account, as was done in [Zie90] for the isothermal case with the air phase at atmospheric pressure.

The physical approach works directly with macroscopic variables. However, the distinction between a macroscopic and microscopic domain is not so clear as in the previous sections, because macroscopic variables are sometimes directly used in the microscopic domain.

For the sake of simplicity, small displacements are assumed for the solid phase. The governing equations in the form needed for finite strain analysis are those of the previous section. For all queries regarding the assumed hypotheses the interested reader is referred to the first part of this chapter.

2.6.1 The physical model

The voids of the skeleton are filled partly with water and partly with moist air (mixture of dry air and water vapour), which is referred to as gas. The degree of water saturation S_w is given as the ratio between the pore space occupied by the water and the total pore volume in a representative elementary volume element

$$S_w = \frac{dv^w}{dv^w + dv^g} \quad [2.133]$$

In the following equations the super or subscript π refers to the generic phase, $\pi=s$ to the solid phase, $\pi=w$ to water and $\pi=g$ to gas. The volume of the R.E.V. is dv , while the partial volumes are dv^s , dv^w and dv^g . Their sum is dv while the sum of the respective fluid volumes is $dv^T = dv^w + dv^g$. The definition of the degree of gas saturation S_g is

$$S_g = \frac{dv^g}{dv^w + dv^g} \quad [2.134]$$

and both degrees of saturation sum to one i.e.

$$S_w + S_g = 1 \quad [2.135]$$

The porosity n is defined as the ratio between the volume of voids and the total volume of the R.E.V.,

$$n = \frac{dv^w + dv^g}{dv} \quad [2.136]$$

As in the first part of this chapter, the stress is defined as tension positive for the solid phase, while pore pressure is defined as compressive positive for fluids. The water pressure p_w and the gas pressure p^g are related through the capillary pressure p^c

$$p^c = p^g - p^w \quad [2.137]$$

The relation [2.137] is determined experimentally and usually shows hysteresis characteristics, which are ignored in this case. Equation [2.137] is numerically inverted to obtain

$$S_\pi = S_\pi(p^c, T, \varepsilon_v^p) \quad [2.138]$$

The constitutive law of the solid phase is introduced through the concept of effective stress

$$\sigma' = \sigma + \mathbf{I} p^s \quad [2.139]$$

which stipulates that the main characteristics of the solid phase constitutive relation can be written in terms of σ where σ is the total stress tensor, \mathbf{I} the second order unit tensor and p^s is the average pressure of both the water and air surrounding the grains. In the case of immiscible two-phase flow we need a simple averaging technique for the calculation of p^s as described in section 2.2. Thus the modified effective stress principle may be obtained as stated previously. The effective stress resulting from equation [2.138] is also referred to as Bishop's stress.

$$\bar{\sigma} = \frac{1}{dv} \int_{dv} \sigma dv_m = \frac{1}{dv} \left[\int_{dv^s} \sigma dv_m + \int_{dv^f} \sigma dv_m \right] \quad [2.140]$$

where $\bar{\sigma}$ is the macroscopic total stress tensor

For the fluid phases, the stress tensor is given by

$$\sigma^\pi = \tau^\pi - \mathbf{I} p^\pi \quad [2.141]$$

where σ^π is the intrinsic phase averaged stress tensor in the π phase

τ^π is the shear stress

Under the assumption that the shear stress τ^π is negligible in fluids, we obtain

$$\bar{\sigma} = (1-n)\sigma^s - n\mathbf{I}[S_g p^g + S_w p^w] \quad [2.142]$$

The term in square brackets of equation [2.141] represents the intrinsically averaged (or mean) pressure p^s of the fluid phases i.e.

$$p^s = (S_g p^g + S_w p^w) \quad [2.143]$$

This weighted pore pressures produce a stress state in the grains, but, for the moment, we assume these will not undergo any deformation due to this stress, i.e. we introduce the hypothesis of incompressible grains. The deformation of the solid skeleton, which depends on the effective stress, will be a function of the grain rearrangement only.

Equation [2.142] can be modified to

$$\begin{aligned}\sigma &= (1-n)\sigma^s - n\mathbf{I}p^s \\ &= (1-n)(\sigma^s + \mathbf{I}p^s) - (1-n)\mathbf{I}p^s - n\mathbf{I}p^s \\ &= \sigma' - \mathbf{I}p^s\end{aligned}\quad [2.144]$$

where the overbar for the total stress has been omitted.

The stress tensor is split into two components: the pore pressure effect and the part which deforms the solid skeleton, i.e. the effective stress. This latter is given by

$$\sigma' = (1-n)(\sigma^s + \mathbf{I}p^s) \quad [2.145]$$

Equation [2.144] results in a splitting of the stress tensor similar to that of Terzaghi's principle, which, in presence of several fluid phases reads

$$\sigma' = \sigma + \mathbf{I}(S_w p^w + S_g p^g) \quad [2.146]$$

For greater generality, a corrective term known as Biot's constant, has to be introduced to account for the deformability of the grains [B&W57]. Therefore a more general expression of the effective stress is assumed as follows

$$\sigma' = \sigma + \mathbf{I}\alpha(S_w p^w + S_g p^g) \quad [2.147]$$

where the corrective coefficient α will be determined in section 2.6.2. Note that this equation differs substantially from the previous one: for the determination of α we need the constitutive equations of the solid phase. This effective stress is indicated in this chapter by σ'' as in [Zie90].

Another, more intuitive way of deriving equation [2.145] follows Bishop [Bis59] and Skempton [Ske61]. Here the microscopic and macroscopic aspects are somewhat mixed. We consider for this purpose the mean stresses, i.e.

$$\hat{\sigma} = \text{tr} \frac{\sigma}{3} \quad [2.148]$$

and

$$\hat{\sigma}' = \text{tr} \frac{\sigma'}{3} \quad [2.149]$$

If the pores (Figure 2.4) are filled with water and air, then due to the surface tension effect we have

$$p^w < p^g \quad [2.150]$$

If the degree of saturation is relatively low, the water is present as menisci and the corresponding pressure acts over an area χ per unit gross area, [A&D56].

Consequently, the equivalent pore pressure is given by

$$\chi p^w + (1-\chi) p^g \quad [2.151]$$

and the equivalent pore pressure may be written as

$$p^g - \chi(p^g - p^w) \quad [2.152]$$

or

$$p^w + (1 - \chi)(p^g - p^w) \quad [2.153]$$

For the fully saturated case, Bishop suggested the following expression for the mean effective stress $\hat{\sigma}'$

$$\hat{\sigma}' = \hat{\sigma} + [p^g - \chi(p^g - p^w)] \quad [2.154]$$

For the full stress tensor, this equation assumes the form

$$\sigma' = \sigma + \mathbf{I} [p^g - \chi(p^g - p^w)] \quad [2.155]$$

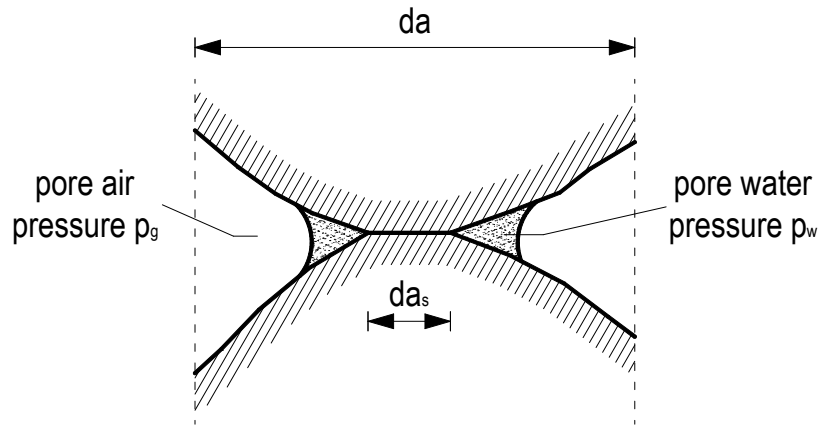


Figure 2.4: Contact area between two grains in the partially saturated case

The coefficient χ is not the same as for problems involving shear strength and consolidation [Ske61]. For a given degree of saturation the coefficient χ must be determined experimentally for both types of problems.

In general the pressure is implied as being an absolute value, but in many soil mechanics problems relative pressures are used and p^g is often assumed to be equal to the atmospheric pressure. If this is the case and the atmospheric pressure is assumed as the reference pressure then the effective stress principle becomes

$$\sigma' = \sigma + \mathbf{I} \chi p^w \quad [2.156]$$

The comparison between [2.146] and [2.155] is noteworthy. The former may be written as a function of the degree of saturation S_w

$$\sigma = \sigma' - \mathbf{I} [p^g - S_w(p^g - p^w)] \quad [2.157]$$

and coincides with equation [2.155] if $\chi = S_w$.

The coefficient χ is related to the area of contact between solid and fluids, whereas the degrees of saturation S_π depend on the volume occupied by the π phase. We define the volume fraction as

$$\eta^\pi = \frac{dv^\pi}{dv} \quad [2.158]$$

and cross sectional area fraction as

$$\alpha^\pi = \frac{da^\pi}{da} \quad [2.159]$$

For the case of microstructurally isotropic constituents, such that α^π is independent of the orientation of the surface, and assuming that

$$\alpha^\pi = \alpha^\pi(\eta^\pi) \quad [2.160]$$

it can be shown that [Mor72]

$$\alpha^\pi = \eta^\pi \quad [2.161]$$

This conclusion coincides with the basic supposition of Delesse's law, see section 2.2.1.

If this assumption regarding the area and volume fraction is valid, then little difference exists between the definition of Bishop's coefficient χ and the degree of water saturation S_w . Bishop's equation [2.154] has been experimentally validated by means of a triaxial tests carried out on soil samples [Ske61].

The assumption

$$\chi = S_w \quad [2.162]$$

is acceptable for many materials as shown experimentally in [B&B63].

However, other expressions may also be used, e.g. by Gudehus for clay [Gud95]

$$\chi = S(2 - S) \quad [2.163]$$

If the solid phase is completely surrounded by a single wetting fluid phase, which is the only one in direct contact with the porous medium, then Li and Zienkiewicz [L&Z92] use equation [2.156] with $\chi = 1$, as in the case of a fully saturated porous medium. This assumption is widely used when the two fluids are water and bitumen: only water is in contact with the solid grains.

A new expression for the effective stress principle in fully saturated conditions only, involving four parameters, has been proposed by Lade and de Boer [L&B96] and experimentally tested. This formulation, based on principles of mechanics is valid for all types of materials. A distinction is made between the compressibilities of the grain particles and the skeleton due to total stresses and pore pressures.

Two distinct expressions are then obtained for effective stresses in granular material and in solid rock with interconnected pores respectively. For various special conditions these expressions become similar to the expressions found in the literature, in particular to the expression used here with Biot's constant α . Lade and de Boer [L&B96] conclude that Terzaghi's proposed effective stress principle works well for stress magnitudes encountered in most geotechnical applications, but significant deviations occur at very high stresses.

2.6.2 Constitutive equations

For a full account of the constitutive relationships used the reader is referred to section 2.4, and only a few equations, needed for the remaining part of this section, are recalled. In particular an expression for Biot's constant α is derived, which was omitted in section 2.4.

The averaged pore pressure p^s of the fluids occupying the void space induce a hydrostatic stress distribution in the solid phase. The ensuing deformation is a purely volumetric strain

$$\varepsilon_v^s = -\frac{p^s}{K_s} \quad [2.164]$$

where K_s is the averaged bulk modulus of the solid grains.

As stated previously, the effective stress causes all relevant deformation of the solid skeleton. The constitutive relationship may be written as

$$d\sigma' = D_T \left[(d\varepsilon - d\varepsilon^c - d\varepsilon_v^s - d\varepsilon^o) \right] \quad [2.165]$$

where $d\sigma'$ is the stress responsible for all deformations, except for the grain compressibility

$d\varepsilon$ represents the total strain of the solid

D_T is the tangent constitutive tensor

$$D_T = D_T(\sigma', \varepsilon, \dot{\varepsilon}) \quad [2.166]$$

$d\varepsilon^c = g(\sigma')dt$ accounts for the creep strain

$d\varepsilon^o$ represents all other strains in the solid skeleton not directly dependent on effective stress

A modified effective stress σ'' will now be introduced which will also account for grain compression. This allows the use of Biot's constant α . Omitting, for brevity, $d\varepsilon^c$ and $d\varepsilon^o$ we obtain

$$d\sigma' = D_T \left[(d\varepsilon - d\varepsilon_v^s) \right] = D_T [d\varepsilon] + D_T [I] \frac{dp^s}{3K_s} \quad [2.167]$$

Consequently, the effective stress equation written in incremental form becomes

$$d\sigma = d\sigma' - I dp^s = d\sigma'' + D_T [I] \frac{dp^s}{3K_s} - I dp^s \quad [2.168]$$

where σ'' represents the stress responsible for all deformation of the solid.

For the following developments we use indicial notation and the Kronecker Symbol δ instead of the unit tensor I .

It can be immediately verified that equation [2.168] can be written as given by Zienkiewicz and Shiomi [Z&S85]

$$d\sigma_{ij} = d\sigma''_{ij} - \frac{1}{3} \left(\delta_{mn} \delta_{nm} - \delta_{mn} D_{mnkl} \delta_{kl} \frac{1}{3K_s} \right) \delta_{ij} dp^s \quad [2.169]$$

For an isotropic, elastic material

$$\delta_{mn} D_{mnkl} \delta_{kl} = \frac{3E}{1-2\nu} = 9K_T \quad [2.170]$$

where E is the Young's modulus

ν is the Poisson's ratio

K_T is the bulk modulus of the overall skeleton

Hence equation [2.169] can be written as

$$d\sigma_{ij} = d\sigma''_{ij} - \left(1 - \frac{K_T}{K_s} \right) \delta_{ij} dp^s = d\sigma''_{ij} - \alpha \delta_{ij} dp^s \quad [2.171]$$

where α is Biot's constant.

The resultant expression of the constitutive relationship is therefore

$$d\sigma'' = D_T d\varepsilon \quad [2.172]$$

The intrinsic pore pressure p^π of the π fluid phase causes a purely volumetric strain of that phase, which is represented by

$$\varepsilon_v^\pi = -\frac{p^\pi}{K_\pi} \quad [2.173]$$

2.6.3 Governing equations

In the following a material coordinate system is employed for the solid phase and a spatial coordinate system for the fluid phases; convective terms, unless specified otherwise, are neglected. Because of this choice of reference systems the fluid velocities are conveniently referred to the solid phase by means of the relative velocities for water and gas respectively

$$\mathbf{v}^{ws} = \mathbf{v}^w - \mathbf{v}^s \quad [2.174]$$

$$\mathbf{v}^{gs} = \mathbf{v}^g - \mathbf{v}^s \quad [2.175]$$

and the accelerations, without convective terms, are

$$\mathbf{a}^w = \mathbf{a}^s + \mathbf{a}^{ws} \quad [2.176]$$

$$\mathbf{a}^g = \mathbf{a}^s + \mathbf{a}^{gs} \quad [2.177]$$

where \mathbf{a}^{ws} is the acceleration of water relative to the solid phase and \mathbf{a}^{gs} the relative acceleration of gas.

2.6.3.1 Linear momentum balance equation of the multiphase medium

The linear momentum balance equation for the multiphase system is the sum of the dynamics equations for the individual constituents, but relative to the solid phase via equations [2.176] and [2.176]

$$-\rho \mathbf{a}^s - n S_w \rho^w \mathbf{a}^{ws} - n S_g \rho^g \mathbf{a}^{gs} + \text{div } \boldsymbol{\sigma} + \rho \mathbf{g} = 0 \quad [2.178]$$

where

$$\rho = (1-n)\rho^s + n S_w \rho^w + n S_g \rho^g \quad [2.179]$$

is the averaged density of the multiphase systems

ρ^s is the intrinsic density of the solid phase, i.e. the density referred to the volume occupied by the solid phase only, as opposed to the volume occupied by the multiphase system

ρ^w is the intrinsic density of water

ρ^g the intrinsic density of gas

\mathbf{g} an acceleration usually related to gravitational effects

The linear momentum balance equation for each fluid phase yields the generalized form of Darcy's law, where the dissipative terms arising in a multiphase flow system at the interfaces are taken into account through the relative permeabilities

$$n S_w \mathbf{v}^{ws} = \frac{\mathbf{k} k^{rw}}{\mu_w} \left[-\text{grad } p^w + \rho^w (\mathbf{g} - \mathbf{a}^s - \mathbf{a}^{ws}) \right] \quad [2.180]$$

$$nS_g \mathbf{v}^{gs} = \frac{\mathbf{k}k^{rg}}{\mu_g} [-\mathit{grad} p^g + \rho^g(\mathbf{g} - \mathbf{a}^s - \mathbf{a}^{gs})] \quad [2.181]$$

Where \mathbf{k} is the intrinsic permeability

k^{rw} and k^{rg} the relative permeabilities of water and gas

μ_w and μ_g are the dynamic viscosities

The relative permeabilities vary between 0 and 1 and are a function of the degree of saturation; the dynamic viscosities are temperature dependent. In the generalized form of Darcy's law for the gas phase the body forces are usually neglected. The L.H.S. of equations [2.180] and [2.181] are multiplied by the volume fractions nS_π because Darcy's law is expressed in terms of volume averaged relative velocities. These are the velocities measured from experiment work.

2.6.3.2 Mass balance equations

The summation of mass balance equations of mass and fluid, with opportune arrangements and yields the so-called continuity equation of the fluid phase i.e.

$$\frac{(1-n)}{\rho^s} \frac{\partial \rho^s}{\partial t} + \mathit{div} \mathbf{v}^s + \frac{n}{\rho^\pi} \frac{\partial \rho^\pi}{\partial t} + \frac{n}{S_\pi} \frac{\partial S_\pi}{\partial t} + \frac{1}{S_\pi \rho^\pi} (nS_\pi \rho^\pi \mathbf{v}^{\pi s}) = \pm \frac{\dot{m}}{\rho^\pi S_\pi} \quad [2.182]$$

We consider first the continuity equation for water. Introduction of the constitutive relationships for the time derivatives of water density and solid density, of the pressure in the solid phase, and multiplication by S_w allows the continuity equation for water and then with the introduction of Darcy's law and of the definition of capillary pressure yields

$$\begin{aligned} & \left(\frac{\alpha - n}{K_s} S_w^2 + \frac{nS_w}{K_w} \right) \frac{\partial p^w}{\partial t} + \frac{\alpha - n}{K_s} S_w S_g \frac{\partial p^g}{\partial t} + \alpha S_w \mathit{div} \mathbf{v}^s \\ & - \beta_{sw} \frac{\partial T}{\partial t} + \left(\frac{n - \alpha}{K_s} S_w \rho^c + n \right) \frac{\partial S_w}{\partial t} \\ & + \frac{1}{\rho^w} \mathit{div} \left\{ \rho^w \frac{\mathbf{k}k^{rw}}{\mu_w} [-\mathit{grad} p^w + \rho^w(\mathbf{g} - \mathbf{a}^s - \mathbf{a}^{ws})] \right\} = - \frac{\dot{m}}{\rho^w} \end{aligned} \quad [2.183]$$

In the same way the continuity equation for gas is obtained

$$\begin{aligned} & \frac{\alpha - n}{K_s} S_w S_g \frac{\partial p^w}{\partial t} + \frac{\alpha - n}{K_s} S_g^2 \frac{\partial p^g}{\partial t} - \left(n + \frac{\alpha - n}{K_s} \rho^c S_g \right) \frac{\partial S_w}{\partial t} \\ & - \beta_s (\alpha - n) S_g \frac{\partial T}{\partial t} + \alpha S_g \mathit{div} \mathbf{v}^s + \frac{nS_g}{\rho^g} \frac{\partial}{\partial t} \left(\frac{\rho^g M_g}{\Theta R} \right) \\ & + \frac{1}{\rho^g} \mathit{div} \left\{ \rho^g \frac{\mathbf{k}k^{rg}}{\mu_g} [-\mathit{grad} p^g + \rho^g(\mathbf{g} - \mathbf{a}^s - \mathbf{a}^{gs})] \right\} = - \frac{\dot{m}}{\rho^g} \end{aligned} \quad [2.184]$$

2.6.3.3 Energy balance equation

By subtracting the kinetic energy from a global energy balance, the balance equation of thermal energy may be written for constituent π as [Bir60]

$$\frac{\partial}{\partial t}(\rho^\pi E^\pi) = -\text{div}(\rho^\pi E^\pi \mathbf{v}^\pi) - \text{div} \tilde{\mathbf{q}}^\pi - \bar{p}^\pi \text{div} \mathbf{v}^{\pi s} + \tau^\pi \cdot \text{grad} \mathbf{v}^\pi + \rho^\pi R^\pi \quad [2.185]$$

where E^π is the specific internal energy

τ is the deviatoric part of the stress tensor

\bar{p}^π the hydrostatic part of the stress tensor

The L.H.S. represents the rate of accumulation of internal energy in a control volume. The R.H.S. terms express respectively the rate of internal energy change due to convection and to conduction, the reversible rate of internal energy increase due to pressure, the irreversible rate of internal energy increase by viscous dissipation and the contribution of heat sources.

In small strain the energy balance equation becomes

$$\rho^\pi \frac{\partial E^\pi}{\partial t} + \rho^\pi \mathbf{v}^\pi \cdot \text{grad} E^\pi = -\text{div} \tilde{\mathbf{q}}^\pi - \bar{p}^\pi \text{div} \mathbf{v}^\pi + \tau^\pi \cdot \text{grad} \mathbf{v}^\pi + \rho^\pi R^\pi \quad [2.186]$$

The irreversible part of the internal energy increase by viscous dissipation is neglected in what follows. It is convenient to express this equation in terms of temperature and heat capacity instead of internal energy [Bir60]. This is done through the concept of enthalpy. Hence with sufficient accuracy for geomechanical applications the energy balance equation can be rewritten as

$$\rho^\pi C_p^\pi \left(\frac{\partial T^\pi}{\partial t} + \mathbf{v}^\pi \cdot \text{grad} T^\pi \right) = -\text{div} \tilde{\mathbf{q}}^\pi + \rho^\pi R^\pi \quad [2.187]$$

for $\pi=s,w$, which for the purpose of the energy balance only may be considered as incompressible, and

$$\rho^\pi C_p^g \left(\frac{\partial T^g}{\partial t} + \mathbf{v}^g \cdot \text{grad} T^g \right) = -\text{div} \tilde{\mathbf{q}}^g + \frac{\partial p^g}{\partial t} + \mathbf{v}^g \cdot \text{grad} p^g + \rho^g R^g \quad [2.188]$$

where C_p^g is the specific heat at constant pressure

Some insignificant terms which are related to the mechanical work induced by density variations due to temperature changes of the water and solid phases have been neglected.

Gas pressure changes are usually very slow and their gradients small in geomaterials, hence the time derivatives of gas pressure, as well as the convective terms, are negligible with respect to other terms in equation [2.188]. Also, because gas pressure changes are usually small when compared to atmospheric pressure, the specific heat at constant pressure may be utilised instead of specific heat at constant volume.

A local equilibrium state is assumed to hold i.e.

$$T^s = T^w = T^g = T \quad [2.189]$$

We also introduce the constitutive equation for heat fluxes, and add together equations [2.187] and [2.188], and introduce the appropriate heat sources to obtain the following form of the energy balance equation

$$\left(\rho C_p \right)_{\text{eff}} \frac{\partial T}{\partial t} + \left(\rho^w C_p^w \mathbf{v}^w + \rho^g C_p^g \mathbf{v}^g \right) \cdot \text{grad} T - \text{div}(\chi_{\text{eff}} \text{grad} T) = -\dot{m} \Delta H_{\text{vap}} \quad [2.190]$$

where ΔH_{vap} is the latent heat of evaporation

The convective heat flux in the solid phase has been neglected.

2.7 QUASI STATIC CASE

The relationship shown in 2.6.3 are now presented for quasi static conditions. In poor words, the equations are rewritten by not taking into account the terms in which appear the acceleration, so is possible neglect the terms a^w , a^s , a^{ws} , a^g and a^{gs} used in the relationship [2.176] and [2.177].

For this work of PhD, the equations used are those in quasi static condition.

2.7.1.1 Linear momentum balance equation of the multiphase medium

The equation [2.178] becomes

$$\mathit{div} \sigma + \rho \mathbf{g} = 0 \quad [2.191]$$

Where, as for the case seen in 2.6.3.1,

$$\rho = (1 - n)\rho^s + n S_w \rho^w + n S_g \rho^g \quad [2.192]$$

is the averaged density of the multiphase systems

ρ^s is the intrinsic density of the solid phase

ρ^w is the intrinsic density of water

ρ^g the intrinsic density of gas

\mathbf{g} is the gravity acceleration

2.7.1.2 Mass balance equations

The equations [2.183] and [2.184] becomes

$$\begin{aligned} & \left(\frac{\alpha - n}{K_s} S_w^2 + \frac{n S_w}{K_w} \right) \frac{\partial p^w}{\partial t} + \frac{\alpha - n}{K_s} S_w S_g \frac{\partial p^g}{\partial t} + \alpha S_w \mathit{div} \mathbf{v}^s \\ & - \beta_{sw} \frac{\partial T}{\partial t} + \left(\frac{n - \alpha}{K_s} S_w \rho^c + n \right) \frac{\partial S_w}{\partial t} \\ & + \frac{1}{\rho^w} \mathit{div} \left\{ \rho^w \frac{\mathbf{k} k^{rw}}{\mu_w} [-\mathit{grad} p^w + \rho^w \mathbf{g}] \right\} = 0 \end{aligned} \quad [2.193]$$

In the same way the continuity equation for gas is obtained

$$\begin{aligned} & \frac{\alpha - n}{K_s} S_w S_g \frac{\partial p^w}{\partial t} + \frac{\alpha - n}{K_s} S_g^2 \frac{\partial p^g}{\partial t} - \left(n + \frac{\alpha - n}{K_s} \rho^c S_g \right) \frac{\partial S_w}{\partial t} \\ & - \beta_s (\alpha - n) S_g \frac{\partial T}{\partial t} + \alpha S_g \mathit{div} \mathbf{v}^s + \frac{n S_g}{\rho^g} \frac{\partial}{\partial t} \left(\frac{p^g M_g}{\Theta R} \right) \\ & + \frac{1}{\rho^g} \mathit{div} \left\{ \rho^g \frac{\mathbf{k} k^{rg}}{\mu_g} [-\mathit{grad} p^g + \rho^g \mathbf{g}] \right\} = 0 \end{aligned} \quad [2.194]$$

2.7.1.3 Energy balance equation

The equation [2.190] write in 2.6.3.3 not change for the quasi static case but, using Darcy' law, can be rewritten in a complete mode as follow

$$\begin{aligned} & (\rho C_p)_{eff} \frac{\partial T}{\partial t} + \rho^w C_p^w \left[\frac{k k^{rw}}{\mu^w} [-grad(p^g) + grad(p^c) + \rho^w g] \right] \cdot grad T \\ & \rho^g C_p^g \left[\frac{k k^{rg}}{\mu^g} [-grad(p^g) + \rho^g g] \right] \cdot grad T - div(\chi_{eff} grad T) = -\dot{m} \Delta H_{vap} \end{aligned} \quad [2.195]$$

2.7.1.4 Further developments of the model

The same equations see for this model, hence the linear momentum balance equation, the mass balance equations and the energy balance equation, were developed by considering air dissolved in water by Gawin and Sanavia. For further information, see [G&S10/1] and [G&S10/2].

2.8 BOUNDARY AND INITIAL CONDITIONS

For the model closure the initial and boundary conditions are needed. The initial conditions specify the full fields of primary state variables at time $t=t_0$, in the whole analysed domain B and on its boundary ∂B :

$$\partial B = \partial B_\pi \cup \partial B_\pi^q \quad \pi = g, c, T, \mathbf{u} \quad [2.196]$$

$$\begin{aligned} \rho^g &= \rho_0^g \\ \rho^c &= \rho_0^c \\ T &= T_0 \\ \mathbf{u} &= \mathbf{u}_0 \end{aligned} \quad \text{on } B \cup \partial B \quad [2.197]$$

The boundary conditions (BCs) can be of Dirichlet's type on ∂B_π for $t \geq t_0$:

$$\begin{aligned} \rho^g &= \hat{\rho}^g \quad \text{on } \partial B_g \\ \rho^c &= \hat{\rho}^c \quad \text{on } \partial B_c \\ T &= \hat{T} \quad \text{on } \partial B_T \\ \mathbf{u} &= \hat{\mathbf{u}} \quad \text{on } \partial B_u \end{aligned} \quad [2.198]$$

or of Cauchy's type (the mixed BCs) on ∂B_π^q for $t \geq t_0$:

$$(n S_g \rho^{ga} v^{gs} + \mathbf{J}_d^{ga}) \cdot \mathbf{n} = q^{ga} \quad \text{on } \partial B_g^q \quad [2.199]$$

$$(n S_w \rho^w v^{ws} + n S_g \rho^{gw} v^{gs} + \mathbf{J}_d^{gw}) \cdot \mathbf{n} = q^{gw} + q^w + \beta_c (\rho^{gw} - \rho_\infty^{gw}) \quad \text{on } \partial B_c^q \quad [2.200]$$

$$(n S_w \rho^w v^{ws} \Delta H_{vap} - \chi_{eff} grad T) \cdot \mathbf{n} = q^T + q^w + \alpha_c (T - T_\infty) + e \sigma_0 (T^4 - T_\infty^4) \quad \text{on } \partial B_T^q \quad [2.201]$$

$$\boldsymbol{\sigma} \cdot \mathbf{n} = \bar{\mathbf{t}} \quad \text{on } \partial B_u^q \quad [2.202]$$

where $\mathbf{n}(\mathbf{x}, t)$ is the unit normal vector

$q^{ga}(\mathbf{x}, t)$ is the imposed fluxes of dry air

$q^{gw}(\mathbf{x},t)$ is the imposed fluxes of vapour

$q^w(\mathbf{x},t)$ is the imposed fluxes of liquid water

$q^T(\mathbf{x},t)$ is the imposed imposed heat flux

$\bar{\mathbf{t}}(\mathbf{x},t)$ is the imposed traction vector related to the total Cauchy stress tensor $\sigma(\mathbf{x},t)$

$\rho_\infty^{gw}(\mathbf{x},t)$ is the mass concentration of water vapour

$T_\infty(\mathbf{x},t)$ is the temperature in the far field of undisturbed gas phase

$e(\mathbf{x},t)$ is the emissivity of the interface

$\sigma_0(\mathbf{x},t)$ is the Stefan-Boltzmann constant

$\beta_c(\mathbf{x},t)$ is the convective heat exchange coefficients

$\alpha_c(\mathbf{x},t)$ is the convective mass exchange coefficients

The boundary conditions with only imposed fluxes are called Neumann' BCs. The purely convective boundary conditions for heat and moisture exchange are also called Robin' BCs.

References

- [A&D56] Aitchison, G.D., and Donald, I.B., Effective stress in unsaturated soils, Proc. 2nd Australia-New Zealand Conf. Soil Mech., 1956, 192-199.
- [ASH93] ASHRAE Handbook, Fundamentals Volume, ASHRAE, Atlanta, 1993.
- [B&B63] Bishop, A.W. and Blight, G.E.: Some aspects of effective stress in saturated and partly saturated soils, *Géotechnique*, 13(1963), 177-197.
- [B&C66] Brooks, R.N., and Corey, A.T., Properties of porous media affecting fluid flow, *J. Irrig. Drain. Div. Am. Soc. Civ.Eng.*, 92(IR2) (1966), 61-68.
- [B&C81] Bear, J. and Corapcioglu, Y., Mathematical model for regional land subsidence due to pumping. 2. Integrated aquifer subsidence equation for vertical and horizontal displacements, *Water Resour. Res.*, 17(1981), 947-958.
- [B&D83] Bear, J. and Bachmat, Y., Transport phenomena in porous media - Basic equations, from *Fundamentals of Transport Phenomena in Porous Media* (Bear, J. and Corapcioglu, M. Y., eds.), Nato ASI Series, Nijhoff, Dordrecht, 1984, 5-61.
- [B&S78] Bomberg M., Shirliffe, C.J., Influence of moisture gradients on heat transfer through porous building materials. Thermal transmission measurements of insulation, ASTM STP 660, R.P. Tye, ed., ASTM, 211-233, 1978.
- [B&W57] Biot, M.A., and Willis, P.G., The elastic coefficients of the theory of consolidation, *J. Appl. Mech.*, 24, 594-601, 1957.
- [Bag93] Baggio, P., Bonacina, C., Strada, M., Trasporto di calore e di massa nel calcestruzzo cellulare. *La Termotecnica*, 45(1993), 53-60.
- [Bio41/1] Biot, M.A., General theory of three-dimensional consolidation, *J. Appl. Phys.*, 12 (1941), 155-64.
- [Bio41/2] Biot, M.A., Consolidation settlement under a rectangular load, *J. Appl. Phys.*, 12 (1941), 426-30.
- [Bio55] Biot, M.A., Theory of elasticity and consolidation for a porous anisotropic solid, *J. Appl. Phys.*, 26 (1955), 182-5.
- [Bio56/1] Biot, M.A., General solution of the equation of elasticity and consolidation for a porous material, *J. Appl. Mech.*, 23 (1956), 91-6.
- [Bio56/2] Biot, M.A., Theory of deformation of a porous viscoelastic anisotropic soil, *J. Appl. Phys.*, 27 (1956), 459-67.
- [Bio63] Biot, M.A., Theory of stability and consolidation of a porous medium under initial stress, *J. Math. Mech.*, 12 (1963), 521-41.
- [Bir60] Bird, R.B., Stewart, E.W., Lightfoot, E.N., *Transport Phenomena*, John Wiley & Sons, 1960.
- [Bis59] Bishop, A.V., The principle of effective stress. *Teknisk Ukeblad*, 39 (1959), 859-863.
- [C&N63] Coleman, B.D., and Noll, W., The thermodynamics of elastic materials with heat conduction and viscosity, *Arch. Ration. Mech. Anal.*, 13(1963), 168-178.
- [C&T92] Chen, W.F. and Tsui, Y., Limitations to the large strain theory, *Int. J. Num. Meth. Eng.*, 33(1992), 101-114.
- [Cor57] Corey, A.T., Measurement of water and air permeability in unsaturated soil, *Soil Sci. Soc. Am. Proc.*, 21,1 (1957), 7-10.

-
- [deB91] de Boer, R., Ehlers, W., Kowalski S. and Plischka, J., Porous media, a survey of different approaches, Forschungsbericht aus dem Fachbereich Bauwesen, 54, Universität-Gesamthochschule Essen, 1991.
- [E&S64] Eringen A.C. and Suhubi, E.S., Nonlinear Theory of simple micro-elastic solids. *Int. J. Engng. Sci.* 2 (1964), 189-203.
- [Ehl89] Ehlers, W., Poröse Medien, ein kontinuumsmechanisches Modell auf der Basis der Mischungstheorie, Forschungsbericht aus dem Fachbereich Bauwesen, 47, Universität Gesamthochschule Essen, 1989.
- [G&H91/1] Gray, W.G., and Hassanizadeh S.M., Unsaturated flow theory including interfacial phenomena, *Water Resour. Res.*, Vol. 27(1991), 1855-1863.
- [G&H91/2] Gray, W.G., and Hassanizadeh, S.M., Paradoxes and realities in unsaturated flow theory, *Water Resour. Res.*, Vol. 27(1991), 1847-1854.
- [G&S10/1] Gawin D., L. Sanavia, Simulation of cavitation in water saturated porous media considering effects of dissolved air. *Transport in porous media*, 81, 141-160 (2010). DOI: 10.1007/s11242-009-9391-4.
- [G&S10/2] D. Gawin, Sanavia L., A unified approach to numerical modelling of fully and partially saturated porous materials by considering air dissolved in water. *Computer Modeling in Engineering & Sciences* (Accepted).
- [Gaw95] Gawin, D., Baggio, P. and Schrefler, B.A., Coupled heat, water and gas flow in deformable porous media, *I.J. Num. Methods in Fluids*, 20 (1995), 969-987.
- [Gud95] Gudehus, G., A comprehensive concept for non-saturated granular bodies, *Proc. 1st Int. Conf.on Unsaturated Soils*, Paris 1995, Balkema Rotterdam.
- [H&G79/1] Hassanizadeh, M. and Gray W.G., General conservation equations for multiphase systems: 1 Averaging procedure, *Adv. Water Resources*, 2 (1979), 131-144.
- [H&G79/2] Hassanizadeh, M. and Gray W.G., General conservation equations for multiphase systems: 2. Mass, momenta, energy and entropy equations, *Adv. Water Resources*, 2(1979), 191-203.
- [H&G80/3] Hassanizadeh, M. and Gray W.G., General conservation equations for multiphase systems: 3. Constitutive theory for porous media flow, *Adv. Water Resources*, 3(1980), 25-40.
- [Has86/1] Hassanizadeh, S.M., Derivation of basic equations of mass transport in porous media, Part. 1 Macroscopic balance laws, *Adv. Water Resources*, Vol. 9(1986), 196-206.
- [Has86/2] Hassanizadeh, S.M., Derivation of basic equations of mass transport in porous media, Part. 2 Generalized Darcy's law and Fick's law, *Adv. Water Resources*, Vol. 9(1986), 207-222.
- [L&B96] Lade, P.V., de Boer, R., The concept of effective stress for soil, concrete and rock, to appear in *Géotechnique*, (1996).
- [L&C88] Lemaitre, J. and Chaboche J.L., *Mécanique des matériaux solides*, Dunod, Paris 1988.
- [L&S98] Lewis R.W. and Schrefler B.A. *The Finite Element Method in the Static and Dynamic Deformation and Consolidation of Porous Media*. J. Wiley, Chichester 1998.
- [L&Z92] Li, X., Zienkiewicz, O.C., Multiphase flow in deforming porous media and finite element solutions, *Computers and Structures*, 45(1992), 211-227.
- [M&S93] Moran, M.J. and Shapiro, H.N., *Fundamentals of Engineering Thermodynamics*, 2nd ed., J. Wiley, New York, 1993.
- [Mol86] Molenkamp, F., Limits to the Jaumann stress rate, *Int. J. Num. Anal. Meth. Geomech.*, 10(1986), 151-176.
-

- [Mor72] Morland, L.W., A simple constitutive theory for a fluid saturated porous solid, *Journal Geophys. Res.* 77(1972), 890-900.
- [S&S89] Simoni, L. and Schrefler, B.A., F.E. solution of a vertically averaged model for regional land subsidence. *Int. J. Num. Meth. Eng.*, 27(1989), 215-230.
- [S&W79] Sampaio, R. and Williams W.O., Thermodynamics of diffusing mixtures, *Journal de Mécanique*, Vol. 18(1979), 19-45.
- [S&Z93] Schrefler, B.A., Zhan, X.Y., A fully coupled model for water flow and airflow in deformable porous media, *Water Resour. Res.*, 29(1993), 155-167.
- [San05] L. Sanavia, F. Pesavento, B.A. Schrefler, Finite element analysis of non-isothermal multiphase geomaterials with application to strain localization simulation, *Computational Mechanics* Vol. 466, (2005) (DOI 10.1007/s00466 -005-0673-6).
- [Sch95] Schrefler, B.A., Zhan, X., Simoni, L., A coupled model for water flow, airflow and heat flow in deformable porous media, *I.J. Heat and Fluid Flow*, 5 (1995), 531-547.
- [Ske61] Skempton, A.W., Effective stress in soil, concrete and rocks, from 'Pore Pressure and Suction in Soils', Butterworths London 1961, 4-16.
- [Z&S85] Zienkiewicz, O.C., and Shiomi, T., Dynamic behaviour of saturated porous media: the general Biot's formulation and its numerical solution, *Int. J. Num. Anal. Meth. Geom.*, 8(1985), 71-96.
- [Zie90] Zienkiewicz, O.C., Xie, Y.M., Schrefler, B.A., Ledesma, A., Bicanic, N., Static and dynamic behaviour of soils: a rational approach for quantitative solutions. II Semi-saturated problems. *Proc. R. Soc. London. A* 429 (1990), 311-321.

3 FEM MODEL

3.1 THE CODE COMES-GEO

3.1.1 Introduction

The COMES-GEO code carries out the mechanical analysis of porous materials with interconnected pores in which the flow of one or more fluid phases takes place.

The interactions between fluid and solid phases are taken into account. Geomaterials (soils, rocks, concrete), are the most common examples of such porous media. The general purpose codes, currently available in the market, do not deal with more than a single fluid phase. Therefore it is not possible to carry out realistic numerical studies of porous materials structures in partially saturated conditions as:

1. seismic analysis of soil dams where in the upper part wide zones, containing pores filled with air and water, are present;
2. stability analysis of soil slopes;
3. simulation of the subsidence phenomena in presence of gas extraction from deep reservoir. In this case water and different gases are present in the pores. The gas reservoirs in the northern Adriatic Sea are an important example in Italy.

The COMES-GEO code, developed by the University of Padua, is able to deal with these problems and also with many others applications in the environmental geomechanics.

Due to the high frequency of earthquakes in Italy associated with the rich historical and architectural heritage potentially affected by seismic or subsidence phenomena (Ravenna, Chioggia, Venezia), it is absolutely necessary to provide the scientific community and the public institutions (as civil guard) with a COMES-GEO-like code.

Some simplified versions of the same code are already successfully applied to problems of environmental geomechanics in Holland, United Kingdom and South Africa.

The problem unknowns are the following: temperature, capillary pressure, gas pressure and displacements. These data allow the calculation of interesting derived outputs (saturation, stress-strain fields).

To reach the solution of the problem using the considered model, four balance equations are imposed (see chapter 2): mass of the dry air, mass of the water species (both liquid water and vapour; phase change are considered); energy conservation of the mixture and the linear momentum of the multiphase medium. They are completed by an appropriate set of constitutive and state equations, as well as some thermodynamic relationships.

COMES-GEO allows any finite element analysis in plane strain and axialsymmetric conditions, using four node bilinear elements or Serendipity eight node elements or Lagrange nine node elements.

The source is written in FORTRAN 90.

3.1.2 Finite Element Method

Numerical solution to the mathematical system presented in chapter 2, is done through use of the finite element method. In what follows, we describe the particular method employed for the spatial discretization of the numerical system. Specifically, we have elected to apply the Galerkin form of the method of weighted residuals (MWR) to produce an integral representation of the basic conservation laws.

These relations are then specialized to finite element method.

For further information see Sanavia et al. [San05] and [San06].

3.1.2.1 Method of Weighted Residuals: discretization in space

To apply the MWR to the particular problem at hand, we assume that the region of interest Ω is divided into a number of simply shaped regions, the finite elements, as shown in Figure 3.1.

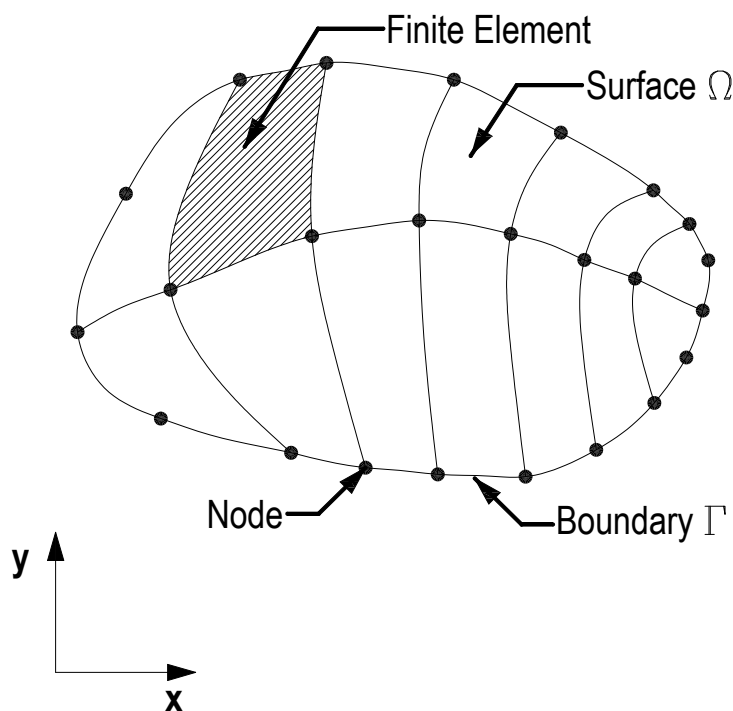


Figure 3.1: Schematic division in simply regions

Within each element, a set of nodal points is established at which the dependent variables p_g , p_c , T , u_x and u_y are evaluated, where

1. p_g is the pressure of gas (dry air, vapour or any other perfect gas) expressed in Pa
2. p_c is the capillary pressure (or suction) expressed in Pa
3. T is the temperature expressed in K
4. u_x and u_y are the displacement expressed in m

For the purpose of developing the equations for these nodal unknowns, an individual element is separated from the assemblage.

Within each element, it is assumed that the dependent variables can be expressed in terms of approximating function to shape functions by:

$$\rho_g(t) = N_p \bar{\rho}_g(t) \quad [3.1]$$

$$\rho_c(t) = N_p \bar{\rho}_c(t) \quad [3.2]$$

$$T(t) = N_t \bar{T}(t) \quad [3.3]$$

$$u(t) = N_u \bar{u}(t) \quad [3.4]$$

where the upper line indicates the nodal values. Substitution of the relations [3.1], [3.2], [3.2] and [3.4] into the partial differential equations see in chapter 2, and boundary conditions, will result in a set of residual equations due to the approximate nature of relations [3.1], [3.2], [3.2] and [3.4].

The MWR is then used to reduce the residual expression to zero in a weighted integral sense through the introduction of:

$$\int_{\Omega} \mathbf{N}_x \mathbf{R}_x d\Omega + \int_{\Gamma} \mathbf{N}_x \mathbf{R}_x d\Gamma = \mathbf{0} \quad [3.5]$$

where $\mathbf{x}^T = \{\bar{\rho}_g, \bar{\rho}_c, \bar{T}, \bar{u}\}$

\mathbf{N}_x are weighting or test functions

\mathbf{R} is the residual for a field equation

$\mathbf{R}_x(\text{b.c.})$ is the residual for the boundary condition

The integral or weak form of the heat and mass transfer equations (and of the other ones required to complete the model), obtained by means of the Galerkin procedure (weighted residuals), [Z&T89] and [Z&T91], can be expressed in matrix form as [Gaw96] and [S&G96]:

$$\begin{aligned} \mathbf{C}_{gg} \bar{\rho}_g + \mathbf{C}_{gc} \bar{\rho}_c + \mathbf{C}_{gT} \bar{T} + \mathbf{C}_{gu} \bar{u} + \mathbf{K}_{gg} \bar{\rho}_g + \mathbf{K}_{gc} \bar{\rho}_c + \mathbf{K}_{gT} \bar{T} + \mathbf{f}_g &= \mathbf{0} \\ \mathbf{C}_{cg} \bar{\rho}_g + \mathbf{C}_{cc} \bar{\rho}_c + \mathbf{C}_{cT} \bar{T} + \mathbf{C}_{cu} \bar{u} + \mathbf{K}_{cg} \bar{\rho}_g + \mathbf{K}_{cc} \bar{\rho}_c + \mathbf{K}_{cT} \bar{T} + \mathbf{f}_c &= \mathbf{0} \\ \mathbf{C}_{Tg} \bar{\rho}_g + \mathbf{C}_{Tc} \bar{\rho}_c + \mathbf{C}_{TT} \bar{T} + \mathbf{C}_{Tu} \bar{u} + \mathbf{K}_{Tg} \bar{\rho}_g + \mathbf{K}_{Tc} \bar{\rho}_c + \mathbf{K}_{TT} \bar{T} + \mathbf{f}_T &= \mathbf{0} \\ \mathbf{C}_{uu} \bar{u} + \mathbf{C}_{ug} \bar{\rho}_g + \mathbf{C}_{uc} \bar{\rho}_c + \mathbf{C}_{uT} \bar{T} + \mathbf{f}_u &= \mathbf{0} \end{aligned} \quad [3.6]$$

The above non-symmetric, non-linear and coupled system of ordinary differential equations can be rewritten in compact form as:

$$\mathbf{C}(\mathbf{x}) \dot{\mathbf{x}} + \mathbf{K}(\mathbf{x}) \mathbf{x} + \mathbf{f}(\mathbf{x}) = \mathbf{0} \quad [3.7]$$

where $\mathbf{x}^T = \{\bar{\rho}_g, \bar{\rho}_c, \bar{T}, \bar{u}\}$

and the non-linear (matrix) coefficients $\mathbf{C}(\mathbf{x})$, $\mathbf{K}(\mathbf{x})$ and $\mathbf{f}(\mathbf{x})$ are obtained by assembling the sub-matrices indicated in [3.6].

3.1.2.2 Linearization: Discretization in time

Finite differences in time, [Z&T89] and [Z&T91], are used for the solution of the initial value problem over a finite time step

$$\Delta t = t_{n+1} - t_n \quad [3.8]$$

where n is the time step number

Following the Generalised Trapezoidal Method as shown for instance in [L&S98], equation [3.7] is rewritten at time t_{n+1} using the relationships

$$\left. \frac{\partial \mathbf{x}}{\partial t} \right|_{n+\Theta} = \frac{\mathbf{x}_{n+1} - \mathbf{x}_n}{\Delta t} \quad [3.9]$$

$$\mathbf{x}_{n+\Theta} = (1-\Theta)\mathbf{x}_n + \Theta\mathbf{x}_{n+1} \quad \text{with } \Theta = [0,1] \quad [3.10]$$

where \mathbf{x}_n is the state vector at time t_n

\mathbf{x}_{n+1} is the state vector at time t_{n+1}

Δt is the time step length

thus obtaining

$$\mathbf{G}(\mathbf{x}_{n+1}) = (\mathbf{C} + \Theta \Delta t \mathbf{K})_{n+\Theta} \mathbf{x}_{n+1} - (\mathbf{C} - (1-\Theta) \Delta t \mathbf{K})_{n+\Theta} \mathbf{x}_n - \Delta t \mathbf{F}_{n+\Theta} = 0 \quad [3.11]$$

Linearized analysis of accuracy and stability suggest the use of $\Theta \geq 1/2$. In the present work implicit one-step time integration has been performed ($\Theta = 1$).

After time integration the non-linear system of equation is linearized, thus obtaining the equations system that can be solved numerically (in compact form)

$$\left. \frac{\partial \mathbf{G}}{\partial \mathbf{x}} \right|_{\mathbf{x}_{n+1}^i} \cdot \Delta \mathbf{x}_{n+1}^{i+1} \cong -\mathbf{G}(\mathbf{x}_{n+1}^i) \quad [3.12]$$

where $(\bullet)_{n+1}^{i+1}$ indicates the current iteration (i+1) in the current time step (n+1)

The Jacobian matrix has the following form

$$\left. \frac{\partial \mathbf{G}}{\partial \mathbf{x}} \right|_{\mathbf{x}_{n+1}^i} = \begin{bmatrix} \frac{\partial G_g}{\partial \bar{\mathbf{p}}_g} & \frac{\partial G_g}{\partial \bar{\mathbf{p}}_c} & \frac{\partial G_g}{\partial \bar{\mathbf{T}}} & \frac{\partial G_g}{\partial \bar{\mathbf{u}}} \\ \frac{\partial G_c}{\partial \bar{\mathbf{p}}_g} & \frac{\partial G_c}{\partial \bar{\mathbf{p}}_c} & \frac{\partial G_c}{\partial \bar{\mathbf{T}}} & \frac{\partial G_c}{\partial \bar{\mathbf{u}}} \\ \frac{\partial G_T}{\partial \bar{\mathbf{p}}_g} & \frac{\partial G_T}{\partial \bar{\mathbf{p}}_c} & \frac{\partial G_T}{\partial \bar{\mathbf{T}}} & \frac{\partial G_T}{\partial \bar{\mathbf{u}}} \\ \frac{\partial G_u}{\partial \bar{\mathbf{p}}_g} & \frac{\partial G_u}{\partial \bar{\mathbf{p}}_c} & \frac{\partial G_u}{\partial \bar{\mathbf{T}}} & \frac{\partial G_u}{\partial \bar{\mathbf{u}}} \end{bmatrix} \quad [3.13]$$

Owing to the strong coupling between the mechanical, thermal and the pore fluids problem, a monolithic solution of [3.12] is preferred using a Newton scheme, equation [3.8] can be rewritten as:

$$\begin{aligned} & \frac{1}{\Delta t} \left[\frac{\partial}{\partial \mathbf{x}} \mathbf{C}(\mathbf{x}'_{n+1}) (\mathbf{x}'_{n+1} - \mathbf{x}_n) + \mathbf{C}(\mathbf{x}'_{n+1}) \right] \Delta \mathbf{x}'_{n+1} + \\ & + \left[\frac{\partial}{\partial \mathbf{x}} \mathbf{K}(\mathbf{x}'_{n+1}) \mathbf{x}'_{n+1} + \mathbf{K}(\mathbf{x}'_{n+1}) + \frac{\partial}{\partial \mathbf{x}} \mathbf{f}(\mathbf{x}'_{n+1}) \right] \Delta \mathbf{x}'_{n+1} = \\ & = - \left[\mathbf{C}(\mathbf{x}'_{n+1}) \frac{\mathbf{x}'_{n+1} - \mathbf{x}_n}{\Delta t} + \mathbf{K}(\mathbf{x}'_{n+1}) \mathbf{x}'_{n+1} + \mathbf{f}(\mathbf{x}'_{n+1}) \right] \end{aligned} \quad [3.14]$$

Finally, the solution vector $\mathbf{x}^T = \{\bar{\mathbf{p}}_g, \bar{\mathbf{p}}_c, \bar{\mathbf{T}}, \bar{\mathbf{u}}\}$ is then updated by the incremental relationship

$$\mathbf{x}_{n+1}^{l+1} = \mathbf{x}_{n+1}^l + \Delta \mathbf{x}_{n+1}^l \quad [3.15]$$

For the convergence and error analysis of the method applied here the interested reader is referred to [G&S96].

3.1.3 Finite Element Library

Three basic elements are utilized in the COMES-GEO code: the isoparametric quadrilateral elements with four and eight node and the Serendipity nine node lagrangian element.

Within a particular element, the state's variables are approximated using linear or quadratic shape functions.

$$\rho_g = \rho_g(t) = \mathbf{N}_p \bar{\mathbf{p}}_g(t) \quad [3.16]$$

$$\rho_c = \rho_c(t) = \mathbf{N}_p \bar{\mathbf{p}}_c(t) \quad [3.17]$$

$$T = T(t) = \mathbf{N}_t \bar{\mathbf{T}}(t) \quad [3.18]$$

$$u = u(t) = \mathbf{N}_u \bar{\mathbf{u}}(t) \quad [3.19]$$

Basic concepts of Finite Element Method element construction and isoparametric element formulation are thoroughly described e.g. by Zienkiewicz [Z&T89].

The interpolation functions for any elements show below can be found in [Z&T89].

3.1.3.1 Four node quadrilateral elements

The basic four node quadrilateral element used in the code has 20 degrees of freedom as shown in Figure 3.2.

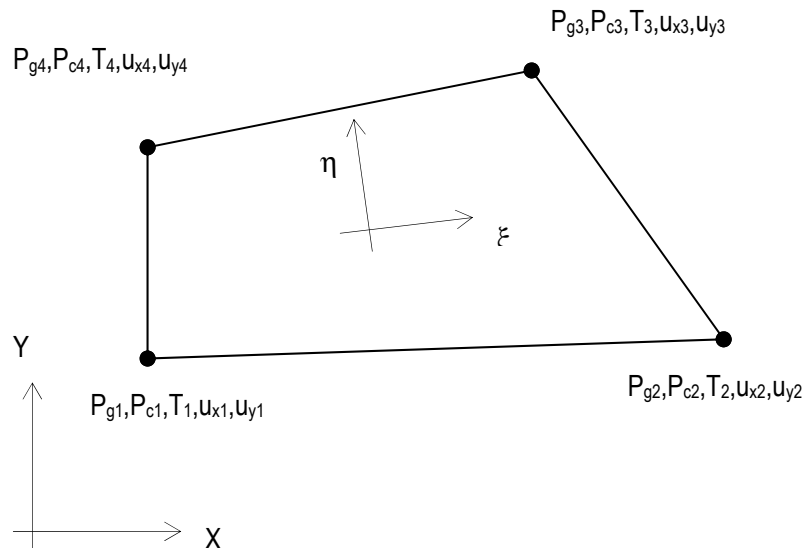


Figure 3.2: 4 node quadrilateral element

3.1.3.2 Eight node quadrilateral elements

The basic four node quadrilateral element used in the code has 40 degrees of freedom as shown in Figure 3.3.

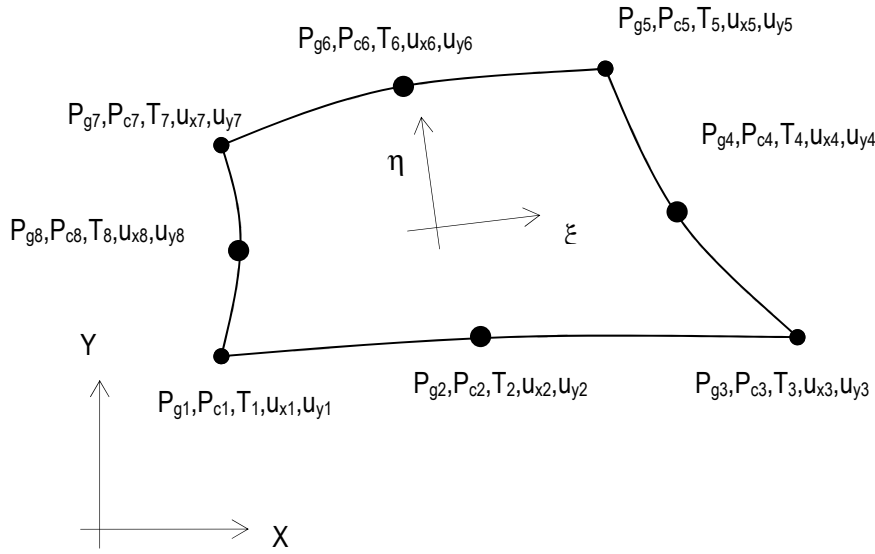


Figure 3.3: 8 node quadrilateral element

3.1.3.3 Nine node quadrilateral elements

The basic nine node quadrilateral element used in the code has 45 degrees of freedom as shown in Figure 3.4.

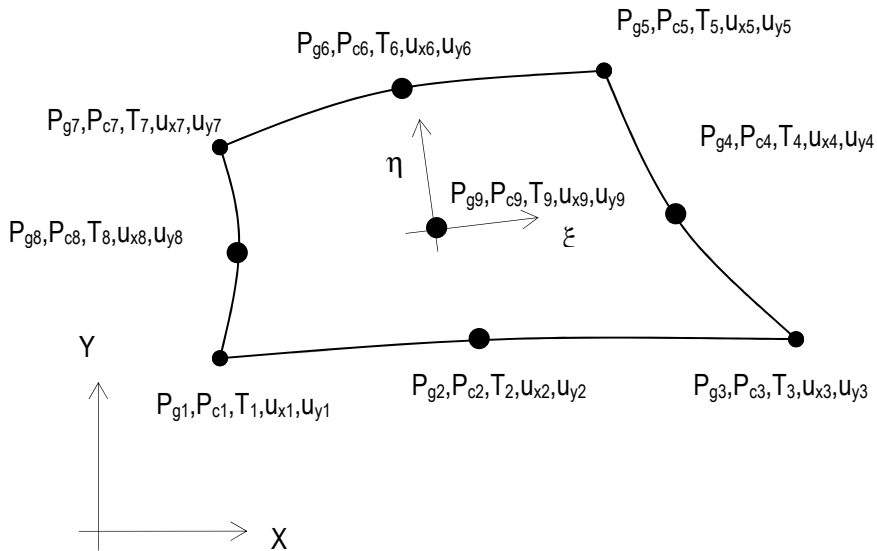


Figure 3.4: 9 node quadrilateral element

3.1.3.4 Mixed elements

The mixed element is shown in Figure 3.4 and is an element with eight nodes where the nodes on the corner are the only ones with all the d.o.f.

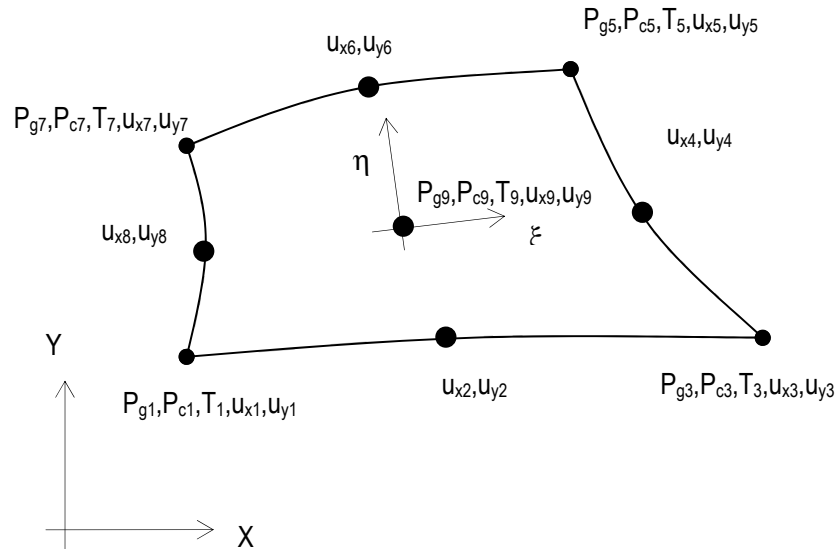


Figure 3.5: Mixed element

3.1.4 Numerical Integration

As far as the numerical integration is concerned, the classical Gauss method is implemented in the code.

In this method the required matrix integrals, used in F.E.M., are in practice evaluated numerically using, for the case treated here:

$$\int \mathbf{F}(r, s) dr ds = \sum_{i,j} \alpha_{ij} \mathbf{F}(r_i, s_j) \quad [3.20]$$

The above formula is directly applicable to the calculation of matrices of rectangular elements, in which all integration limits are -1 to +1. Thus we can apply the one-dimensional integration formulas successively in each direction. As the analytical evaluation of multi-dimensional integrals, in this procedure, successively, the innermost integral is evaluated by keeping the variables corresponding to the other integrals constant.

Therefore, we have for a two dimensional integral:

$$\int_{-1}^{+1} \int_{-1}^{+1} \mathbf{F}(r, s) dr ds = \sum_i \alpha_i \int_{-1}^{+1} \mathbf{F}(r_i, s) ds \quad [3.21]$$

or

$$\int_{-1}^{+1} \int_{-1}^{+1} \mathbf{F}(r, s) dr ds = \sum_{i,j} \alpha_i \alpha_j \mathbf{F}(r_i, s_j) \quad [3.22]$$

In COMES-GEO code we have the possibility to use different orders of integration. The possible numerical integration are presented in the following table, but for the kind of problems resolved using COMES-GEO, fully coupled and strongly non-linear, it is suggest to use eight node quadrilateral elements with a 3x3 numerical integration.

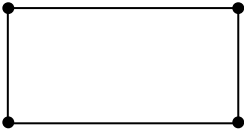
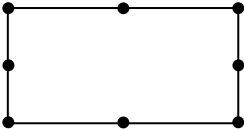
Type of element	Order of integration	Note
	2x2	There is not stabilization in case of reduced interpolation (i.e. with 1 gauss point)
	3x3	also 2x2 is available

Table 3.1: Type of element and order of integration

3.1.5 Matrix Solution Procedure

When the solution algorithms of the theory section are applied to a given iteration or time step, the general result is a matrix equation of the form:

$$Ax = b$$

In the problem considered here the **A** matrix is large (e.g. several thousand equations), sparse, banded, and generally unsymmetric.

The solution of the equations system [3.14] may be approached by a direct method.

The solution procedure used in COMES-GEO is a form of Gauss elimination developed by Irons, called frontal solution method. In particular it is a super fast frontal elimination routine using diagonal pivoting reduced fill-in version which assembles the contribution of each element to form the global stiffness matrix and global load vector and to solve the resulting set of simultaneous equations by Gaussian direct elimination [Bia03].

The main feature of the frontal solution technique is that it assembles the equations and eliminates the variables at the same time.

In fact the basic premise of the frontal method is that the process of assembling the system matrix **A**, from the individual element matrices and the reduction of **A** by standard Gauss elimination may be efficiently intertwined.

In processing each element in sequence, the frontal procedure passes through the following steps:

1. assembly of element equations into global matrix **A**;
2. check each equation in the assembled system to determine if all contributions to this equation have been made;

3. condense from the system (by Gaussian elimination) the equations for all degrees of freedom that have been completely assembled;
4. return to step 1. for the next element.

By combining the assembly and reduction process, computer storage is effectively minimized since only the currently “active” (i.e. incompletely assembled) degrees of freedom are retained in the core storage.

Following the reduction of the matrix \mathbf{A} to an upper triangular form, a back-substitution algorithm completes the solution process for the vector \mathbf{x} .

Since the frontal method is structured around the individual element, it is especially adaptable for general purpose code with an element library.

The processing of higher order elements (e.g. quadratic basis functions) is also handled efficiently by frontal method.

The frontal procedure in COMES-GEO employs diagonal pivoting reduced fill-in. In our case it is a total pivoting which is related to the numerical stability in a strong manner, and works on rows and columns to find the “pivot”. The pivoting technique allows improving the convergence of the numerical system.

3.1.6 Convergence and error analysis

The discretization in space of the balance equations (and of the other ones required to complete the model) with the standard Galerkin method (weighted residuals), results in a non-symmetric, non-linear and coupled system of ordinary differential equations as shown in the section 3.1.2:

$$\mathbf{C}(\mathbf{x})\dot{\mathbf{x}} + \mathbf{K}(\mathbf{x})\mathbf{x} + \mathbf{f}(\mathbf{x}) = \mathbf{0} \quad [3.23]$$

where $\mathbf{x}^T = \{\bar{\mathbf{p}}_g, \bar{\mathbf{p}}_c, \bar{\mathbf{T}}, \bar{\mathbf{u}}\}$

and the non-linear (matrix) coefficients $\mathbf{C}(\mathbf{x})$, $\mathbf{K}(\mathbf{x})$ and $\mathbf{f}(\mathbf{x})$ are obtained by assembling the sub-matrices indicated in [3.6].

We assume consistency and convergence of the finite element discretization in space.

The time discretization is accomplished through a fully implicit finite difference scheme (backward difference)

$$\mathbf{A}\mathbf{x}_{n+1} - \mathbf{B}\mathbf{x}_n - \mathbf{F} = \mathbf{0} \quad [3.24]$$

where

$$\mathbf{A} = \mathbf{C}(\mathbf{x}_{n+1}) + \mathbf{K}(\mathbf{x}_{n+1})\Delta t \quad [3.25]$$

$$\mathbf{B} = \mathbf{C}(\mathbf{x}_{n+1}) \quad [3.26]$$

$$\mathbf{F} = -\mathbf{f}(\mathbf{x}_{n+1})\Delta t \quad [3.27]$$

where n is the time step number

Δt the time step length

We focus our attention on the global error

$$\mathbf{e}_{n+1}^L = \tilde{\mathbf{x}}_{n+1} - \tilde{\mathbf{x}}_{n+1}^L \quad [3.28]$$

where $\tilde{\mathbf{x}}_{n+1}$ is the exact solution of the equation [3.24]

L is the number of performed iterations for the time step $n+1$

To simplify calculations, we assume that there are not round-off errors generated by the algorithm, except those introduced by the initial values at time t_0 .

If we replace \mathbf{x}_{n+1} and \mathbf{x}_n in equation [3.24] by the corresponding exact values, we obtain:

$$\mathbf{A}\tilde{\mathbf{x}}_{n+1} = \mathbf{B}\tilde{\mathbf{x}}_n + \tilde{\mathbf{F}} + \mathbf{r}_{n+1} \quad [3.29]$$

where \mathbf{r}_{n+1} is the local truncation error of equation [3.24]

The calculated numerical solution \mathbf{x}_{n+1}^L satisfies equation [3.24], so we can subtract equation [3.24] written for \mathbf{x}_{n+1}^L and \mathbf{x}_n^L respectively from the equation [3.29].

This results in:

$$\mathbf{A}\mathbf{e}_{n+1}^L = \mathbf{B}\mathbf{e}_n^L + \mathbf{r}_{n+1} \quad [3.30]$$

Neither symmetry not positive definiteness of the matrices is assumed here.

By a recursive application for the index n , we have from equation [3.29] that:

$$\begin{aligned} \mathbf{e}_{n+1}^L = & (\mathbf{A}\mathbf{B}^{-1})_{n+1} \cdots (\mathbf{A}\mathbf{B}^{-1})_1 \mathbf{e}_0^0 + \sum_{k=0}^{n-1} (\mathbf{A}\mathbf{B}^{-1})_{n+1} \cdots \\ & \cdots (\mathbf{A}\mathbf{B}^{-1})_{n+1-k} (\mathbf{A}^{-1})_{n-k} \mathbf{r}_{n-k} + (\mathbf{A}^{-1})_{n+1} \mathbf{r}_{n+1} \end{aligned} \quad [3.31]$$

The total error \mathbf{e}_{n+1}^L is influenced by the local truncation error \mathbf{r}_k , being $k \leq n+1$ and by the initial round-off error \mathbf{e}_0^0 made at the starting step, because then for $n=0$ and $L=0$

$$\mathbf{e}_0^0 = \tilde{\mathbf{x}}_0 - \mathbf{x}_0^0 \quad [3.32]$$

where $\tilde{\mathbf{x}}_0 = \mathbf{x}_0$ is the exact solution of the equation [3.24]

Thus

$$\|\mathbf{A}^{-1}\mathbf{B}\| < 1 \quad \forall n \quad [3.33]$$

where $\|\cdot\|$ is the spectral norm

is the sufficient stability condition for applied solution procedure.

The stability condition and the consistency property

$$\mathbf{r}_k = \mathbf{O}(\Delta t^2) \quad [3.34]$$

together with the iteration convergence, indicated below, are sufficient for the above procedure to be globally convergent.

Considering the non-linearity of the system of equations [3.24] the solution is obtained with a Newton-Raphson type procedure [3.14] and [3.15].

3.2 PLASTICITY IN SOILS

The aim of this PhD thesis is, as its title suggest, the implementation of advanced constitutive models. These advanced models are of two different types, the first one belong to ACMEG family and the second one to Generalized Plasticity family.

The ACMEG models are modified Cam-Clay models based on Critical State concept developed with the Classical Plasticity theory, while the second family models is based on the Generalized Plasticity [Z&M84] [M&Z84].

In this part we will first give a short summary of the classic elastoplastic models for soils (see for further details section 4.5 of [L&S98]).

3.2.1 Classical elastoplasticity

In the case of classical elastoplasticity both Mohr-Coulomb and critical state yield surfaces will be considered in the present work. The critical state component requires an associated flow rule, whereas the Mohr-Coulomb component can also consider a non-associated flow rule. A more extensive development of the theory presented in this section can be found elsewhere, e.g. Zienkiewicz [Zie77], Nayak and Zienkiewicz [N&Z72], Naylor [Nay75] and Humpheson [Hum76].

A yield criterion defines the limits of elasticity under any possible combination of stresses. When written in terms of stress components, this is called a yield function and represents a surface in the n-dimensional stress space, which separates the elastic state from an outer zone of impermissible stress states. The position and size of the surface depends upon the initial yield surface and the hardening law which specifies the manner in which the surface changes during plastic flow. Hardening is considered here to depend only on plastic strain $\boldsymbol{\varepsilon}^P$.

The yield surface F can therefore be defined as

$$F(\boldsymbol{\sigma}', \boldsymbol{\varepsilon}^P) = 0 \quad [3.35]$$

Irreversible (plastic) straining occurs when the stress state reaches the yield surface, while for $F < 0$ the behaviour is elastic. The direction of the plastic strain is defined by the plastic potential surface $Q(\boldsymbol{\sigma}')$.

The increment of plastic strains is given by the flow rule

$$d\boldsymbol{\varepsilon}^P = \lambda \frac{\partial Q}{\partial \boldsymbol{\sigma}'} \quad [3.36]$$

where λ is a yet unknown scalar (plastic multipliers) giving the amplitude of the plastic strain

If $F \equiv Q$ the flow rule is said to be associated.

Differentiating equation [3.35] gives the relationship

$$\left(\frac{\partial F}{\partial \boldsymbol{\sigma}'} \right)^T d\boldsymbol{\sigma}' + \left(\frac{\partial F}{\partial \boldsymbol{\varepsilon}^P} \right)^T d\boldsymbol{\varepsilon}^P = 0 \quad [3.37]$$

If the flow rule [3.31] is taken into account, then equation [3.37] becomes

$$\left(\frac{\partial F}{\partial \boldsymbol{\sigma}'} \right)^T d\boldsymbol{\sigma}' + \left(\frac{\partial F}{\partial \boldsymbol{\varepsilon}^P} \right)^T d\lambda \frac{\partial Q}{\partial \boldsymbol{\sigma}'} = 0 \quad [3.38]$$

hence

$$d\lambda = - \frac{\left(\frac{\partial F}{\partial \boldsymbol{\sigma}'} \right)^T d\boldsymbol{\sigma}'}{\left(\frac{\partial F}{\partial \boldsymbol{\varepsilon}^P} \right)^T \left(\frac{\partial Q}{\partial \boldsymbol{\sigma}'} \right)} \quad [3.39]$$

Once the elastic limit has been exceeded for an elastoplastic model, the total strain $d\boldsymbol{\varepsilon}$ can be expressed as the sum of the elastic and the plastic components $d\boldsymbol{\varepsilon}^e$ and $d\boldsymbol{\varepsilon}^p$. This is valid for small-strain plasticity theory, which is always assumed in this work and can also be used in finite strain situations when an updated Lagrangian procedure is used:

$$d\boldsymbol{\varepsilon} = d\boldsymbol{\varepsilon}^e + d\boldsymbol{\varepsilon}^p = \mathbf{D}^{e-1} d\boldsymbol{\sigma}' + d\lambda \frac{\partial Q}{\partial \boldsymbol{\sigma}'} = 0 \quad [3.40]$$

where \mathbf{D}^e is the tangent elastic stiffness matrix

In the present context only isotropic linear elasticity is considered, so that \mathbf{D}^e is defined by

$$D^e = \frac{E}{(1+\nu)(1-2\nu)} \begin{bmatrix} 1-\nu & \nu & \nu & 0 & 0 & 0 \\ & 1-\nu & \nu & 0 & 0 & 0 \\ & & 1-\nu & 0 & 0 & 0 \\ & & & \frac{1-2\nu}{2} & 0 & 0 \\ & & & & \frac{1-2\nu}{2} & 0 \\ & & & & & \frac{1-2\nu}{2} \end{bmatrix} \quad [3.41]$$

Premultiplying equation [3.40] by $\left(\frac{\partial F}{\partial \boldsymbol{\sigma}'}\right)^T \mathbf{D}^e$, and substituting for $\left(\frac{\partial F}{\partial \boldsymbol{\sigma}'}\right)^T d\boldsymbol{\sigma}'$ by means of equation [3.38], leads to the following

$$\left(\frac{\partial F}{\partial \boldsymbol{\sigma}'}\right)^T \mathbf{D}^e d\boldsymbol{\varepsilon} = -\left(\frac{\partial F}{\partial \boldsymbol{\varepsilon}^p}\right)^T d\lambda \frac{\partial Q}{\partial \boldsymbol{\sigma}'} + \left(\frac{\partial F}{\partial \boldsymbol{\sigma}'}\right)^T \mathbf{D}^e d\lambda \frac{\partial Q}{\partial \boldsymbol{\sigma}'} \quad [3.42]$$

The term $d\lambda$ is now obtained from equation [3.42] and may be substituted into equation [3.40], premultiplying by \mathbf{D}^e and rearranging gives the equation defining the tangent elastoplastic modulus matrix \mathbf{D}^{ep}

$$d\boldsymbol{\sigma}' = \left[\mathbf{D}^e - \frac{D^e \left(\frac{\partial Q}{\partial \boldsymbol{\sigma}'}\right) \left(\frac{\partial F}{\partial \boldsymbol{\sigma}'}\right)^T \mathbf{D}^e}{-\left(\frac{\partial F}{\partial \boldsymbol{\varepsilon}^p}\right)^T \left(\frac{\partial Q}{\partial \boldsymbol{\sigma}'}\right) + \left(\frac{\partial F}{\partial \boldsymbol{\sigma}'}\right)^T \mathbf{D}^e \left(\frac{\partial Q}{\partial \boldsymbol{\sigma}'}\right)} \right] d\boldsymbol{\varepsilon} \quad [3.43]$$

Construction of the elastoplastic constitutive matrix requires the vectors $\frac{\partial Q}{\partial \boldsymbol{\sigma}'}$, $\frac{\partial F}{\partial \boldsymbol{\sigma}'}$ and $\frac{\partial F}{\partial \boldsymbol{\varepsilon}^p}$ to be evaluated. These vectors will be formulated in the follows sections for the Mohr-Coulomb and critical state yield surfaces.

The surfaces will be defined using the stress invariants p , q and ϑ . It is therefore necessary to evaluate the derivatives of these invariants with respects to $\boldsymbol{\sigma}'$.

From the definition of the invariants (see 6.2) it follows that

$$\frac{\partial p}{\partial \sigma'} = \begin{bmatrix} \frac{1}{3} \\ \frac{1}{3} \\ \frac{1}{3} \\ 0 \\ 0 \\ 0 \end{bmatrix} \quad [3.44]$$

$$\frac{\partial q}{\partial \sigma'} = \begin{bmatrix} 2\sigma_x - \sigma_y - \sigma_z \\ 2\sigma_y - \sigma_x - \sigma_z \\ 2\sigma_z - \sigma_x - \sigma_y \\ 6\tau_{xy} \\ 6\tau_{yz} \\ 6\tau_{xz} \end{bmatrix} \quad [3.45]$$

Differentiating ϑ yields

$$3 \cos \vartheta_0 d\vartheta_0 = -\frac{27}{2q^3} \left(dJ'_3 - \frac{3J'_3}{q} dq \right) \quad [3.46]$$

so that

$$\frac{\partial \vartheta}{\partial \sigma'} = \frac{\partial \vartheta_0}{\partial \sigma'} = \frac{9}{2q^3 \cos(3\vartheta_0)} \left[\frac{3J'_3}{q} - \frac{\partial q}{\partial \sigma'} - \frac{\partial J'_3}{\partial \sigma'} \right] \quad [3.47]$$

For the plane stress and axial symmetry $\tau_{yz}=0$ and $\tau_{zx}=0$, so

$$|J'_3| = (\sigma_z - p)[(\sigma_x + p)(\sigma_y + p) - \tau_{xy}^2] \quad [3.48]$$

and

$$\frac{\partial |J'_3|}{\partial \sigma'} = \begin{bmatrix} (\sigma_x + p)(\sigma_z + p) \\ (\sigma_y + p)(\sigma_z + p) \\ (\sigma_x + p)(\sigma_y + p) - \tau_{xy}^2 \\ -2(\sigma_z + p)\tau_{xy} \\ 0 \\ 0 \end{bmatrix} + \frac{1}{9} \begin{bmatrix} q^2 \\ q^2 \\ q^2 \\ 0 \\ 0 \\ 0 \end{bmatrix} \quad [3.49]$$

This derivatives are replaced in 6.2.

3.2.2 Mohr-Coulomb yield surface

Mohr's theory of failure involves the construction of an envelope for all possible circles of stress that can be drawn for a particular problem. These envelopes are generally curved but are usually replaced by a straight line.

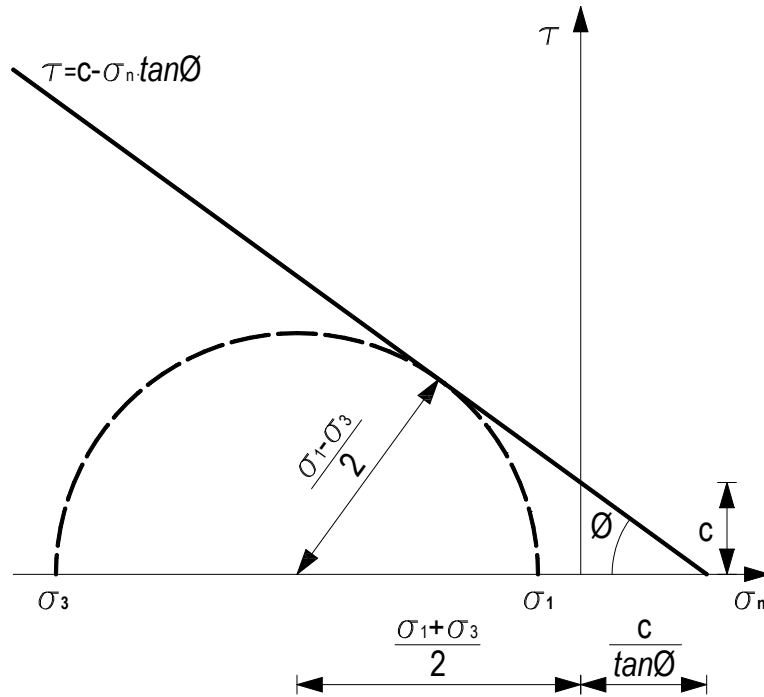


Figure 3.6: Mohr-Coulomb failure envelope

This is equivalent to assuming that the soil conforms to the Coulomb failure criterion [Cou1776], which states there is a linear relationship between the shear stress τ at failure and the normal stress, σ_n (Figure 3.6):

$$\tau = c + \sigma_n \tan \phi \tag{3.50}$$

where c is the apparent cohesion

ϕ is the angle of internal friction

From Figure 3.6 it may be deduced that

$$\sin \phi = \frac{\frac{(\sigma_1 - \sigma_3)}{2}}{\frac{c}{\tan \phi} + \frac{(\sigma_1 + \sigma_3)}{2}} \tag{3.51}$$

or, by rearranging.

$$(\sigma_1 - \sigma_3) = 2c \cos \phi + (\sigma_1 + \sigma_3) \sin \phi \tag{3.52}$$

where σ_1 and σ_3 are the major and minor principal stresses at failure. This yield criterion is independent of the intermediate principal stress σ_2 and is therefore not a complete generality of the true behaviour. This criticism applies to any yield criterion that can be represented by a single line in a two dimensional stress space.

The sum and the difference of the maximum and minimum principal stresses are, considering the definition of stress invariants

$$\sigma_1 - \sigma_3 = \frac{2}{\sqrt{3}} q \cos \vartheta_0 \quad [3.53]$$

$$\sigma_1 + \sigma_3 = 2p + \frac{2}{3} q \sin \vartheta_0 \quad [3.54]$$

which, after substitution into equation [3.52], results in the following expression for the Mohr-Coulomb failure surface

$$F = (\sqrt{3} \cos \vartheta_0 - \sin \vartheta_0 \sin \varnothing) q - 3p \sin \varnothing - 3c \cos \varnothing = 0 \quad [3.55]$$

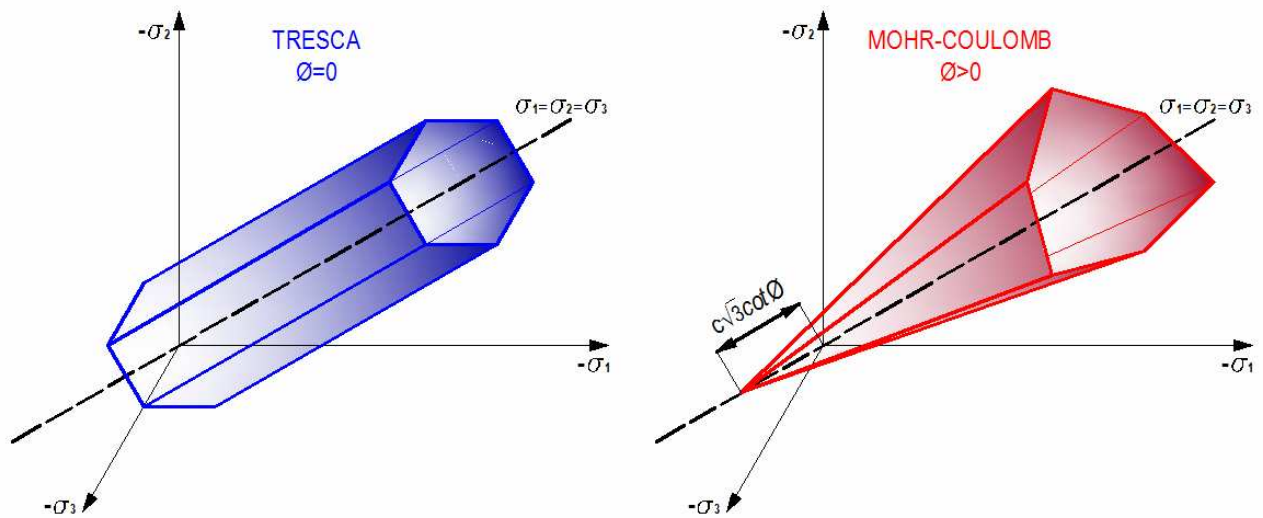


Figure 3.7: Mohr-Coulomb and Tresca yield surfaces in the principal stress space

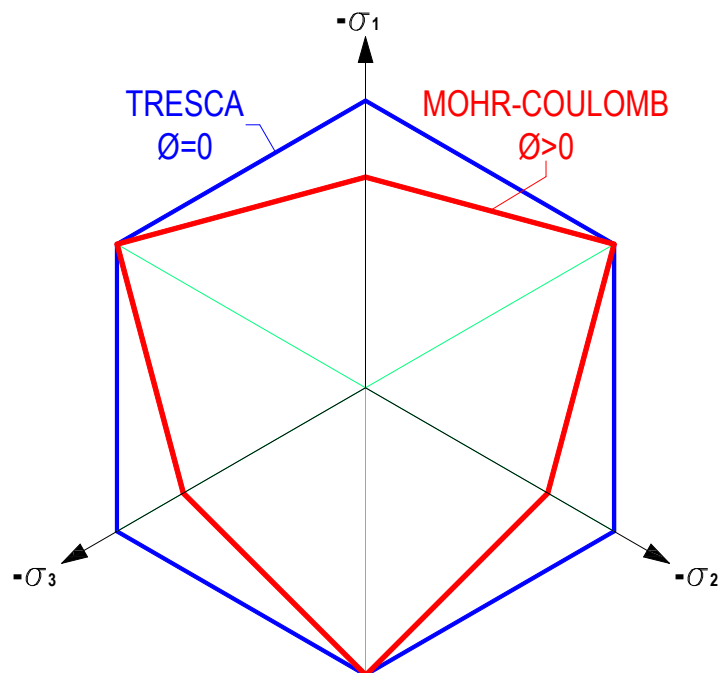


Figure 3.8: Mohr-Coulomb and Tresca yield surfaces in the π -plane

In a principal stress space, equation [3.55] represents an irregular right hexagonal pyramid, the axis of which lies along the space diagonal (Figure 3.7). The π -plane section of the yield surface is shown in Figure 3.8.

The plastic potential surface $Q(p, q, \vartheta_0) = 0$, passing through the current stress point can be obtained in a similar manner. The direction of plastic straining in the τ - σ_n plane is usually expressed by the normal to a line defined as follows

$$\tau = \bar{c} + \sigma_n \tan \psi \quad [3.56]$$

where the value of \bar{c} ensures that the line passes through the current stress point

ψ is the dilatancy angle

The potential surface Q , in terms of p, q, ϑ_0 can be obtained in the same way as the yield surface and results in the following expression

$$Q = (\sqrt{3} \cos \vartheta_0 - \sin \vartheta_0 \sin \psi)q - 3p \sin \psi - 3\bar{c} \cos \psi = 0 \quad [3.57]$$

Equations [3.55] and [3.56] may be applied to either total or effective stresses by taking into account the appropriate material properties.

When $\vartheta = \psi = 0$, which is the case in the total stress analysis of undrained, saturated soil, both surfaces assume the form of a Tresca prism. In the principal stress space this surface is represented by a regular hexagonal cylinder with its axis also lying along the space diagonal (Figure 3.7 and Figure 3.8).

Strain hardening or softening may be dealt with by making c a function of volumetric plastic strain by using the following equation

$$\frac{dc}{d\varepsilon_v^p} = \frac{c}{\chi} \quad [3.58]$$

where χ is a constant

The vectors $\frac{\partial Q}{\partial \sigma'}, \frac{\partial F}{\partial \sigma'}$ and $\frac{\partial F}{\partial \varepsilon^p}$ required for the constitutive matrix of equation [3.43] are now derived. The chain

rule of differentiation gives

$$\frac{\partial F}{\partial \sigma'} = \frac{\partial F}{\partial p} \frac{\partial p}{\partial \sigma'} + \frac{\partial F}{\partial q} \frac{\partial q}{\partial \sigma'} + \frac{\partial F}{\partial \vartheta} \frac{\partial \vartheta}{\partial \sigma'} \quad [3.59]$$

where

$$\frac{\partial F}{\partial p} = -3 \sin \vartheta \quad [3.60]$$

$$\frac{\partial F}{\partial q} = \sqrt{3} \cos \vartheta_0 - \sin \vartheta_0 \sin \vartheta \quad [3.61]$$

$$\frac{\partial F}{\partial \vartheta} = -(\sqrt{3} \sin \vartheta_0 + \cos \vartheta_0 \sin \vartheta)q \quad [3.62]$$

Similarly

$$\frac{\partial Q}{\partial \sigma'} = \frac{\partial Q}{\partial p} \frac{\partial p}{\partial \sigma'} + \frac{\partial Q}{\partial q} \frac{\partial q}{\partial \sigma'} + \frac{\partial Q}{\partial \vartheta} \frac{\partial \vartheta}{\partial \sigma'} \quad [3.63]$$

where

$$\frac{\partial Q}{\partial \rho} = -3 \sin \psi \quad [3.64]$$

$$\frac{\partial Q}{\partial q} = \sqrt{3} \cos \vartheta_0 - \sin \vartheta_0 \sin \psi \quad [3.65]$$

$$\frac{\partial Q}{\partial \vartheta} = -(\sqrt{3} \sin \vartheta_0 + \cos \vartheta_0 \sin \psi) q \quad [3.66]$$

Equation [3.55] and [3.58] also lead to

$$\frac{\partial F}{\partial \boldsymbol{\varepsilon}^p} = \frac{\partial F}{\partial \varepsilon_v^p} \frac{\partial \varepsilon_v^p}{\partial \boldsymbol{\varepsilon}^p} + \frac{\partial F}{\partial \varepsilon_q^p} \frac{\partial \varepsilon_q^p}{\partial \boldsymbol{\varepsilon}^p} \quad [3.67]$$

but

$$\frac{\partial F}{\partial \varepsilon_q^p} \frac{\partial \varepsilon_q^p}{\partial \boldsymbol{\varepsilon}^p} = 0 \quad [3.68]$$

hence

$$\begin{aligned} \frac{\partial F}{\partial \boldsymbol{\varepsilon}^p} &= \frac{\partial F}{\partial \varepsilon_v^p} \frac{\partial \varepsilon_v^p}{\partial \boldsymbol{\varepsilon}^p} = \frac{\partial F}{\partial c} \frac{\partial c}{\partial \varepsilon_v^p} \frac{\partial \varepsilon_v^p}{\partial \boldsymbol{\varepsilon}^p} = \\ &= 3 \cos \emptyset \frac{\partial c}{\partial \varepsilon_v^p} [-1 \ -1 \ -1 \ 0 \ 0 \ 0]^T = \\ &= \frac{3c}{\chi} \cos \emptyset [-1 \ -1 \ -1 \ 0 \ 0 \ 0]^T \end{aligned} \quad [3.69]$$

since

$$[-1 \ -1 \ -1 \ 0 \ 0 \ 0] \frac{\partial Q}{\partial \boldsymbol{\sigma}'} = \frac{\partial Q}{\partial \rho} \quad [3.70]$$

it follow that

$$\left(\frac{\partial F}{\partial \boldsymbol{\varepsilon}^p} \right)^T \frac{\partial Q}{\partial \boldsymbol{\sigma}'} = \frac{3c}{\chi} \cos \emptyset \frac{\partial Q}{\partial \rho} = -\frac{qc}{\chi} \cos \emptyset \sin \psi \quad [3.71]$$

which is needed for the constitutive matrix.

3.2.3 Critical state model

The critical state model is a form of elastoplastic isotropic strain-hardening law. It introduces a distinction between yielding and ultimate collapse by using the concept of a critical state line in conjunction with a strain-dependent yield surface. A soil is at the critical state [R&P63] if, during continuous deformation, there is no change in the void ratio and the effective stress components. In this model a soil undergoing shear deformation can pass through a yield point without collapse and continue to deform until eventually the critical state line is reached, where ideal plasticity conditions exist. The soil continues to deform without further change of void ratio or stress. Starting from two alternative assumptions regarding the dissipation of energy during plastic yielding.

Roscoe and Schofield [R&S63] and Schofield and Wroth [S&W68] proposed the 'Cam clay' model and Roscoe and Burland [R&B68] the 'modified Cam clay' model.

3.2.3.1 Modified Cam Clay model

The modified Cam clay model fits experimental data quite satisfactorily and is selected here. Its yield surface is an ellipse in the p-q plane (Figure 3.9) and is defined by the equation

$$F = \frac{q^2}{M_{cs}^2} - 2p \cdot p_c(\varepsilon_v^p) + p^2 = 0 \quad [3.72]$$

where M_{cs} is the slope of the failure line in the p-q plane

$p_c(\varepsilon_v^p)$ is the current semidiameter of the ellipse in the p-direction

The full surface is a surface of revolution about the q-axis and is therefore defined by p and q only.

As the ellipse changes in magnitude, the locus of the critical state points is a pyramid with its apex at the origin shown by the critical state line in the plane (Figure 3.9). The flow rule is associative, i.e. $F \equiv Q$ and the principle of normality therefore applies to the yield surface. Since the surface is smooth, the direction of plastic straining is uniquely defined for every point of the surface. At the intersection of the critical state line and the ellipse, the normal to the yield surface is vertical. Hence at this point no component of plastic volumetric strain exists and all the plastic strain is distortional: the soil can deform at a constant volume.

The yield surface is therefore strain dependent and expands or contracts as the soil hardens or softens. Strain hardening is associated with compaction and strain softening with a volume increase. The initial size of the ellipse is governed by the maximum preconsolidation pressure $2p_{c0}$ to which the soil has previously been subjected during its past history. If the soil has been overconsolidated at some time in its history, then p_{c0} may be quite large and the soil could sustain substantial loads before any yielding occurred. For a stress path of type 1-2 (Figure 3.9) the plastic strain vector normal to the ellipse produces a plastic volumetric decrease which causes the soil to harden. The ellipse expands until eventually position 2 is reached, at which point no further volumetric strain occurs. The soil flows as a frictional fluid with constant volume.

The stress 3-4 shows a strain-softening behaviour due to the expansion of the material. Consequently, the ellipse decreases in size and eventually at point 4 the no-volume-change limit is reached and collapse occurs at constant volume. Many investigators have serious misgivings about the validity of the strain-softening behaviour thus described [Zie75].

The strain-hardening law uses the consolidation parameter λ and κ obtained by isotropic loading and unloading of normally consolidated soil. The parameter λ is the slope of the void ratio versus $\ln(p)$ plot during loading whereas, κ is the initial value of the slope during rebound (Figure 3.11). From the geometry of Figure 3.11 it may be seen that the relationship between the plastic component of the void ratio change and the mean stress p is given by

$$(e - e_0)^p = -(\lambda - \kappa)(\ln 2p_c - \ln 2p_{c0}) \quad [3.73]$$

or

$$\ln\left(\frac{p_c}{p_{c0}}\right) = -\frac{(e - e_0)^p}{(\lambda - \kappa)} \quad [3.74]$$

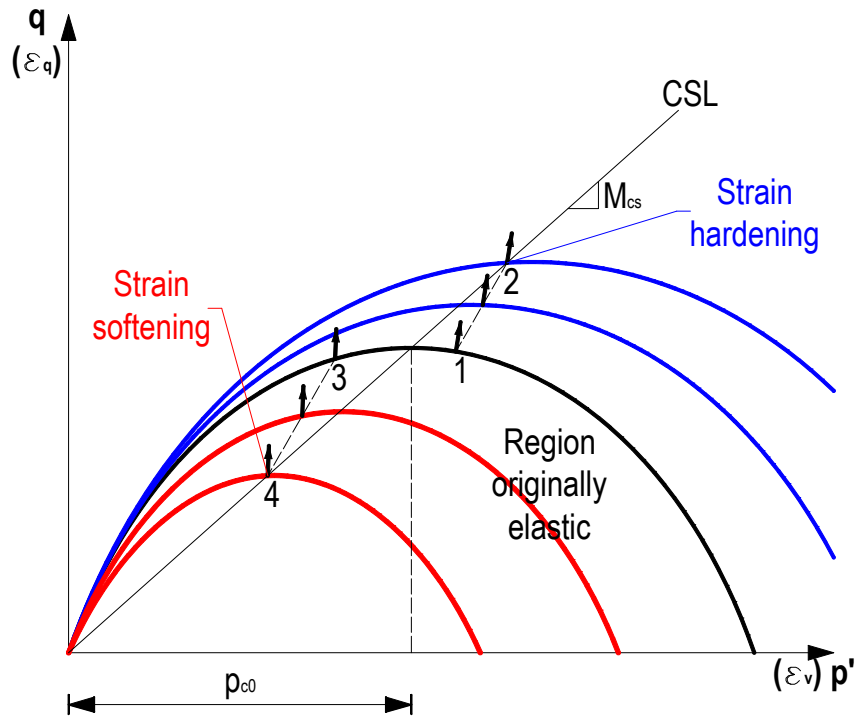


Figure 3.9: Modified Cam clay model in the space of the two stress invariants p and q

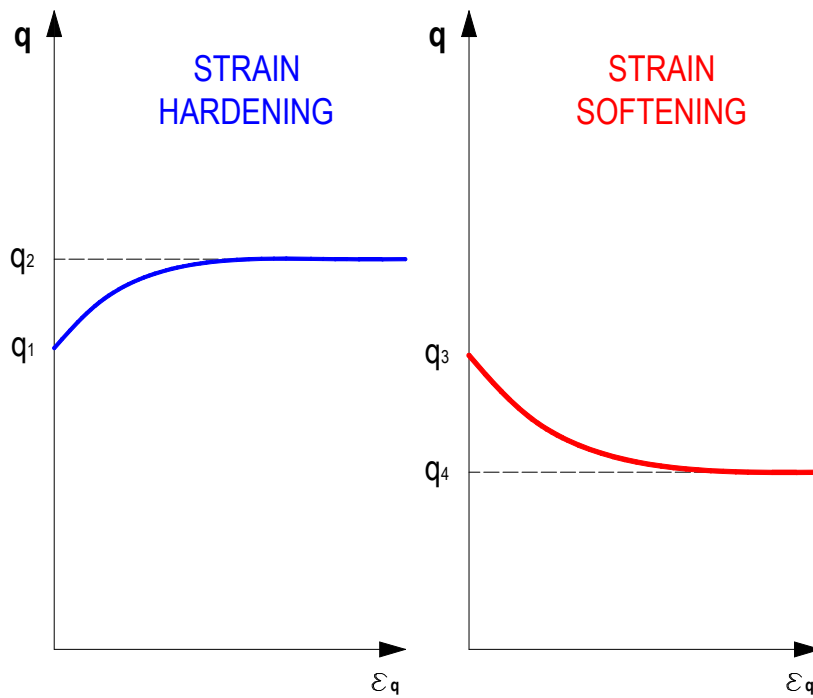


Figure 3.10: Strain hardening and strain softening behaviour in modified Cam clay model

The changes in volumetric strain are related to changes in void ratio as follows

$$\epsilon_v - \epsilon_{v0} = -\frac{e - e_0}{1 + e} \tag{3.75}$$

Hence equation [3.74] may be rewritten in the form

$$p_c = p_{c0} \cdot e^{\frac{(\varepsilon_v - \varepsilon_{v0})^p}{\chi}} \quad [3.76]$$

where $\chi = \frac{\lambda - \kappa}{1 - e_0}$ is an empirical constant.

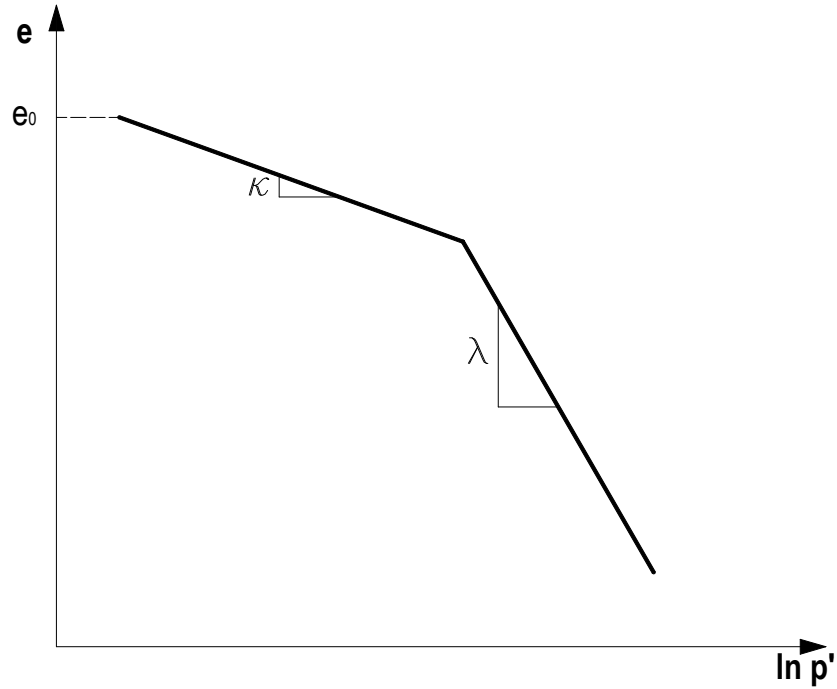


Figure 3.11: Consolidation parameters λ and κ

Denoting the accumulated plastic volumetric strain by h , i.e.

$$h = \int d\varepsilon_v^p = (\varepsilon_v - \varepsilon_{v0})^p \quad [3.77]$$

the hardening law assumes the form

$$p_c = p_{c0} \cdot e^{\frac{h}{\chi}} \quad [3.78]$$

The derivatives $\frac{\partial F}{\partial \sigma'}$ and $\frac{\partial F}{\partial \sigma^p}$ required to set up the constitutive matrix are next obtained. From equation [3.72] it

follows that

$$\frac{\partial F}{\partial \sigma'} = \frac{\partial F}{\partial p} \frac{\partial p}{\partial \sigma'} + \frac{\partial F}{\partial q} \frac{\partial q}{\partial \sigma'} \quad [3.79]$$

where

$$\frac{\partial F}{\partial p} = 2(p - p_c) \quad [3.80]$$

$$\frac{\partial F}{\partial q} = \frac{2q}{M_{cs}^2} \quad [3.81]$$

Equation [3.72] also lead to

$$\frac{\partial F}{\partial \boldsymbol{\varepsilon}^p} = \frac{\partial F}{\partial \varepsilon_v^p} \frac{\partial \varepsilon_v^p}{\partial \boldsymbol{\varepsilon}^p} + \frac{\partial F}{\partial \varepsilon_q^p} \frac{\partial \varepsilon_q^p}{\partial \boldsymbol{\varepsilon}^p} \quad [3.82]$$

but

$$\frac{\partial F}{\partial \varepsilon_q^p} \frac{\partial \varepsilon_q^p}{\partial \boldsymbol{\varepsilon}^p} = 0 \quad [3.83]$$

hence

$$\frac{\partial F}{\partial \boldsymbol{\varepsilon}^p} = \frac{\partial F}{\partial \varepsilon_v^p} \frac{\partial \varepsilon_v^p}{\partial \boldsymbol{\varepsilon}^p} = \left(-2\rho \frac{\partial p_c}{\partial \varepsilon_v^p} \right) [-1 \ -1 \ -1 \ 0 \ 0 \ 0]^T \quad [3.84]$$

Equation [3.76] leads to the following result

$$\frac{dp_c}{p_c} = \frac{d\varepsilon_v^p}{\chi} \quad [3.85]$$

Hence, equation [3.84] becomes

$$\frac{\partial F}{\partial \boldsymbol{\varepsilon}^p} = \frac{-2\rho \cdot p_c}{\chi} [-1 \ -1 \ -1 \ 0 \ 0 \ 0]^T \quad [3.86]$$

From equations [3.43], [3.72] and [3.76] it can be seen that before defining the parameters of the modified Cam clay model, a knowledge of E , ϵ , p_{c0} , M_{cs} , θ_0 , λ and χ is required. A more general critical state model involving the third stress invariant is discussed in the next section. This requires one more parameter.

3.2.3.2 p-q- ϑ Critical State Model

The generalisation of the model to include the effect of the variation of the third stress invariant ϑ is achieved by letting the slope of the critical state line vary with ϑ . Zienkiewicz et al. [Zie75] developed an elliptical model whose π -plane section was the same as that of the Mohr-Coulomb surface. An alternative to that model uses the critical state ellipse only in the subcritical region (to the right of the critical region, to the right of the critical state line) whereas the supercritical region may be cut off by a Mohr-Coulomb surface [Hum76].

The model dealt with here consists of the full ellipse with a Mohr-Coulomb, π -plane section and with the critical state line passing through the origin [Dru59]

$$F = [p - \alpha_p(\varepsilon_v^p)]^2 + \left[\frac{q}{n(\vartheta)} \right]^2 - a^2(\varepsilon_v^p) = 0 \quad [3.87]$$

where $\alpha_p(\varepsilon_v^p)$ is the p-coordinate of the centre of the elliptical surface

$n(\vartheta)$ is the ratio of the diameters in the q and p directions, defined by the Mohr-Coulomb equation for $c=0$

$a(\varepsilon_v^p)$ is the semi-diameter of the ellipse in the p-direction (Figure 3.12)

Plastic yielding is again of the associated form and strain hardening depends on the plastic changes of void ratio or volumetric strain. From inspection of the critical state line passing through the origin, it follows that

$$\frac{d\alpha_p}{\alpha_p} = \frac{da}{a} \quad [3.88]$$

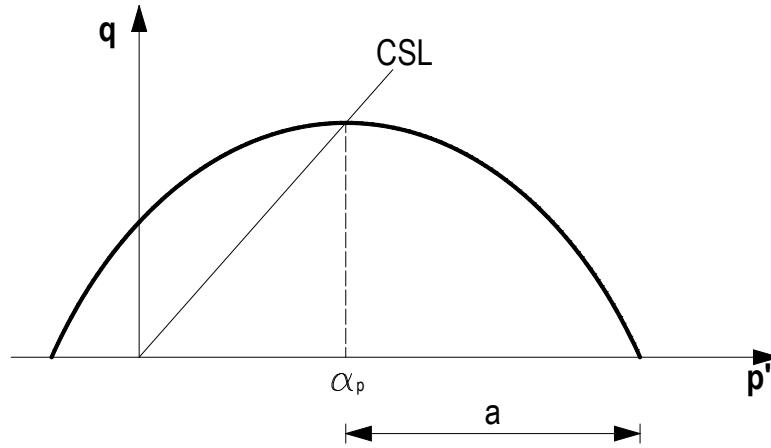


Figure 3.12: p-q- ϑ critical state model

The hardening rule can be obtained in a similar manner [Dru59] as in the previous section, resulting in

$$\alpha_p = \alpha_{p0} \cdot e^{\frac{h}{\chi}} \quad [3.89]$$

and

$$a = a_0 \cdot e^{\frac{h}{\chi}} \quad [3.90]$$

hence

$$\frac{d\alpha_p}{\alpha_p} = \frac{da}{a} = \frac{d\varepsilon_v^p}{\chi} \quad [3.91]$$

A formula is required for one more term; n is needed to define the yield surface of equation [3.87].

It is assumed that the 'critical state' lies on a Mohr-Coulomb surface for which c equals zero. From equation [3.55] with c=0 it follows that

$$M_{cs} = \frac{\partial q}{\partial p} = \frac{3 \sin \varnothing}{\sqrt{3} \cos \vartheta_0 - \sin \vartheta_0 \sin \varnothing} \quad [3.92]$$

The geometry of Figure 3.12 reveals that

$$n(\vartheta) = \frac{\alpha_p M_{cs}}{a} = \frac{\alpha_p}{a} \frac{3 \sin \varnothing}{\sqrt{3} \cos \vartheta_0 - \sin \vartheta_0 \sin \varnothing} \quad [3.93]$$

The derivatives $\frac{\partial F}{\partial \sigma'}$ and $\frac{\partial F}{\partial \varepsilon^p}$, required for the constitutive matrix, are now derived. Hence, for equations [3.87] and

[3.88] it can be seen that

$$\frac{\partial F}{\partial \sigma'} = \frac{\partial F}{\partial p} \frac{\partial p}{\partial \sigma'} + \frac{\partial F}{\partial q} \frac{\partial q}{\partial \sigma'} + \frac{\partial F}{\partial \vartheta} \frac{\partial \vartheta}{\partial \sigma'} \quad [3.94]$$

where

$$\frac{\partial F}{\partial p} = 2(p - \alpha_p) \quad [3.95]$$

$$\frac{\partial F}{\partial q} = \frac{2q}{n^2} \quad [3.96]$$

$$\frac{\partial F}{\partial \vartheta} = \frac{-2q^2}{n^3} \frac{dn}{d\vartheta} = -\frac{2q^2}{n^2} \frac{\sqrt{3} \sin \vartheta_0 - \cos \vartheta_0 \sin \vartheta}{\sqrt{3} \cos \vartheta_0 - \sin \vartheta_0 \sin \vartheta} \quad [3.97]$$

From equations [3.87] and [3.91], and also [3.84], obtain

$$\begin{aligned} \frac{\partial F}{\partial \boldsymbol{\varepsilon}^p} &= \left[-2(p - \alpha_p) \frac{\partial \alpha_p}{\partial \boldsymbol{\varepsilon}_v^p} - 2a \frac{\partial a}{\partial \boldsymbol{\varepsilon}_v^p} \right] [-1 \ -1 \ -1 \ 0 \ 0 \ 0]^T \\ &= -\frac{2}{\chi} [(p - \alpha_p) \alpha_p + a^2] [-1 \ -1 \ -1 \ 0 \ 0 \ 0]^T \end{aligned} \quad [3.98]$$

Finally, the product $\left(\frac{\partial F}{\partial \boldsymbol{\varepsilon}^p} \right)^T \left(\frac{\partial Q}{\partial \boldsymbol{\sigma}'} \right)$ appearing in the constitutive matrix is given by

$$\begin{aligned} \left(\frac{\partial F}{\partial \boldsymbol{\varepsilon}^p} \right)^T \left(\frac{\partial Q}{\partial \boldsymbol{\sigma}'} \right) &= -\frac{2}{\chi} [(p - \alpha_p) \alpha_p + a^2] \left(-\frac{\partial Q}{\partial \sigma'_{11}} - \frac{\partial Q}{\partial \sigma'_{22}} - \frac{\partial Q}{\partial \sigma'_{33}} \right) \\ &= -\frac{2}{\chi} [(p - \alpha_p) \alpha_p + a^2] \frac{\partial Q}{\partial p} \end{aligned} \quad [3.99]$$

For associated flow,

$$\frac{\partial Q}{\partial p} = \frac{\partial F}{\partial p} = 2(p - \alpha_p) \quad [3.100]$$

using [3.95], so

$$\left(\frac{\partial F}{\partial \boldsymbol{\varepsilon}^p} \right)^T \left(\frac{\partial Q}{\partial \boldsymbol{\sigma}'} \right) = -\frac{4}{\chi} [(p - \alpha_p) \alpha_p + a^2] (p - \alpha_p) \quad [3.101]$$

3.2.4 Corners of Yield and Potential Surfaces

The Mohr-Coulomb potential surface and the elliptic p-q- ϑ surface show corners for $\vartheta_0 = \pm \frac{\pi}{6}$, where the plastic strain direction is no longer uniquely defined. In the Mohr-Coulomb case there is a further complexity when $q = 0$, at the apex of the potential surface. In the case of associative plastic flow, Drucker [Dru59] concluded that the plastic strain direction is confined by the normals to the conjoint potential surfaces. For simplicity, in the models described here, the plastic strain direction is assumed to lie in the planes for which $\vartheta_0 = \pm \frac{\pi}{6}$ and at the apex of the Mohr-Coulomb potential surface, in the negative direction of the p-axis [Nor80].

3.2.5 Advanced constitutive model

The advanced constitutive models implemented in this work are described in Chapters 4, 5, 6 and 7.

3.3 SIMULATION METHOD

3.3.1 Introduction

Numerical validation of the implementation of the advanced models described in Chapters 4, 5, 6 and 7 are performed by using a single finite element with four node and 2×2 gauss points, eight node with 2×2 or 3×3 gauss points and 100 eight node elements. Three different types of tests have been used: isotropic compression, oedometric compression and triaxial compression.

In the following a brief summary on the type of elements used, the simulations performed and the F.E.M. modelling approach are given.

3.3.2 Finite elements used for the numerical validation

As mentioned before, the finite elements used for the numerical validations are the isoparametric quadrilateral elements with four or eight node.

One single element (see 3.1.3.2 and Figure 3.3 for the eight node) is used for almost all simulations as described in section 3.3.4. If not otherwise specified one eight node element has been used.

Figure 3.13 depicts this element, with dimensions chosen of 1×1 m as explained in section 3.3.4.

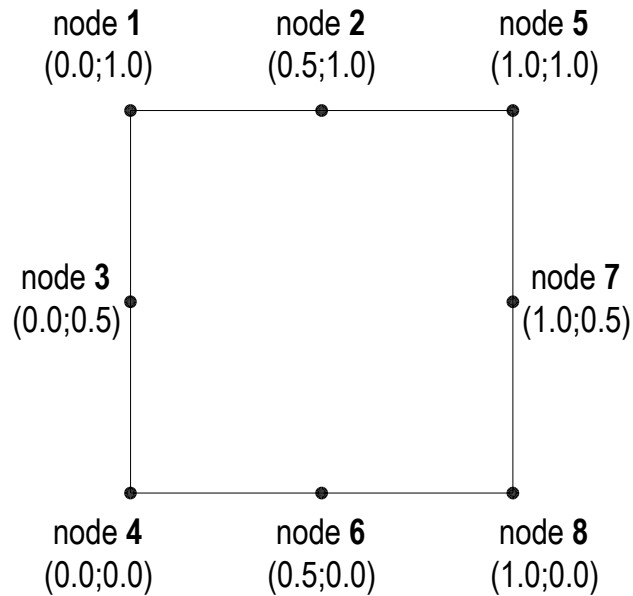


Figure 3.13: 8 node quadrilateral element

As reported in Figure 3.15, the degrees of freedom of this element are 5 for each node.

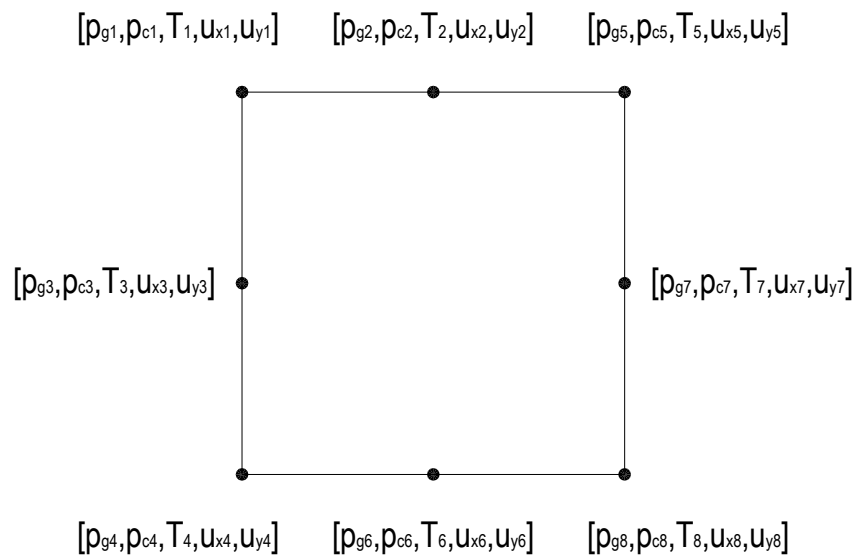


Figure 3.14: Degree of freedom for the 8 node element

3.3.3 Types of tests

The types of test that we have simulated are three: isotropic compression, oedometric compression and triaxial compression. All these three types of test are performed in axisymmetric conditions because the geotechnical samples are usually cylindrical.

We will depict below for each kind of test the boundary and loading conditions (Figure 3.15, Figure 3.17 and Figure 3.19).

Node 5, for each test, has been selected to plot stress and strain variables.

3.3.3.1 Isotropic compression

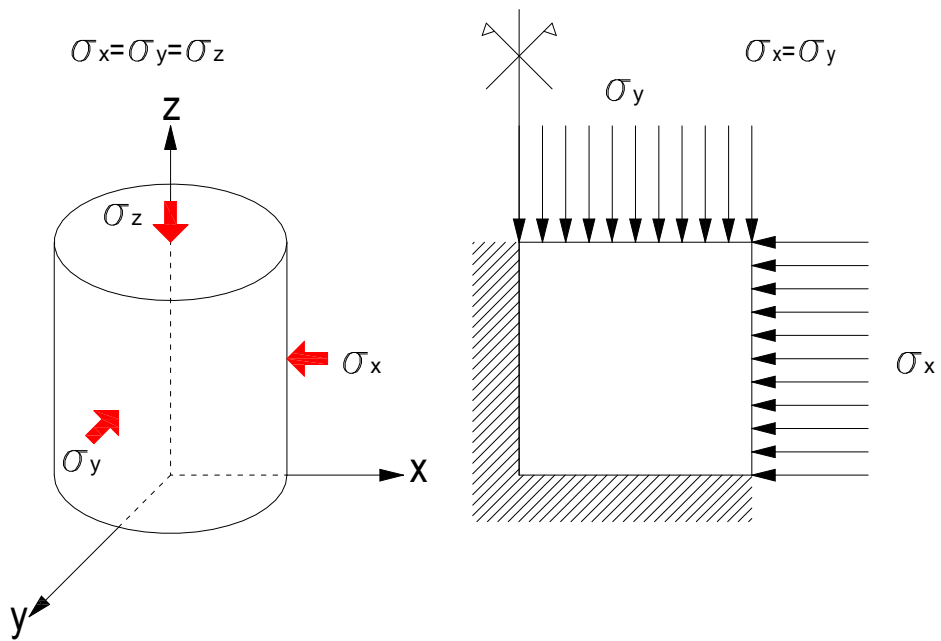


Figure 3.15: Scheme of the isotropic compression test

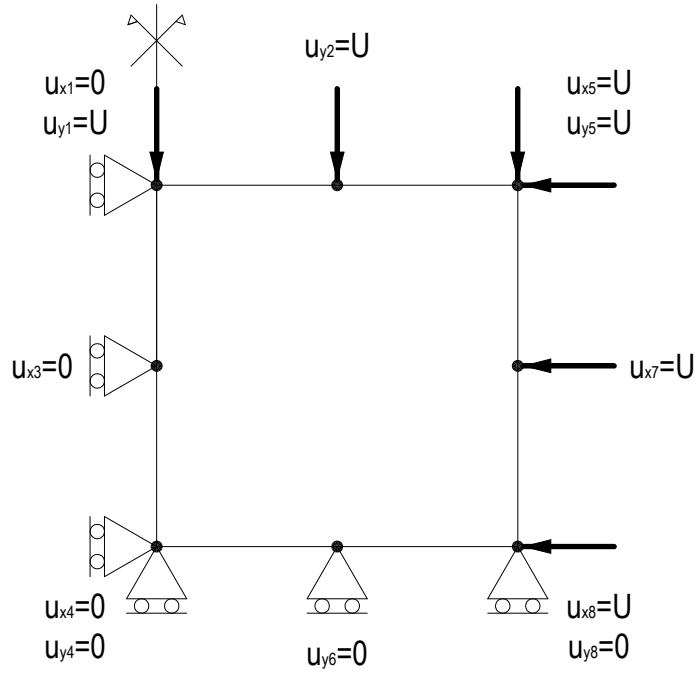


Figure 3.16: Mesh of the isotropic compression test

3.3.3.2 Oedometric compression

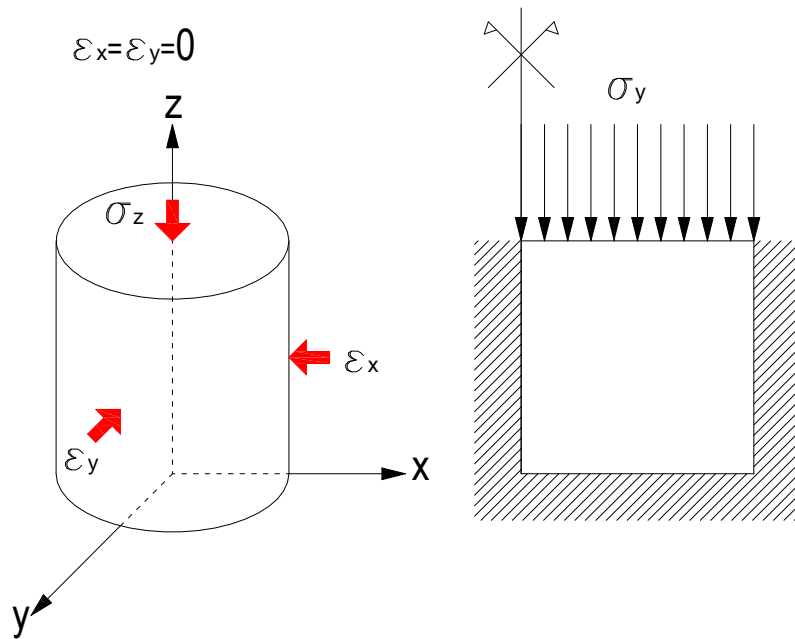


Figure 3.17: Scheme of the oedometric compression test

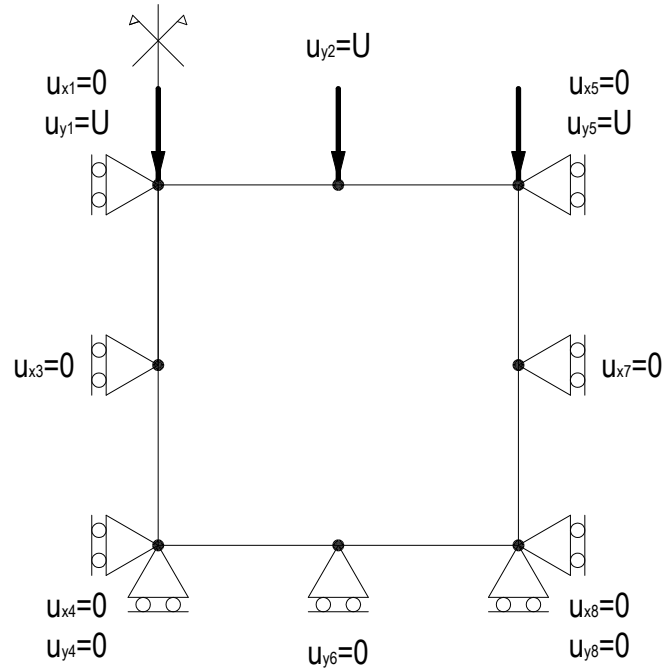


Figure 3.18: Mesh of the oedometric compression test

3.3.3.3 Triaxial compression

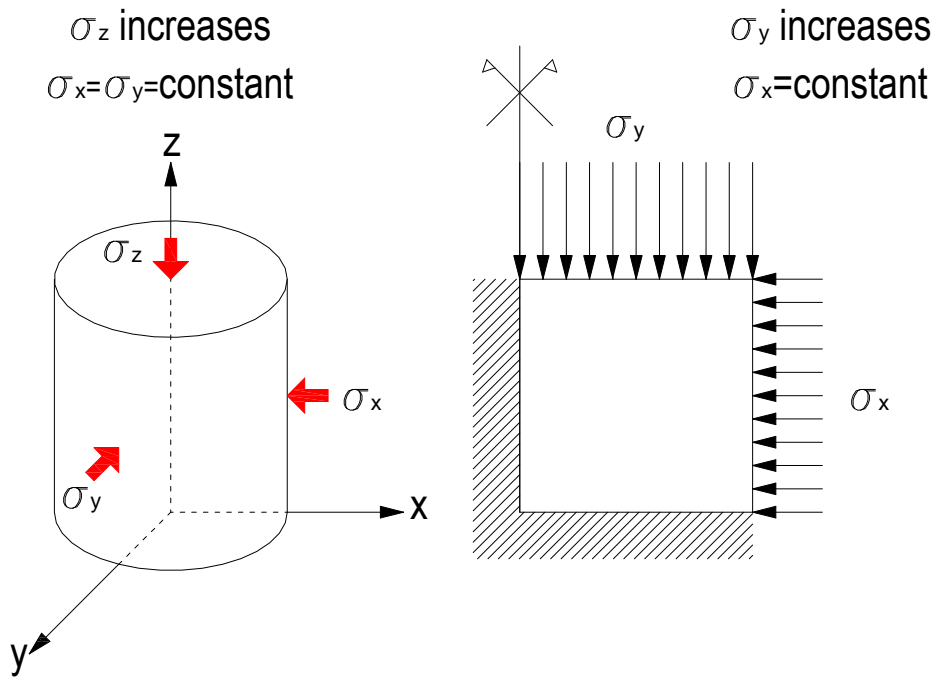


Figure 3.19: Scheme of the triaxial compression test

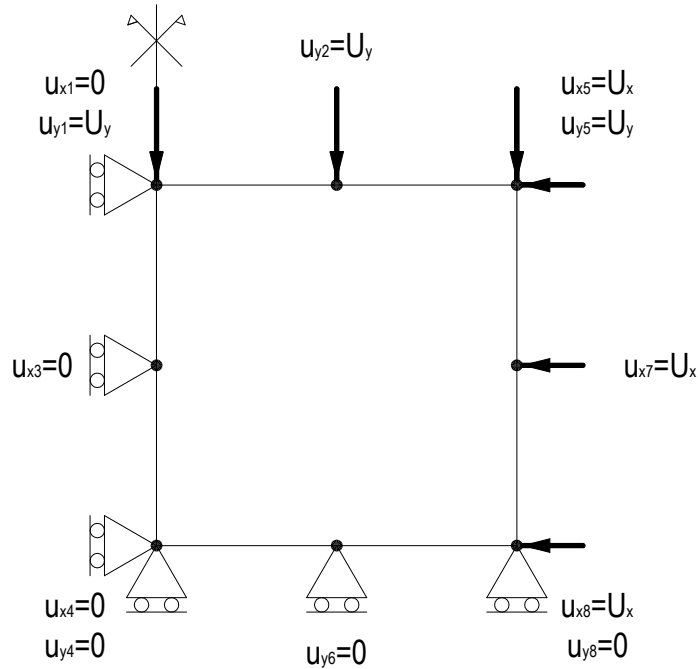


Figure 3.20: Mesh of the triaxial compression test

N d.o.f.	d.o.f.	N. condition	Value	u.o.m.
1	p^g	1	Impose p^g	Pa
		2	Impose air flux	$\frac{kg}{m^2s}$
2	p^c	1	Impose p^c	Pa
		2	Impose vapour flux	$\frac{kg}{m^2s}$
		3	Impose value of RH	%
		4	Impose vapour pressure	Pa
3	T	1	Impose T	K
		2	Impose heat flux	$\frac{W}{m^2K}$
		3	Impose room T (convective)	K
		4	Impose room T (radiation)	K
4	u_x	1	Impose u_x	m
		2	Impose σ_x	Pa
5	u_y	1	Impose u_y	m
		2	Impose σ_y	Pa

Table 3.2: Model conditions

3.3.4 Remarks on the F.E.M. modelling approach

As mentioned before, one single eight node square element of 1 m has been usually adopted to simulate the isotropic, oedometric and triaxial tests of the validation phase of this work.

The dimension of this element was chosen for simplicity so that the axial strain equals the axial displacement (in small strain).

Moreover, during the computations, gravity acceleration was neglected. This was motivated from the experimental behaviour of the samples during the common geotechnical laboratory tests, in which the effect of the gravity load on the stress field can be neglected due to the small dimension of the samples (i.e. 72×19 mm, Figure 3.21) and the applied confining pressure. In addition, also the model drivers neglect the gravity load.

The quadratic element was preferred to the linear one because it is the typical finite element used to discretize the 2D displacement field of saturated and unsaturated porous media.

Accuracy of the numerical solution was analyzed by solving the same isotropic compression test (see 4.4.3 Elastoplastic isotropic compression in isothermal condition) with 1 quadratic element of the dimension of a geotechnical sample (Figure 3.21 integrated with 3×3 gauss points), 30 quadratic element (Figure 3.22), 1 quadratic element of unit

dimension (Figure 3.23 and Figure 3.24 integrated with 2x2 or 3x3 gauss points respectively), 100 quadratic element (Figure 3.25) and also discretizing the unit domain with 1 quadratic four node element (Figure 3.26 integrated with 2x2 gauss points).

Figure 3.27 and Figure 3.28 show the numerical results, where it can be observed that the solution obtained with 1 unit element is accurate from the numerical point of view. Instead the Figure 3.29 shows that the numerical solution obtained with the use of 1 four node element is also accurate.

As a further remark it is observed that in case of strain localization test, a suitable spatial discretization has to be used in [San06].

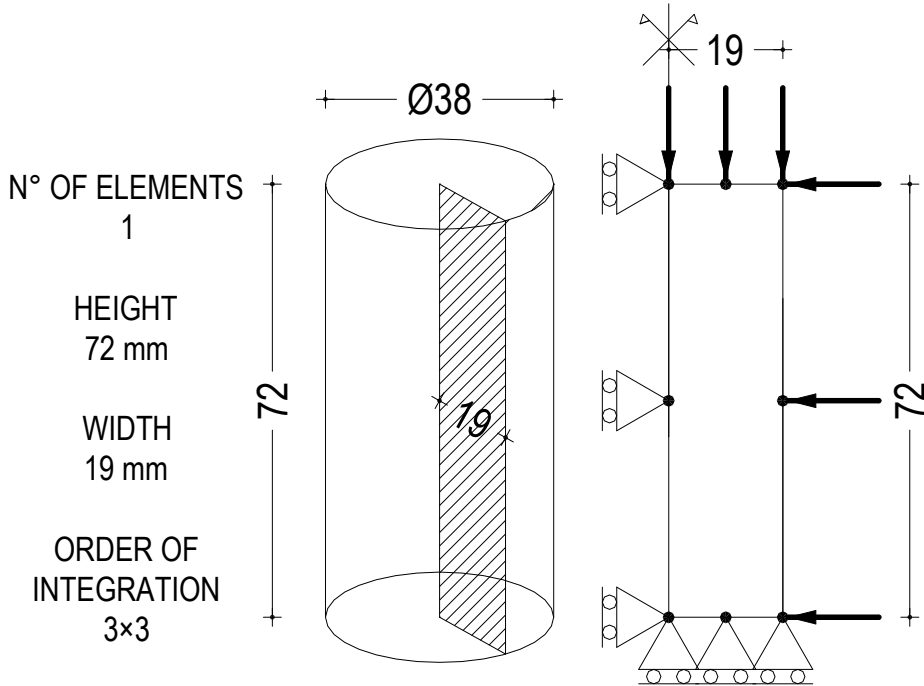


Figure 3.21: Eight node quadrilateral element used

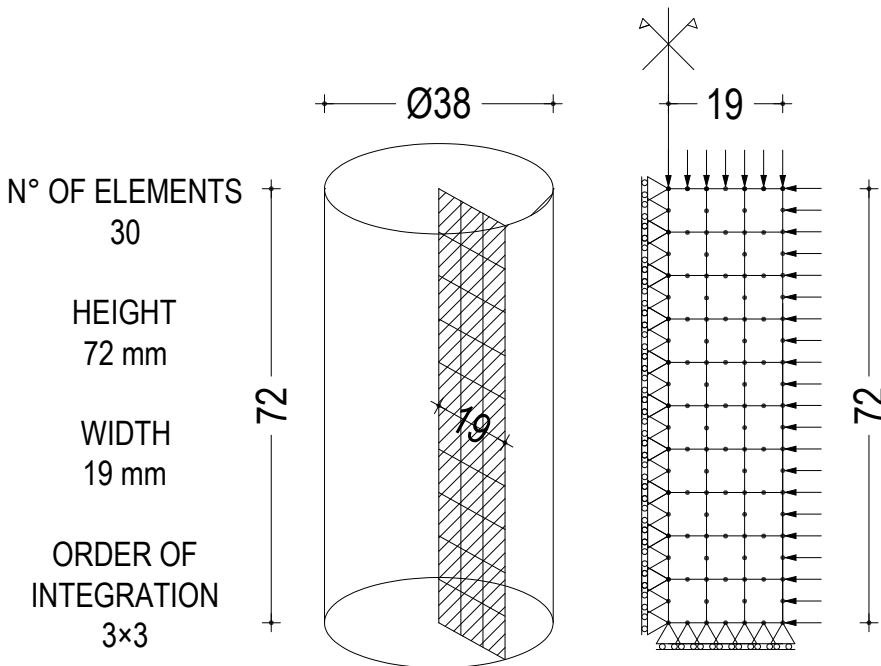


Figure 3.22: Eight node quadrilateral elements used

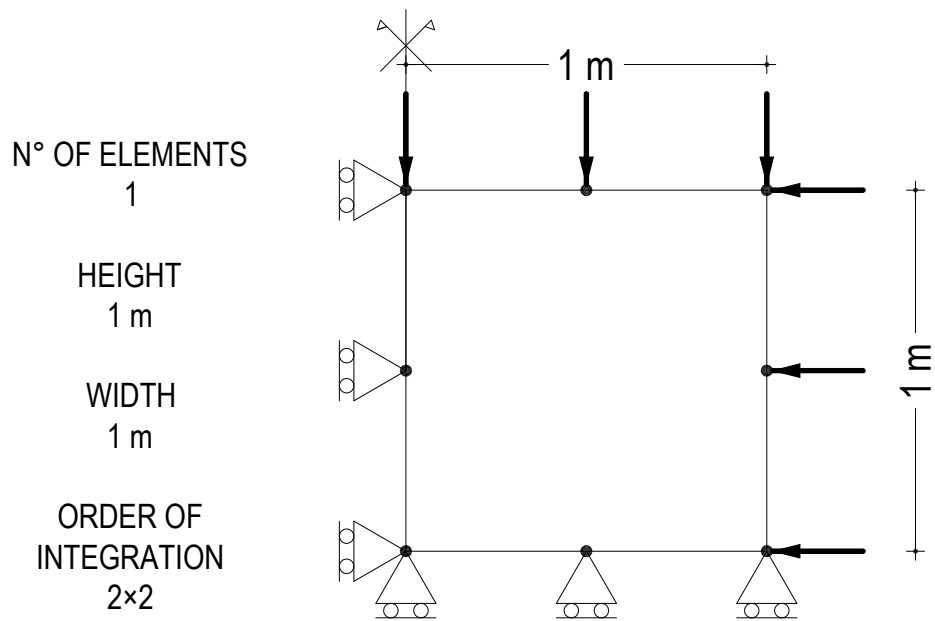


Figure 3.23: Eight node quadrilateral element used

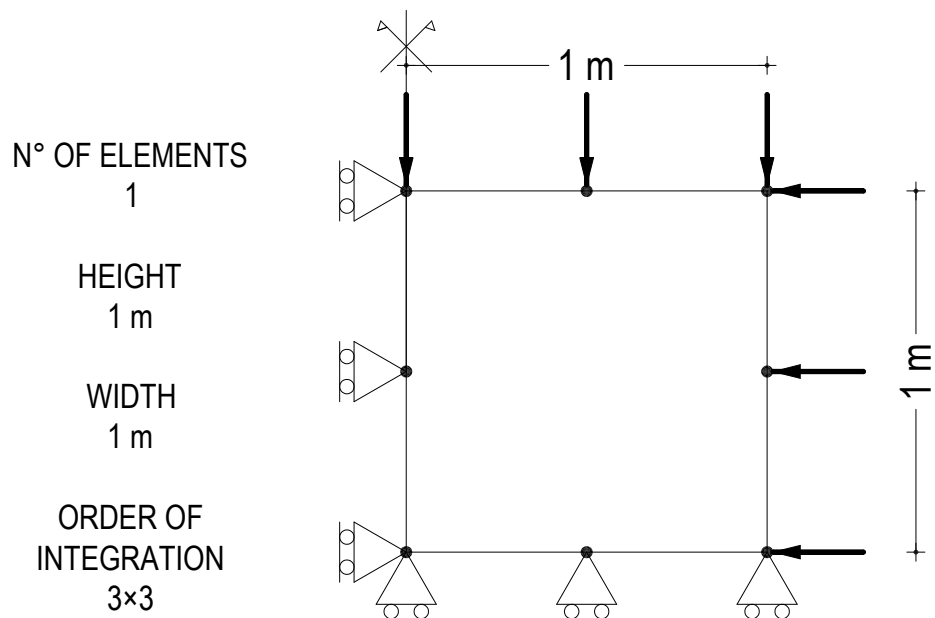


Figure 3.24: Eight node quadrilateral element used

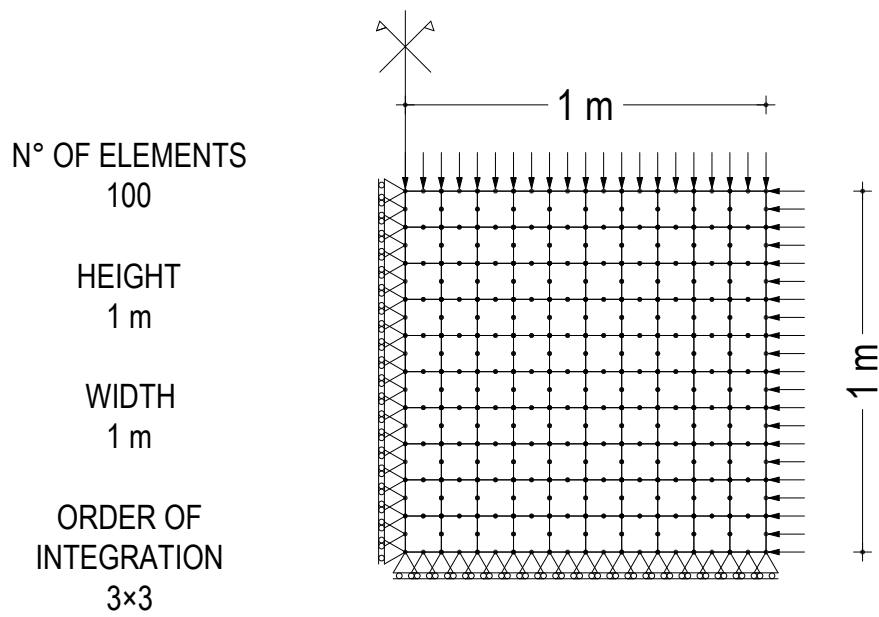


Figure 3.25: Eight node quadrilateral elements used

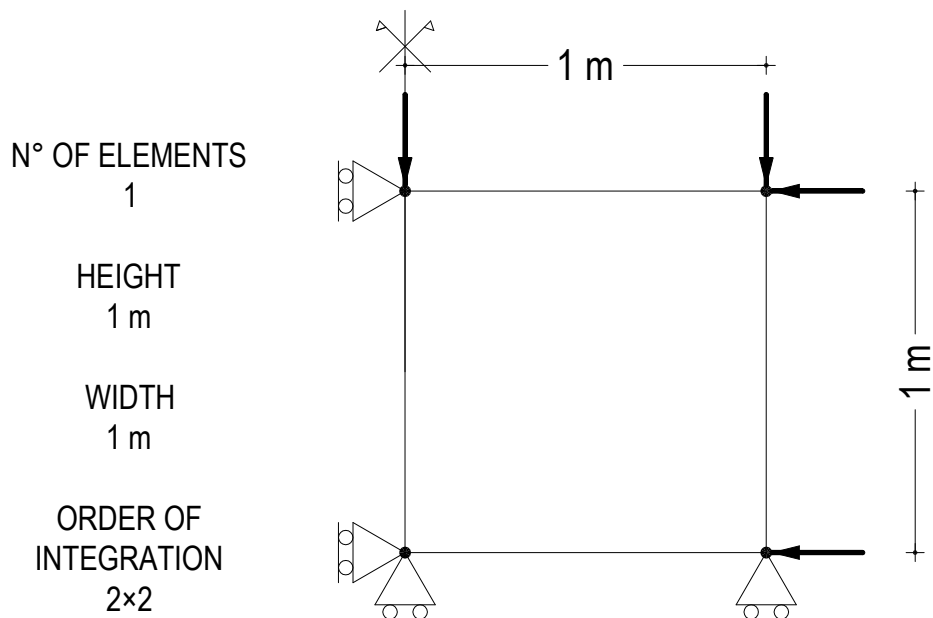


Figure 3.26: Four node quadrilateral element used

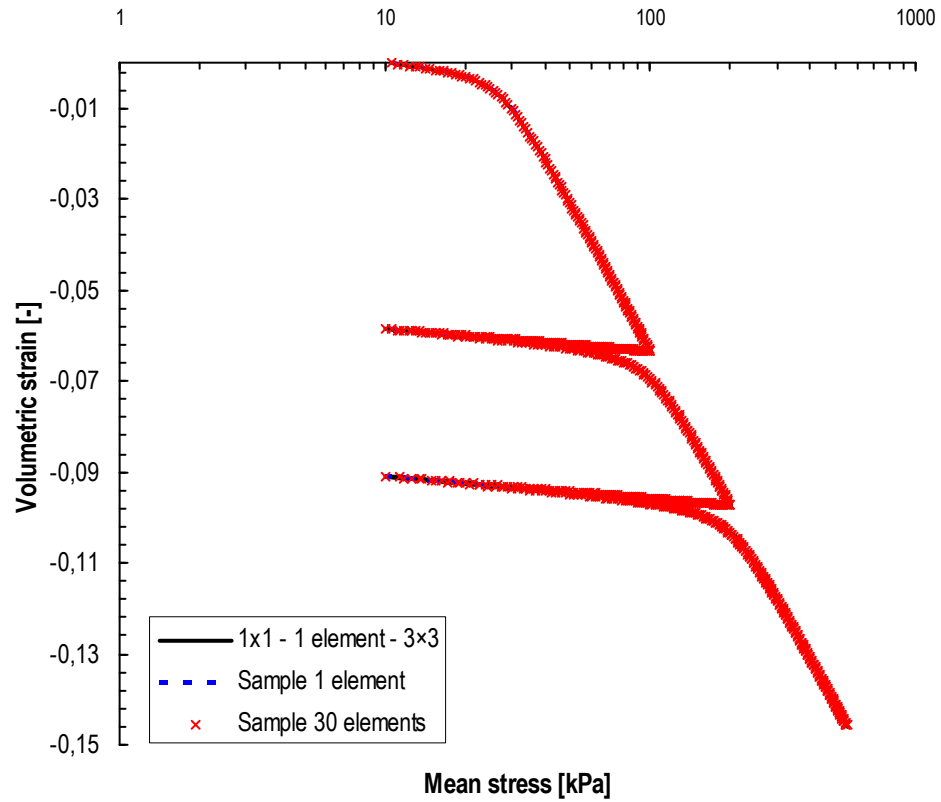


Figure 3.27: Comparison with different meshes and sample dimensions

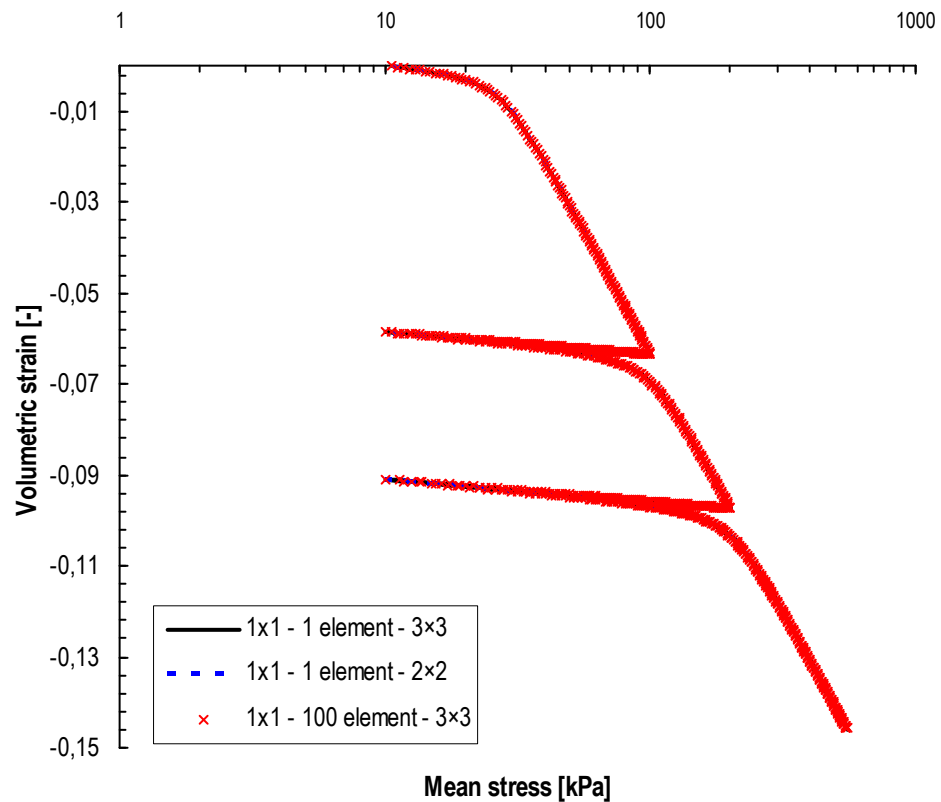


Figure 3.28: Comparison with the same sample dimensions and different discretizations

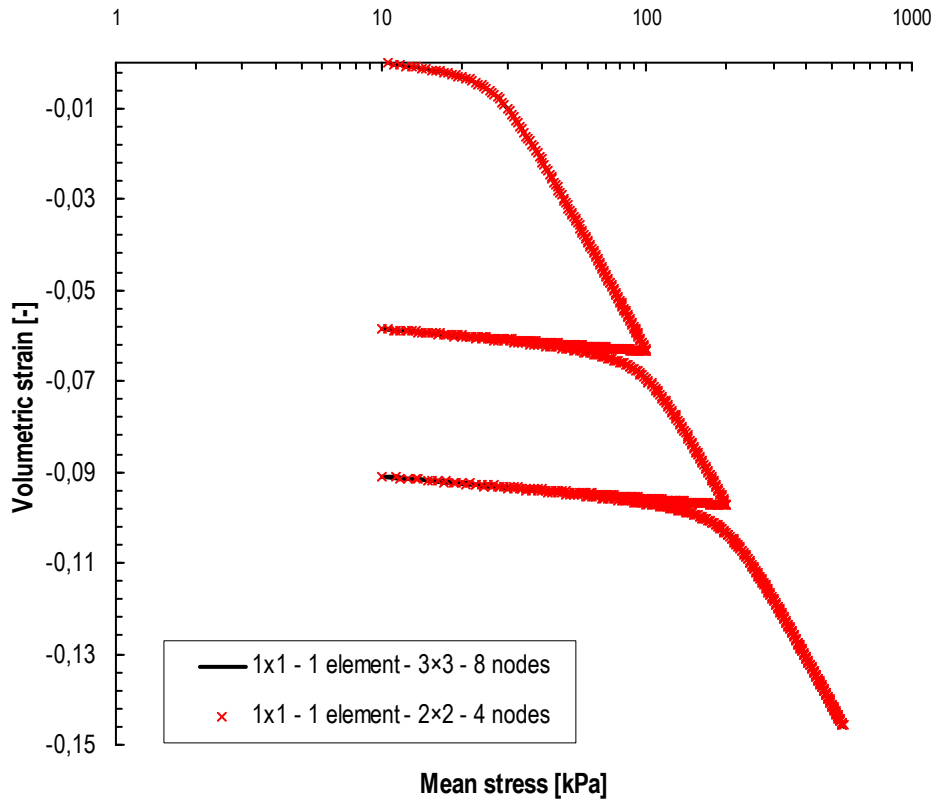


Figure 3.29: Comparison with the same sample dimensions and different elements

References

- [Bia03] Bianco, M., Bilardi, G., Pesavento, F., Pucci, G., Schrefler, B.A.: A frontal solver tuned for fully coupled non-linear hygro-thermo-mechanical problems. *Int. J. Numer. Meth. Engng.* 57, 1801-1818 (2003).
- [Cou1776] Coulomb, C. A. (1776) Essai sur une application des règles des maximis et minimis a quelques problèmes de statique relatifs a l'architecture. *Mem. Acad. Ro. Pres. Divers Sav.* 5, 7.
- [Dru59] Drucker, D. C. (1959) A definition of stable inelastic material. *Trans. ASME.* 26, 00-00.
- [G&S96] D.Gawin, B.A.Schrefler, 'Thermo-hydro-mechanical analysis of partially saturated porous materials', *Engng.Comp.*, 13(7), 113-143 (1996).
- [Gaw96] D.Gawin, P.Baggio, B.A.Schrefler, 'Modelling heat and moisture transfer in deformable porous building materials', *Arch. of Civil Engng.* 42(3), 325-349, (1996).
- [Hum76] Humpheson. C. (1976) Finite element analysis of elasto-visco-plastic soils. PhD thesis. University College of Swansea.
- [L&S98] Lewis R.W. and Schrefler B.A. *The Finite Element Method in the Static and Dynamic Deformation and Consolidation of Porous Media.* J. Wiley, Chichester 1998.
- [M&Z84] Mroz. Z. and Zienkiewicz. O. C. (1984) Uniform formulation of constitutive equations for clays and sands. *Mechanics of Engineering Materials.* C. S. Desai and R. H. Gallagher (eds). Wiley, Chichester. Ch. 22, pp. 415-449.
- [N&Z72] Nayak. G. C. and Zienkiewicz. O. C. (1972) Convenient form of stress invariants for plasticity. *Proc. ASCE.* 98 (ST4). 949-53.
- [Nay75] Naylor, D. J. (1975) Non-linear finite element models for soils. PhD thesis. University College of Swansea.
- [Nor80] Norris, V. A. (1980) The elasto-plastic analysis of soil consolidation with special reference to kinematic hardening. PhD thesis, University College of Swansea.
- [R&B68] Roscoe. K. H. and Burland, J. B. (1968) On the generalised stress-strain behaviour of 'wet' clay, in *Engineering Plasticity.* Heyman, J., Lechie, F. A. Cambridge University Press. Cambridge. pp. 535-609.
- [R&P63] Roscoe. K. H. and Poorooshasb, H. B. (1963) A theoretical and experimental study of strains in triaxial compression tests on normally consolidated clays. *Géotechnique.* 13(1). 12-34.
- [R&S63] Roscoe. K. H. Schofield. A. N. and Thurairajah, A. (1963) Yielding of clays in states weter than critical. *Géotechnique.* 13(3), 211-10.
- [S&G96] B.A.Schrefler, D.Gawin, The effective stress principle: incremental or finite form? *Int. J. for Num. and Anal. Meth. in Geomechanics,* 20(11), 785-815, (1996).
- [S&W68] Schofield. A. N. and Wroth. C. P. (1968) *Critical State Soil Mechanics.* McGraw-Hill, New York.
- [San05] L. Sanavia, F. Pesavento, B.A. Schrefler, Finite element analysis of non-isothermal multiphase geomaterials with application to strain localization simulation, *Computational Mechanics* Vol. 466, (2005) (DOI 10.1007/s00466 -005-0673-6).
- [San06] Sanavia L., F. Pesavento, B.A. Schrefler (2006) Finite element analysis of non-isothermal multiphase geomaterials with application to strain localisation simulation, *Computational Mechanics,* 37 (4), 331-348.

- [Z&M84] Zienkiewicz. O. C. and Mroz. Z. (1984) Generalized plasticity formulation and applications to geomechanics. *Mechanics of Engineering Materials*. C. S. Desai and R. H. Gallagher (eds). Wiley, Chichester. Ch. 33, pp. 655-679.
- [Z&T89] Zienkiewicz O. C., Taylor R. L., *The Finite Element Method*, Vol. 1, 4th ed., Mc Graw Hill, London (1989).
- [Z&T91] Zienkiewicz O. C., Taylor R. L., *The Finite Element Method*, Vol. 2, 4th ed., Mc Graw Hill, London (1991).
- [Zie75] Zienkiewicz, O. C. Humpheson, C. and Lewis, R. W. (1975) Associated and non-associated viscoplasticity and plasticity in soil mechanics. *Géotechnique*, 25(4), 67 1 -89.
- [Zie77] Zienkiewicz. O. C. (1977) *The Finite Element Method*. McGraw-Hill. London.

4 THE THERMO-ELASTO-PLASTIC CONSTITUTIVE MODEL

ACMEG-T

4.1 TEMPERATURE EFFECTS IN SOILS

4.1.1 Thermal problem in soils

Thermal effects in geomechanical problems are important for several specific applications as, for instance, nuclear waste isolation and the use of soil deposits for heat energy storage. Some other applications are related to geothermal structures, petroleum drilling, injection and production activity, zones around buried high-voltage cables and in soil tests for to take into account the thermal problem during the time from the situ to the laboratory. In more of the applications mentioned above, the temperature values considered are between 5 and 95 °C, but, in case of failure situation for nuclear waste storage, the temperature can reach 400 °C. Research work has shown that an increase in temperature affects soil characteristics (friction angle, permeability, elastic modulus, etc.) and behaviour is different for the influence of soil type or stress state or drainage condition or more.

The effect of the temperature, and in greater way the effect of the high temperature, on soils behaviour is not completely clear, although the relevance of the thermo-mechanical applications and the many test in the literature. This is due to the complex influence of temperature on the behaviour of soils, and the fact that thermo-mechanical testing of soils is much more complex than conventional isothermal testing. In fact, for the presence of temperature is necessary an additional reliable system with specific property. System must maintains constant temperature on sample, must have an heating equipment that work independently from the other part and more.

In this chapter, for the ACMEG-T model, the soils that we want to model are clay. The model has been developed by the research group of the Professor Lyesse Laloui in Lausanne at the EPFL, Ecole Polytechnique Federale de Lausanne, [M&L97] and [L&C08], and it represents an extension in non-isothermal conditions of the modified CAM-CLAY model.

4.1.2 Thermo-mechanical behaviour of soils

Clay is a material with a not common behaviour under non isothermal conditions. In fact, in normally consolidated conditions (NC), clay contracts under heating, and this is atypical of the normal material, while in over consolidated conditions, clay dilate under heating (see Figure 4.2). Another important aspect of clay under heating is that a not negligible part of this contractive deformation is irreversible. Moreover, from the experimental tests, it is possible to note that the variation of volume is non-linear during heating and linear upon cooling.

The irreversibility of strain due to thermal loading is an evident thermal hardening.

It is clearly impossible to simulate this behaviour with a thermo-elastic model cause the irreversibility of strain, it is necessary a more complex model, a thermo-elastoplastic model.

Plasticity induced by temperature, is due to and explained by a combination of certain mechanisms at micro level. The first one is the partial collapse of the soil structure and a decrease in void ratio until a number of additional bonds are formed, these bonds are able to allow the soil to carry the stress at the higher temperature [C&M68]. The second micro-mechanical processes is the thermal degradation of the adsorbed layer, which tends to group particles closer together and may produce large voids between the platelet aggregates [Pus87]. Another mechanism is the difference in rigidity and in thermal expansion between the dissimilar minerals forming the solid skeleton that generates a modification of the contact force networks as temperature increases [Kin76]. The last mechanism of soil under temperature increase, if the particle arrangement are assumed to be fixed, is the increase of pore size and the inter-particle distance due to the thermal expansion of each soil constituent that would produce a global dilation of the solid skeleton. This change the equilibrium between the Van der Waals attractive forces and the electrostatic repulsive forces, which results in the particles rearranging to reach a new equilibrium [Lal01].

A good indicator of the importance of the water-mineral interactions in clays is the soil plasticity index, Demarks and Charles [D&C82] show this aspect for six different clays at normally consolidated state. The volumetric thermo-plastic strain of normally consolidated soil, reported by unit temperature change, seems to increase when the plasticity index increases (Figure 4.1).

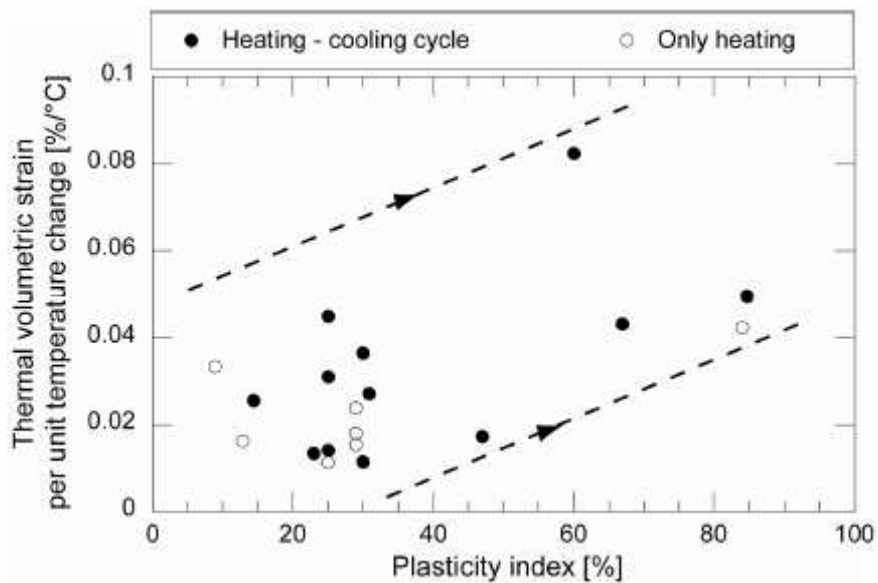


Figure 4.1: Relation between the plasticity index and the temperature-induced contractile strain (redrawn from [Fra08]).

Authors	Clay type	T_0 [°C]	T_1 [°C]	ΔT [°C]	Thermal Cycle	I_p [%]	ϵ_v [%]	$\epsilon_v/^\circ C$ [%/°C]
Campanella and Mitchell (1968), Campanella (1965)	Remoulded illite	5	60	55	Yes	47	0.95	0.017
Paaswell (1967)	Penn soil	30	60	30	No	8.9	1	0.033
Plum and Ersig (1969)	Illite	24	50	26	No	84	1.1	0.042
Hueckel and Baldi (1990)	Boom clay	22	80	58	Yes	25	1.8	0.031
	Pontida clay	22	60	38	No	12.9	0.62	0.016
Robinet et al. (1997)	Bassin Parisien clay	20	80	60	Yes	30	0.69	0.011
	Boom clay	20	80	60	Yes	25	0.85	0.014
Abuel-Naga et al. (2007)	Bangkok clay	22	90	68	Yes	60	5.6	0.082
Del Olmo et al. (1996), Hueckel et al. (1998)	Spanish clay	20	100	80	Yes	23	1.08	0.013
Laloui and Cekerevac (2003)	Kaolin clay	20	95	75	No	23	0.85	0.011
Demarks and Charles (1982)	Atlantic Marine clay	25	50	25	Yes	25	1.24	0.049
	Atlantic Marine clay	25	50	25	Yes	84.7	1.08	0.043
	Atlantic Marine clay	25	50	25	Yes	66.9	0.68	0.027
	Atlantic Marine clay	25	50	25	Yes	30.8	0.64	0.025
Burghignoli et al. (2000)	Todi clay	22	48	26	Yes	14.4	0.95	0.036
Sultan et al. (2002)	Boom clay	22	100	78	Yes	30	3.5	0.044
Towhata et al. (1993)	MC clay	20	90	70	No	25	1.66	0.023
	MC clay	20	90	70	No	29	1.08	0.015
	MC clay	20	90	70	No	29	1.26	0.018

Table 4.1: Contractile volumetric strain induced by a temperature change at constant mean effective stress in different NC clay. Correlation with the plasticity index of the soil. Thermal cycle: Yes: Heating-cooling cycle; No: only heating. (Redrawn from [Fra08]).

Different by the behaviour of NC clays under temperature increase are OC clays. Indeed, the latter show an almost completely reversible deformation after a thermal cycle of heating and cooling. The micro-mechanical processes that could explain the thermoplasticity of NC soils remain active for highly OC soils but, the low stress level does not supply enough acting force between particles to modify the soil structure. In that sense, the particle arrangement remains fixed, and only thermo-elastic strain is produced.

In conclusion the typical behaviour of NC clays under a thermal cycle of heating and cooling is the production of irreversible deformations of contraction and the behaviour of OC clays is, at the opposite, the reversibility of the deformations of dilatation (Figure 4.2).

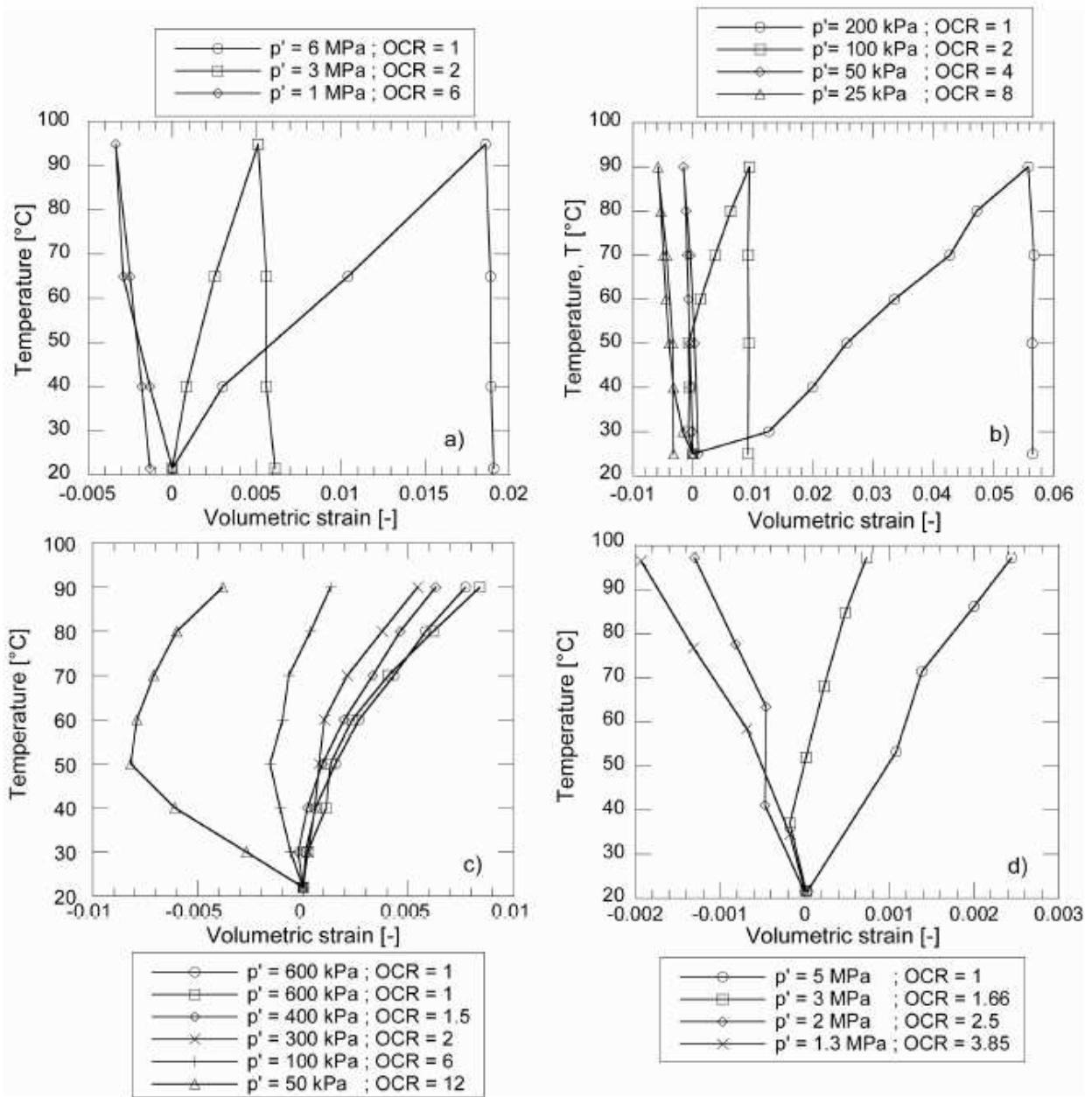


Figure 4.2: Typical volumetric strain induced by heating-cooling cycles at different overconsolidation ratios. (a) Boom clay [Ba91]; (b) Bangkok clay [A-N07]; (c) Kaolin clay [C&L04]; (d) Pasquasia clay [De096]. (Redrawn from [Fra08]).

4.1.3 Temperature effect on preconsolidation pressure

In this work, is indicate with p'_c the preconsolidation pressure, that is the stress yield limit that separates the elastic part from the plastic one in terms of behaviour under isotropic or oedometric conditions. Several results from the literature show a decrease in the preconsolidation pressure with increasing temperature. Laloui and Cekerevac [L&C03] proposed the following equation to describe this thermo-mechanical behaviour:

$$p'_c = p'_{c0} \left[1 - \gamma_T \log\left(\frac{T}{T_0}\right) \right] \quad [4.1]$$

where p'_c is the preconsolidation pressure at a given temperature T

p'_{c0} is the preconsolidation pressure at the reference temperature T_0

γ_T is a material parameters

Others author proposed the following different relations:

$$p'_c = p'_{c0} e^{[-\alpha(T-T_0)]} \quad \text{Cui et al., 2000} \quad [4.2]$$

$$p'_c = p'_{c0} + 2[a_1(T - T_0) + a_2(T - T_0)|T - T_0|] \quad \text{Hueckel and Baldi, 1990} \quad [4.3]$$

$$p'_c = p'_{c0} [1 + C(T - T_0)] \quad \text{Boudali et al., 1994} \quad [4.4]$$

$$p'_c = p'_{c0} \left(\frac{T}{T_0}\right)^n \quad \text{Moritz, 1995} \quad [4.5]$$

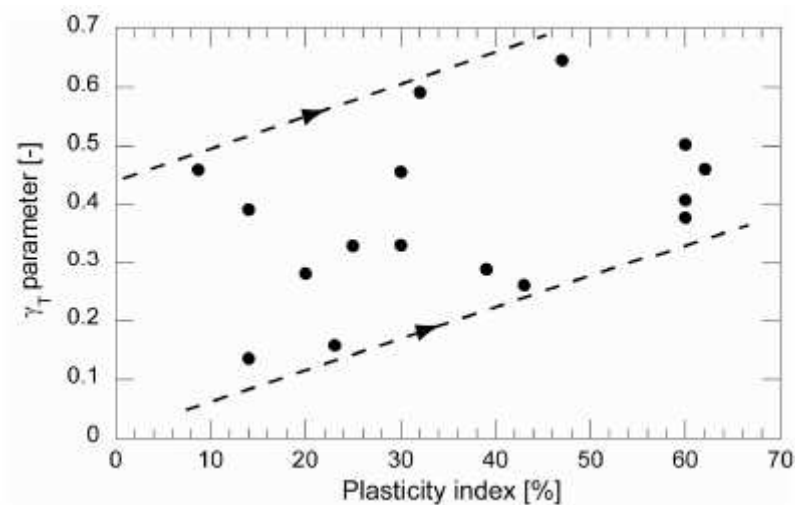


Figure 4.3: Relation between I_p and γ_T (redrawn from [Fra08]).

Authors	Clay type	I_p [%]	T_0 [°C]	T_1 [°C]	T_1/T_0 [-]	p'_{c0} [kPa]	p'_{c1} [kPa]	p'_{c1}/p'_{c0} [-]	γ_T [-]
Tidfors and Sällfors (1989)	Backebol clay	60	7	30	4.28	62	46	0.74	0.41
Campanella and Mitchell (1968)	Remoulded illite	47	25	51	2.04	200	160	0.8	0.65
Boudali et al. (1994)	Bertheville clay	25	5	35	7	68	49	0.72	0.33
	Louiseville clay	39	5	35	7	198	150	0.76	0.29
	Saint-Jean	14	5	35	7	1040	921	0.89	0.14
	Vianney clay								
Burghignoli et al. (2000)	Todi clay	30	18	48	2.66	184	158	0.89	0.33
Marques et al. (2004)	Saint-Roch de l'Achigan clay	43	10	50	5	165	135	0.82	0.26
Eriksson (1989)	Lulea clay	60	5	55	11	61	37	0.61	0.38
Abuel Naga et al. (2006)	Bangkok clay	60	25	90	3.6	200	144	0.72	0.50
Hueckel and Baldi (1990)	Pontida clay	14	22	90	4.09	2500	1900	0.76	0.4
Cekerevac (2003)	Kaolin clay	23	22	95	4.32	600	540	0.9	0.16
Sultan et al. (2002)	Boom clay	30	22	100	4.54	6000	4200	0.7	0.46
Robinet et al (1997)	Kaolinite	20	20	60	3	1500	1300	0.86	0.28
	Smectite	62	20	60	3	1500	1170	0.78	0.46
Despax (1976)	Argile noire	32	20	95	4.75	-	-	-	0.6
Salager et al. (2008)	Sion silt	8.7	22	80	3.64	-	-	-	0.46

Table 4.2: I_p , γ_T and reduction of p'_{c0} from T_0 and T_1 (redrawn from [Fra08]).

4.1.4 Temperature effects on shearing behaviour

In terms of elastic behaviour of soil, experimental results show what the temperature has a stiffening effect. Cekerevac and Laloui [C&L04] observed an higher soil stiffness in Kaolin clay (Figure 4.4 a) as for Kuntiwattanukul et al. [Kun95] in MC clay where, the increase of the secant modulus is confirmed both for NC clay and OC clay (Figure 4.4 b). Approximately the same results were found from Abuel-Naga [A-N05] in Bangkok clay.

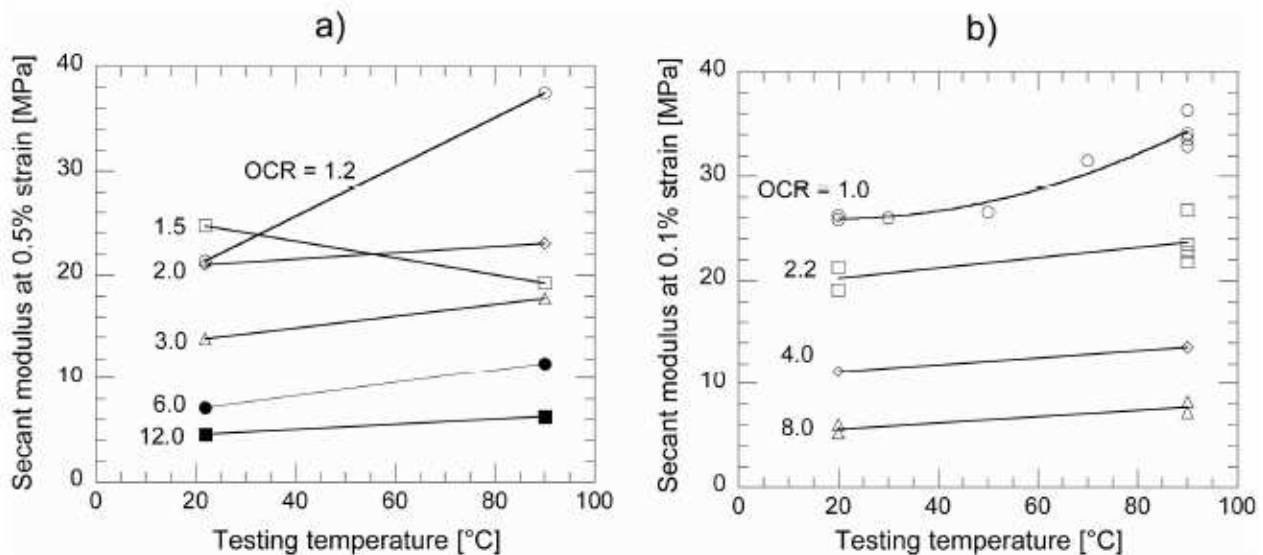


Figure 4.4: Secant elastic modulus at different temperature for a) Kaolin clay [C&L04] and b) MC clay [Kun95]. (Redrawn from [Fra08])

Burghignoli et al. [Bur00] instead found that in Tody clay there is not a significant effect of temperature on stiffness of material if the temperature is the highest temperature experienced by the soil. However, they noted that a thermal cycle performed before triaxial shearing tends to increase the stiffness of the soil.

Not unique is the behaviour of soil under the increase of temperature in terms of shear strength, some research in fact had found a decrease in strength with heating and others, contrariwise, had found slightly increase of strength.

A series of experimental results summarised by Cekerevac and Laloui [C&L04] tend to confirm that the friction angle at the critical state can either slightly increase or decrease with temperature. However, comparison is not always possible due to the variability in experimental techniques, stress and strain paths and drainage conditions during heating and shearing. For instance, Hueckel and Pellegrini [H&P89] observed that the slope of the friction angle at the critical state of Pontida clay is unaffected by temperature under both drained and undrained shearing. In contrast, the same authors noticed a slight increase in friction angle of Boom clay under undrained shearing.

In term of maximal deviatoric stress, Cekerevac [Cek03] in tests performed in a Kaolin clay and Kuntiwattanukul et al. [Kun95] in tests performed MC clay observed a slight increase in the peak strength during heating (Figure 4.5).

Because of the different results found in literature it is not possible to draw any general conclusion. In fact, for instance, Abuel-Naga et al. [A-N06] also noticed an increase of the maximal deviatoric stress upon triaxial shearing of normally consolidated Bangkok clay, while Hueckel et al. [Hue98] suggested that the peak strength of a Spanish clay decreases by about 25% for a temperature increase from 22° to 120 °C.

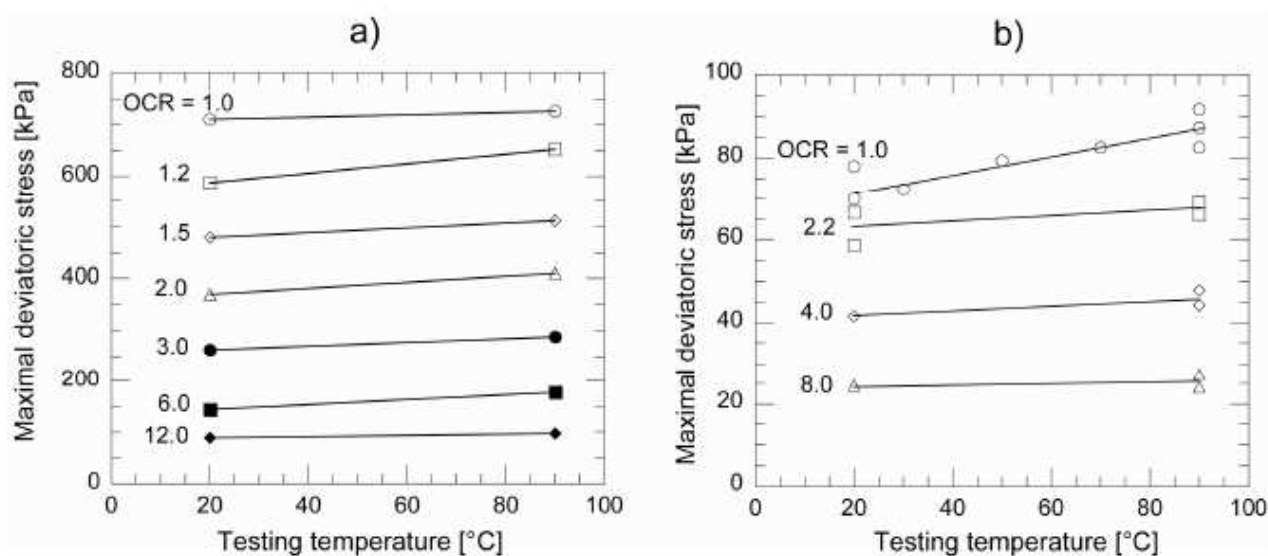


Figure 4.5: Maximal deviatoric stress at different temperature for a) Kaolin clay [Cek03] and b) MC clay [Kun95]. (Redrawn from [Fra08])

4.2 ACMEG-T MODEL

4.2.1 Introduction

The ACMEG-T model [Lal05] [L&F08] is the extension to non-isothermal conditions of the model ACMEG [M&L97] and [L&C08]. The model can reproduce the different behaviour of NC and OC clay, the decrease of preconsolidation pressure, and if present, the variation of frictional angle value with temperature.

Here, the considered temperature range is from 5 °C to 95 °C.

4.2.2 ACMEG Model

The ACMEG model ([M&L97] and [L&C08]) (Advanced Constitutive Model for Environmental Geomechanics), here presented as in [Fra08], is composed of two parts, one that take into account the volumetric response upon isotropic compression, and one that take into account the stress-strain behaviour upon soil distortions (deviatoric loading).

The model considers under isotropic conditions:

1. the effect of stress level on the elastic rigidity of soil;
2. the plastic volumetric strain generated when the preconsolidation pressure is surpassed;
3. the progressive transition between the reversible elastic and the irreversible elasto-plastic response;
4. the existence of an elastic nucleus in the stress space in which the produced strains are fully reversible;
5. the volumetric response of soil upon several isotropic loading-unloading-reloading cycles (without accommodations effects).

The model considers under deviatoric conditions:

1. the effect of stress level on the elastic rigidity of soil;
2. the unique critical state reached upon various distortional paths;
3. the hardening process occurring from the elastic domain to the critical state of normally or slightly overconsolidated soils;
4. the peak behaviour observed on distortion paths of highly overconsolidated soils;
5. the progressive transition between the reversible responses and the full mobilization of the hardening or softening processes;
6. the existence of an elastic nucleus in the stress space in which the produced strains are fully reversible;
7. the accurate volumetric response upon distortional paths which can involve a non-associated flow rule.

4.2.2.1 Non linear elasticity

The elastic moduli present a strong dependency from the mean effective stress and the equations governing this phenomenon are:

$$K=K_{ref} \left(\frac{p'}{p'_{ref}} \right)^{n_e} \quad [4.6]$$

for the bulk modulus, and:

$$G=G_{ref} \left(\frac{p'}{p'_{ref}} \right)^{n_e} \quad [4.7]$$

for the shear modulus

where K_{ref} is the bulk modulus at the reference mean effective stress p'_{ref}

G_{ref} is the shear modulus at the reference mean effective stress p'_{ref}

n_e is a material parameter

It is possible prove that this non-linear elasticity relation is non-conservative in terms of the work input. Indeed, upon any purely elastic loading-unloading path for which the final stress state corresponds to the initial one, the total work input

must be null. The use of the proposed elastic module does not guarantee such a conservation condition. In other words the elastic behaviour of model is ipoelastic.

4.2.2.2 The multi-mechanism theory

Starting from the Original Cam-Clay model and its deviatoric yielding mechanism, adding an isotropic mechanism in agreement with Hujoux [Huj79], it is possible to build a two-mechanism model.

The isotropic mechanism have the following form:

$$f_{iso} = p' - p'_c = 0 \quad [4.8]$$

where p'_c is the preconsolidation pressure and evolves according to the equation

$$p'_c = p'_{c0} e^{(\beta \varepsilon_v^p)} \quad [4.9]$$

where β is the plastic compressibility modulus

The two yield functions define a closed domain in the effective stress space inside which the behaviour of the material is reversible. If the volumetric plastic strain increases due to the activation of one of the mechanisms, the yield limit of the other mechanism will also move. When the two mechanisms are activated simultaneously, two consistency conditions must be met leading to two interrelated plastic multipliers ($\lambda^{p_{iso}}$ and $\lambda^{p_{dev}}$). Thus, the total increment of volumetric plastic strain is:

$$d\varepsilon_v^p = d\varepsilon_v^{p,iso} + d\varepsilon_v^{p,dev} \quad [4.10]$$

where $d\varepsilon_v^{p,iso}$ is the volumetric plastic strain induced by the isotropic mechanism

$d\varepsilon_v^{p,dev}$ is the volumetric plastic strain induced by the deviatoric mechanism

4.2.2.3 Improvement of deviatoric mechanism of Cam Clay model

Ratio between the preconsolidation pressure and the critical pressure is equal to 2.718 in the Original Cam Clay model. In the ACMEG model, this ratio it is not constant, but, as in realty, depends from the material and it is indicate with d [Huj79]. The deviatoric yield limit begins now:

$$f_{dev} = q - Mp' \left(1 - \ln \frac{d \cdot p'}{p'_c} \right) = 0 \quad [4.11]$$

where

$$d = \frac{p'_c}{p'_{cr}} \quad [4.12]$$

and where p'_{cr} is the critical pressure.

Moreover, for simulate better the heavily overconsolidated soils, the Cam Clay model is modified by introducing the parameter b for the control of the shape of the yield limit. The deviatoric yield limit begins as:

$$f_{dev} = q - Mp' \left(1 - b \cdot \ln \frac{d \cdot p'}{p'_c} \right) = 0 \quad [4.13]$$

This expression is similar to the failure locus proposed by Nova and Wood [N&W79] with $b = \frac{\beta^*}{M}$, where β^* is a parameter of the Nova-Wood model. The b parameter varies from 0 (corresponding to a Mohr-Coulomb criterion) to 1 (for the Original Cam-Clay model) as shown in Figure 4.6. As stated by Hujeux [Huj85], the role of this parameter is particularly important for highly overconsolidated soils. Generally, the value of b is lower for sand than for clays.

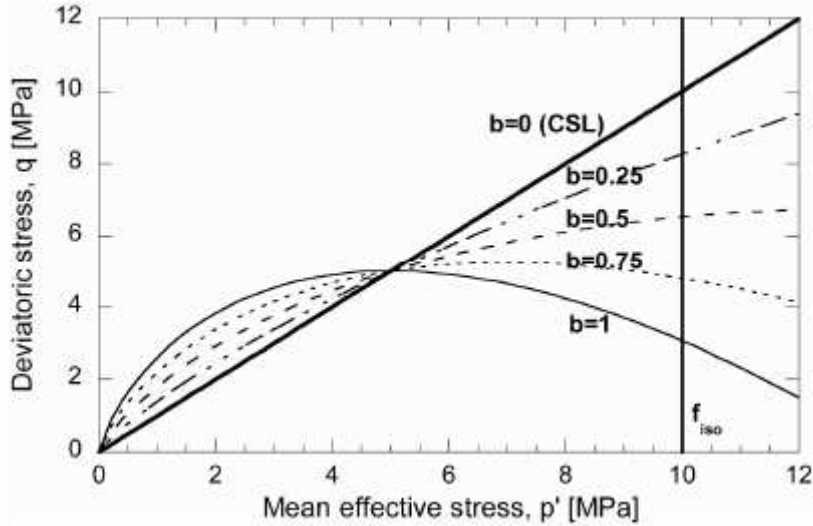


Figure 4.6: Deviatoric yield limit for different values of b (redrawn from [Fra08])

4.2.2.4 Degree of mobilization of the isotropic mechanism

Typical isotropic compression experimental results on a remoulded soil, as shown in Figure 4.7, clearly exhibit progressive mobilization of the plasticity before reaching the virgin consolidation line.

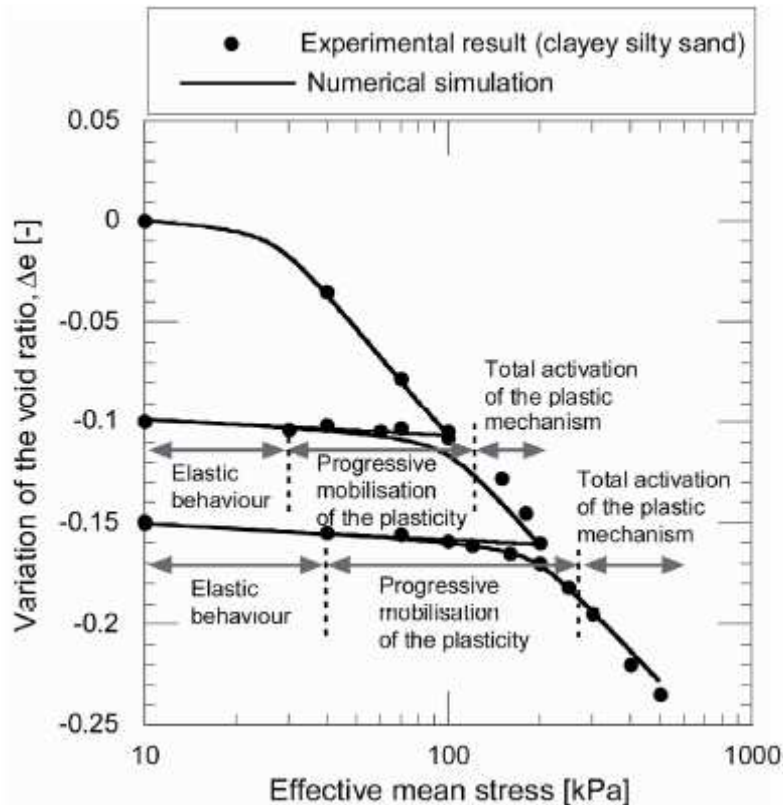


Figure 4.7: Comparison between experimental results [Jam03] and a numerical simulation (redrawn from [Fra08])

Therefore, even before surpassing the isotropic yield limit (i.e. the preconsolidation pressure), the soil undergoes generally irreversible strains upon isotropic loading. This behavioural feature can have a major effect on the response of an overconsolidated soils submitted to loading-unloading cycles. In order to reproduce this effect, the model needs to be improved by means of an additional constitutive artifice. The isotropic yield limit is modified as follows [Huj79]:

$$f_{iso} = p' - p'_c \cdot r_{iso} = 0 \quad [4.14]$$

where r_{iso} is the degree of mobilization of the isotropic mechanism.

During loading, r_{iso} is a hyperbolic function of the volumetric plastic strain induced by the isotropic mechanism (Figure 4.8), $\varepsilon_v^{p,iso}$:

$$r_{iso} = r_{iso}^e + \frac{\varepsilon_v^{p,iso}}{c + \varepsilon_v^{p,iso}} \quad [4.15]$$

and (see [Huj85] and [Fra08])

$$dr_{iso} = \frac{(1 - r_{iso})^2}{c} d\varepsilon_v^{p,iso} \quad [4.16]$$

where c is a material parameter

r_{iso}^e is the radius of the isotropic elastic nuclei inside which the produced strains are fully reversible.

During unloading the behaviour is purely elastic.

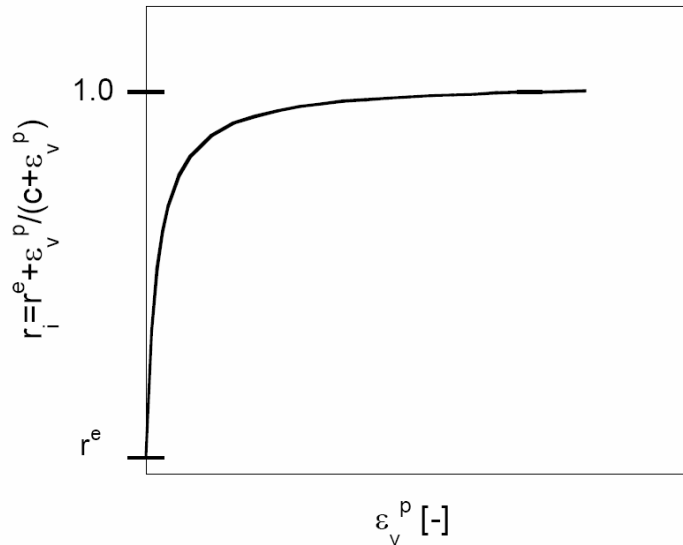


Figure 4.8: dependence of r_{iso} by volumetric plastic strain

In the same way as the isotropic mechanism, the deviatoric mechanism needs to be enhanced by a progressive plasticity process inside the external deviatoric yield limit. Hujeux [Huj79] proposed to introduce an additional hardening variable, the deviatoric plastic strain ε_d^p , governing the evolution of the degree of mobilization of the deviatoric mechanism r_{dev} . The deviatoric yield limit is modified as follows:

$$f_{dev} = q - Mp' \left(1 - b \cdot \ln \frac{d \cdot p'}{p'_c} \right) \cdot r_{dev} = 0 \quad [4.17]$$

During loading, r_{dev} is an hyperbolic function of the deviatoric plastic strain ε_d^p :

$$r_{dev} = r_{dev}^e + \frac{\varepsilon_d^p}{a + \varepsilon_d^p} \quad [4.18]$$

and (see [Huj85] and [Fra08])

$$dr_{dev} = \frac{(1 - r_{dev})^2}{a} d\varepsilon_d^p \quad [4.19]$$

where a is a material parameter

r_{dev}^e is the radius of the deviatoric elastic nuclei inside which the produced strains are fully reversible.

4.2.2.5 Isotropic plastic mechanism

Here, the constitutive equations are summarized in a concise way. Within the small strain assumptions, the total strain increment vector can be written as follow:

$$d\varepsilon_{ij} = d\varepsilon_{ij}^e + d\varepsilon_{ij}^p \quad [4.20]$$

and, the total strain increment induced by plasticity (hardening of the material) is a linear combination of two irreversible processes: an isotropic as well as a deviatoric process. Therefore, the “total” plastic strain increment, $d\varepsilon_{ij}^p$, is the sum of “partial” plastic strain increments, induced by the isotropic and the deviatoric mechanisms, $d\varepsilon_{ij}^{p,iso}$ and $d\varepsilon_{ij}^{p,dev}$, respectively:

$$d\varepsilon_{ij}^p = d\varepsilon_{ij}^{p,iso} + d\varepsilon_{ij}^{p,dev} \quad [4.21]$$

The isotropic yield limit f_{iso} is:

$$f_{iso} = p' - p'_c \cdot r_{iso} = 0 \quad [4.22]$$

where $p'_c = p'_{c0} e^{(\beta \varepsilon_v^p)}$

$$r_{iso} = r_{iso}^e + \frac{\varepsilon_v^{p,iso}}{c + \varepsilon_v^{p,iso}}$$

The flow rule is assumed to associated ($f_{iso}=g_{iso}$) and hence:

$$d\varepsilon_{ii}^{p,iso} = \lambda_{iso}^p \frac{\partial g_{iso}}{\partial \sigma'_{ii}} = \frac{\lambda_{iso}^p}{3} \quad [4.23]$$

The plastic multiplier, λ_{iso}^p , is determined using Prager’s consistency equation [Pra49].

4.2.2.6 Deviatoric plastic mechanism

The deviatoric yield limit f_{dev} is:

$$f_{dev} = q - Mp' \left(1 - b \cdot \ln \frac{d \cdot p'}{p'_c} \right) \cdot r_{dev} = 0 \quad [4.24]$$

where $M = \frac{6 \sin \Phi'}{3 - \sin \Phi'}$ is the slope of the critical state line (CSL) in the p' - q plane,

$$r_{dev} = r_{dev}^e + \frac{\varepsilon_d^p}{a + \varepsilon_d^p}$$

Φ' is the friction angle at critical state

Assuming the following dilatancy rule,

$$\frac{d\varepsilon_v^p}{d\varepsilon_d^p} = \alpha \left(M - \frac{q}{p'} \right) \quad [4.25]$$

the plastic potential can be write as:

$$g_{dev} = q - \frac{\alpha}{\alpha - 1} Mp' \left[1 - \frac{1}{\alpha} \left(\frac{d \cdot p'}{p'_c} \right)^{\alpha - 1} \right] = 0 \quad [4.26]$$

and thus, the hardening rule is:

$$d\varepsilon_{ij}^{p,dev} = \lambda_{dev}^p \frac{\partial g_{dev}}{\partial \sigma'_{ij}} = \lambda_{dev}^p \frac{1}{Mp'} \left[\frac{\partial q}{\partial \sigma'_{ij}} + \alpha \left(M - \frac{q}{p'} \right) \cdot \frac{1}{3} \delta_{ij} \right] \quad [4.27]$$

where $\frac{\partial q}{\partial \sigma'_{ij}} = \frac{3}{2q} (\sigma'_{ij} - p')$ if $i=j$

$$\frac{\partial q}{\partial \sigma'_{ij}} = \frac{3}{q} \sigma'_{ij} \quad \text{if } i \neq j$$

$$d\varepsilon_v^{p,dev} = \lambda_{dev}^p \frac{\partial g_{dev}}{\partial p'} = \lambda_{dev}^p \frac{\alpha}{Mp'} \left[M - \frac{q}{p'} \right] \quad [4.28]$$

$$d\varepsilon_v^p = \lambda_{dev}^p \frac{\partial g_{dev}}{\partial q} = \lambda_{dev}^p \frac{1}{Mp'} \quad [4.29]$$

The plastic multiplier, λ_{dev}^p , is determined using Prager's consistency equation [Pra49].

4.2.2.7 Coupling between the two mechanisms

The isotropic and the deviatoric yield limits are coupled through the hardening variable, ε_v^p which appears in the expression of the two yield limits. When the two mechanisms are activated simultaneously, the total volumetric plastic strain increment, $d\varepsilon_v^p$, is the sum of the volumetric plastic strain increments due to each mechanism:

$$d\varepsilon_v^p = \lambda_{dev}^p \frac{\partial g_{dev}}{\partial p'} + \lambda_{iso}^p \frac{\partial g_{iso}}{\partial p'} = \lambda_{dev}^p \frac{\alpha}{Mp'} \left[M - \frac{q}{p'} \right] + \lambda_{iso}^p \quad [4.30]$$

The two consistency conditions must be met simultaneously, leading to the solving of two equations with two unknowns [Riz96]:

$$\begin{aligned} d\mathbf{F} &= \frac{\partial \mathbf{F}}{\partial \boldsymbol{\sigma}'} : d\boldsymbol{\sigma}' + \frac{\partial \mathbf{F}}{\partial \pi} \frac{\partial \pi}{\partial \lambda^p} \lambda^p = \mathbf{j} : d\boldsymbol{\sigma}' - \mathbf{H} \lambda^p \leq 0 \\ \lambda^p &\geq 0 \\ d\mathbf{F} \cdot \lambda^p &= 0 \end{aligned} \quad [4.31]$$

$$d\mathbf{F} = \begin{bmatrix} df_{iso} \\ df_{dev} \end{bmatrix} \quad [4.32]$$

where $\boldsymbol{\pi}$ is the internal variable vector

\mathbf{j} is the gradient of stress of the loading vectors function \mathbf{F} :

$$\mathbf{j} = \begin{bmatrix} \frac{\partial f_{iso}}{\partial \sigma'_{11}} & \frac{\partial f_{iso}}{\partial \sigma'_{22}} & \frac{\partial f_{iso}}{\partial \sigma'_{33}} & \frac{\partial f_{iso}}{\partial \sigma'_{12}} & \frac{\partial f_{iso}}{\partial \sigma'_{13}} & \frac{\partial f_{iso}}{\partial \sigma'_{23}} \\ \frac{\partial f_{dev}}{\partial \sigma'_{11}} & \frac{\partial f_{dev}}{\partial \sigma'_{22}} & \frac{\partial f_{dev}}{\partial \sigma'_{33}} & \frac{\partial f_{dev}}{\partial \sigma'_{12}} & \frac{\partial f_{dev}}{\partial \sigma'_{13}} & \frac{\partial f_{dev}}{\partial \sigma'_{23}} \end{bmatrix} \quad [4.33]$$

$\boldsymbol{\lambda}^p$ is the plastic multiplier vector

$$\boldsymbol{\lambda}^p = \begin{bmatrix} \lambda^p_{iso} \\ \lambda^p_{dev} \end{bmatrix} \quad [4.34]$$

\mathbf{H} is the matrix of hardening moduli $H_{\alpha\beta} = -\frac{\partial f_{\alpha}}{\partial \lambda^p_{\beta}}$

$$\mathbf{H} = \begin{bmatrix} H_{ii} & H_{id} \\ H_{di} & H_{dd} \end{bmatrix} \quad [4.35]$$

where

$$\begin{aligned} H_{ii} &= -\frac{\partial f_{iso}}{\partial r_{iso}} \frac{\partial r_{iso}}{\partial \lambda^p_{iso}} - \frac{\partial f_{iso}}{\partial \varepsilon_v^p} \frac{\partial \varepsilon_v^p}{\partial \lambda^p_{iso}} = \rho'_c \frac{(1-r_{iso})^2}{c} + \rho'_c \cdot \beta \cdot r_{iso} \\ H_{id} &= -\frac{\partial f_{iso}}{\partial r_{dev}} \frac{\partial r_{dev}}{\partial \lambda^p_{dev}} - \frac{\partial f_{iso}}{\partial \varepsilon_v^p} \frac{\partial \varepsilon_v^p}{\partial \lambda^p_{dev}} = -\frac{\partial f_{iso}}{\partial \varepsilon_v^p} \frac{\partial \varepsilon_v^p}{\partial \lambda^p_{dev}} = \rho'_c \cdot \beta \cdot r_{iso} \frac{1}{Mp'} \left(M - \frac{q}{\rho'} \right) \alpha \\ H_{di} &= -\frac{\partial f_{dev}}{\partial r_{iso}} \frac{\partial r_{iso}}{\partial \lambda^p_{iso}} - \frac{\partial f_{dev}}{\partial \varepsilon_v^p} \frac{\partial \varepsilon_v^p}{\partial \lambda^p_{iso}} = -\frac{\partial f_{dev}}{\partial \varepsilon_v^p} \frac{\partial \varepsilon_v^p}{\partial \lambda^p_{iso}} = Mp' \cdot b \cdot \beta \cdot r_{dev} \\ H_{dd} &= -\frac{\partial f_{dev}}{\partial r_{dev}} \frac{\partial r_{dev}}{\partial \lambda^p_{dev}} - \frac{\partial f_{dev}}{\partial \varepsilon_v^p} \frac{\partial \varepsilon_v^p}{\partial \lambda^p_{dev}} = -\left(1 - b \cdot \ln \frac{\rho' d}{\rho'_c} \right) \frac{(1-r_{dev})^2}{a} - b \cdot \beta \left(M - \frac{q}{\rho'} \right) \alpha \cdot r_{dev} \end{aligned} \quad [4.36]$$

$d\mathbf{F} \leq 0$ expresses Prager's consistency condition [Pra49] extended to multiple dissipation processes [Riz96]. The elasto-plastic framework enables the stress increment response with respect to prescribed strain increment to be expressed as:

$$d\boldsymbol{\sigma}' = \mathbf{E} : (d\boldsymbol{\varepsilon} - \mathbf{m} \cdot \boldsymbol{\lambda}^p) \quad [4.37]$$

where \mathbf{E} is the current elastic stiffness tensor of the material

\mathbf{m} defines the collection of flow directions and is:

$$\mathbf{m} = \frac{\partial \mathbf{G}}{\partial \boldsymbol{\sigma}'} = \begin{bmatrix} \frac{\partial g_{iso}}{\partial \sigma'_{11}} & \frac{\partial g_{iso}}{\partial \sigma'_{22}} & \frac{\partial g_{iso}}{\partial \sigma'_{33}} & \frac{\partial g_{iso}}{\partial \sigma'_{12}} & \frac{\partial g_{iso}}{\partial \sigma'_{13}} & \frac{\partial g_{iso}}{\partial \sigma'_{23}} \\ \frac{\partial g_{dev}}{\partial \sigma'_{11}} & \frac{\partial g_{dev}}{\partial \sigma'_{22}} & \frac{\partial g_{dev}}{\partial \sigma'_{33}} & \frac{\partial g_{dev}}{\partial \sigma'_{12}} & \frac{\partial g_{dev}}{\partial \sigma'_{13}} & \frac{\partial g_{dev}}{\partial \sigma'_{23}} \end{bmatrix}^T \quad [4.38]$$

Thus, the consistency equation can be re-written as follows:

$$d\mathbf{F} = \mathbf{j} : \mathbf{E} : d\boldsymbol{\varepsilon} - (\mathbf{H} + \mathbf{j} : \mathbf{E} : \mathbf{m}) \cdot \lambda^p \leq 0$$

$$\lambda^p \geq 0$$

$$d\mathbf{F} \cdot \lambda^p = 0$$

[4.39]

4.3 ACMEG-T MODEL

In this sections, the ACMEG model is modified, taken into account the temperature influence on the behaviour of soils, to obtain the ACMEG-T model.

4.3.1 Thermo elasticity

The non-isothermal case causes, in elasticity, a reversible strain increment:

$$d\varepsilon_{ij}^e = d\varepsilon_{ij}^{me} + d\varepsilon_{ij}^{Te} = E_{ijkl}^{-1} d\sigma'_{kl} - \beta_{T,ij} dT \quad [4.40]$$

where $\beta_{T,ij}$ is the thermal expansion tensor which depends on the temperature, T .

Considering isotropic thermal behaviour, one can express $\beta_{T,ij}$ as $\beta_{T,ij} = \frac{1}{3} \beta'_s \delta_{ij}$ with β'_s being the volumetric thermal expansion coefficient of the solid skeleton.

The volumetric and deviatoric parts of the tensor of the elastic strain increment are, respectively:

$$d\varepsilon_v^e = d\varepsilon_v^{me} + d\varepsilon_v^{Te} = \frac{dp'}{K} - \beta'_s dT \quad [4.41]$$

$$d\varepsilon_d^e = d\varepsilon_d^{me} + d\varepsilon_d^{Te} = \frac{dq}{3G} \quad [4.42]$$

The volumetric thermal expansion coefficient of the solid skeleton, β'_s , it is not constant but increases with temperature and decreases as stress level increases [L&C03]:

$$\beta'_s = [\beta'_{s0} + \xi(T - T_0)] \xi \quad [4.43]$$

where β'_{s0} is the isotropic thermal expansion coefficient at a reference temperature, T_0 (usually ambient temperature)

$$\xi = \left(\frac{p'_{cr0}}{p'} \right)^{n_T}$$

is the ratio between the initial critical state pressure at ambient temperature, p'_{cr0} , and the

mean effective stress, p' and n_T is a material parameter,

$$\xi \text{ is the slope of the variation of } \beta'_s \text{ with respect to the current temperature, } T \text{ and when } \xi = 1$$

ξ could be approximated as proposed by Laloui [La193] with the following relationship:

$$\xi = -\frac{\beta'_{s0}}{100 \text{ } ^\circ\text{C}} \quad [4.44]$$

and its dimension is $^\circ\text{C}^{-2}$.

Obviously, the relation [4.43] with the approximation $\zeta = -\frac{\beta'_{s0}}{100 \text{ }^\circ\text{C}}$ [4.44][4.44], is correct only for temperature between 20 °C (room temperature) and 95 °C, as mentioned. In fact, when $T-T_0$ is greater than 100 °C, the coefficient β'_s begins negative.

4.3.2 Thermo plasticity

The thermo-plastic strain increment can be expressed as the part of the total strain increment which is not recoverable:

$$d\varepsilon_{ij}^p = d\varepsilon_{ij} - d\varepsilon_{ij}^e = d\varepsilon_{ij} + \beta_{T,ij} dT - E_{ijkl}^{-1} d\sigma'_{kl} \quad [4.45]$$

The yield limits of the isotropic and deviatoric mechanism, respectively, are recalled and the temperature-induced modifications of those relations are presented.

4.3.2.1 Isotropic thermo-plastic mechanism

The thermal effect on the isotropic mechanism is introduced through the evolution of the preconsolidation pressure p'_{c0} with temperature (Figure 4.9).

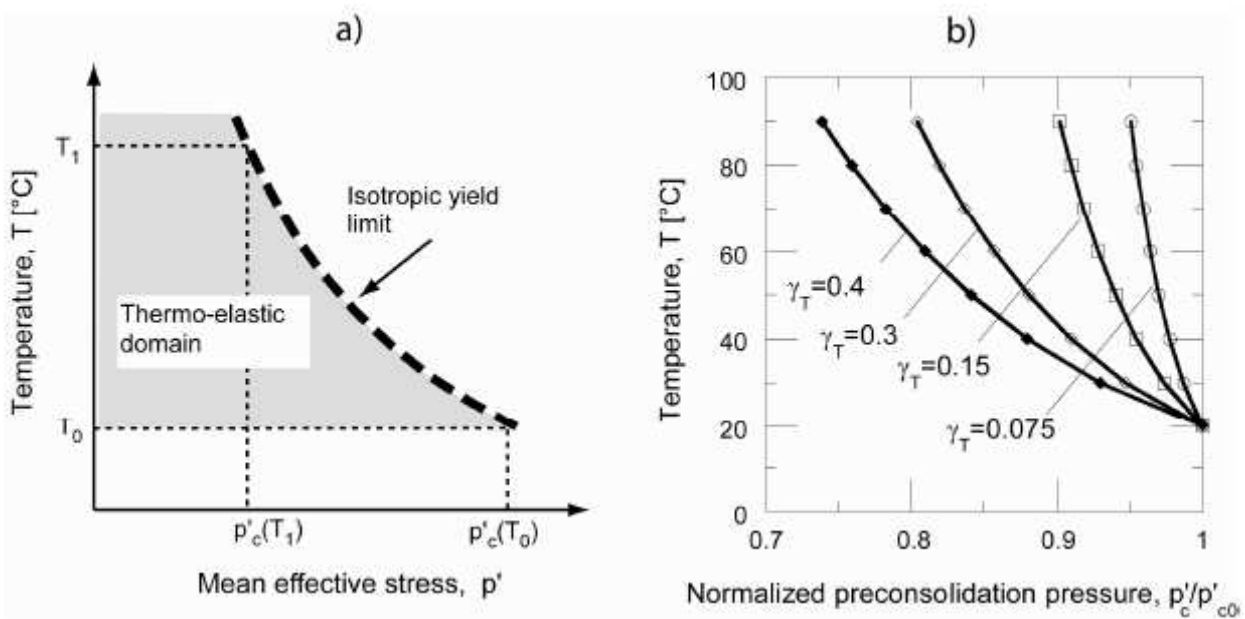


Figure 4.9: a) Isotropic yield limit. b) dependency of p'_c from γ_T [L&C03] (redrawn from [Fra08])

As shown in section 4.1.3, several authors suggested analytical expressions to describe the shrinkage of the yield limit with increasing temperature. The evolution of p'_c with temperature being rapid for low temperature changes and becoming asymptotic for the high ones, the logarithmic function of Laloui and Cekerevac [L&C03] is a very suitable expression to model this phenomenon. The thermo-mechanical evolution of isotropic yield surface is expressed as:

$$f_{iso} = p' - p'_{c0} e^{(\beta'_{c0} p')} \left[1 - \gamma_T \log\left(\frac{T}{T_0}\right) \right] r_{iso} = 0 \quad [4.46]$$

where p'_c is the preconsolidation pressure at a given temperature T

p'_{c0} is the preconsolidation pressure at the reference temperature T_0

γ_T is a material parameters

β is the plastic compressibility modulus

ε_v^p is the volumetric plastic strain

r_{iso} is the degree of plastification of the isotropic mechanism

The flow rule of the isotropic mechanism remains unchanged regarding to the isothermal mechanism [4.23].

4.3.2.2 Deviatoric thermo-plastic mechanism

Starting from the equation seen in section 4.2.2.6 [Huj79]

$$f_{dev} = q - Mp' \left(1 - b \cdot \ln \frac{d \cdot p'}{p'_c} \right) \cdot r_{dev} = 0 \quad [4.47]$$

where p'_c is the preconsolidation pressure

d is the ratio between the preconsolidation pressure, p'_c , and the critical pressure, p'_{cr}

b is a material parameter defining the shape of the deviatoric yield limit

r_{dev} is the degree of plastification of the deviatoric mechanism

M is the slope of the critical state line in the p' - q plane

As shown by Laloui [Lal03], the friction angle may be depend on temperature with the following expression:

$$M = M_0 - g(T - T_0) \quad [4.48]$$

where M_0 is the is the slope of the critical state line at ambient temperature T_0

g is an average slope of variation of friction angle at critical state with temperature

Obviously, if for some soil there is no influence of temperature on the frictional angle, the parameter g is equal to zero.

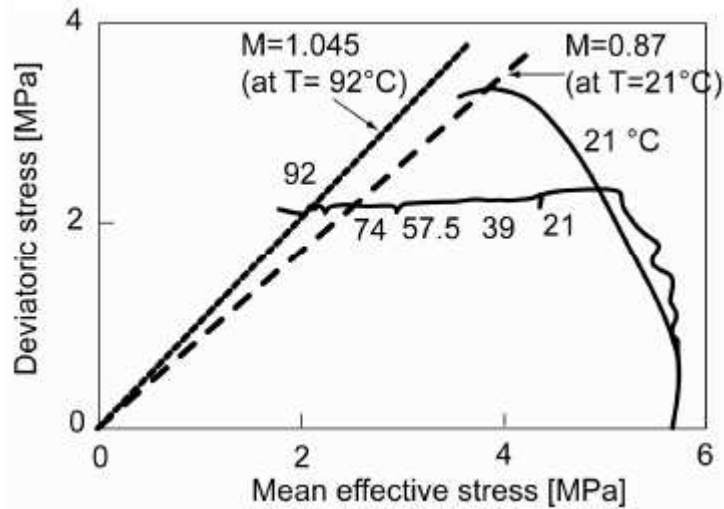


Figure 4.10: Effective stress path on Boom clay in isotropic condition. Influence of temperature on M (redrawn from [Fra08])

Thus, the deviatoric yield surface becomes, under non-isothermal conditions:

$$f_{dev} = q - [M_0 - g(T - T_0)] p' \left(1 - b \cdot \ln \frac{d \cdot p'}{p'_{c0} e^{\beta \varepsilon_v^p} \left[1 - \gamma_T \log \left(\frac{T}{T_0} \right) \right]} \right) \cdot r_{dev} = 0 \quad [4.49]$$

The flow rule of the deviatoric mechanism remains unchanged regarding to the isothermal mechanism [4.25] and [4.29].

4.3.2.3 Coupling between the two thermo-plastic mechanisms

The coupling between the two thermo-plastic mechanisms is similar to the isothermal model. However, inclusion of the derivation of the yield limits with respect to temperature is required in the consistency conditions for multi-mechanism due to the evolution of both yield limits with temperature state [Pra58]. In that sense, the effective stress and the temperature are the two state variables of the model:

$$d\mathbf{F} = \frac{\partial \mathbf{F}}{\partial \boldsymbol{\sigma}'} : d\boldsymbol{\sigma}' + \frac{\partial \mathbf{F}}{\partial T} \cdot dT + \frac{\partial \mathbf{F}}{\partial \pi} \cdot \frac{\partial \pi}{\partial \lambda^p} \cdot \lambda^p = \mathbf{j} : d\boldsymbol{\sigma}' + \mathbf{t} \cdot dT - \mathbf{H} \cdot \lambda^p \leq 0$$

$$\lambda^p \geq 0$$

$$d\mathbf{F} \cdot \lambda^p = 0$$
[4.50]

where \mathbf{t} is the temperature-gradient of the loading function \mathbf{F}

The stress increment is now:

$$d\boldsymbol{\sigma}' = \mathbf{E} : (d\boldsymbol{\varepsilon} - d\boldsymbol{\varepsilon}^{Te} - \mathbf{m} \cdot \lambda^p) = \mathbf{E} : (d\boldsymbol{\varepsilon} - \boldsymbol{\beta}_T dT - \mathbf{m} \cdot \lambda^p)$$
[4.51]

where \mathbf{E} is the current elastic stiffness tensor of the material

\mathbf{m} defines the collection of flow directions and is:

$$\mathbf{m} = \frac{\partial \mathbf{G}}{\partial \boldsymbol{\sigma}'}$$
[4.52]

where \mathbf{G} being the potential vector function

The consistency equation is now:

$$d\mathbf{F} = \mathbf{j} : \mathbf{E} : d\boldsymbol{\varepsilon} - (\mathbf{j} : \mathbf{E} : \boldsymbol{\beta}_T - \mathbf{t}) \cdot dT - (\mathbf{H} + \mathbf{j} : \mathbf{E} : \mathbf{m}) \cdot \lambda^p \leq 0$$

$$\lambda^p \geq 0$$

$$d\mathbf{F} \cdot \lambda^p = 0$$
[4.53]

where

$$\boldsymbol{\beta}_T = \left[\frac{\beta'_s}{3} \quad \frac{\beta'_s}{3} \quad \frac{\beta'_s}{3} \quad 0 \quad 0 \quad 0 \right]^T$$
[4.54]

$$\mathbf{t} = \begin{bmatrix} \frac{\partial f_{iso}}{\partial T} \\ \frac{\partial f_{dev}}{\partial T} \end{bmatrix} = \begin{bmatrix} \rho'_{c0} e^{\beta \varepsilon^p} \frac{\gamma_T}{T \cdot \ln 10} r_{iso} \\ \frac{M \cdot r_{dev} \cdot \rho' \cdot b \cdot \gamma_T}{\left[1 - \gamma_T \log \left(\frac{T}{T_0} \right) \right] T \cdot \ln 10} + \rho' \left[1 - b \cdot \ln \left(\frac{d \cdot \rho'}{\rho'_c} \right) \right] g \cdot r_{dev} \end{bmatrix}$$
[4.55]

4.4 VALIDATION OF THE IMPLEMENTATION OF ACMEG-T MODEL IN COMES-GEO F.E. CODE

4.4.1 Introduction

In this section the implementation of ACMEG-T in COMES-GEO is validated by comparison between the results of the ACMEG-T model's driver and the results obtained with COMES-GEO.

Obviously, the ACMEG-T model is considered validate [Lal05], [San08], [Fra08].

The validation in COMES-GEO is performed by checking separately elastic linear and non linear behaviour and the two plastic mechanisms, first in isothermal conditions and then in non-isothermal conditions. For each analysis is reported the loading path, the material parameters and the most important results. For some of these analysis there is a comparison with experimental results that have been used for the validation of the driver ACMEG-T.

4.4.2 Elastic isotropic compression in non-isothermal condition

In elastic domain, an isotropic compression is simulated, the material is considered first as linear elastic, then as non linear elastic.

The mechanical linear elastic case is a sub-case of the non-linear elastic case, as derived from the relations [4.6] and [4.7] with $n_e = 0$

$$K = K_{ref} \left(\frac{p'}{p'_{ref}} \right)^{n_e} = K_{ref} \left(\frac{p'}{p'_{ref}} \right)^0 = K_{ref} \quad [4.56]$$

$$G = G_{ref} \left(\frac{p'}{p'_{ref}} \right)^{n_e} = G_{ref} \left(\frac{p'}{p'_{ref}} \right)^0 = G_{ref} \quad [4.57]$$

Similarly the thermal linearity, is simulated by the non linear relationship

$$\beta'_s = [\beta'_{s0} + \xi(T - T_0)]_{\xi}^{\xi} = [\beta'_{s0} + 0 \cdot (T - T_0)] \cdot 1 = \beta'_{s0} \quad [4.58]$$

$$\xi = \left(\frac{p'_{cr0}}{p'} \right)^{n_T} \quad [4.59]$$

assuming $\xi = 0$ and $n_T = 0$ from which results $\beta'_s = \beta'_{s0}$.

	n_e	n_T
Case 0	0.0	0.0
Case 1	1.0	0.2
Case 2	0.7	0.4
Case 3	1.0	0.0

Table 4.3: Summary of elastic cases

In addition to the linear elastic case, other three cases are simulated and are reported in Table 4.3.

The other material parameters are the following:

Elastic parameters		
K_{ref} [MPa]	G_{ref} [MPa]	β'_s [°C ⁻¹]
100.00	40.00	$3.0 \cdot 10^{-5}$

Table 4.4: Material parameters of the elastic cases

The loading path is composed, starting from the initial condition of 50 kPa and 20°C of temperature, by four step (Figure 4.11: Isotropic mechanical and thermal loading path):

1. Mechanical compression loading from 50 kPa to 800 kPa
2. Thermal heating from 20°C to 80°C
3. Mechanical compression unloading from 800 kPa to 50 kPa
4. Thermal cooling from 80°C to 20°C

The results are shown in four different plane graphs:

1. Mean stress and Deviatoric stress p - q
2. Mean stress and Volumetric strain p - ϵ_v
3. Temperature and Volumetric strain T - ϵ_v
4. Temperature and Mean stress T - p

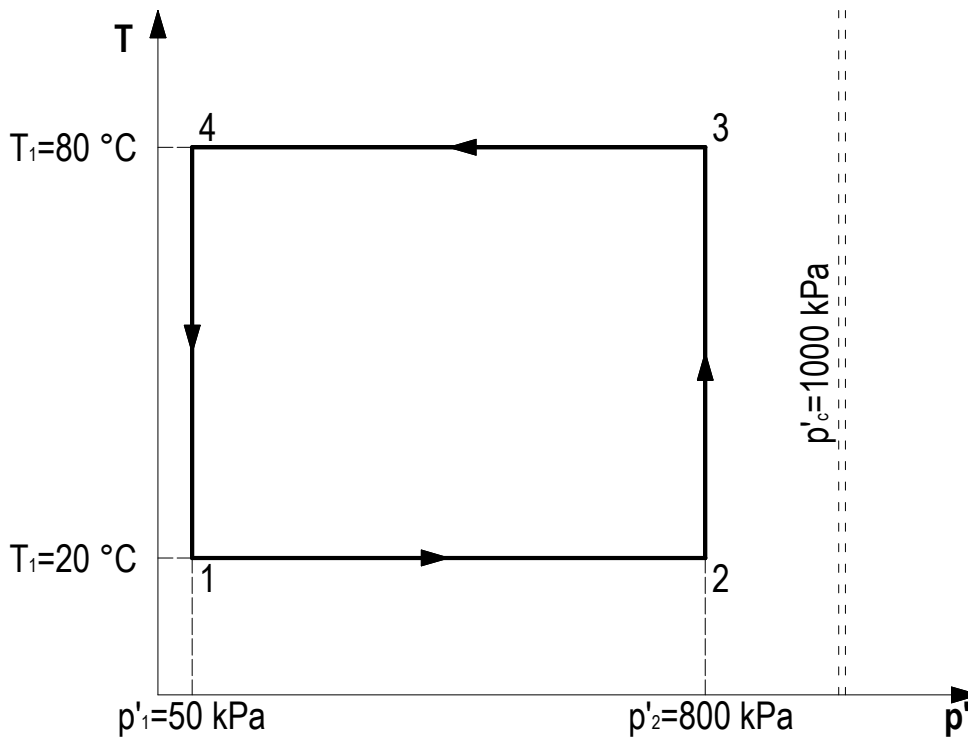


Figure 4.11: Isotropic mechanical and thermal loading path

4.4.2.1 Case 0

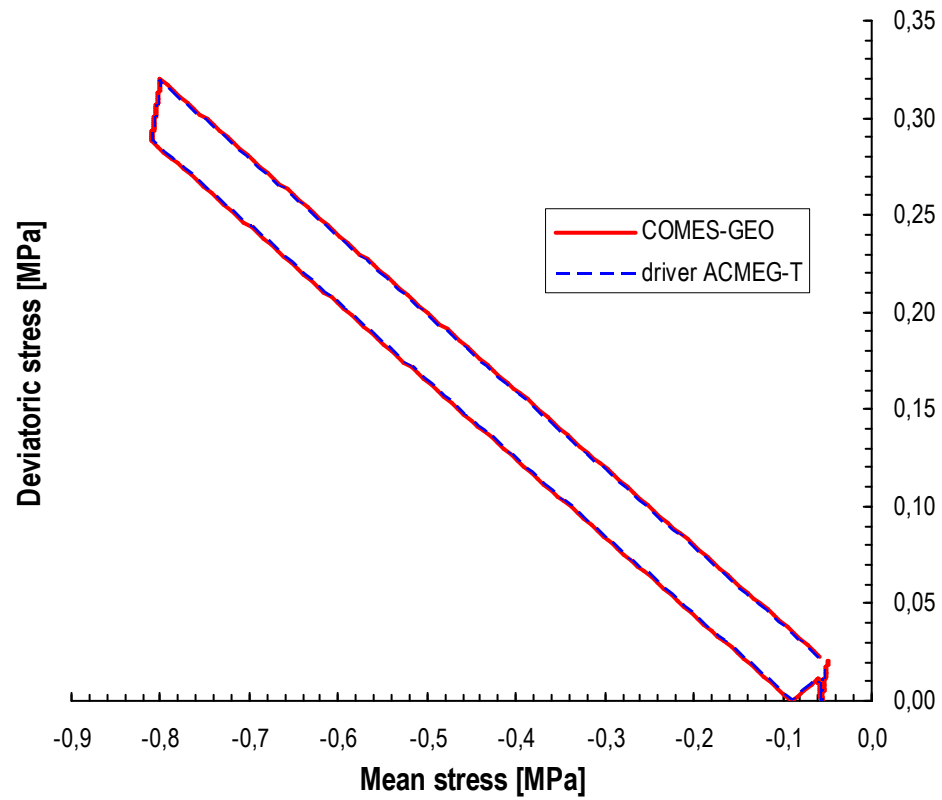
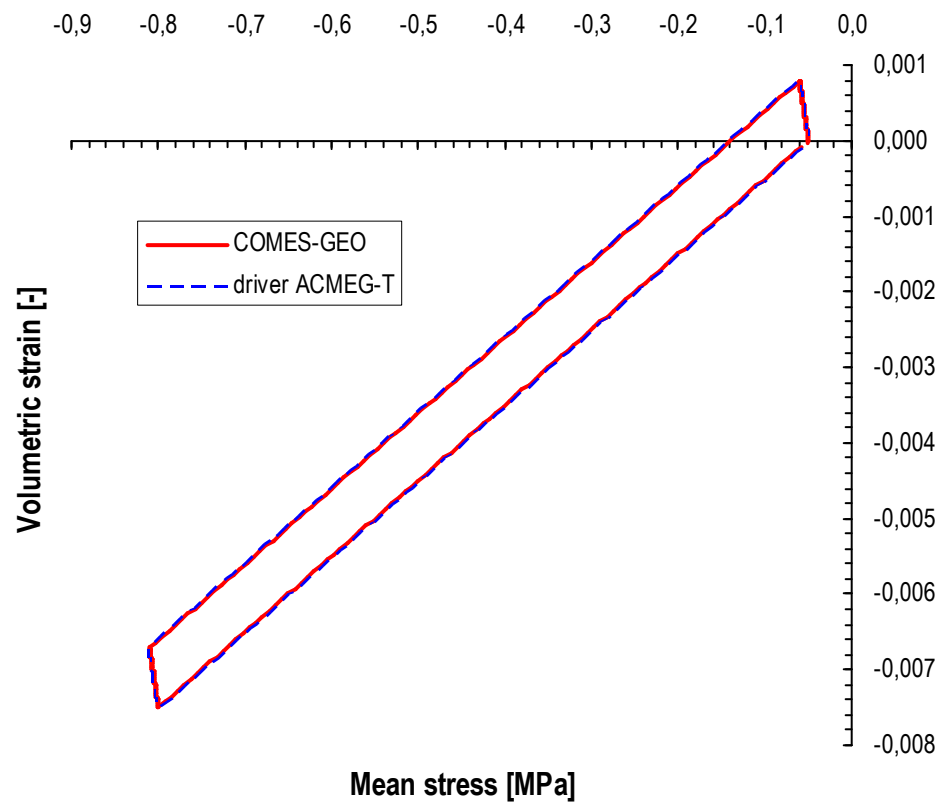


Figure 4.12: Mean stress and Deviatoric stress p-q

Figure 4.13: Mean stress and Volumetric strain p- ϵ_v

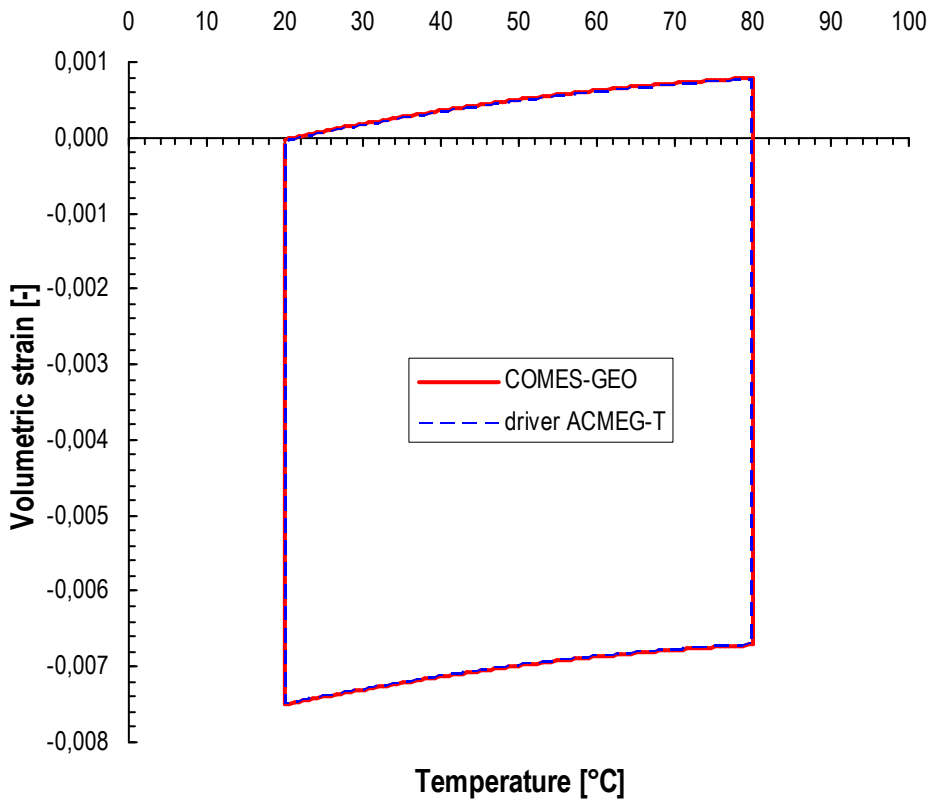


Figure 4.14: Temperature and Volumetric strain T- ϵ_v

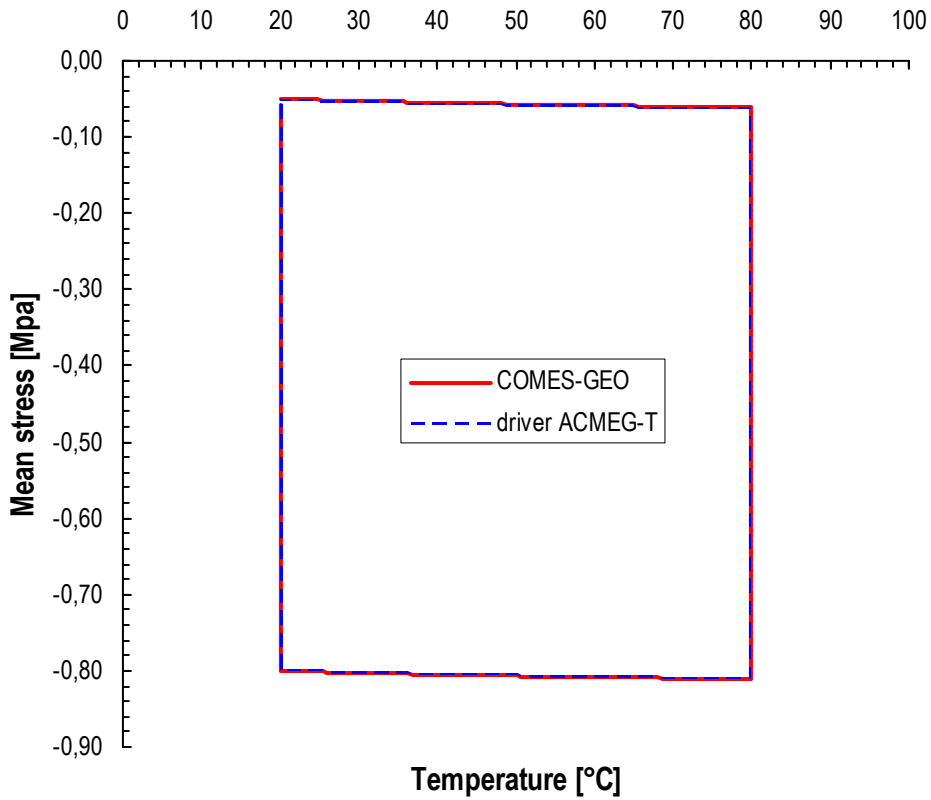


Figure 4.15: Temperature and Mean stress T-p

4.4.2.2 Case 1

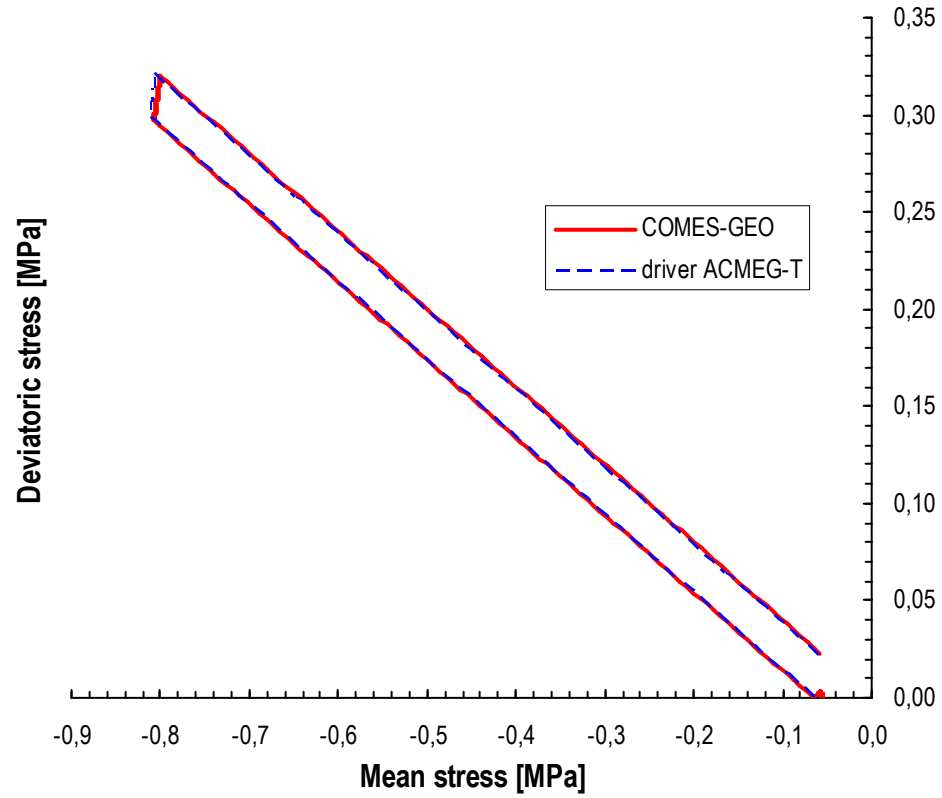
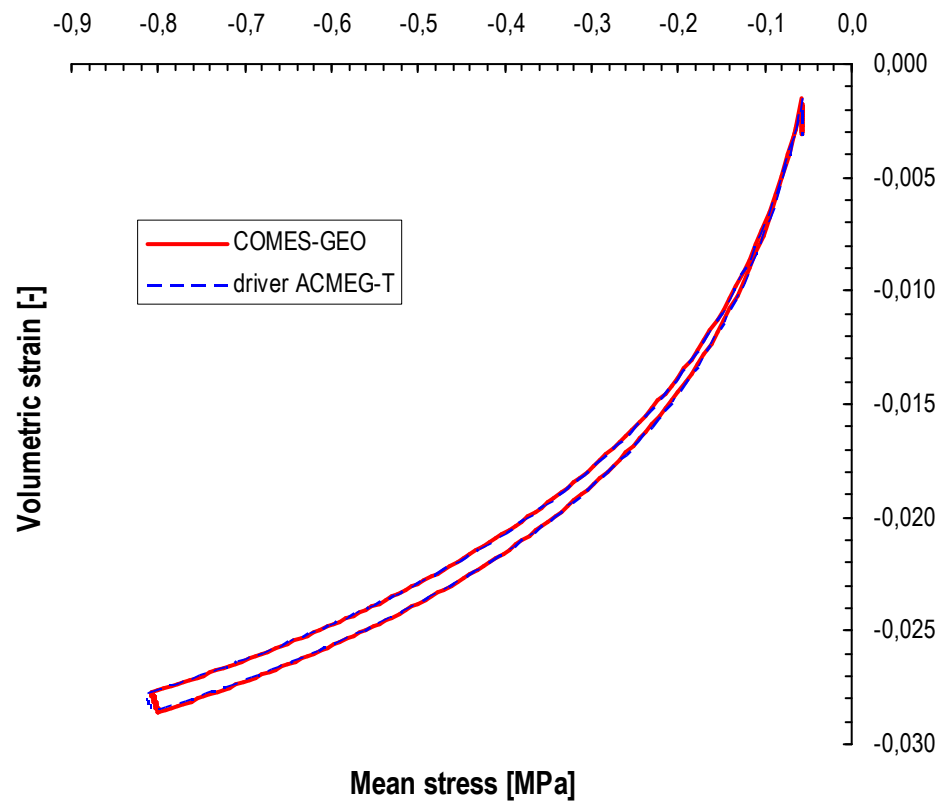


Figure 4.16: Mean stress and Deviatoric stress p-q

Figure 4.17: Mean stress and Volumetric strain p- ε_v

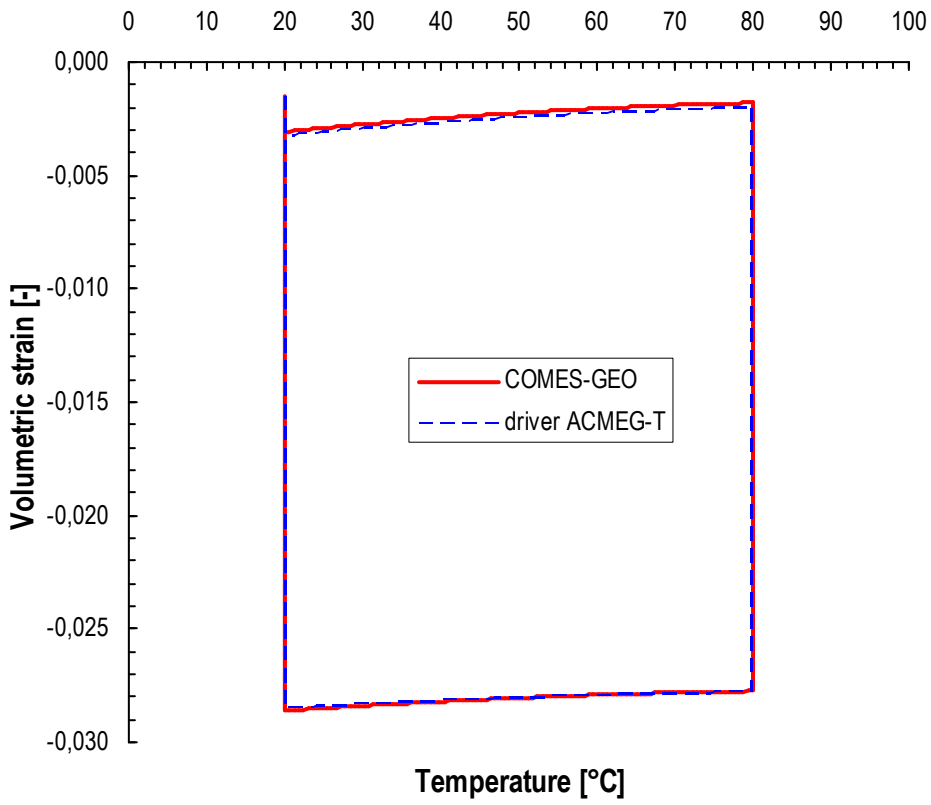


Figure 4.18: Temperature and Volumetric strain T- ϵ_v

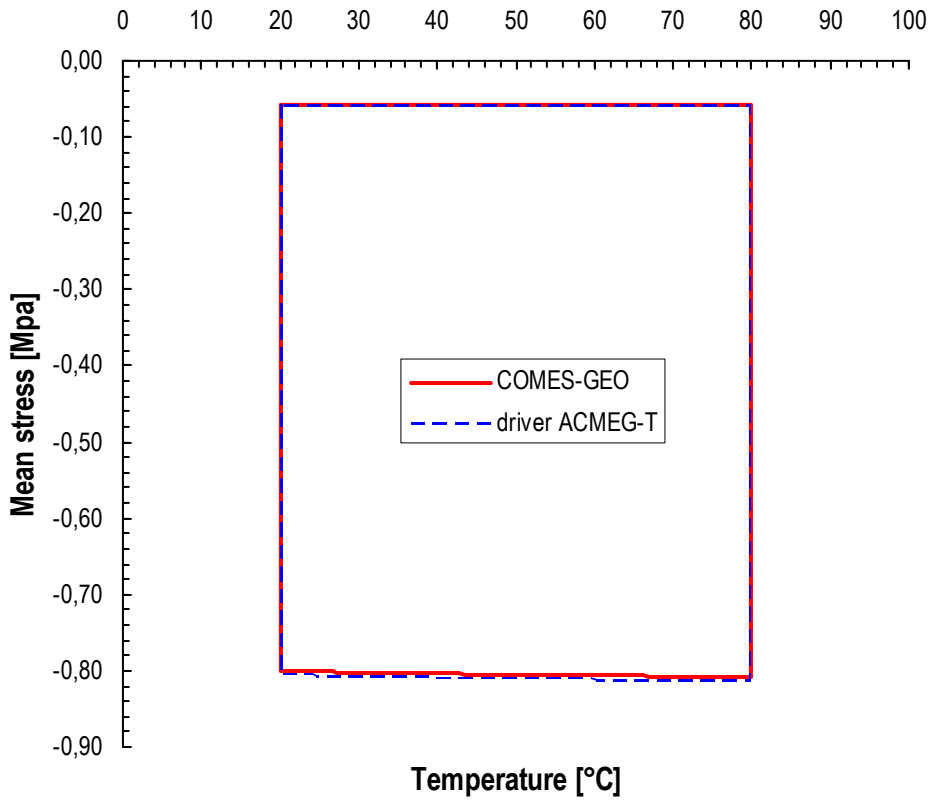


Figure 4.19: Temperature and Mean stress T-p

4.4.2.3 Case 2

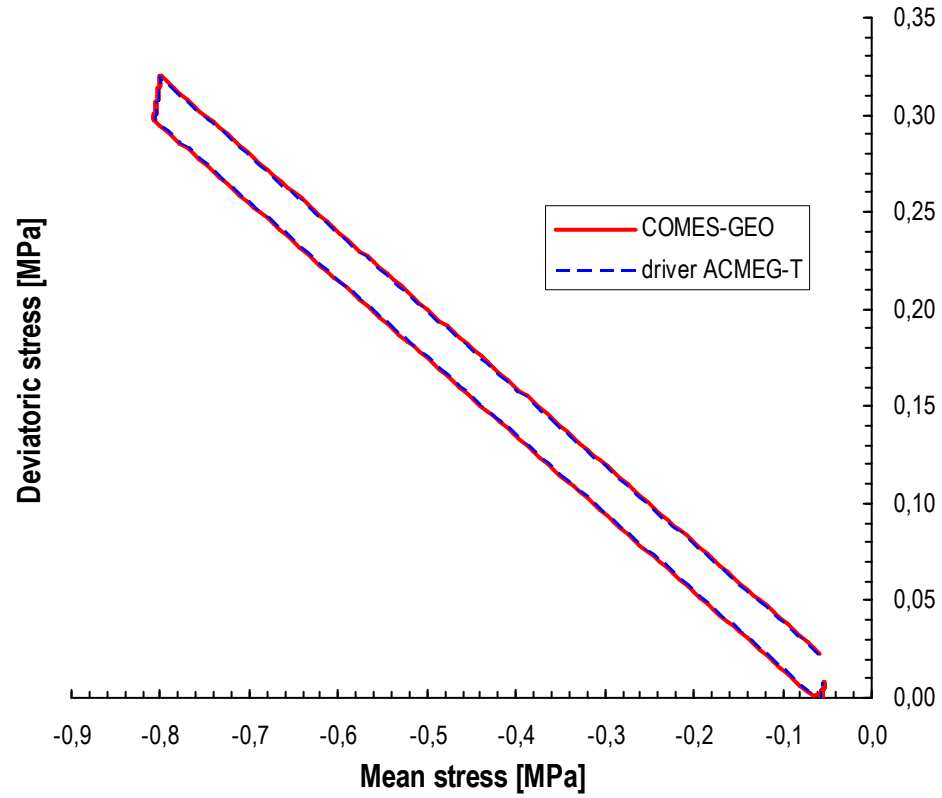
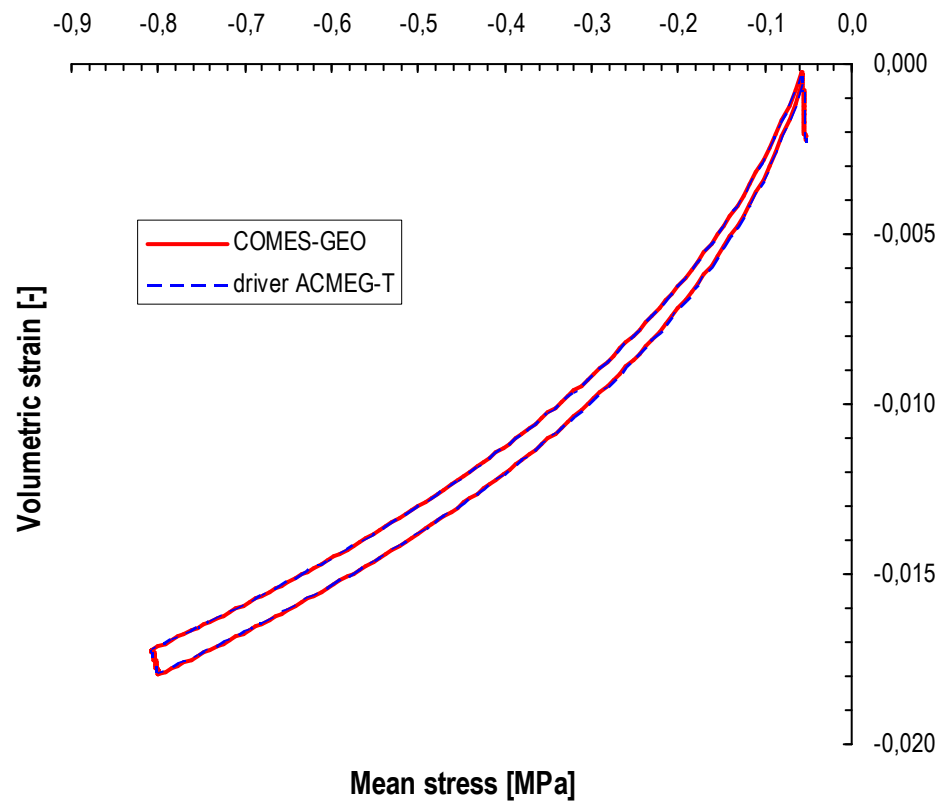


Figure 4.20: Mean stress and Deviatoric stress p-q

Figure 4.21: Mean stress and Volumetric strain p- ε_v

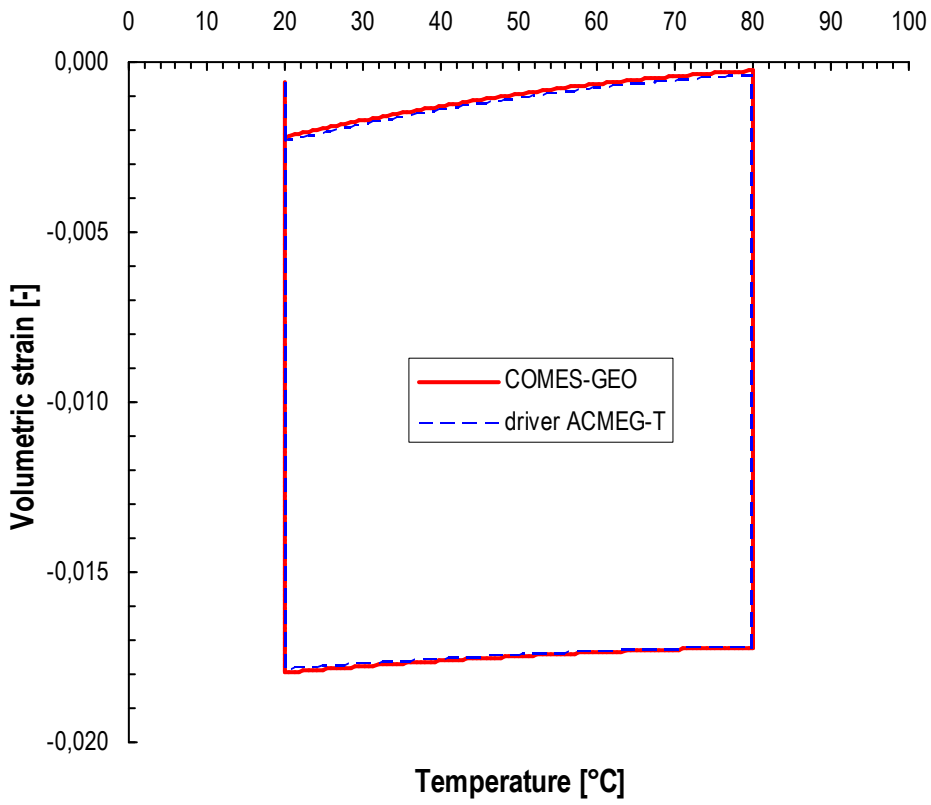


Figure 4.22: Temperature and Volumetric strain T- ϵ_v

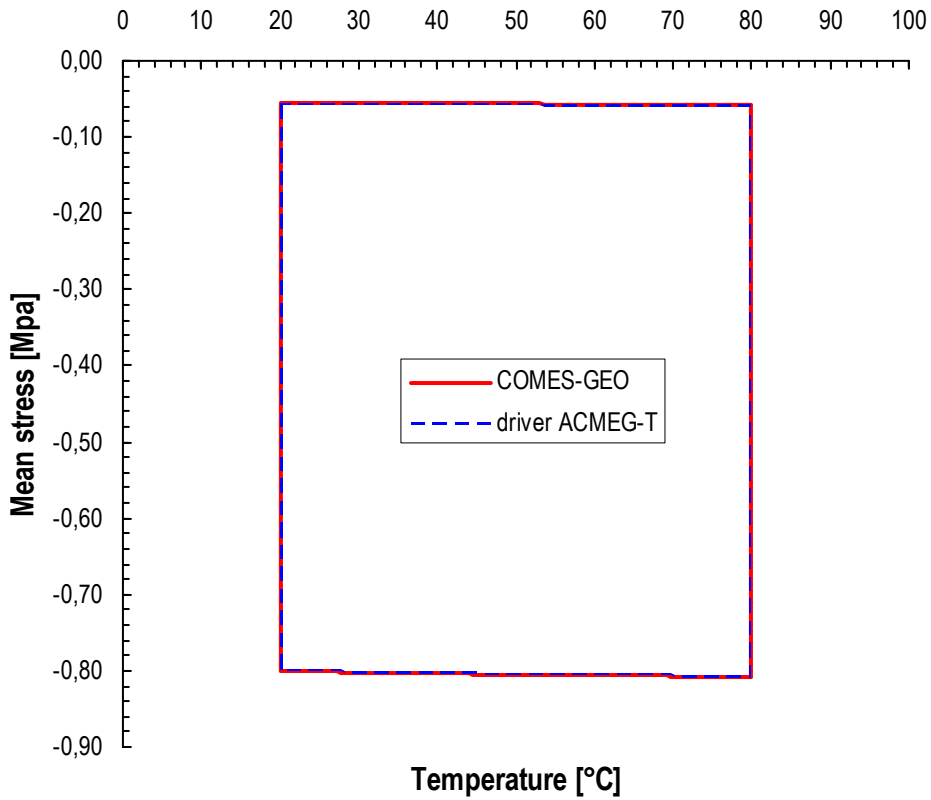


Figure 4.23: Temperature and Mean stress T-p

4.4.2.4 Case 3

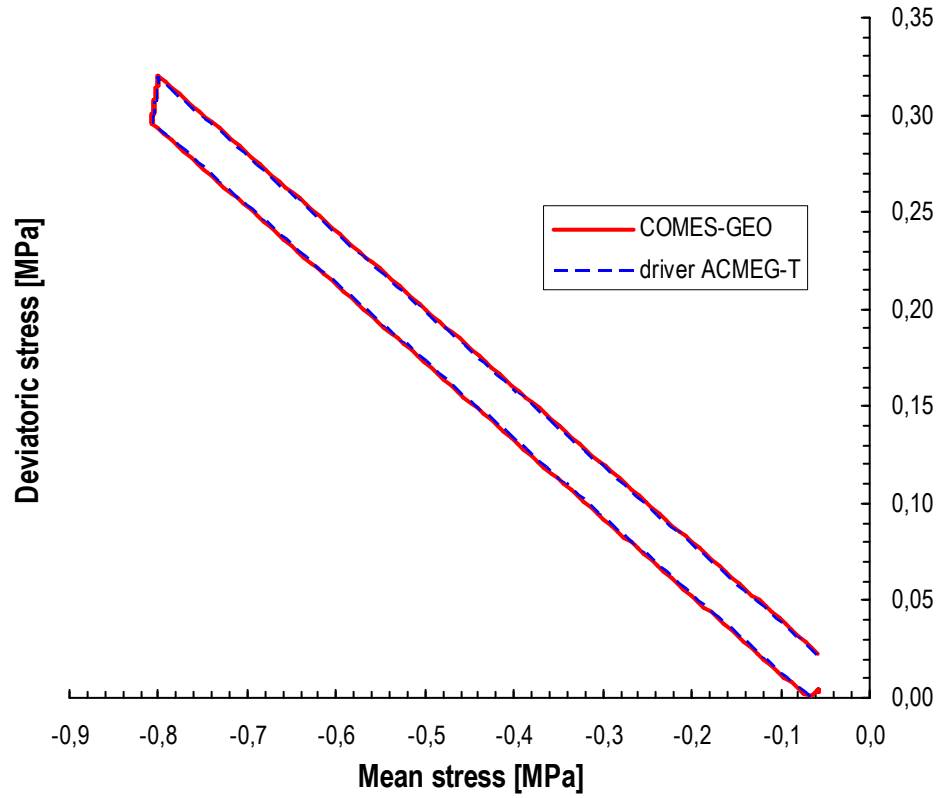
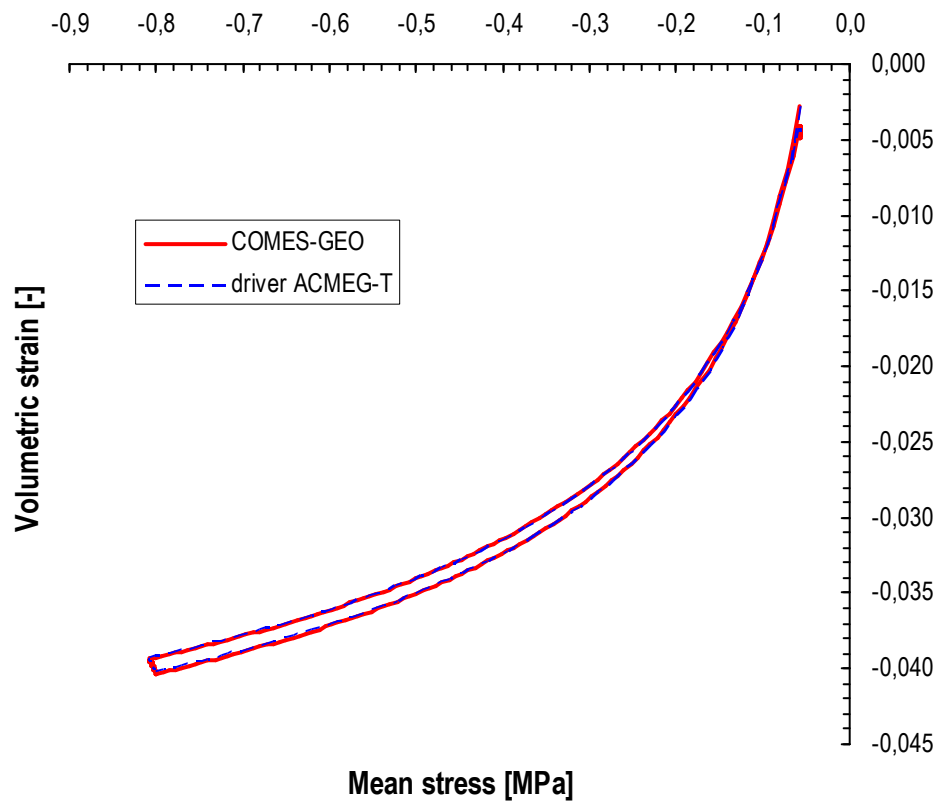


Figure 4.24: Mean stress and Deviatoric stress p-q

Figure 4.25: Mean stress and Volumetric strain p- ε_v

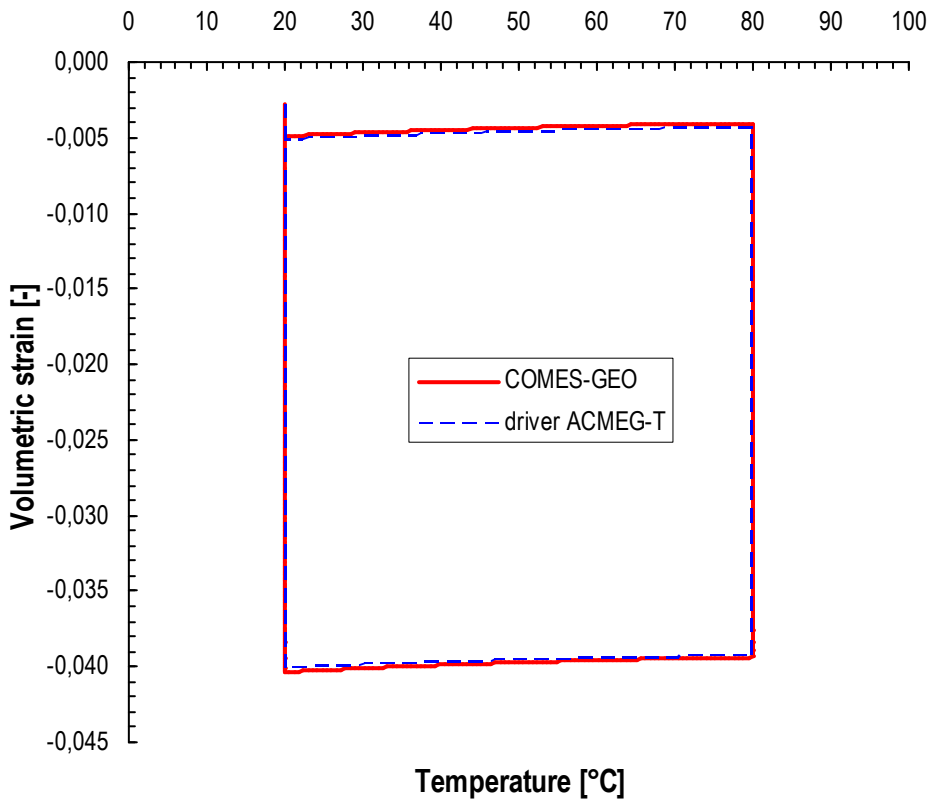


Figure 4.26: Temperature and Volumetric strain T- ϵ_v

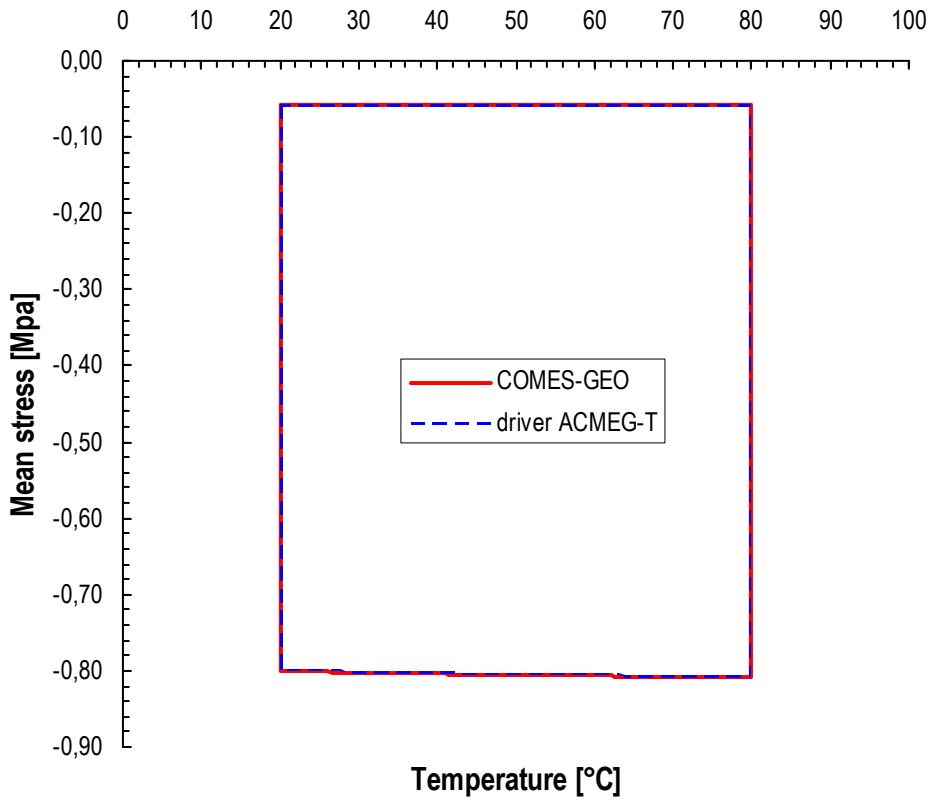


Figure 4.27: Temperature and Mean stress T-p

For the four cases, the linear elastic and the three non linear elastic, graph from Figure 4.12 to Figure 4.29 show the perfect agreement between the FEM results and the results of the drive ACMEG-T. Then, from which it follows that the validation of the elastic part of the model implemented has been obtained.

Moreover it can be noted the difference between the linear elastic and the non linear elastic behaviour in the graph $T-\varepsilon_v$, where for the non linear elasticity the final point at the end of the cycle is different from the starting point, due to the ipoelastic behaviour of the model because of the dependence on the elastic moduli and on the isotropic thermal expansion coefficient from the mean isotropic stress p' .

Another important aspect of this first analysis is the strong dependence of the volumetric strain on the parameters n_e and n_T as shown in Table 4.5.

	n_e	n_T	ε_v^{max}
Case 0	0.0	0.0	-0.0075
Case 1	1.0	0.2	-0.0285
Case 2	0.7	0.4	-0.0179
Case 3	1.0	0.0	-0.0403

Table 4.5: Maximum volumetric strain for the four elastic non linear analysis. The maximum volumetric strain is reached at the end of the mechanical load of 800 kPa (Point 2 of Figure 4.11)

4.4.3 Elastoplastic isotropic compression in isothermal condition

After the validation of the implementation of the elastic part of the model, the plastic one is studied by simulating a pure isotropic case (isotropic compression) in isothermal condition, and in non-isothermal condition to analyze the isotropic mechanism then by analyzing the deviatoric mechanism simulating triaxial tests.

The isotropic compression test consist in a double cycle of mechanical loading and unloading at constant temperature of 20°C, as shown in Figure 4.28, starting from an isotropic stress of 5 kPa.

The material parameters for this simulation are reported in the Table 4.6 and are the parameters of a silty sand deduced from the experimental test performed by Jamin [Jam03] (Figure 4.7).

Elastic parameters			
K_{ref} [MPa]	G_{ref} [MPa]	n_e	β'_{s0} [°C ⁻¹]
100.00	-	1.0	-
Isotropic plastic parameters			
β	c	r_{iso}^e	p'_c [kPa]
22.0	0.001	0.001	28.0

Table 4.6: Material parameters of the plastic isotropic compression

G_{ref} is not necessary for the analysis because the deviatoric mechanism is not activate by the isotropic test. The coefficient β'_s is not necessary because the test is in isothermal condition.

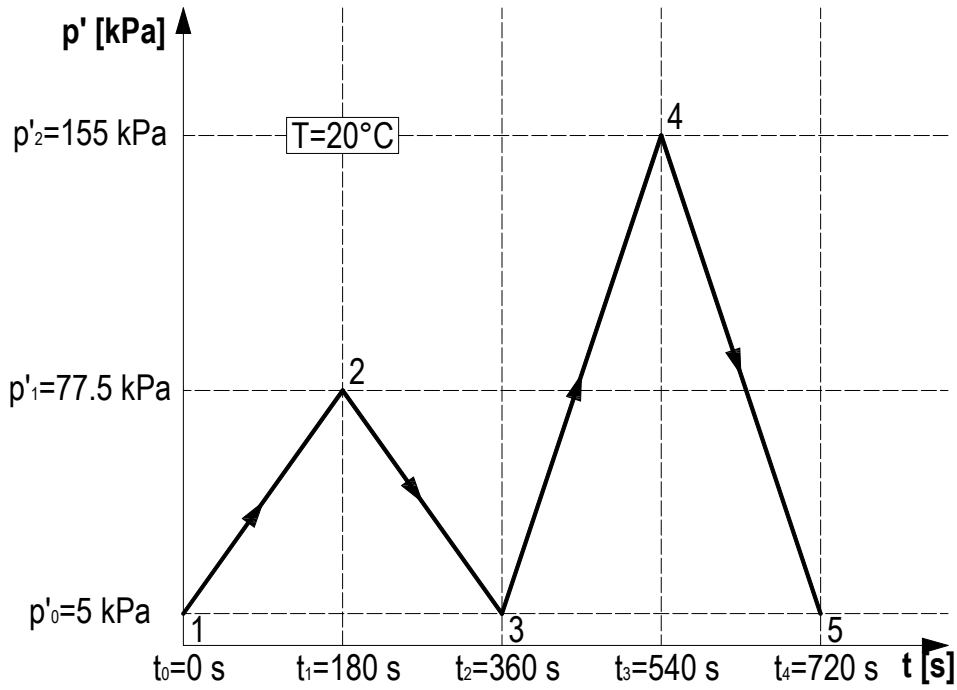


Figure 4.28: Mechanical loading and unloading path

The results of the simulations performed with the F.E. code and with the driver are shown in the $p-\varepsilon_v$ plane (Figure 4.29) where the good agreement of the results can be observed.

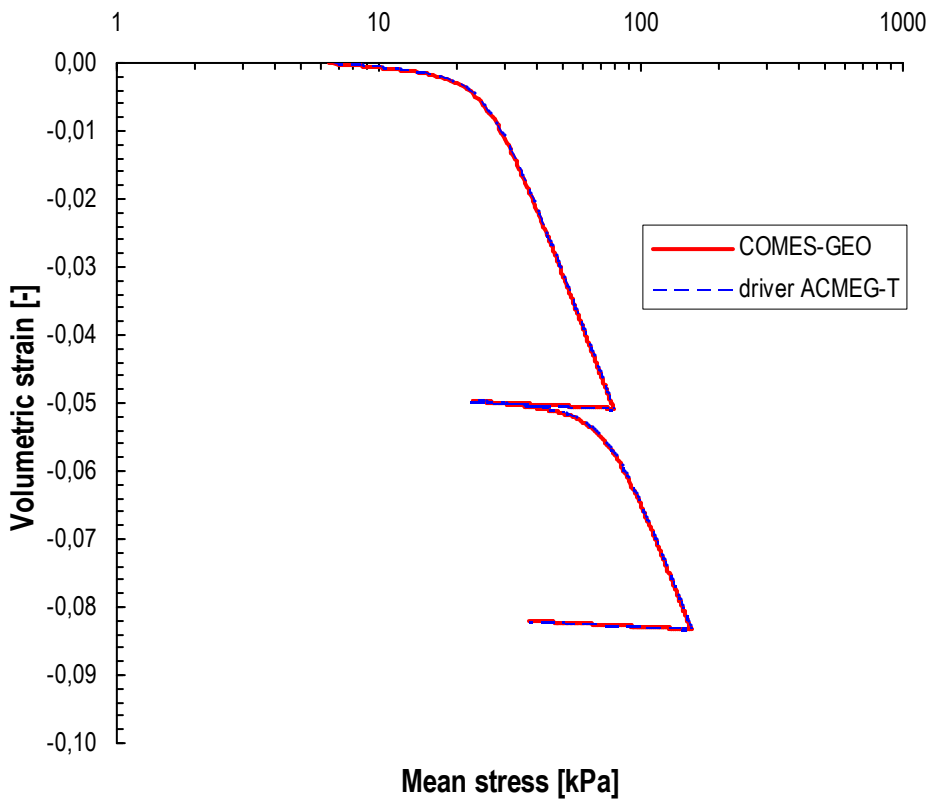


Figure 4.29: Mean stress and Volumetric strain $p-\varepsilon_v$

Moreover, in Figure 4.29 it is possible to compute the value of the material p'_c , κ and λ (see Figure 4.30) and the value of β .

In fact, from the relation of the volumetric strain ε_v from the void ratio e

$$\varepsilon_v = \frac{e_0 - e}{1 + e_0} \quad [4.60]$$

e_0 results as

$$e_0 = \frac{e + \varepsilon_v}{1 - \varepsilon_v} = 1.0677 \quad [4.61]$$

Hence from the plotted graph it is possible to compute κ and λ as

$$\kappa = (1 + e_0) \frac{\Delta x}{\ln \Delta y} = (1 + e_0) \frac{\varepsilon_v^n - \varepsilon_v^{n-1}}{\ln \left(\frac{p'^n}{p'^{n-1}} \right)} = 0.0026495 \quad [4.62]$$

$$\lambda = (1 + e_0) \frac{\Delta x}{\ln \Delta y} = (1 + e_0) \frac{\varepsilon_v^n - \varepsilon_v^{n-1}}{\ln \left(\frac{p'^n}{p'^{n-1}} \right)} = 0.0931369 \quad [4.63]$$

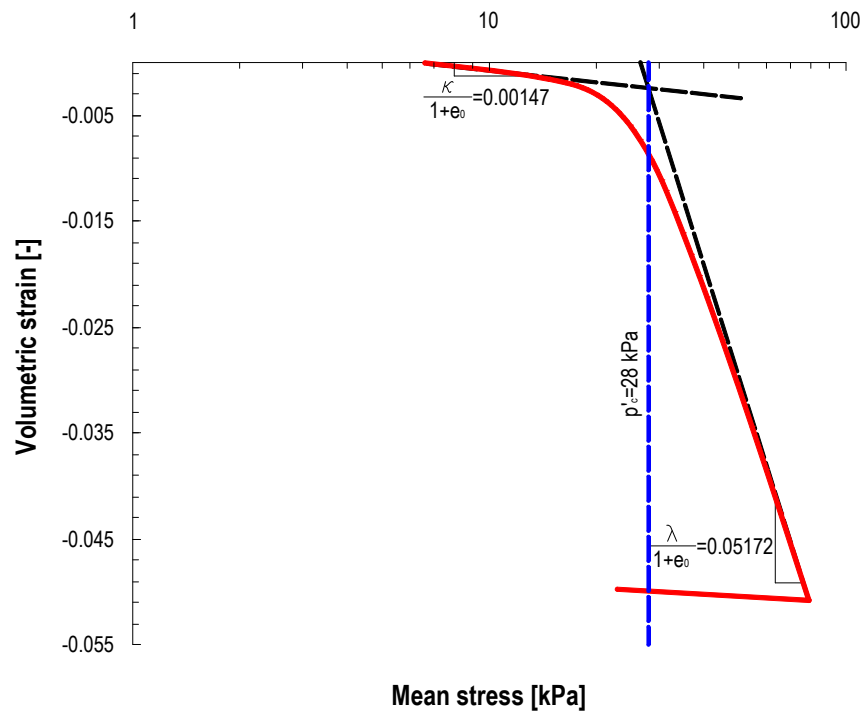


Figure 4.30: Graphic extrapolation of p'_c , κ and λ

From which the parameter β is

$$\beta = \frac{1 + e_0}{\lambda - \kappa} = 22.85 \quad [4.64]$$

similar to the value used in the simulation ($\beta = 22$).

The difference between the imposed value and the extrapolated one is due to the imprecision of the slope of the two lines of the graph due to the effect of the very small value of r_{iso}^e on the elastic and the plastic curves of Figure 4.30. Additionally the experimental test performed by Jamin [Jam03] was simulated and the results of the numerical simulations are showed together with the experimental results (Figure 4.31).

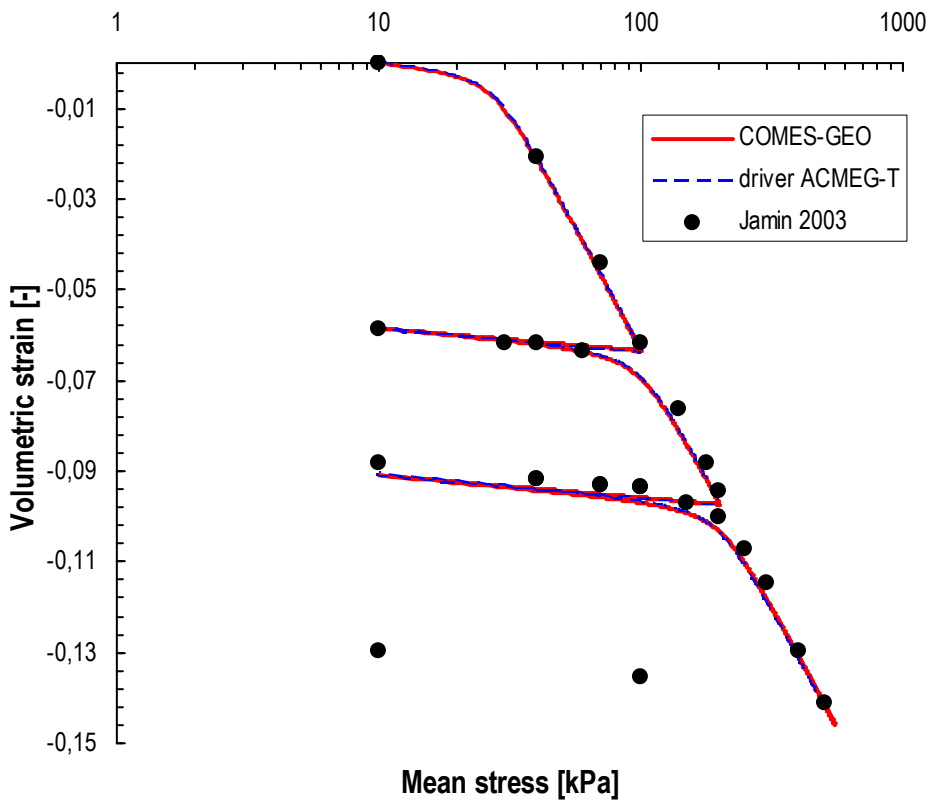


Figure 4.31: Comparison between numerical results by COMES-GEO and driver ACMEG-T and experimental results by Jamin [Jam03]

Also for this simulation, as for the elastic one, the finite element results of COMES-GEO coincide with those of the driver ACMEG-T.

From the simulations of sections 4.4.2 and 4.4.3 it can be concluded that the isotropic mechanism is validate.

4.4.4 Elastoplastic triaxial compression in isothermal condition

This analysis consists in a triaxial compression test obtained by applying vertical deformation from 0% to 30% in a normally consolidated clay the constant temperature of 20°C.

As seen for the sections 4.4.2 and 4.4.3, the results of the two simulation, Finite Elements simulation with COMES-GEO and driver simulation with ACMEG-T, coincide.

Hence, the implementation of ACMEG-T model in COMES-Geo is validated for both the mechanisms in isothermal condition.

Elastic parameters			
K_{ref} [MPa]	G_{ref} [MPa]	n_e	β'_{s0} [°C ⁻¹]
131.30	78.66	1.0	-
Isotropic plastic parameters			
β	c	r_{iso}^e	p'_c [kPa]
43.7	-	-	800.00
Deviatoric plastic parameters			
b	d	ϕ'_0 [°]	r_{dev}^e
1.0	2.0	25	1.0

Table 4.7: Material parameters of the elastoplastic triaxial compression

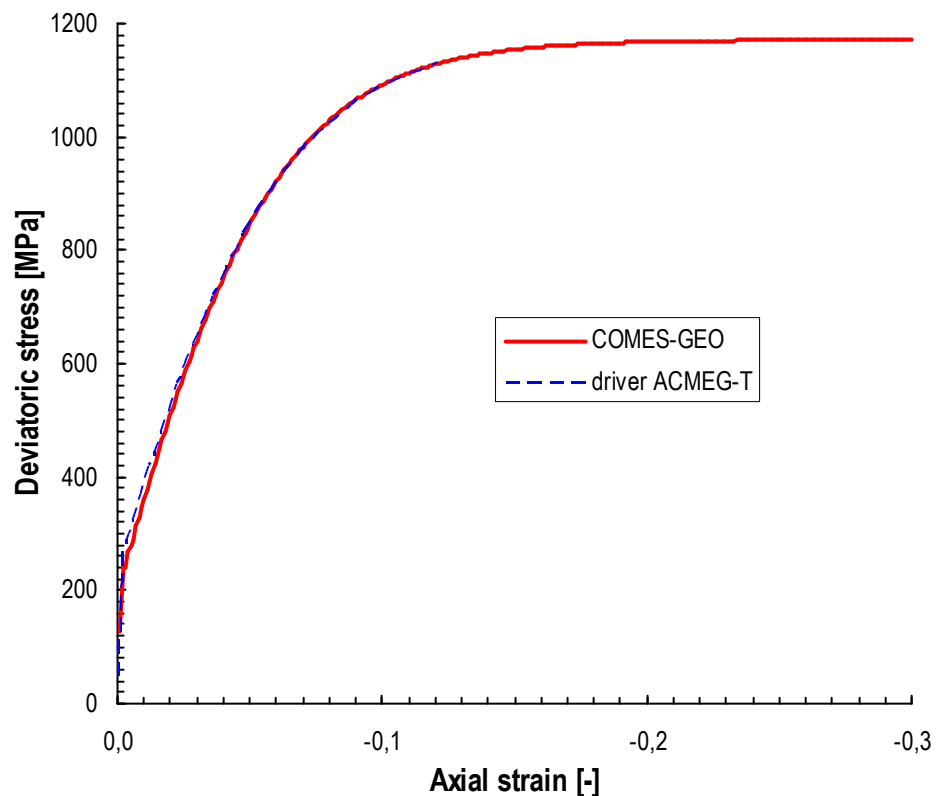


Figure 4.32: Axial strain and Deviatoric stress ε_{1-q}

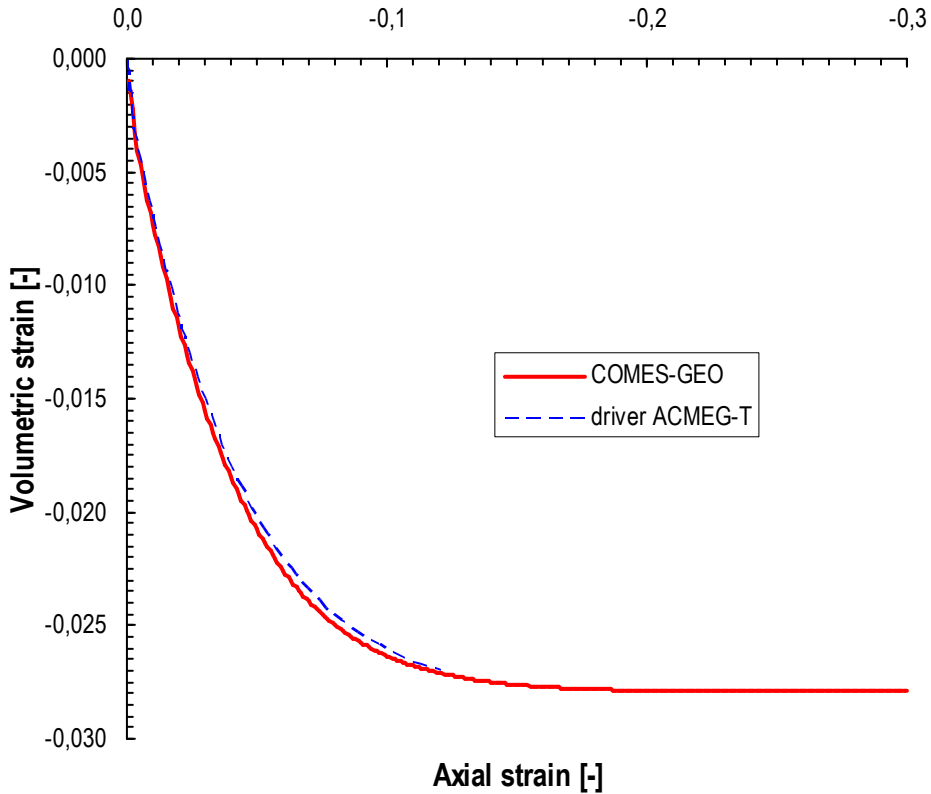


Figure 4.33: Axial strain and Volumetric strain $\varepsilon_1-\varepsilon_v$

Therefore, the next analysis will be done with the aim to validate the model in non-isothermal conditions.

4.4.5 Elastoplastic isotropic compression in non-isothermal condition

For the validation of the isotropic mechanism in non-isothermal conditions, an isotropic compression is performed by applying a thermal cycle. Starting from the ambient temperature of 21.5 °C, the sample is heated until the temperature of 95 °C and then cooled until the initial temperature, 21.5 °C (Figure 4.34).

The material parameters are reported in the Table 4.8 and are those of a Boom clay.

Elastic parameters				
K_{ref} [MPa]	G_{ref} [MPa]	n_e	β'_{s0} [°C ⁻¹]	
150.00	130.00	0.4	$3.0 \cdot 10^{-5}$	
Isotropic plastic parameters				
β	c	r'_{iso}	p'_c [MPa]	γ_T
47.0	0.0004	0.01	6.0	0.18

Table 4.8: Material parameters of Boom clay

The test is repeat for three times for three different degree of consolidation: OCR=1, OCR=2 and OCR=6.

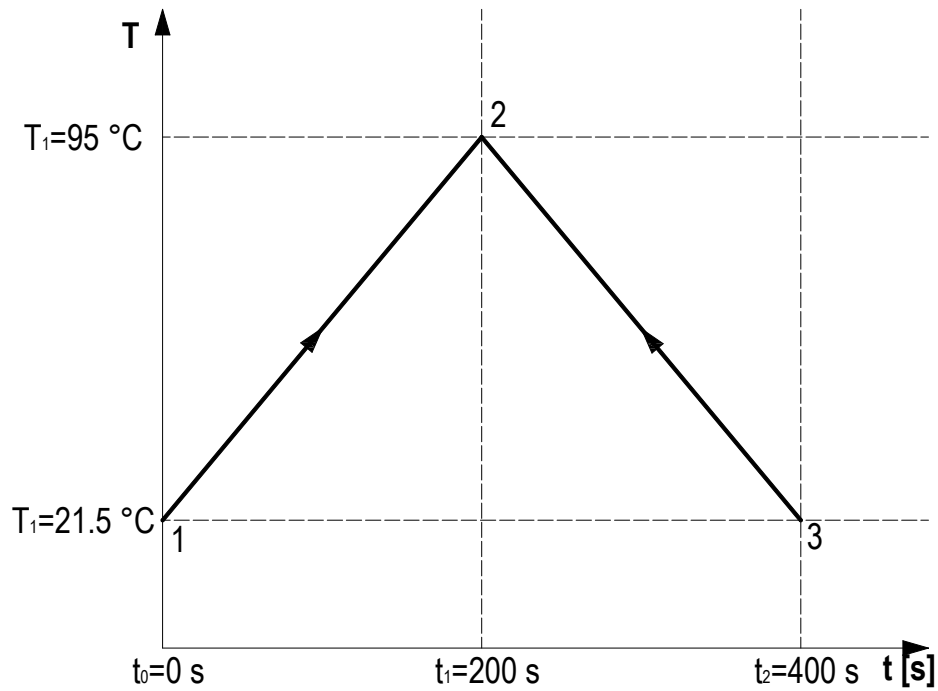


Figure 4.34: Thermal path of heating and cooling

The results of the simulation are shown in the ε_v-T plane, three simulation are shown in Figure 4.35 to outline the behaviour of normal consolidated clay (OCR=1) that contracts with the increase of temperature, while on the contrary, the overconsolidate clay (OCR=6) dilates. Figure 4.35 show also the other main aspect of the behaviour of clays under heating which is the irreversible dilatant deformation for NC clays.

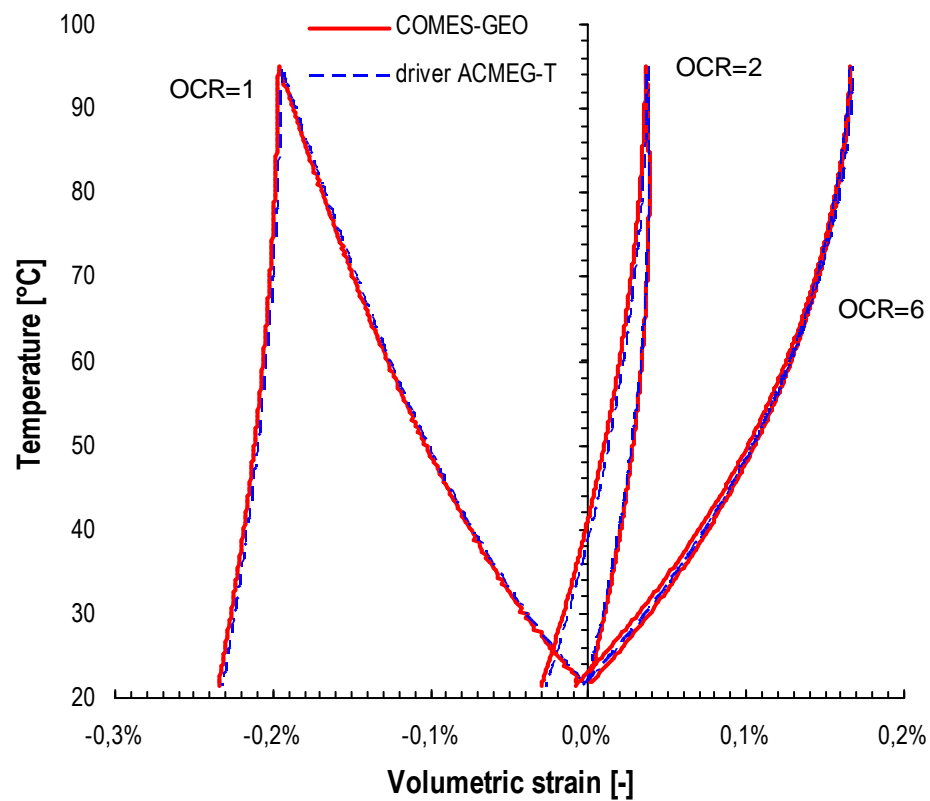


Figure 4.35: Volumetric strain and Temperature ε_v-T

In the following graph there is the comparison between the results of the finite element simulation with COMES-GEO and the experimental results obtained by Baldi [Bal91] on Boom clay for OCR=1 and OCR=2.

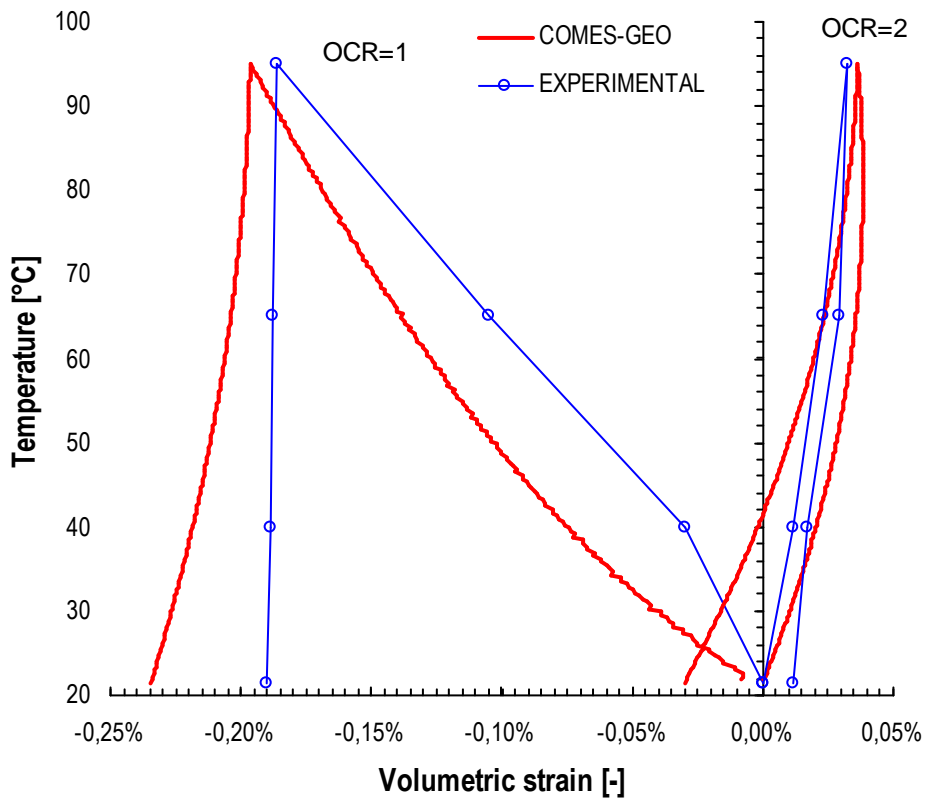


Figure 4.36: Comparison between finite element COMES-GEO and experimental results obtained by Baldi et al. [Bal91] on Boom clay for OCR=1 and OCR=2

4.5 A NON ISOTHERMAL CONSOLIDATION EXAMPLE†

In this section a case of non-isothermal elastic and elasto-plastic consolidation is studied.

The following example aims to validate the finite element formulation solving an initial boundary value problem. It deals with the simulation of a non-isothermal fully saturated consolidation problem, for which the numerical solution of the linear thermo-mechanical problem is known [Abo85].

A column of 7 m height and 2 m width is subjected to an external surface compressive load of 1.0 kPa and to a surface temperature jump of 50 K above the initial ambient temperature of 293.15 K. The material is initially water saturated. The upper surface is drained ($p^w = 0$ Pa); the lateral and the bottom surfaces are insulated. Horizontal displacements are constrained along the vertical boundaries and vertical displacements are constrained at the bottom surface. The column is discretized by nine eight-node isoparametric elements Figure 4.37. Furthermore, 3×3 Gauss integration points are used. The material parameters used in the computation are listed in Table 4.9. Gravity forces are taken into account. Plane strain conditions are assumed.

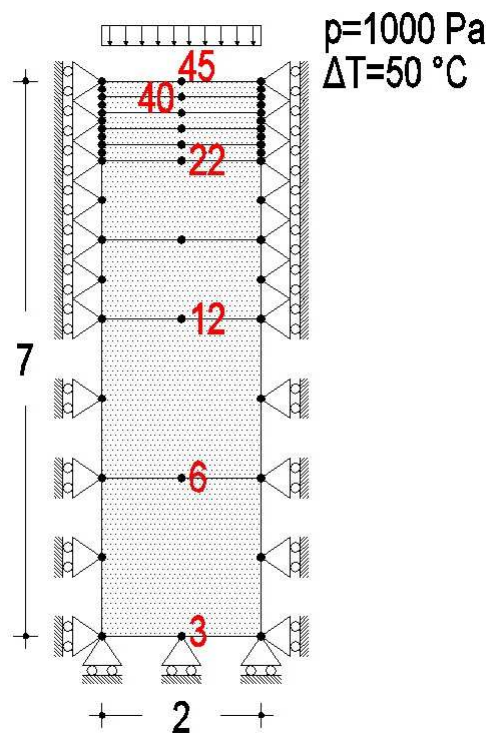


Figure 4.37: Spatial discretization and boundary conditions for the non-isothermal consolidation example

† This section is reproduced from: Sanavia L., François B., Bortolotto R., Luison L., Laloui L. (2008). Finite element modelling of thermo-elasto-plastic water saturated porous materials. *Journal of Theoretical and Applied Mechanics*, 38, 1-2, pp 7-34.

Elastic parameters						
K_{ref} [MPa]	G_{ref} [MPa]	n_e	β'_{s0} [°C ⁻¹]			
10.0	2.14	0	$9.0 \cdot 10^{-7}$			
Isotropic plastic parameters						
β	c	r_{iso}^e	p'_c [kPa]	γ_T		
20.0	0.001	0.001	800.00	0.2		
Diffusive law parameters						
ρ^s [kg/m ³]	n	κ [m ²]	λ_s [W/(m·K)]	c_s [J/(kg·K)]	λ_w [W/(m·K)]	c_w [J/(kg·K)]
2000	0.2	$4.6 \cdot 10^{-17}$	0.84	16760	0.6	4181

Table 4.9: Material parameters for Aboustit example

The case studied in [Abo85], which assumed constant Young modulus ($E = 6.0$ MPa) and Poisson ratio ($\nu = 0.4$) and constant cubic thermal expansion coefficient, is here used as validation example. To this aim, the results of [Abo85] as published in [L&S98] and labelled “Aboustit” in the Figure 4.38 to Figure 4.43, are used to compare the solution obtained with the finite element formulation proposed in this chapter and labelled “COMES-GEO”. The time histories for the water pressure (Figure 4.38), the temperature (Figure 4.39) and the vertical displacement (Figure 4.40) of several nodes of the mesh show the coincidence of the two solutions. The linear behaviour of the thermo-mechanical problem adopting the ACMEG-T model is obtained by using the mechanical moduli independent of the stress state ($n^e = 0$).

As shown all along the present chapter, soils are often subject to irreversible processes induced by thermal effect. In this context, the last simulation extends the problem of Figure 4.37 towards elasto-thermoplastic analysis. The material parameters are listed in Table 4.9, where it can be observed that the linear elasticity is kept for comparison with the previous simulation; thermo-plasticity is introduced by reducing the preconsolidation pressure to get a mechanical and thermal hardening when loaded to 1kPa and introducing the decrease of the isotropic yield surface with temperature.

The comparison between the elastic and the elasto-plastic solution shows that the inclusion of the plasticity effects delays the dissipation of pore water pressure in time (Figure 4.41), because of the reduced thermo-plastic stiffness of the solid skeleton with respect to the elastic one. Moreover, the predicted water pressures at the same time station are therefore higher than those from the elastic analysis.

Temperature evolution is almost not modified with respect to the previous simulation, as it can be observed in Figure 4.42. Indeed, because parameters of thermal conduction and convection are almost independent on porosity changes, at least for this range of volumetric strain, [2.190] remains almost unaffected by mechanical change. On the contrary, the time history for the vertical displacements appears to be strongly affected by the thermo-plastic behaviour of the solid skeleton. In particular, an increase of two order of magnitude for the vertical displacements is observed in Figure 4.43, that makes negligible the thermal component that can be observed in Figure 4.40.

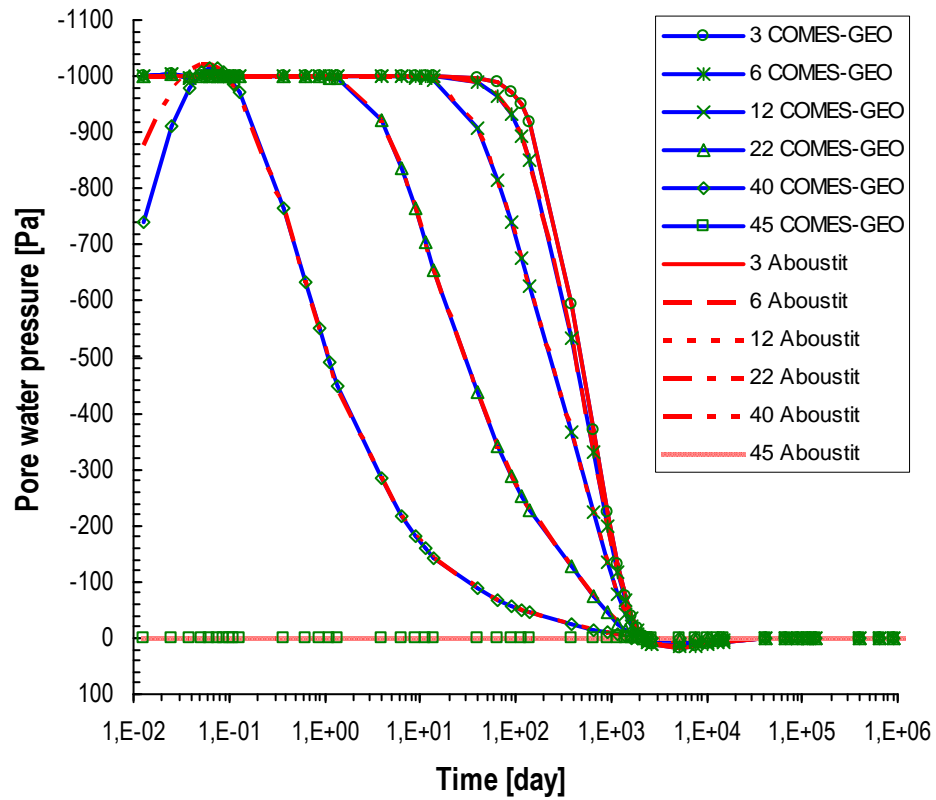


Figure 4.38: Elastic case: Evolution of pore water pressure

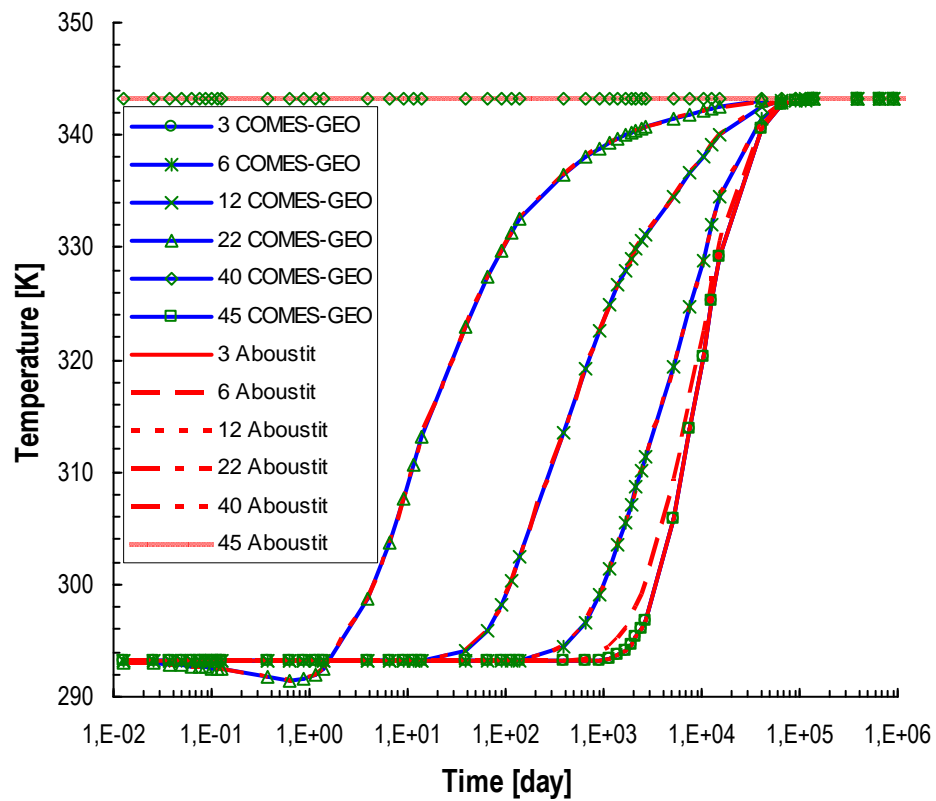


Figure 4.39: Elastic case: Evolution of temperature

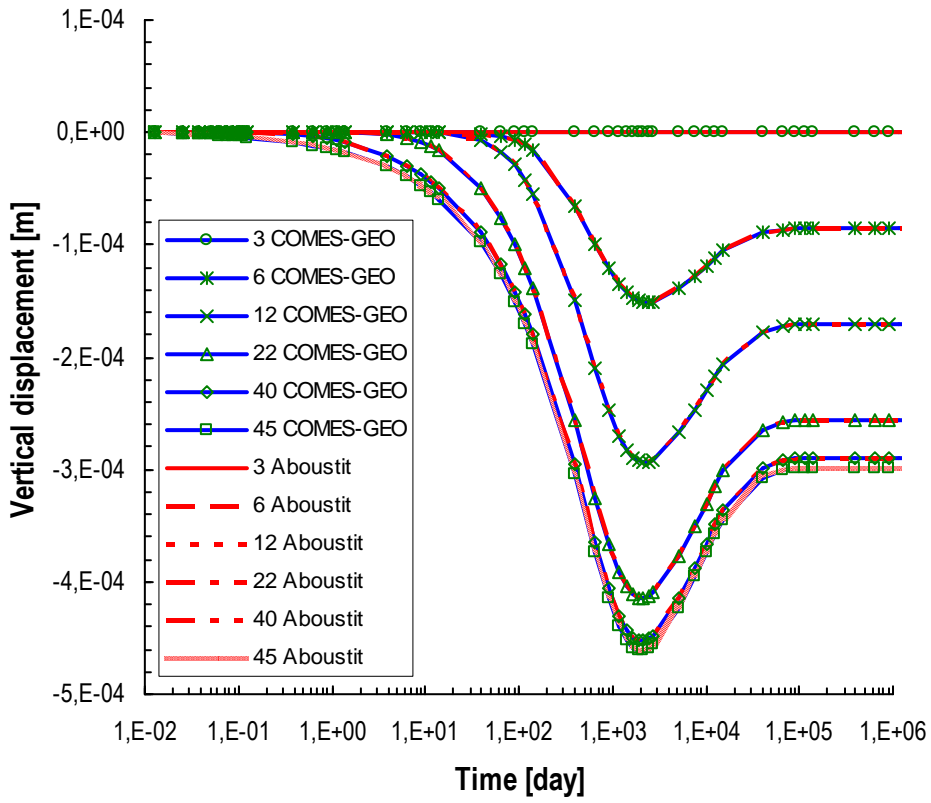


Figure 4.40: Elastic case: Evolution of vertical displacement

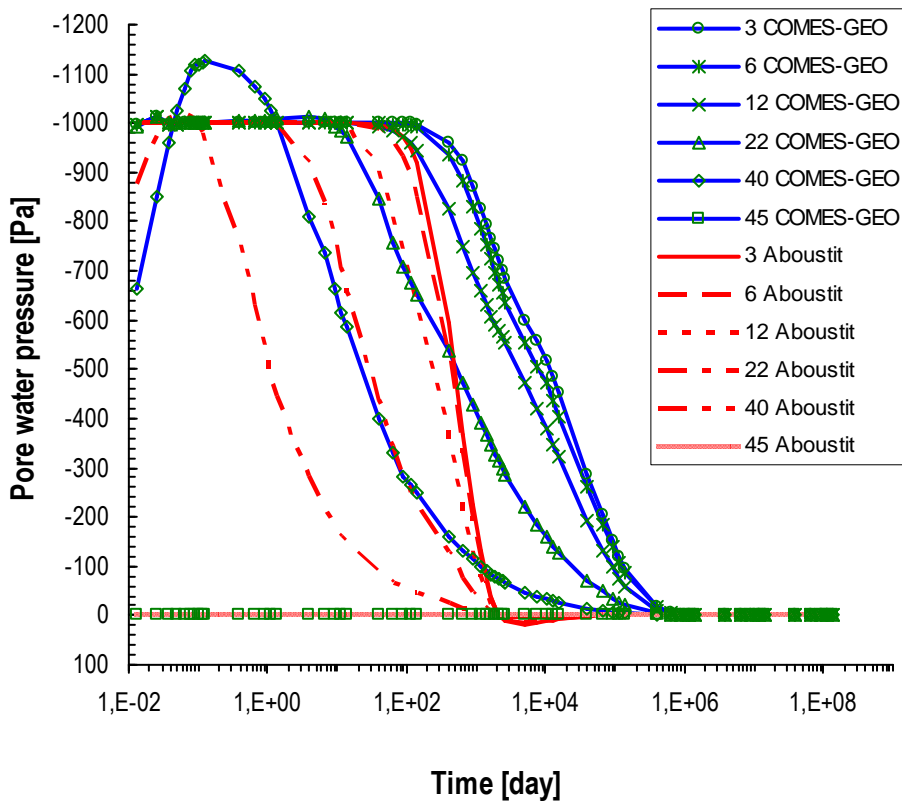


Figure 4.41: Elastoplastic case: Evolution of pore water pressure

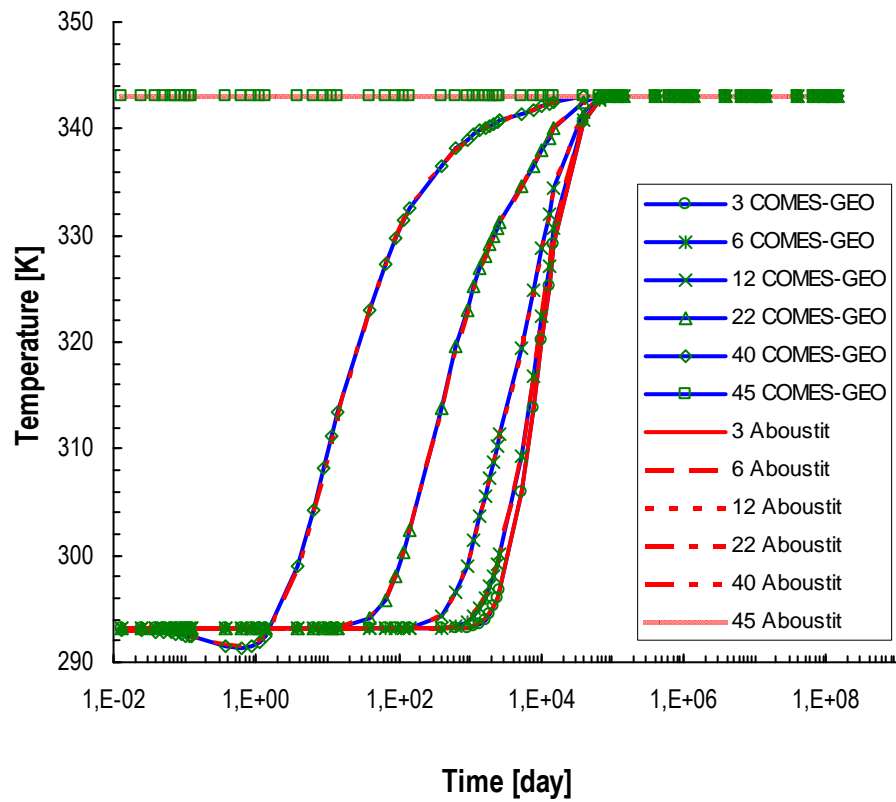


Figure 4.42: Elastoplastic case: Evolution of temperature

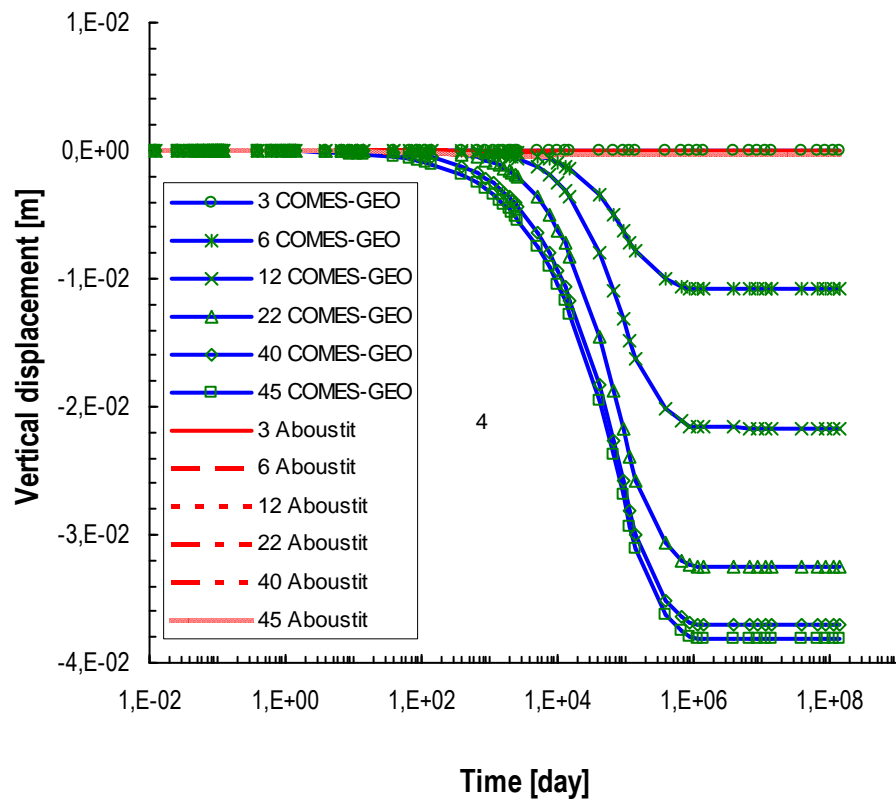


Figure 4.43: Elastoplastic case: Evolution of vertical displacement

References

- [Abo85] Aboustit B.L., Advani S.H. and Lee J.K. (1985). Variational principles and finite element simulations for thermo-elastic consolidation. *International Journal for Numerical and Analytical Methods in Geomechanics*, 9: 49-69.
- [A-N05] Abuel-Naga H.M. (2005). Thermo-mechanical behaviour of soft Bangkok Clay: experimental results and constitutive modelling. PhD Thesis, Asian Institute of Technology, Bangkok, Thailand.
- [A-N06] Abuel-Naga H.M., Bergado D.T., Ramana G.V., Grino L., Rujivipat P. and Thet Y. (2006). Experimental evaluation of engineering behaviour of soft Bangkok clay under elevated temperature. *Journal of Geotechnical and Geoenvironmental Engineering*, 132(7): 902-910.
- [A-N07] Abuel-Naga H.M., Bergado D.T. and Bouazza A. (2007). Thermally induced volume change and excess pore water pressure of soft Bangkok clay. *Engineering Geology*, 89(1-2): 144-154.
- [Bal91] Baldi G., Hueckel T., Peano A. and Pellegrini R. (1991). Developments in modelling of thermohydro-mechanical behaviour of Boom clay and clay-based buffer materials (Vol 1 and 2). EUR 13365/1 and 13365/2, Luxembourg.
- [Bur00] Burghignoli A., Desideri A. and Miliziano S. (2000). A laboratory study on the thermomechanical behaviour of clayey soils. *Canadian Geotechnical Journal*, 37: 764-780.
- [C&L04] Cekerevac C. and Laloui L. (2004). Experimental study of thermal effects on the mechanical behaviour of a clay. *International Journal for Numerical and Analytical Methods in Geomechanics*, 28(3): 209-228.
- [C&M68] Campanella R.G. and Mitchell J.K. (1968). Influence of temperature variations on soil behaviour. *Journal of the Soil Mechanics and Foundation Division, ASCE*, 94: 709-734.
- [Cek03] Cekerevac C. (2003). Thermal effect on the mechanical behaviour of saturated clays: an experimental and constitutive study. PhD Thesis. École Polytechnique Fédérale De Lausanne. Suisse.
- [D&C82] Demarks K.R. and Charles R.D. (1982). Soil volume changes induced by temperature cycling. *Canadian Geotechnical Journal*, 19: 188-194.
- [DeO96] Del Olmo C., Fioravante V., Gera F., Hueckel T., Mayor J.C. and Pellegrini R. (1996). Thermomechanical properties of deep argillaceous formations. *Engineering Geology*, 41: 87-102.
- [Fra08] François B. (2008). Thermo-Plasticity of Fine-Grained Soils at Various Saturation States: Application to Nuclear Waste Disposal. PhD Thesis. École Polytechnique Fédérale De Lausanne. Suisse.
- [H&P89] Hueckel T. and Pellegrini R. (1989). Modelling of thermal failure of saturated clays. *International Symposium on Numerical Models in Geomechanics – NUMOG*: 81-90.
- [Hue98] Hueckel T., Pellegrini R. and Del Olmo C. (1998). A constitutive study of thermo-elasto-plasticity of deep carbonatic clays. *International Journal of Numerical and Analytical Methods in Geomechanics*, 22: 549-574.
- [Huj79] Hujieux J.C. (1979). Calcul numérique de problèmes de consolidation élastoplastique. PhD Thesis, Ecole Centrale, Paris.
- [Huj85] Hujieux J.C. (1985). Une loi de comportement pour le chargement cyclique des sols. *Génie Parasismique*, Les éditions de l'E.N.P.C., Paris: 287-303.
- [Jam03] Jamin F. (2003). Contribution à l'étude du transport de matière et de la rhéologie dans les sols non saturés à différentes températures. PhD Thesis. Université Montpellier II.

-
- [Kin76] Kingery W.D, Bowen H.K. and Uhlmann D.R. (1976). Introduction to Ceramics, 2nd Edition. Wiley, New York.
- [Kun95] Kuntiwattanakul P., Towhata I., Ohishi K. and Seko I. (1995). Temperature effects on undrained shear characteristics of clay. *Soils and Foundations*, 35(1): 147-162.
- [L&C03] Laloui L. and Cekerevac C. (2003). Thermo-plasticity of clays: An isotropic yield mechanism, *Computers and Geotechnics*, 30(8): 649-660.
- [L&C08] Laloui L. and Cekerevac C. (2008). Non-isothermal plasticity model for cyclic behaviour of soils. *International Journal for Numerical and Analytical Methods in Geomechanics*, 32(5): 437-460.
- [L&F08] Laloui L. and François B. (2009) ACMEG-T: A soil thermo-plasticity model. *Journal of Engineering Mechanics*. DOI: 10.1061/(ASCE)EM.1943-7889.0000011.
- [L&S98] Lewis R.W. and Schrefler B.A. *The Finite Element Method in the Static and Dynamic Deformation and Consolidation of Porous Media*. J. Wiley, Chichester 1998.
- [Lal01] Laloui L. (2001). Thermo-mechanical behaviour of soils. *Environmental Geomechanics*. EPFL Press, Lausanne: 809-843.
- [Lal05] Laloui L., Cekerevac C. and François B. (2005) Constitutive modelling of the thermo-plastic behaviour of soils. *Revue Européenne de Génie Civil*, 9(5-6): 635-650.
- [Lal93] Laloui L. (1993). Modélisation du comportement thermo-hydro-mécanique des milieux poreux anélastique. PhD Thesis, Ecole Centrale de Paris.
- [M&L97] Modaressi H. and Laloui L. (1997). A thermo-viscoplastic constitutive model for clays. *International Journal for Numerical and Analytical Methods in Geomechanics*, 21(5): 313–315.
- [N&W79] Nova R. and Wood D.M. (1979). A constitutive model for sand in triaxial compression. *International Journal for Numerical and Analytical Methods in Geomechanics*, 3: 255–278.
- [Pra49] Prager W. (1949). Recent developments in mathematical theory of plasticity. *Journal of Applied Physics*, 20(3): 239-241.
- [Pra58] Prager W. (1958). Non-isothermal plastic deformation. *Koninklijk-Nederland Akademie Van Wetenschappen Te Amsterdam - Proceedings of the section of sciences- B*, 61, 176-182.
- [Pus87] Pusch R. (1987). Permanent crystal lattice contraction, primary mechanism in thermally induced alteration of Na-bentonite. *Scientific Basis for Nuclear Waste Management X*. MRS, Pittsburgh, 84: 792-802.
- [Riz96] Rizzi E., Maier G. and Willam K. (1996). On failure indicators in multi-dissipative materials. *International Journal of Solids and Structures*, 33(20-22): 3187-3214
- [San08] Sanavia L., François B., Bortolotto R., Luison L., Laloui L. (2008). Finite element modelling of thermo-elasto-plastic water saturated porous materials. *Journal of Theoretical and Applied Mechanics*, 38, 1-2, pp 7-34.

5 THE THERMO-HYDRO-ELASTO-PLASTIC CONSTITUTIVE MODEL ACMEG-TS

5.1 PARTIAL SATURATION IN SOIL

Most soils in nature are in condition of partial saturation, and hence is of fundamental importance the development of constitutive model able to take into account the effects of this state.

As explained in the previous sections, the soils are composed by a solid porous skeleton with voids. The voids can be filled with water, and soils are said fully saturated, or can be filled with water and air, and soils in this case are defined as unsaturated or partially saturated. If in a saturated soil the pore fluid pressure can generally be assumed as a neutral stress, on the contrary, under unsaturated conditions, a new internal stress, namely the suction, s , or the capillary pressure, p^c , (seen in chapter 2), plays a significant role in the behaviour of unsaturated soils and must be, directly or indirectly, considered in the formulation of the stress-strain relationship. The relative amounts of the pore air and pore water phases play a key role in the mechanical properties of the unsaturated soils. This proportion, usually defined by the degree of saturation, S_w , should be considered, directly or indirectly, in the complete description of the hydro-mechanical soil state.

The degree of saturation is defined as (see 2.6.1):

$$S_w = \frac{dv^w}{dv^w + dv^g} \quad [5.1]$$

where dv^w is the volume of voids filled with water

dv^g is the volume of voids filled with the air phase, that can be assumed to be a mixture of dry air and vapour

S_w is connected to the p^c through experimental laws that was proposed during the years from some authors as shown in 5.3.

As seen in 2.6, for unsaturated soils we need of an appropriate definition of the effective stress.

Starting from the well known relationship by Terzaghi [Ter36]

$$\sigma'_{ij} = \sigma_{ij} - p^w \delta_{ij} \quad [5.2]$$

the effective stress σ'_{ij} must used for unsaturated soils has been proposed by Bishop [2.155] is

$$\sigma'_{ij} = \sigma_{ij} - p^g \delta_{ij} + \chi(p^g - p^w) \delta_{ij} = \sigma_{net,ij} + \chi \cdot p^c \delta_{ij} \quad [5.3]$$

where $\sigma_{net,ij} = \sigma_{ij} - p^g \delta_{ij}$

$$p^c = p^g - p^w$$

As shown in 2.6.1, equation [2.162], we assume that

$$\chi = S_w \quad [5.4]$$

as proposed by Schrefler [Sch84].

Others authors proposed expressions for χ which depend on a suction ratio rather than on the degree of saturation [Ait60] [K&K98]. From a micromechanical standpoint, theoretical approaches were also developed to evaluate the χ parameter by examining the forces and fluid pressures that arise in unsaturated soils with idealized soil particles. That kind of analysis shows that the shape and the arrangement of grains, as well as the contact angle at the solid-liquid interface, may have a significant impact on the behaviour of the χ parameter [L&L04].

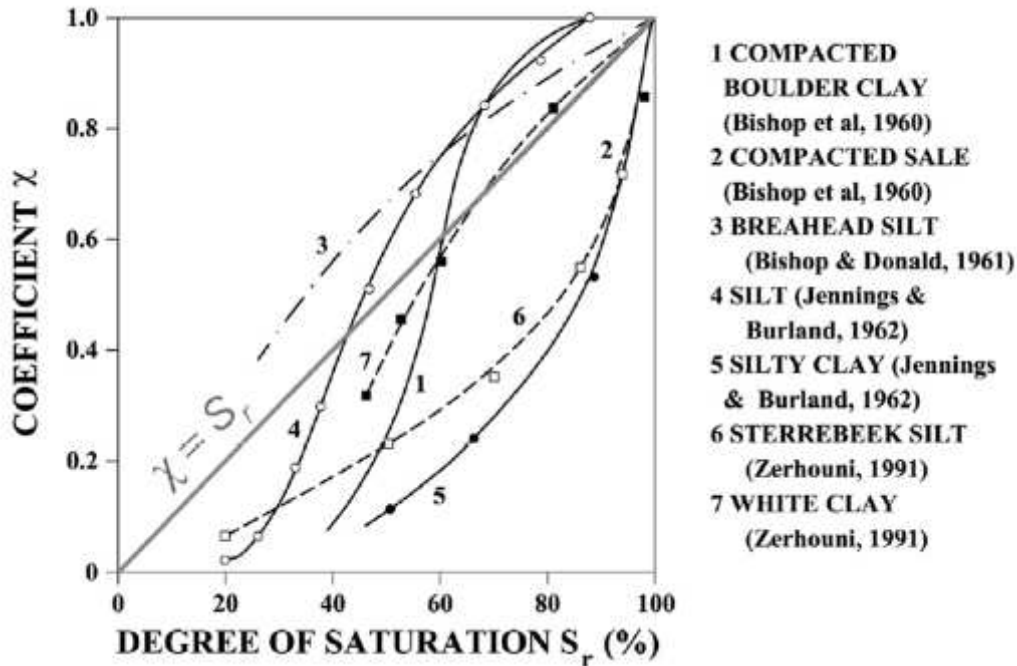


Figure 5.1: Effective stress parameter with respect to the degree of saturation for various soils, as reported in [Zer91]. Here S_r is the notation used for the degree of saturation. (Redrawn from [Fra08]).

5.1.1 Mechanical behaviour

This section presents the stress-strain behaviour of unsaturated soils under isothermal conditions [Fra08]. It will be shown that the mechanical response of partially saturated soils is significantly affected by the soil suction. The characterization of the mechanical response of unsaturated soils depends strongly on the stress reference used in the representation of the experimental results. The curves obtained from laboratory tests are usually displayed according to net stresses because they are the direct data monitored during the experiments. This provides a consistent framework to analyse the obtained results. However, the pseudo-effective stress approach may bring substantial clarification to some observed features of soil behaviour. Therefore, where possible in this section, the experimental results will be presented using the Bishop-type effective stress with $\chi = S_w$, called the generalized effective stress (Nuth and Laloui [N&L08]), in parallel with the net stress. This interpretation is possible only if the water retention information is available.

5.1.1.1 Effect of suction on the compressive behaviour in isothermal conditions

The apparent preconsolidation pressure increases remarkably upon desaturation. This increase of the elastic domain with suction is narrowly linked to capillary effects. During a consolidation process, the yield limit corresponds to the

stress level that begins to produce a rearrangement of particles. As suction increases, air enters in pores and the menisci that form at the air-water interface stabilize the particle-particle contact. This stabilizing effect pushes back the soil yielding limit.

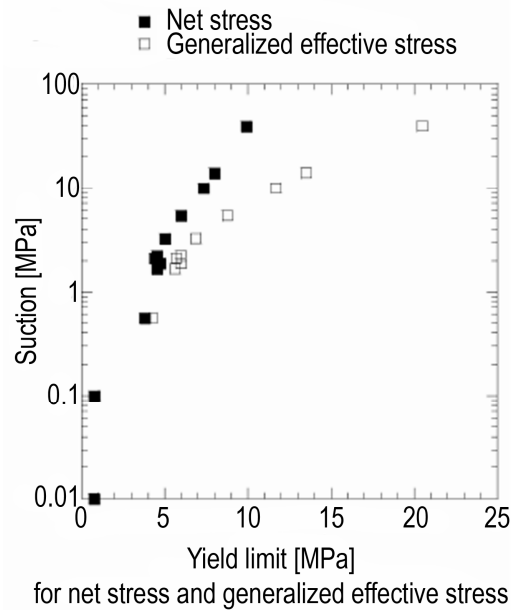


Figure 5.2: Evolution of the yielding limit with respect to suction determined from oedometric compression tests on compacted Boom clay at ambient temperature [Rom99] (redrawn from [Fra08])

Figure 5.2 shows the evolution of the preconsolidation pressure with suction, as determined from compression tests on compacted Boom clay in both net stress and generalized effective stress [Rom99]. The evolution of the preconsolidation pressure appears to be rapid for low values of suction and then becomes asymptotic for higher ones. The Figure 5.2 also shows that the increase in the elastic limit is noticeable only for suction higher than a given limit suction, the air-entry suction, which is the capillary pressure value at which air begins to enter the pores. Above this limit, a logarithmic function might be suitable to model this phenomenon. Based on its similarity with the temperature effect and the evolution law proposed by Laloui and Cekerevac [L&C03], Nuth and Laloui [N&L07] proposed the same logarithmic formulation to quantify the one-to-one relationship between suction and the preconsolidation pressure in the generalized effective stress reference:

$$\begin{aligned}
 s \leq s_e &\Rightarrow p'_c(s) = p'_{c0} \\
 s > s_e &\Rightarrow p'_c(s) = p'_{c0} \left(1 + \gamma_s \log\left(\frac{s}{s_e}\right) \right)
 \end{aligned}
 \tag{5.5}$$

where p'_{c0} is the preconsolidation pressure at saturation

$p'_c(s)$ is the preconsolidation pressure at a given suction s

s_e is the air-entry suction

γ_s is a material parameter

In the saturated domain (i.e. for suction lower than the air-entry suction value), equation [5.5] assumes that a positive suction can take place without affecting directly the preconsolidation pressure, which remains equal to its value in fully saturation condition, provided that no volumetric plastic strains are produced during the suction evolution.

Figure 5.3 shows the logarithmic law [5.5] compared with the experimental data referred to two different soil type.

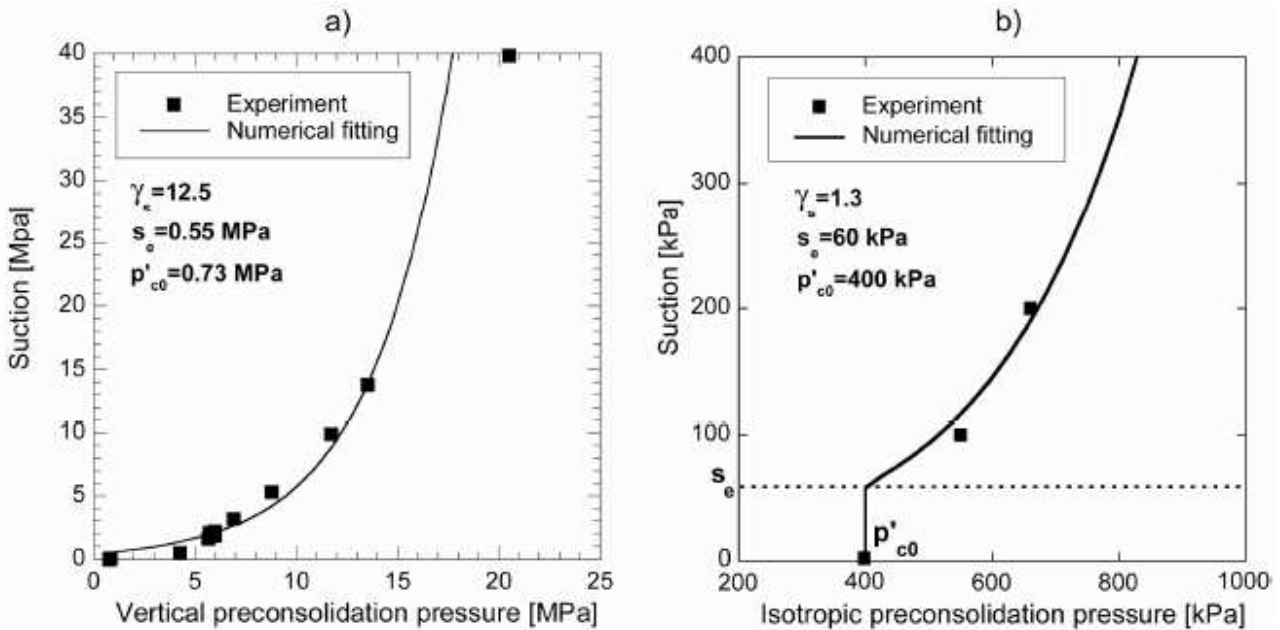


Figure 5.3: Comparison between experimental data and value predicted by the law [5.5]. a) Oedometric test on Boom clay [Rom99] b) Isotropic compression test on Sion silt [Gei99]. (Redrawn from [Fra08]).

5.1.1.2 Effect of suction on the compressive behaviour in non-isothermal conditions

In addition to the observed behaviour of unsaturated soils at ambient temperature and of saturated soils under non-isothermal conditions, some coupled effects between suction and temperature arise in soils when unsaturated and non-isothermal conditions are simultaneously met. These interactions must be considered in the development of constitutive models in order to cover the range of thermo-hydro-mechanical couplings occurring in fine-grained soils. These coupling effects, experimentally observed on compression and wetting-drying paths, are described in the following sections.

From experimental programs studying the thermal and the suction effects on the compressive behaviour of soils separately, the experimental results clearly show a decrease of the preconsolidation pressure with temperature and an increase with suction.

However, the combined effects of temperature and suction on the preconsolidation pressure lacks of confirmation. On compacted Boom clay loaded under oedometric conditions, Romero [Rom99] noticed a very small effect due to temperature, regarding the suction effect, on the evolution of the preconsolidation pressure (Figure 5.4 a). However, the results confirm the usual decreases of p'_c with temperature and its increases with suction. Tang et al. [Tan08] observed similar behaviour on MX80 bentonite (Figure 5.4 b).

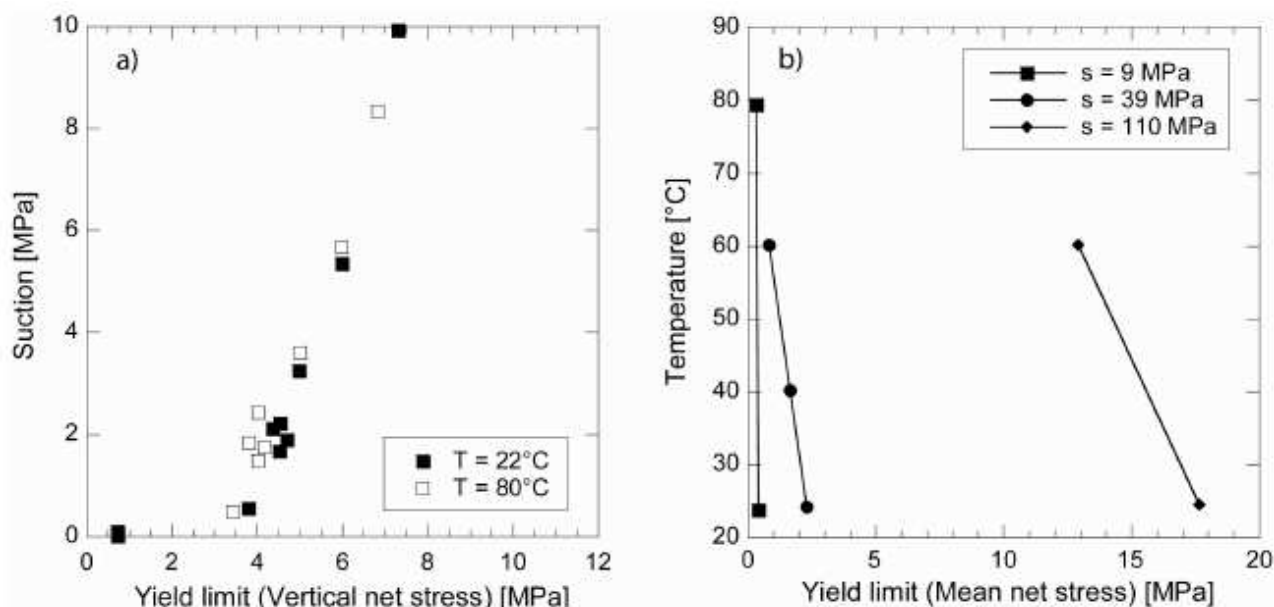


Figure 5.4: Effect of temperature and suction on the yield limit. a) Oedometric test on Boom clay [Rom99] b) Isotropic compression test on MX80 bentonite [Tan08]. (Redrawn from [Fra08]).

5.1.2 Conclusion

For a more complete description of the experimental behaviour of partially saturated soils, in isothermal and non-isothermal conditions, the interested reader can refer to the Phd thesis of Francois [Fra08] at which part of this chapter is referred.

In particular, in the second part of this thesis is presented the influence of temperature on the hydro-mechanical response of unsaturated soils. The analysis performed in the thesis shows the strong link between the mechanical and the water retention behaviour. Hence, because temperature affects both the stress-strain and degree of saturation-suction relationships, temperature plays an important role in the global response of unsaturated soils.

In particular, the generated plastic strains upon various thermo-hydro-mechanical paths have been shown to be closely related to the temperature and suction of the soil. Among other examples, the collapse propensity of a soil, occurring upon soil humidification, is not only affected by the external stress level but also by temperature. Similarly, the elastic domain is enhanced with increasing suction, while it decreases with increasing temperature. This has consequences in terms of volumetric strains, which implies modification of the water retention capability of unsaturated soil. In fact, the water retention curve is affected by the mechanical state of the soil and by the temperature [Fra08]. The denser the soil, the higher its degree of saturation for an equivalent suction. On the other hand, temperature tends to reduce the degree of saturation at a given suction. This behaviour has to be taken into account in a constitutive model, as it has been proposed in section 5.3.

5.2 ACMEG-TS MODEL†

5.2.1 Isotropic plastic mechanism

Similarly to equation [4.14], the yield limit, f_{iso} , of the isotropic plastic mechanism is expressed by :

$$f_{iso} = p' - p'_c \cdot r_{iso} = 0 \quad [5.6]$$

where r_{iso} is the degree of mobilization of the isotropic mechanism.

The enhancement of the isotropic elastic domain with increasing suction is introduced through the evolution of the preconsolidation pressure p'_c Figure 5.5. As experimentally observed, the evolution of p'_c with combined temperature T and suction s can be expressed by a logarithmic function [F&L08]

$$s \leq s_e \Rightarrow p'_c(s, T, \varepsilon_v^p) = p'_{c0} \left(1 - \gamma_T \log \left(\frac{T}{T_0} \right) \right) \quad [5.7]$$

$$s > s_e \Rightarrow p'_c(s, T, \varepsilon_v^p) = p'_{c0} \left(1 - \gamma_T \log \left(\frac{T}{T_0} \right) \right) \left(1 + \gamma_s \log \left(\frac{s}{s_e} \right) \right)$$

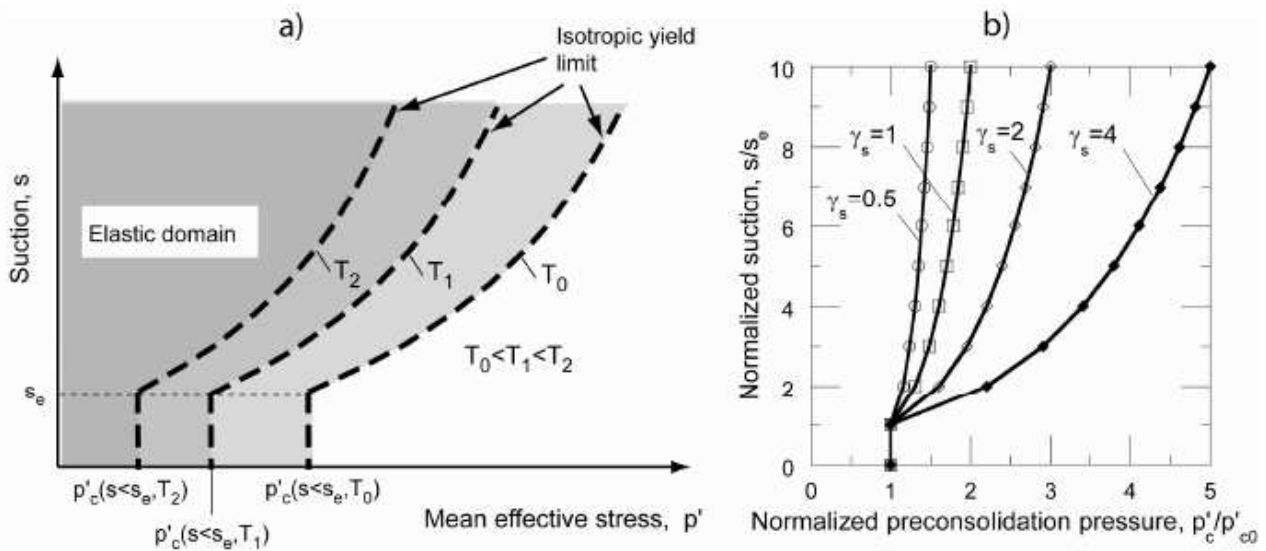


Figure 5.5: a) Evolution of the isotropic yield limit with suction at difference temperatures; b) dependence of the isotropic yield limit on the γ_s parameter. (Redrawn from [Fra08]).

In addition, the mechanical hardening produces an evolution of the preconsolidation pressure with the generated volumetric plastic strain and hence the thermo-hydro-mechanical evolution of the preconsolidation pressure is expressed as

$$s \leq s_e \Rightarrow p'_c(s, T, \varepsilon_v^p) = p'_{c0} \cdot e^{\beta \cdot \varepsilon_v^p} \left(1 - \gamma_T \log \left(\frac{T}{T_0} \right) \right) \quad [5.8]$$

$$s > s_e \Rightarrow p'_c(s, T, \varepsilon_v^p) = p'_{c0} \cdot e^{\beta \cdot \varepsilon_v^p} \left(1 - \gamma_T \log \left(\frac{T}{T_0} \right) \right) \left(1 + \gamma_s \log \left(\frac{s}{s_e} \right) \right)$$

† Reference [F&L08]

where p'_{c0} is the preconsolidation pressure in fully saturation conditions and at temperature T_0

p'_c is the preconsolidation pressure at a given suction s and at the reference temperature T

s_e is the air-entry suction

γ_s is a material parameter for the dependence of preconsolidation pressure on s

γ_T is a material parameter for the dependence of preconsolidation pressure on T

β is the plastic compressibility modulus (the slope of the linear function in the $\varepsilon_V^p - \ln p'_c$ plane)

The flow rule for the isotropic mechanism is given by equation [4.23].

5.2.2 Deviatoric plastic mechanism

Similarly to equation [4.24], the yield limit, f_{dev} , of the deviatoric plastic mechanism is expressed by Hujeux [Huj79]:

$$f_{dev} = q - Mp' \left(1 - b \cdot \ln \frac{d \cdot p'}{p'_c} \right) \cdot r_{dev} = 0 \quad [5.9]$$

where $M = \frac{6 \sin \Phi'}{3 - \sin \Phi'}$ is the slope of the critical state line (CSL) in the p' - q plane

$r_{dev} = r_{dev}^e + \frac{\varepsilon_d^p}{a + \varepsilon_d^p}$ is the degree of plastification of the deviatoric mechanism

Φ' is the friction angle at critical state

b is a material parameter defining the shape of the deviatoric yield limit

d is the ratio between the preconsolidation pressure, p'_c , and the critical pressure, p'_{cr} .

The ACMEG-TS model assumes that the friction angle may depend on temperature by the equation

$$M = M_0 - g(T - T_0) \quad [5.10]$$

where M_0 is the slope of the critical state line at ambient temperature T_0

g is an average slope of variation of friction angle at critical state with temperature

but remains unaffected by suction change in the generalized effective stress reference, as noticed by Nuth and Laloui [N&L08].

The hardening and dilatancy rules of the deviatoric mechanism are expressed by equations [4.25] to [4.29].

5.2.3 Coupling between the two plastic mechanisms

The shape of the elastic domain follows from the combinations of the deviatoric yield limit [4.47] with the thermo-hydro-mechanical evolution of the preconsolidation pressure [5.8]. Figure 5.6 [F&L08] [Fra08] illustrates the effect of suction, temperature and generated volumetric plastic strain on the evolution of the elastic domain.

It must be noted that the temperature and suction dependence of the isotropic yield limit is a one-to-one relationship. Provided that the stress point remains in the elastic domain, a suction and/or a temperature cycle does not modify the final preconsolidation pressure with respect to the initial one, if the final state is identical to the initial one. On the contrary, the volumetric plastic strain produces irreversible modification of the isotropic yield limit. In other words, the volumetric plastic strain is a hardening variable, while temperature and suction are not.

The coupling between the two plastic mechanisms is similar to that in the ACMEG-T model under saturated conditions. However, inclusion of the derivative of the yield limits with respect to suction is required in the consistency conditions for multi-mechanism [4.50] due to the evolution of both yield limits with suction level. The consistency condition of the two yielding mechanisms must be met simultaneously, requiring solution of two equations with two unknowns.

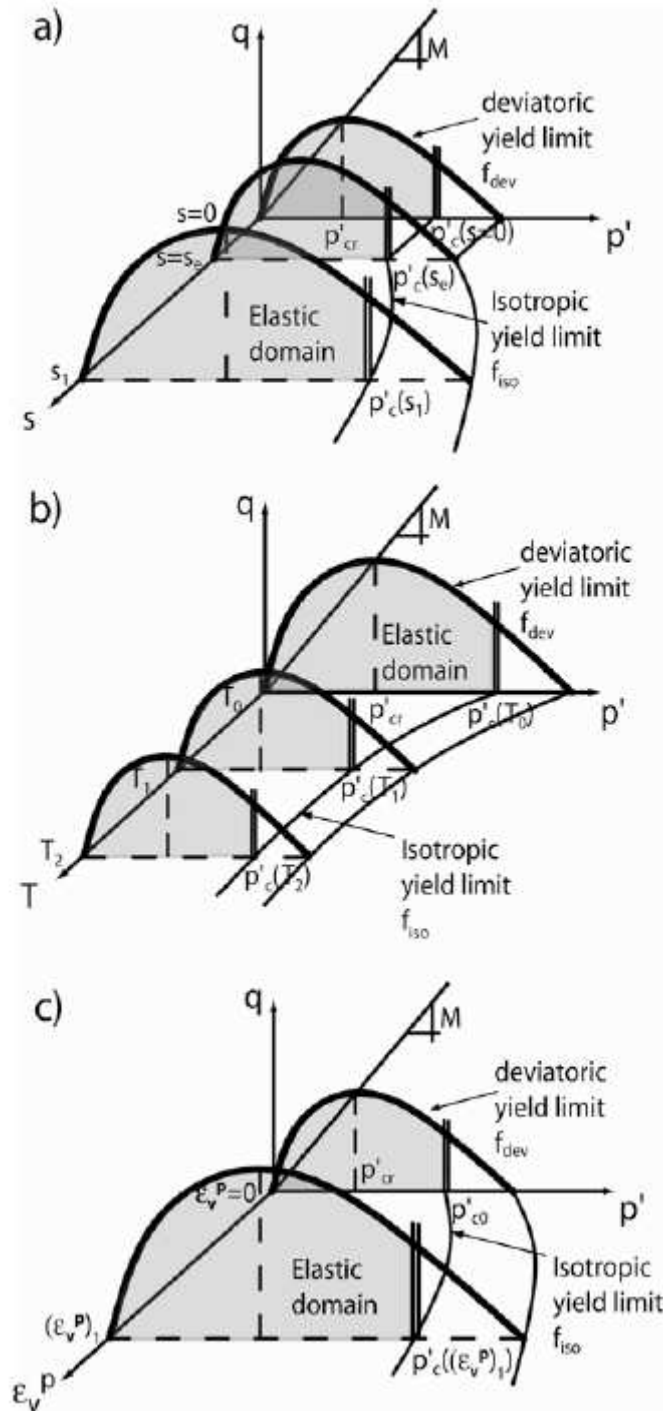


Figure 5.6: Effect of (a) suction, (b) temperature and (c) volumetric plastic strain on the shape of coupled mechanical yield limits [F&L08]. (Redrawn from [Fra08]).

$$d\mathbf{F} = \frac{\partial \mathbf{F}}{\partial \boldsymbol{\sigma}'} : d\boldsymbol{\sigma}' + \frac{\partial \mathbf{F}}{\partial s} \cdot ds + \frac{\partial \mathbf{F}}{\partial T} \cdot dT + \frac{\partial \mathbf{F}}{\partial \pi} \cdot \frac{\partial \pi}{\partial \lambda^p} \cdot \lambda^p = \mathbf{j} : d\boldsymbol{\sigma}' + \mathbf{i} \cdot ds + \mathbf{t} \cdot dT - \mathbf{H} \cdot \lambda^p \leq 0$$

$$\lambda^p \geq 0$$

$$d\mathbf{F} \cdot \lambda^p = 0$$
[5.11]

where $\boldsymbol{\sigma}'$ is the generalized effective stress vector

π is the internal variable tensor

\mathbf{j} collects the stress-gradient

\mathbf{t} is the temperature-gradient of the loading function F

\mathbf{H} is the matrix of hardening moduli $\mathbf{H}_{\alpha\beta} = -\frac{\partial f_{\alpha}}{\partial \lambda_{\beta}^p}$

λ^p is the plastic multiplier vector

$d\mathbf{F} \leq 0$ expresses Prager's consistency condition extended to multiple dissipation processes

\mathbf{i} collects the suction-gradient of the loading function

In the framework of generalized effective stress, Borja [Bor04] proved that including suction in the argument of the yield functions is motivated by thermodynamic considerations.

Within the adopted generalized stress framework, $\boldsymbol{\sigma}'$ depends on s , which makes these two state variables dependent. In order to avoid the two effects of the suction increment (in $d\boldsymbol{\sigma}'$ and ds itself) in the consistency equation, numerical integration at the local (Gauss point) level is performed by considering suction fixed at its final value during the plastic corrector phase. In other words, as suggested by Borja, there is no return map on the suction axis during numerical integration of the model, which makes ds equal to zero in equation [5.11]. Hence, there is no change in the consistency relations with respect to the saturated model, excepted that, at each time step, the value of the preconsolidation pressure is calculated considering the suction at the end of the time step through equation [5.8].

5.3 WATER RETENTION CONSTITUTIVE PART

In 2.4.5 we have seen that the pore size distribution is dependent on the capillary pressure, the temperature and the volumetric strain.

In this section we will summarize the relationship between the degree of saturation S_w and suction s taking into account also the influence of temperature and usually neglected volumetric strain, following [Fra08].

$$S_{\pi} = S_{\pi}(p^c, T, \varepsilon_v) \tag{5.12}$$

Generally speaking all the relationship that can be found in literature are derived from experimental data (see Figure 5.7 and Table 5.1).

For this work the following relationship are used and are called Brooks and Corey, Safai and Pinder (from the name of the authors that have proposed them) and ACMEG-HYDRO (from the name of the model where this law is shown [Fra08]).

These relationship are summarize in the following together with their derivatives necessary for the Jacobian matrix after linearization of the discretized governing equations (see 3.1.2.2).

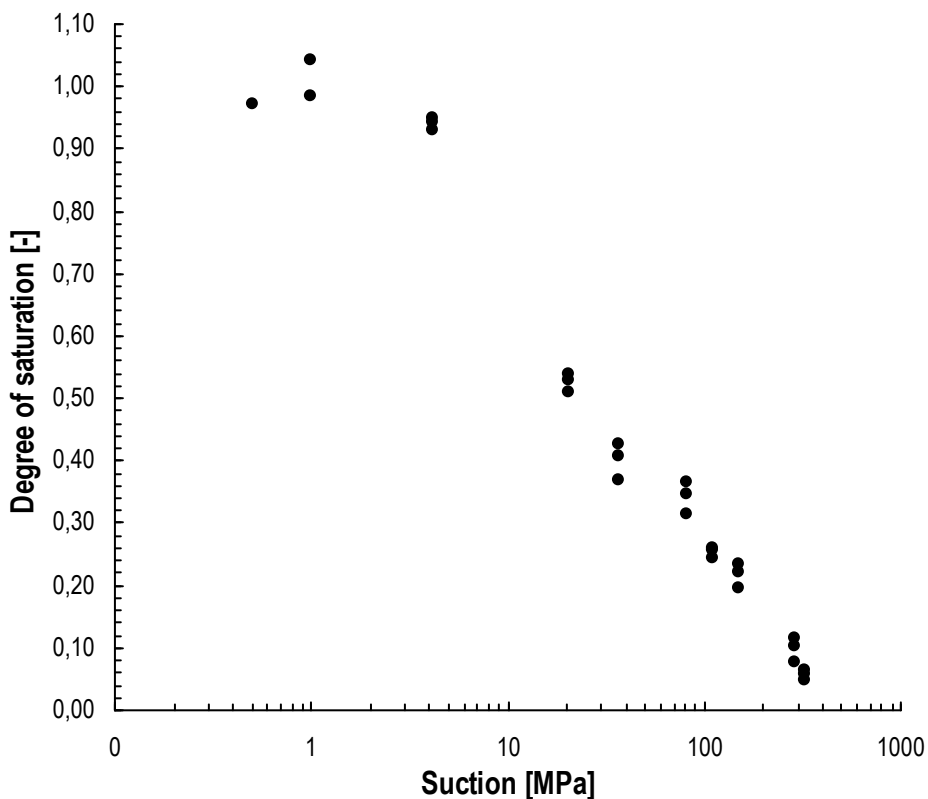


Figure 5.7: Experimental data (from Lyesse Laloui with personal communication)

S [MPa]	S_w
0,50	0,972
1,00	0,983
1,00	1,041
4,12	0,951
4,12	0,931
4,12	0,944
20,41	0,510
20,41	0,539
20,41	0,531
37,13	0,369
37,13	0,407
37,13	0,428
80,89	0,365
80,89	0,315
80,89	0,348
111,08	0,256
111,08	0,242
111,08	0,260
150,00	0,235
150,00	0,221
150,00	0,196
286,86	0,078
286,86	0,115
286,86	0,103
325,79	0,056
325,79	0,064
325,79	0,049

Table 5.1: Experimental data

5.3.1 Brooks and Corey

The relation proposed by Brooks and Corey [B&C64] is the follow

$$S_w = S_w(s) = S_{irr} + \frac{1 - S_{irr}}{1 + \left(\frac{s}{p_{ref} - p_b} \right)^\lambda} \quad [5.13]$$

where S_{irr} is the irreducible degree of saturation

λ is the index of the pore size distribution which is defined as the negative slope of the effective S_w

p_{ref} is the reference pressure

p_b is the bubble pressure

First derivative

$$\frac{\partial S_w}{\partial s} = -\frac{s_\lambda(1 - S_{irr})\lambda}{s(1 + s_\lambda)^2} \tag{5.14}$$

where $s_\lambda = \left(\frac{s}{p_{ref} - p_b}\right)^\lambda$

Second derivative

$$\frac{\partial^2 S_w}{\partial s^2} = -\frac{s_\lambda(1 - S_{irr})\lambda}{s^2(1 + s_\lambda)^2} \left(s_\lambda + \frac{2 \cdot s_\lambda \cdot \lambda}{1 + s_\lambda} - \lambda \right) \tag{5.15}$$

The material parameter filling from the experimental data of Table 5.1 and the graph are

S_{irr}	λ	p_{ref} [MPa]	P_b [MPa]
0.0563	1.5	28.00	0.50

Table 5.2: Parameters for Brooks-Corey (equation [5.13])

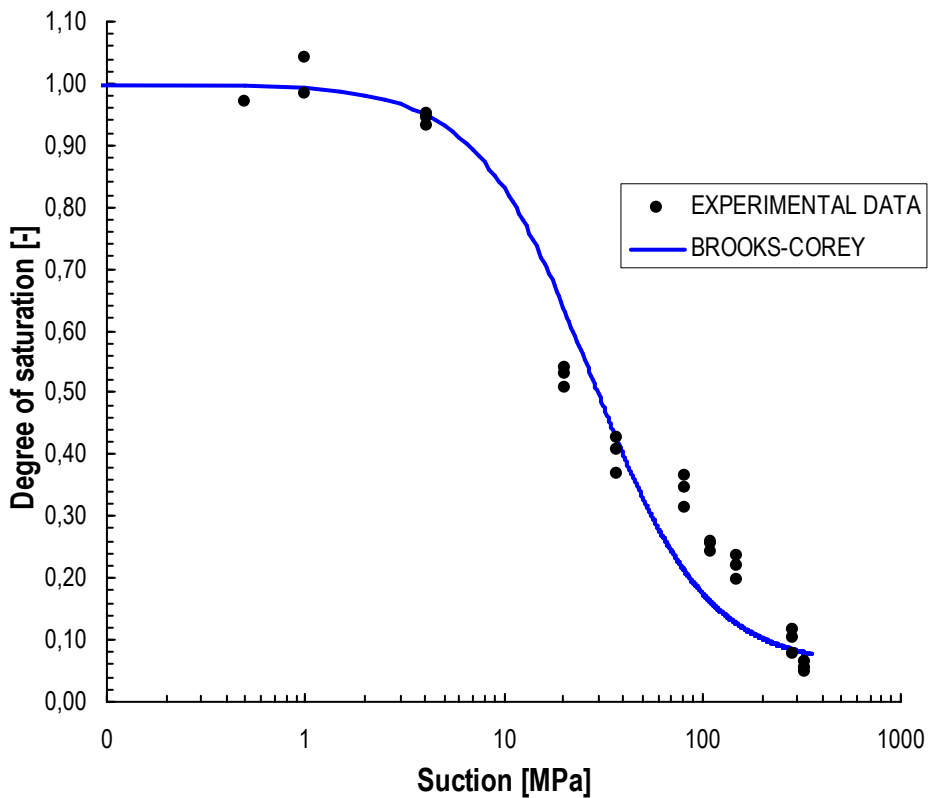


Figure 5.8: Graph of the Brooks and Corey law

5.3.2 Safai and Pinder

The relationship proposed by Safai and Pinder [S&P77] is the following:

$$S_w = S_w(s) = \frac{\Theta'_r}{\Theta'_s} + \frac{1 - \frac{\Theta'_r}{\Theta'_s}}{\left[1 + (\beta s)^\gamma\right]^{r'}} \quad [5.16]$$

where $\frac{\Theta'_r}{\Theta'_s} = S_{irr}$ is the irreducible degree of saturation

β is express in cm^{-1} if s is expressed in cm as the high of a column of water

First and second derivatives are

$$\frac{\partial S_w}{\partial s} = - \frac{r'(\beta s)^\gamma (1 - S_{irr})\gamma}{s \left[1 + (\beta s)^\gamma\right]^{r'+1}} \quad [5.17]$$

$$\frac{\partial^2 S_w}{\partial s^2} = \frac{r'(\beta s)^\gamma (1 - S_{irr})\gamma}{s^2 \left[1 + (\beta s)^\gamma\right]^{r'+1}} \left[1 - \gamma - \gamma \frac{(\beta s)^\gamma}{1 + (\beta s)^\gamma}\right] \quad [5.18]$$

The material parameters filling from the experimental data of the Table 5.1 and the graph are

S_{irr}	β [cm^{-1}]	γ	r'
0.0563	0.035	1.20	1.00

Table 5.3: Parameters for Safai-Pinder (equation [5.16])

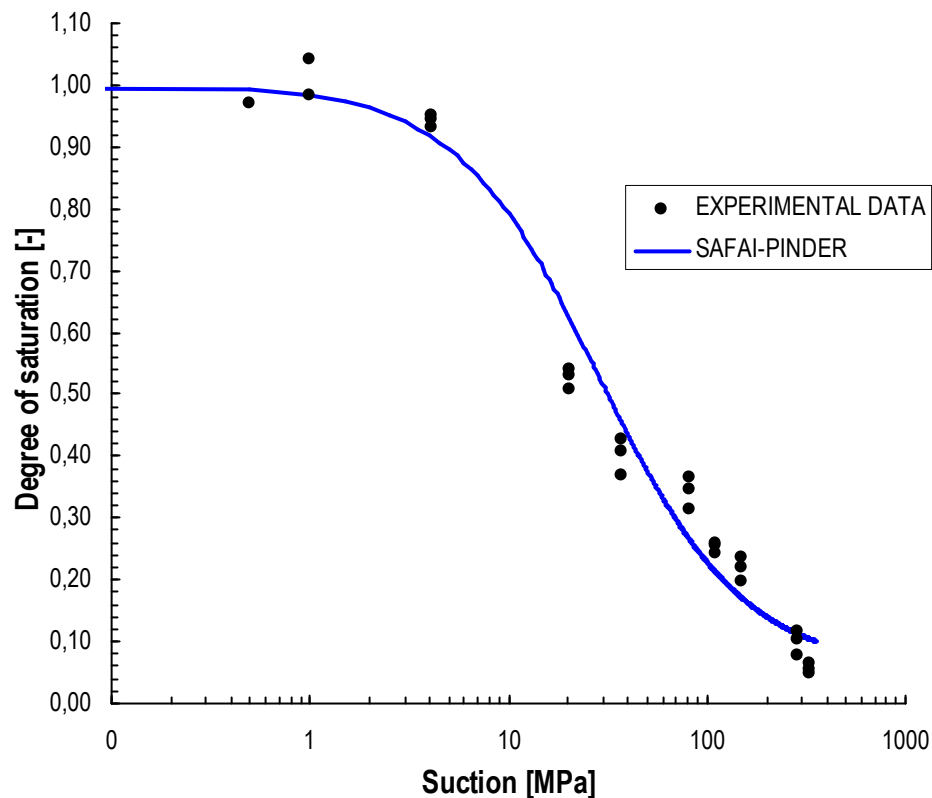


Figure 5.9: Graph of the Safai and Pinder law

5.3.3 ACMEG-HYDRO

If the laws proposed by Brooks and Corey and Safai and Pinder are similar, the retention relationship proposed for the ACMEG-TS model [Fra08] presents three additional features:

1. S_w depend not only from s but also from T (temperature) and ε_v (volumetric strain)
2. it takes into account of the suction entry value s_e
3. it considers the hysteretic behaviour during drying and wetting

The relationship ACMEG-HYDRO is the following:

$$S_w = 1 \quad \text{if} \quad s \leq s_e$$

$$S_w = S_w(s, T, \varepsilon_v) = 1 - \frac{1}{\beta_h} \ln\left(\frac{s}{s_e}\right) \quad \text{if} \quad s > s_e \quad [5.19]$$

with

$$s_e = s_e(T, \varepsilon_v) = s_{e0} \left[1 - \Theta_T \log \frac{T}{T_0} - \Theta_e \log(1 - \varepsilon_v) \right] \quad [5.20]$$

where s_e is the suction entry value

β_h is the slope of the desaturation curve in the $\ln(s)$ - S_w plane (Figure 5.10)

s_{e0} is the suction entry value for $T=T_0$ and $\varepsilon_v=0$

T_0 is the reference temperature

Θ_T is a material parameters describing the evolution of suction entry value with respect to temperature

Θ_e is a material parameters describing the evolution of suction entry value with respect to volumetric strain

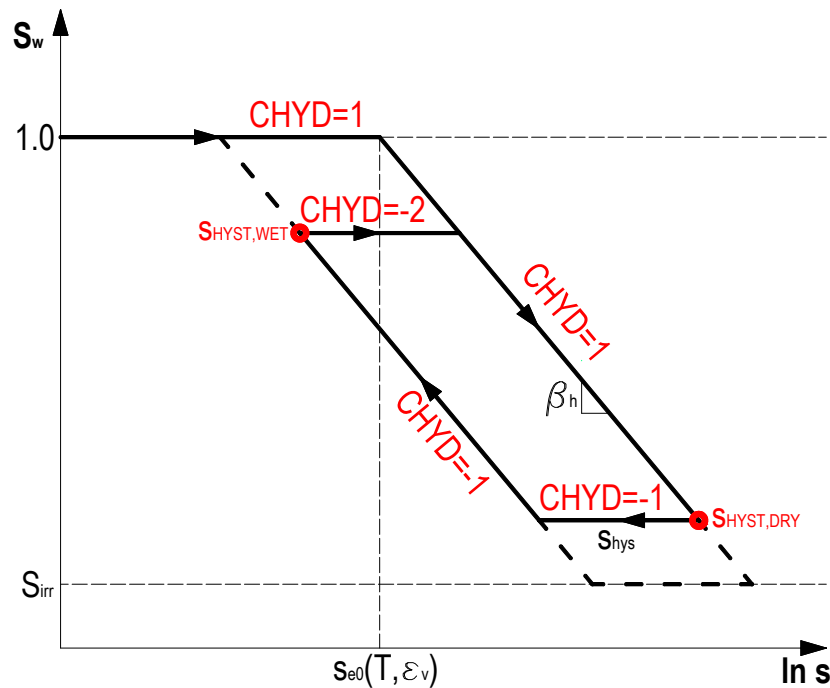


Figure 5.10: Schematic representation of water retention curve ACMEG-HYDRO

It's important note that in the equation [5.20] if the temperature T is $T < T_0$ the value of s_e decrease (because $\log \frac{T}{T_0} > 0$), while if ε_v increase (in this relation ε_v are positive in compression) the value of s_e increase (because $\log(1 - \varepsilon_v) < 0$). In other words, is more easy for the soil enters in partially saturation if temperature increases and is more difficult if ε_v increase.

For the implementation of the ACMEG-HYDRO water retention curve in COMES-GEO we need to introduce the history of the hydraulic load due to hysteresis. For this reason we have introduced a coefficient (CHDY in Figure 5.10) that identifies the drying or wetting part of the retention curve and a memory of the saturation reached.

The hysteresis is modelled with the introduction of the parameter s_{hys} which that is a material parameter considering the size of the water retention hysteresis.

Since S_w also depends on the temperature, the derivatives with respect to this variable is needed.

First derivative

$$\frac{\partial S_w}{\partial s} = -\frac{1}{s\beta_h} \quad [5.21]$$

$$\frac{\partial S_w}{\partial T} = -\frac{\Theta_T s_{e0}}{s_e \beta_h T \ln 10} \quad [5.22]$$

Second derivative

$$\frac{\partial^2 S_w}{\partial s^2} = \frac{1}{s^2 \beta_h} \quad [5.23]$$

$$\frac{\partial^2 S_w}{\partial T^2} = \frac{\Theta_T s_{e0}}{\beta_h s_e T^2 \ln 10} - \frac{\Theta_T^2 s_{e0}^2}{\beta_h s_e^2 T^2 (\ln 10)^2} \quad [5.24]$$

$$\frac{\partial^2 S_w}{\partial s \partial T} = \frac{\partial^2 S_w}{\partial T \partial s} = 0 \quad [5.25]$$

The material parameters fitting the experimental data Figure 5.7 and the graph are

s_{e0} [MPa]	β_h
3.25	4.8

Table 5.4: Parameters for ACMEG-HYDRO (equation [5.19])

For the test case in exam, the parameters Θ_T , Θ_e and S_{hys} have not been reported because the data about different temperature and different volumetric strain were not available.

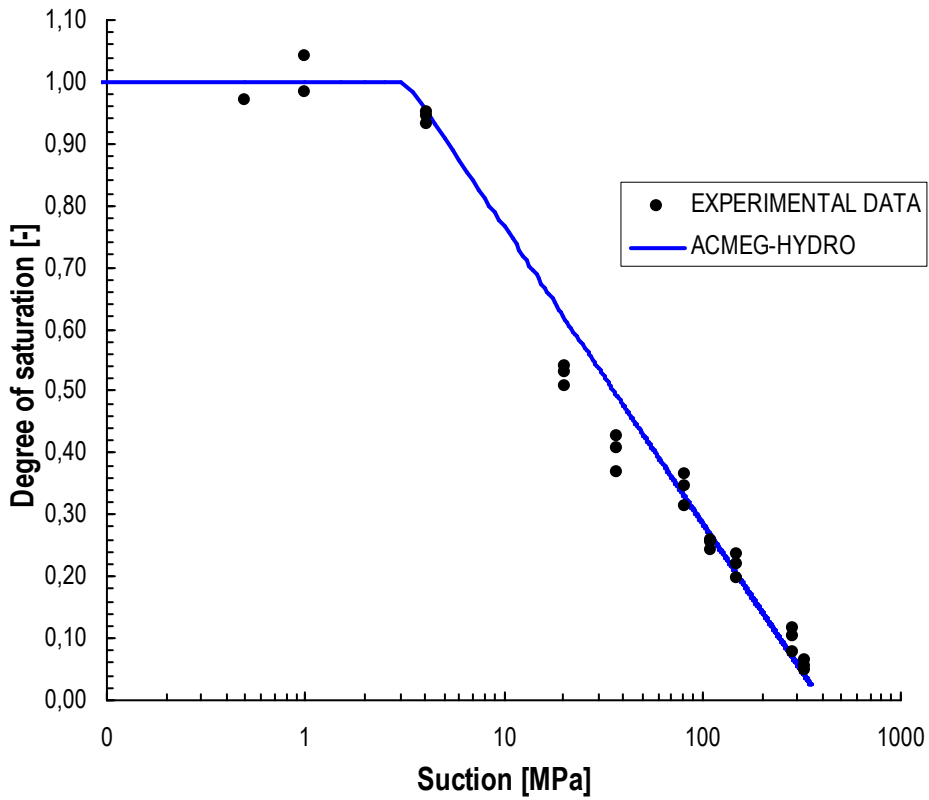


Figure 5.11: Graph of the ACMEG-HYDRO law

5.3.4 Comparison

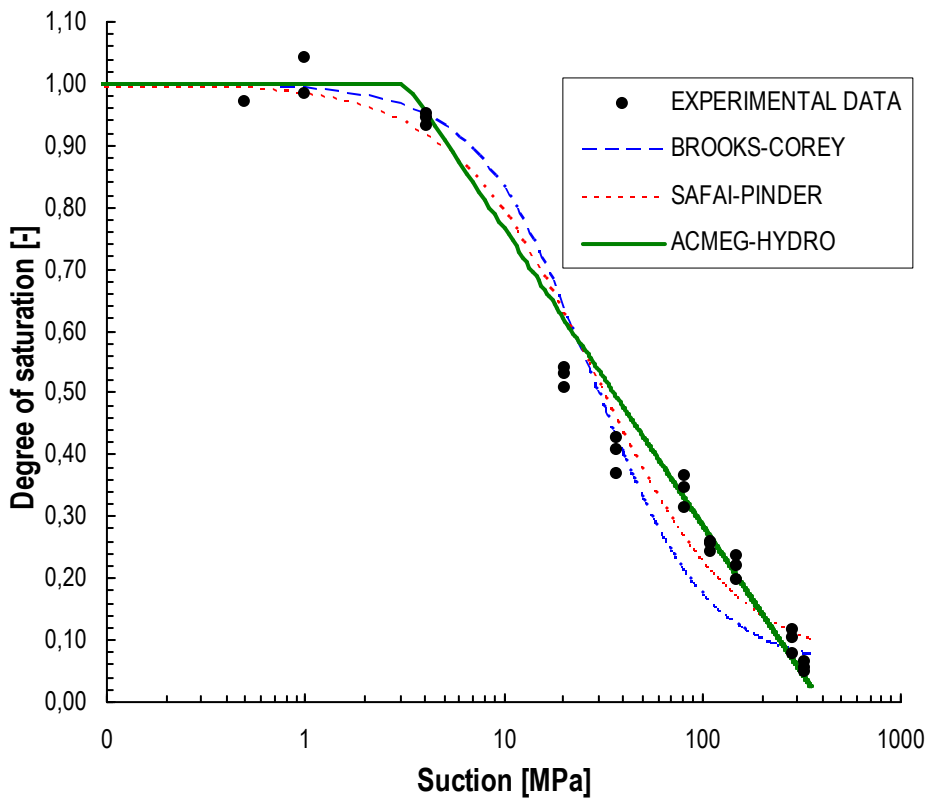


Figure 5.12: Comparison between the experimental data and the values given by the three water retention relationship implemented in COMES-GEO

5.4 VALIDATION OF THE IMPLEMENTATION OF ACMEG-TS MODEL IN COMES-GEO F.E. CODE

In this section the implementation of ACMEG-TS in COMES-GEO is validated by comparison between the results of the ACMEG-T model's driver and the F.E.M. results obtained using COMES-GEO.

As for 4.4: "Validation of the implementation of ACMEG-T model in COMES-GEO" the model ACMEG-TS is considered to validate [Fra08] and [F&L08].

A series of tests are performed starting from experimental or fictitious data for material parameters and type of tests.

5.4.1 Triaxial compression test

Here a series of numerical simulations of triaxial compressions at two confining pressures, two temperatures and three suction levels are presented. The material parameters and the data for the comparison are taken from Appendix D of [Fra08].

Elastic parameters						
K_{ref} [MPa]	G_{ref} [MPa]	n_e	β_s [°C ⁻¹]			
130.00	130.00	0.4	$4.0 \cdot 10^{-5}$			
Isotropic plastic parameters						
β	γ_s	γ_T	c	r_{iso}^e	p'_c [MPa]	
18.0	1.5	0.2	0.012	0.001	6.0	
Deviatoric plastic parameters						
b	d	θ'_0 [°]	g	α	a	r_{dev}^e
0.6	1.3	16	$4.5 \cdot 10^{-4}$	1.0	0.007	0.3
Water retention parameters for Safai and Pinder type law (Equation [5.16])						
S_{irr}	β [cm ⁻¹]	γ	r'			
0.40	0.60	1.80	1.0			

Table 5.5: Material parameters of the triaxial compression

The water retention relationship chosen for this test is the one modified by Safai and Pinder (see Figure 5.13) where the three suctions and the corresponding degree of saturation are:

$$s=0.0 \text{ MPa} \quad S_w=1.000$$

$$s=1.1 \text{ MPa} \quad S_w=0.807$$

$$s=2.5 \text{ MPa} \quad S_w=0.595$$

The two compressive pressures are $\sigma'_c=2.0$ MPa and $\sigma'_c=3.0$ MPa, while the two temperatures are $T=20$ °C and $T=80$ °C (only for the case with $s=2.5$ MPa).

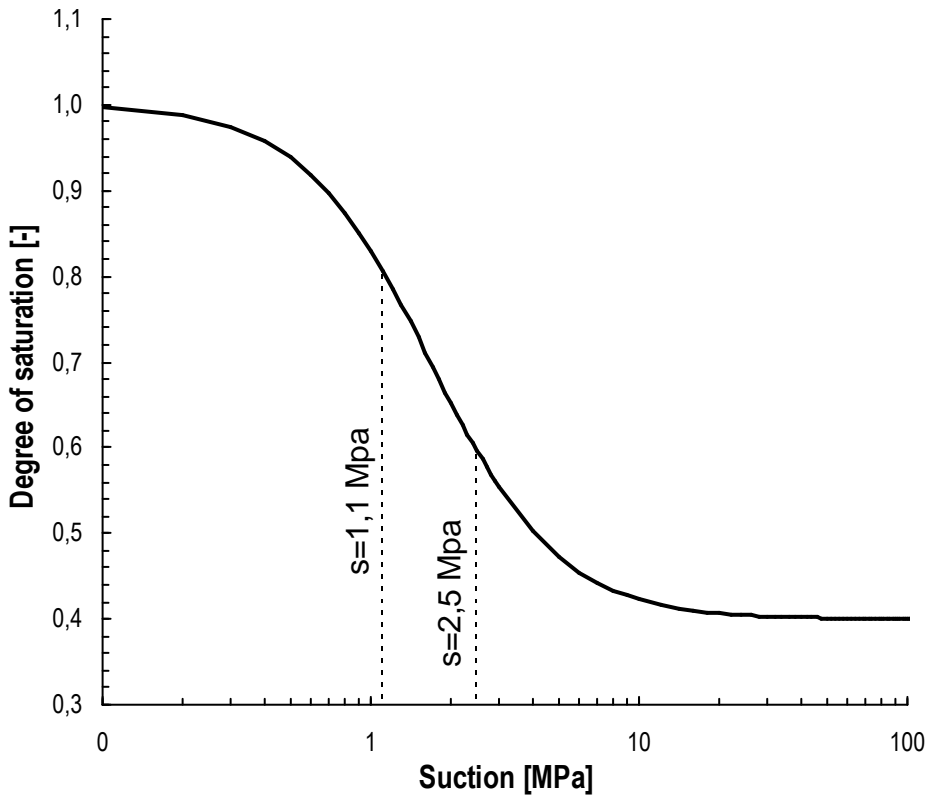


Figure 5.13: Water retention constitutive law Safai and Pinder for this series of simulation

In the tests run by Francois [Fra08] ($s_{e0}=0.5$ MPa, $\beta_h=4.0$) the water retention curve used is the ACMEG-HYDRO. As is possible to observe from Figure 5.14 for the chosen suctions, the degree of saturation coincides.

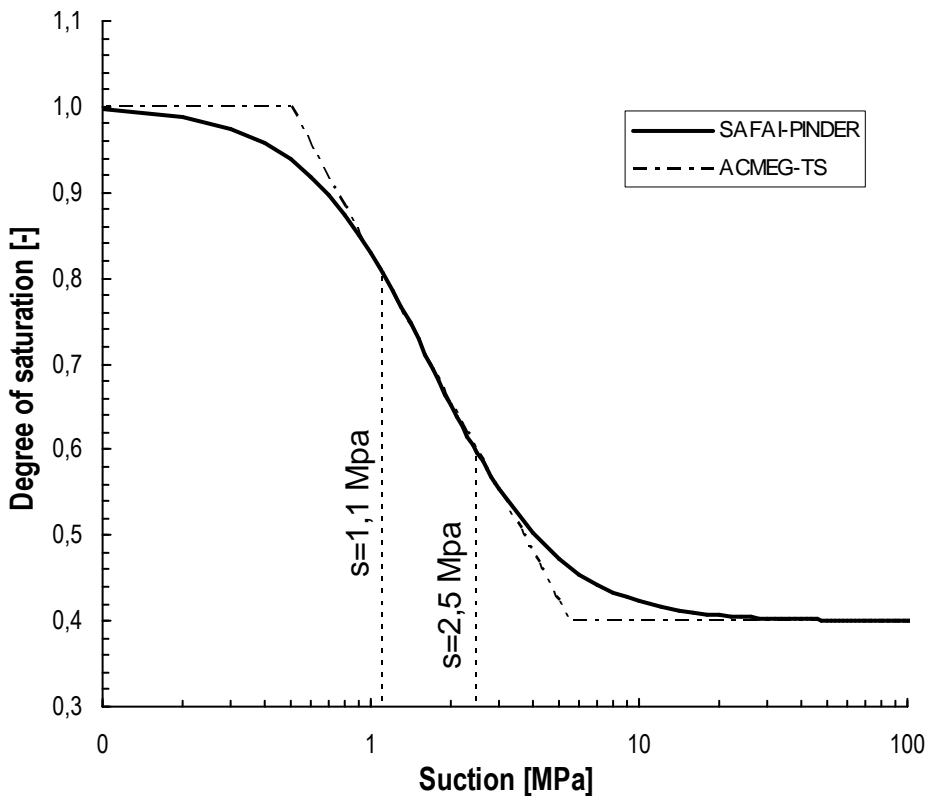
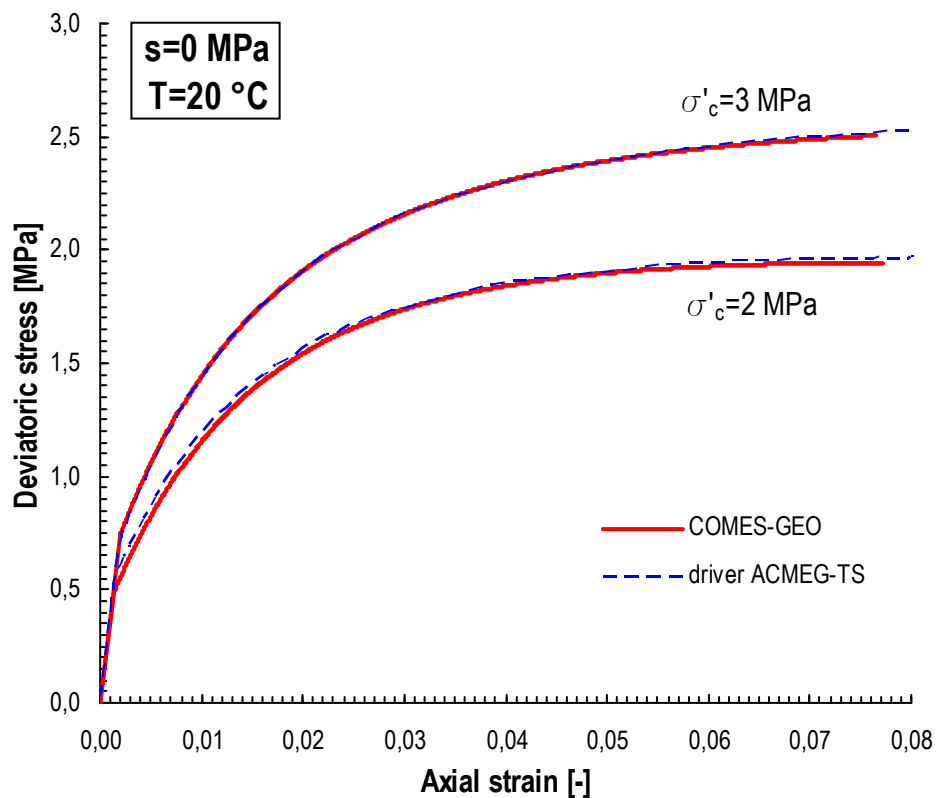
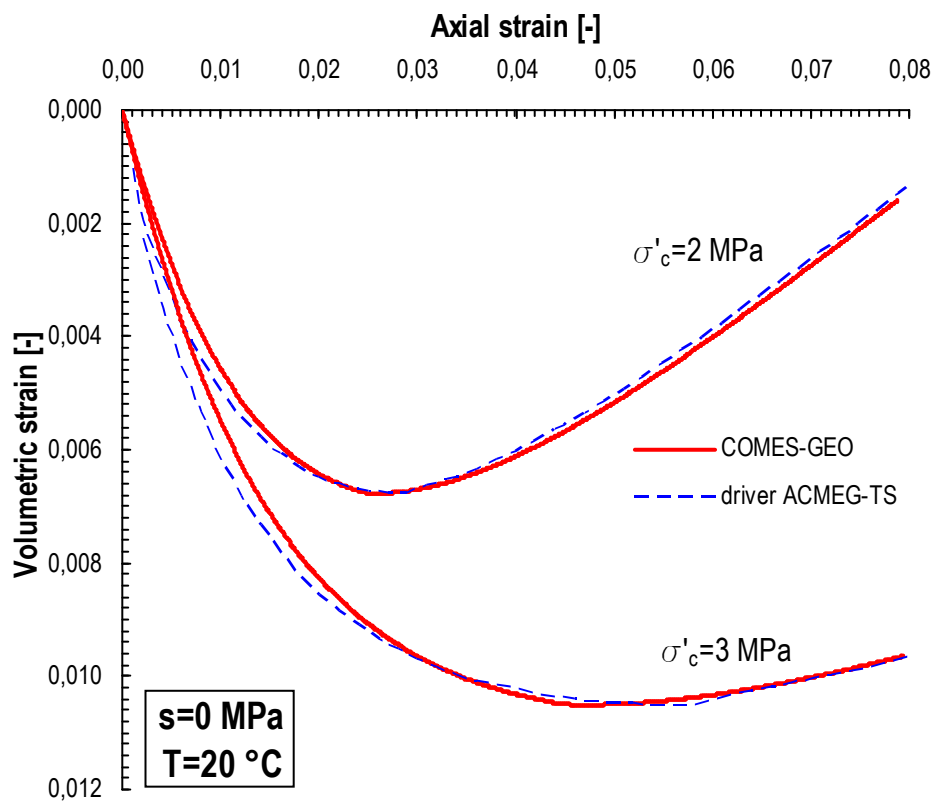


Figure 5.14: Comparison between the SAFAI-PINDER (COMES-GEO) and ACMEG-TS water retention law used

Figure 5.15: Axial strain versus Deviatoric Stress for $s=0.0$ MPa and $T=20$ °CFigure 5.16: Axial strain versus Volumetric strain for $s=0.0$ MPa and $T=20$ °C

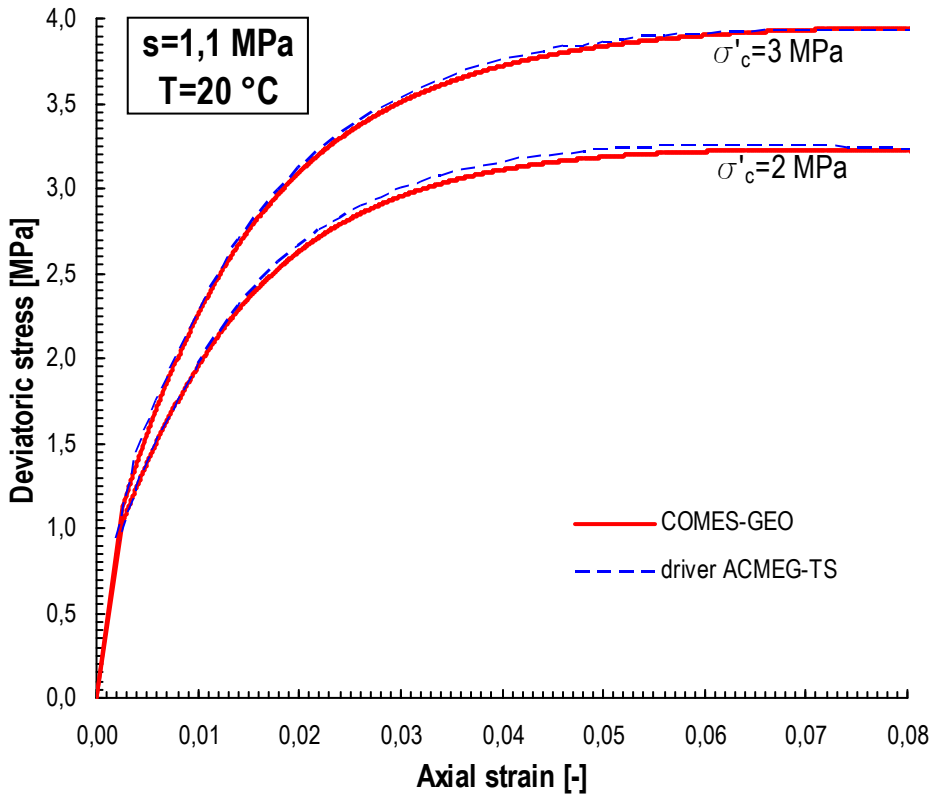


Figure 5.17: Axial strain versus Deviatoric Stress for $s=1.1$ MPa and $T=20$ °C

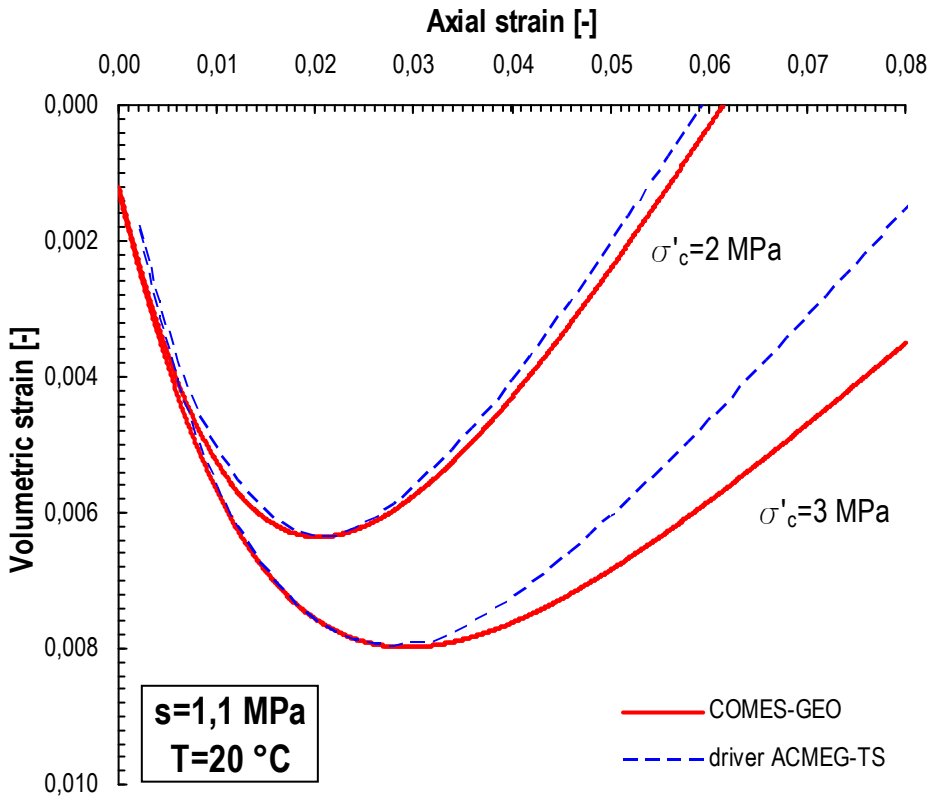


Figure 5.18: Axial strain versus Volumetric strain for $s=1.1$ MPa and $T=20$ °C

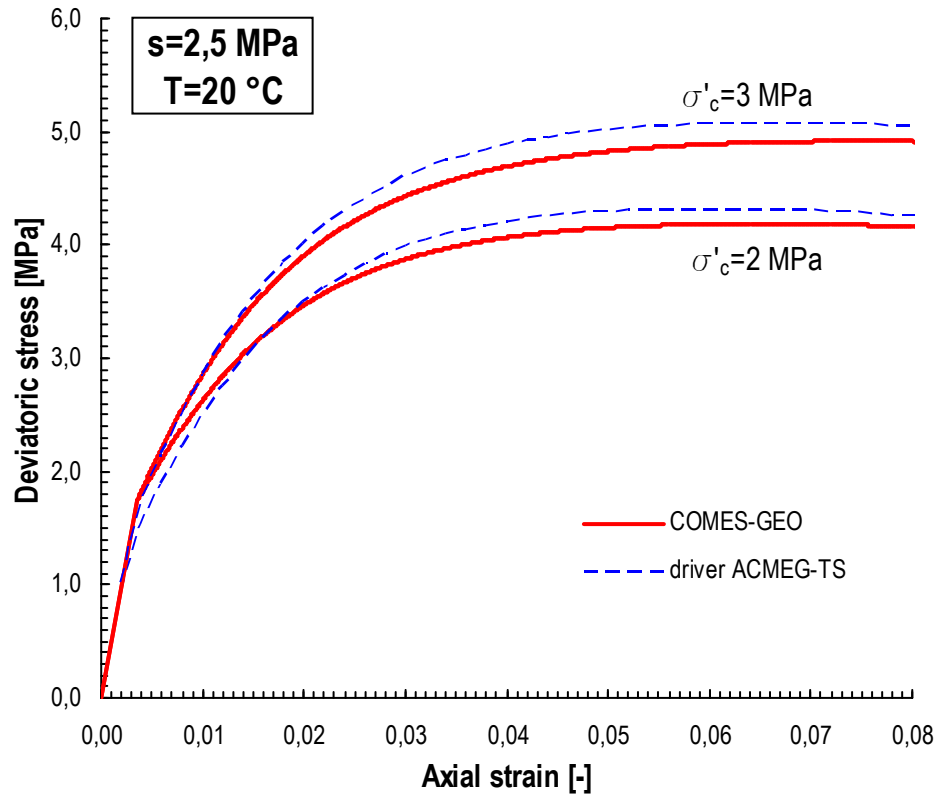


Figure 5.19: Axial strain versus Deviatoric Stress for $s=2.5 \text{ MPa}$ and $T=20 \text{ °C}$

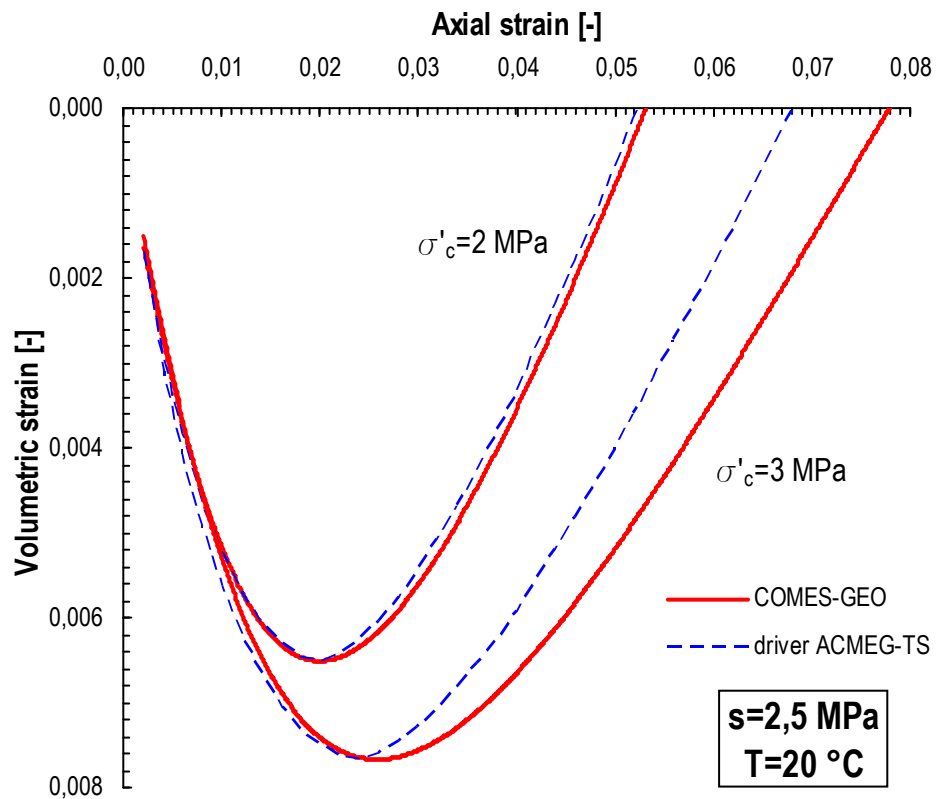


Figure 5.20: Axial strain versus Volumetric strain for $s=2.5 \text{ MPa}$ and $T=20 \text{ °C}$

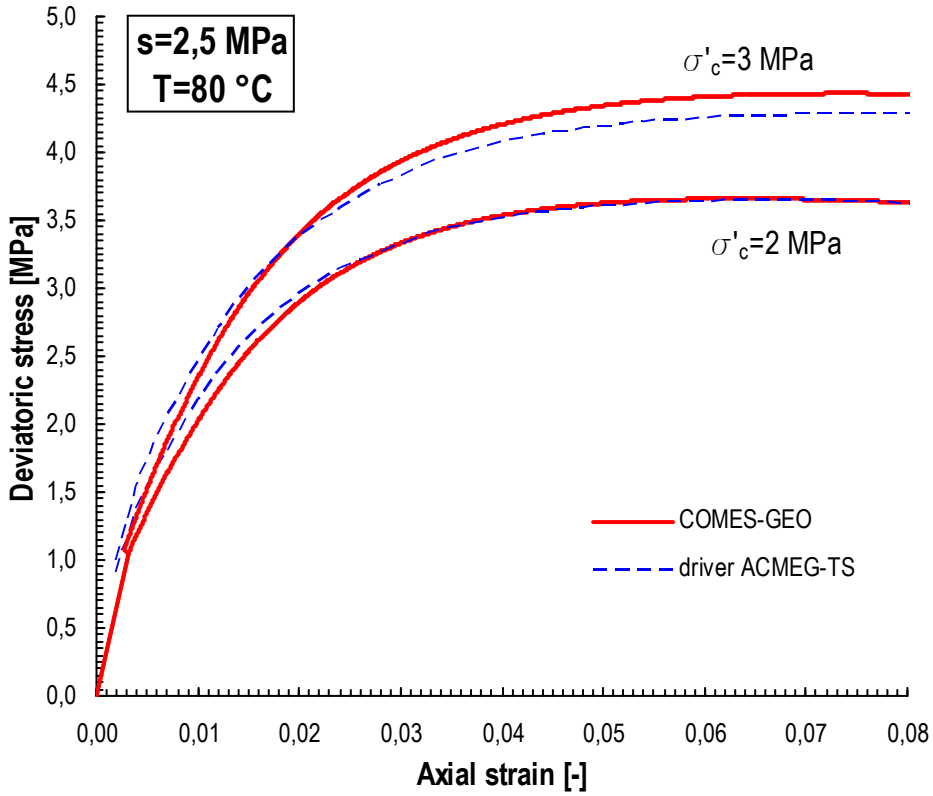


Figure 5.21: Axial strain versus Deviatoric Stress for $s=2.5 \text{ MPa}$ and $T=80 \text{ }^\circ\text{C}$

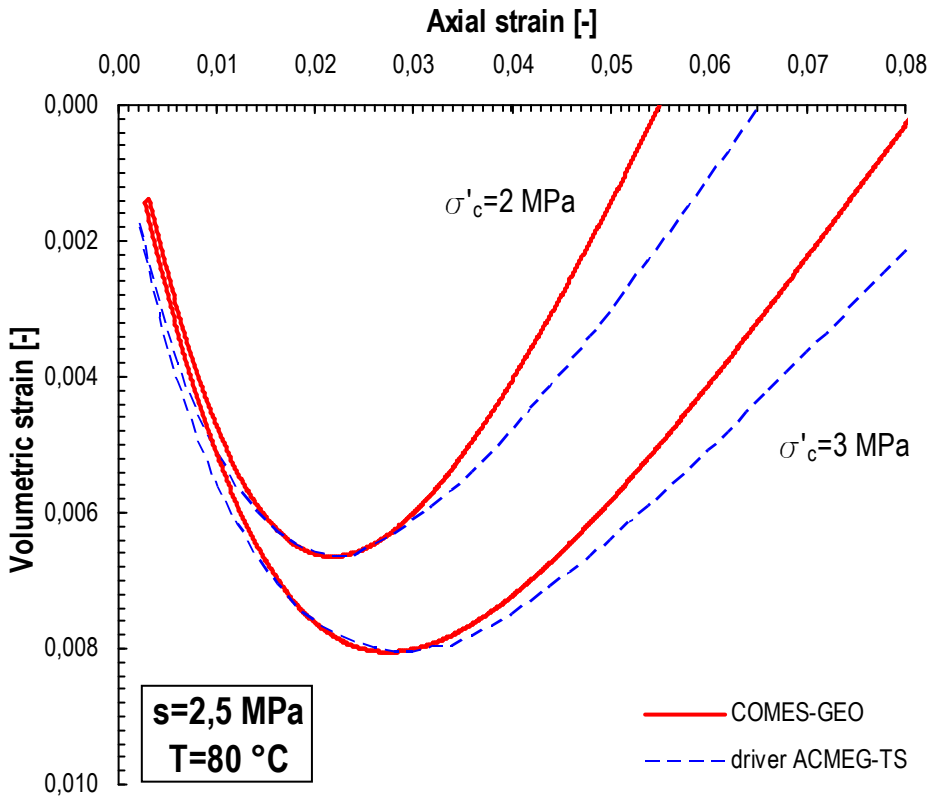


Figure 5.22: Axial strain versus Volumetric strain for $s=2.5 \text{ MPa}$ and $T=80 \text{ }^\circ\text{C}$

The results check difference between the F.E. and the driver simulation in the ε_γ - ε_v plane. This is due to the different water retention law used; in fact, the simulation performed with COMES-GEO considers the water saturation dependent by suction only while the simulation performed with the driver ACMEG-TS, considers also the volumetric strain contribution.

The comparison of the results obtained with the driver ACMEG-TS and the F.E. code COMES-GEO (Figure 5.15 to Figure 5.22) shows a good agreement for different degree of saturation (i.e. different suction), for different temperature and for different confining pressure.

5.4.2 Oedometric compression tests

Here a comparison with experimental results of oedometric tests on Sion silt is shown. Triaxial tests are used by Francois [Fra08] for the calibration of the material parameters.

The triaxial tests are performed at the room temperature ($T=22$ °C) and in fully saturation conditions ($s=0$ kPa), while the oedometric tests are performed at different temperature ($T=22$ °C and $T=80$ °C) and at different suctions ($s=0$ kPa and $s=300$ kPa).

The water retention curve is depicted in Figure 5.23 and the relation ACMEG-HYDRO is used.

The material parameters are listed in Table 5.6.

Elastic parameters						
K_{ref} [MPa]	G_{ref} [MPa]	n_e	β'_s [°C ⁻¹]			
30.00	19.00	0.5	4.2·10 ⁻⁵			
Isotropic plastic parameters						
β	γ_s	γ_T	c	r_{iso}^e	p'_c [MPa]	
50.0	0.6	0.46	0.001	0.15	0.60	
Deviatoric plastic parameters						
b	d	\emptyset'_0 [°]	g	α	a	r_{dev}^e
1.0	2.0	30	0.0	1.0	0.0035	0.01
Water retention parameters (ACMEG-TS model)						
s_{e0} [MPa]	β_H					
0.05	2.52					

Table 5.6: Material parameters of Sion silt

The oedometric tests consist in two successive loading and unloading paths. Starting from the slurry state (i.e. quasi virgin state) the first load is applied to consider the entire THM history of the material. Then, after the first unloading, the

second load is applied to simulate the real behaviour of the material. The initial preconsolidation pressure of the slurry has been adjusted for each simulation to fit with experimental results. Results are shown only for the second loading and unloading path.

Two comparisons with the experimental results and with those predicted from the driver [Fra08] are shown.

In the following, the results of the triaxial test used for the calibration of the material parameters are shown in Figure 5.24 to Figure 5.31, then the results predicted for the oedometric tests are depicted in Figure 5.32 to Figure 5.35.

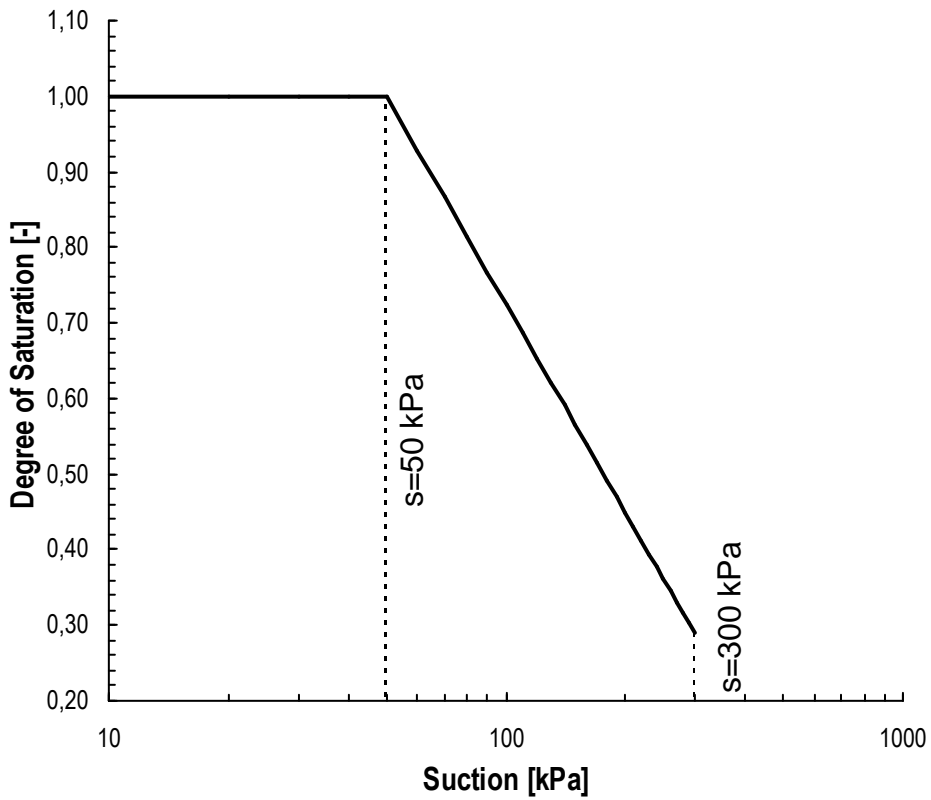
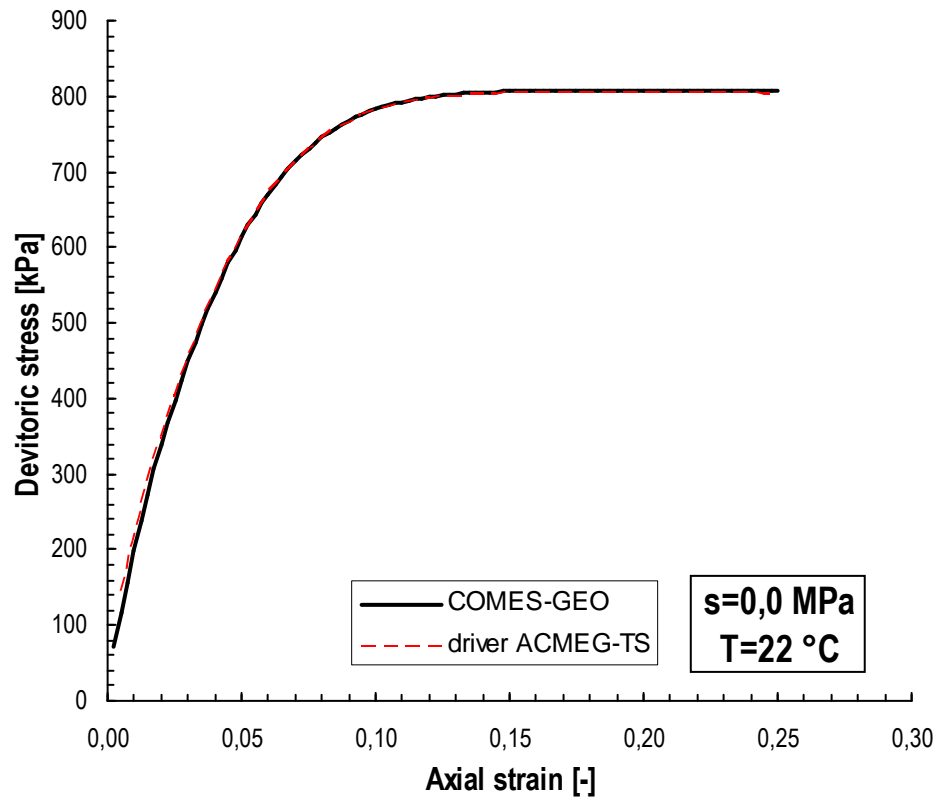
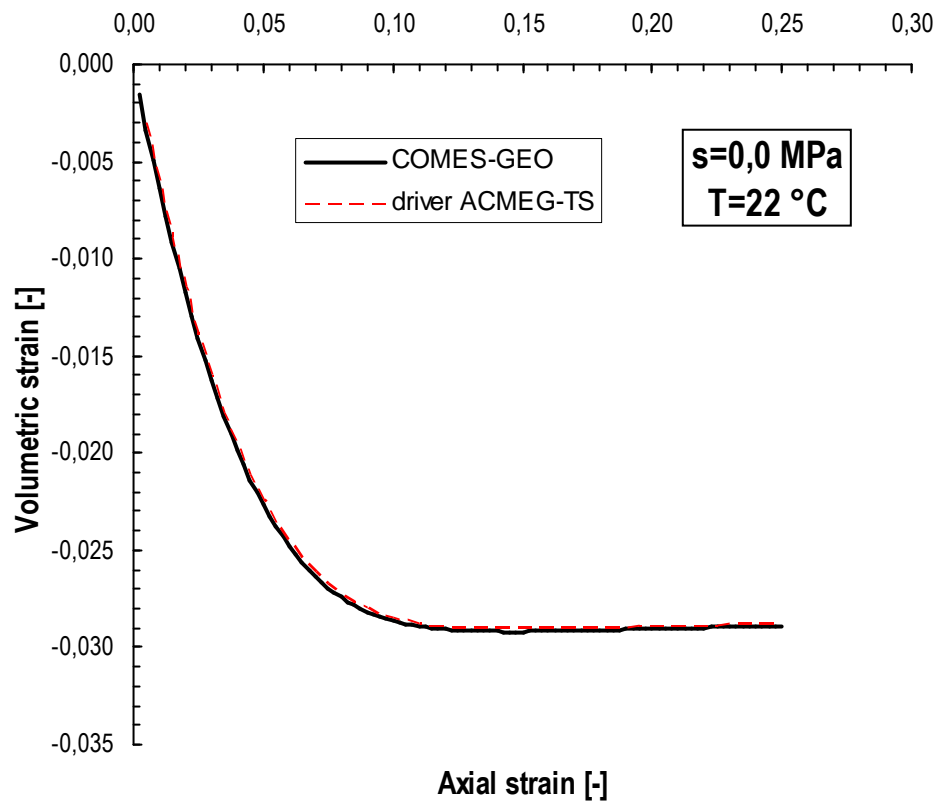


Figure 5.23: Water retention curve for Sion silt

5.4.2.1 Triaxial tests

Figure 5.24: Axial strain versus Deviatoric Stress for $s=0.0 \text{ MPa}$ and $T=22 \text{ }^\circ\text{C}$ Figure 5.25: Axial strain versus Volumetric strain for $s=0.0 \text{ MPa}$ and $T=22 \text{ }^\circ\text{C}$

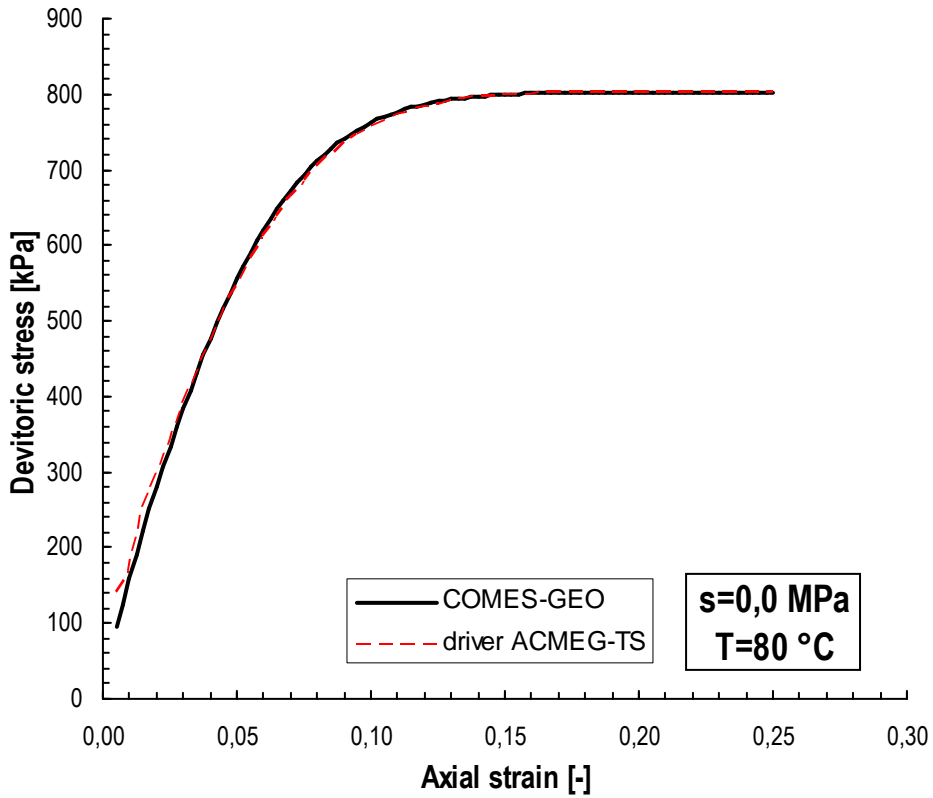


Figure 5.26: Axial strain versus Deviatoric Stress for $s=0.0$ MPa and $T=80$ °C

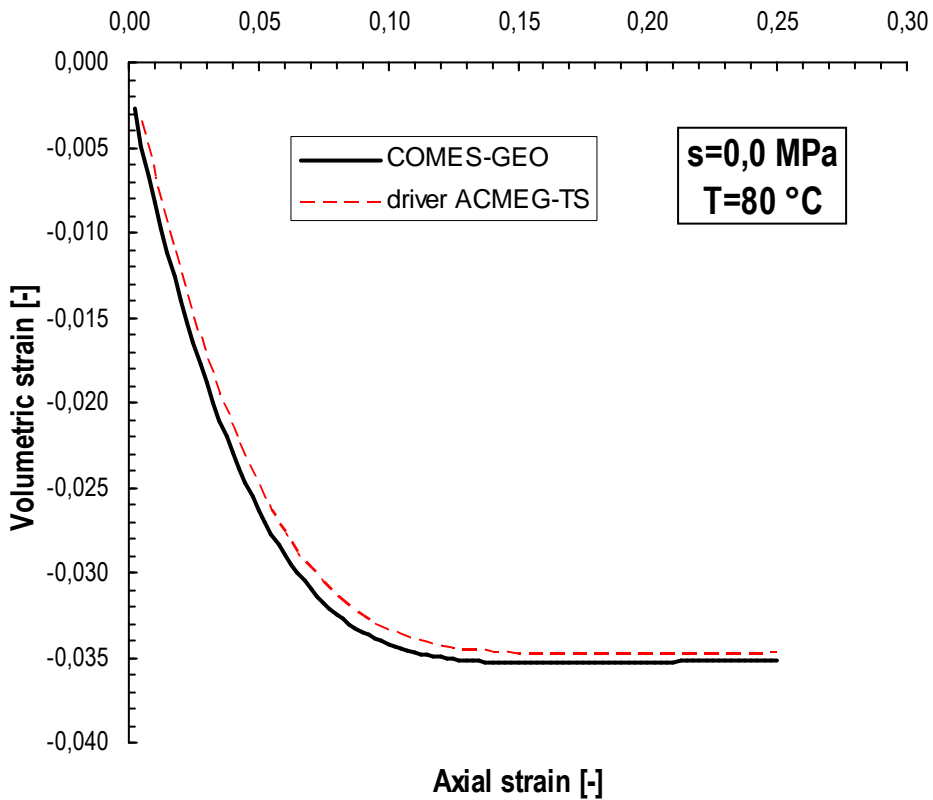


Figure 5.27: Axial strain versus Volumetric strain for $s=0.0$ MPa and $T=80$ °C

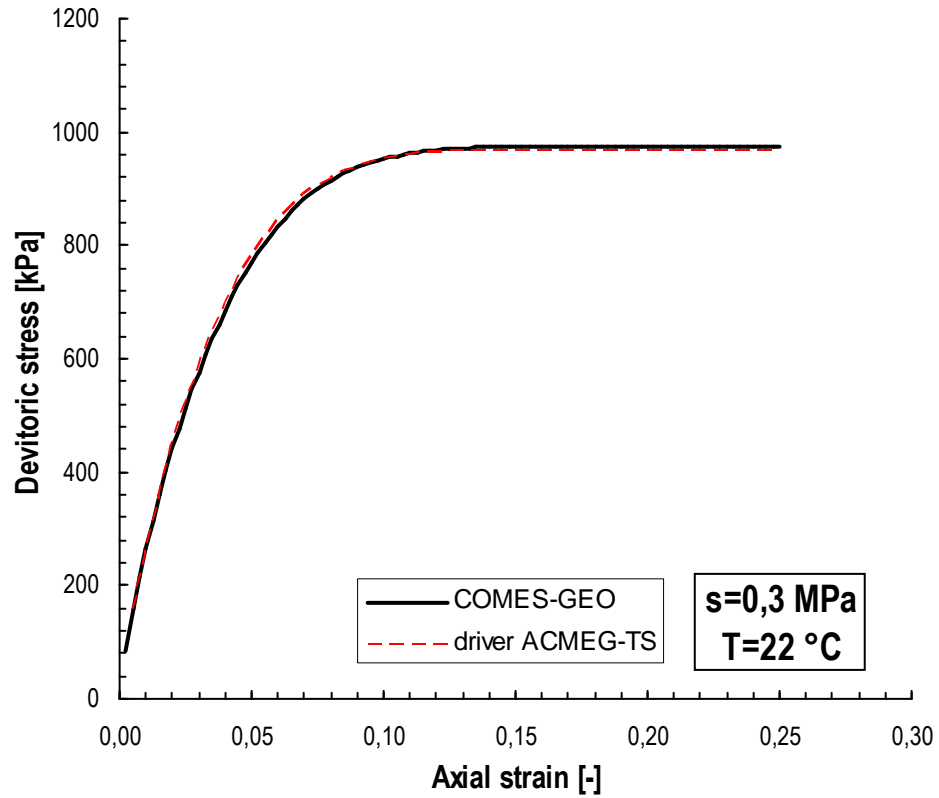


Figure 5.28: Axial strain versus Deviatoric Stress for $s=0.3 \text{ MPa}$ and $T=22 \text{ }^\circ\text{C}$

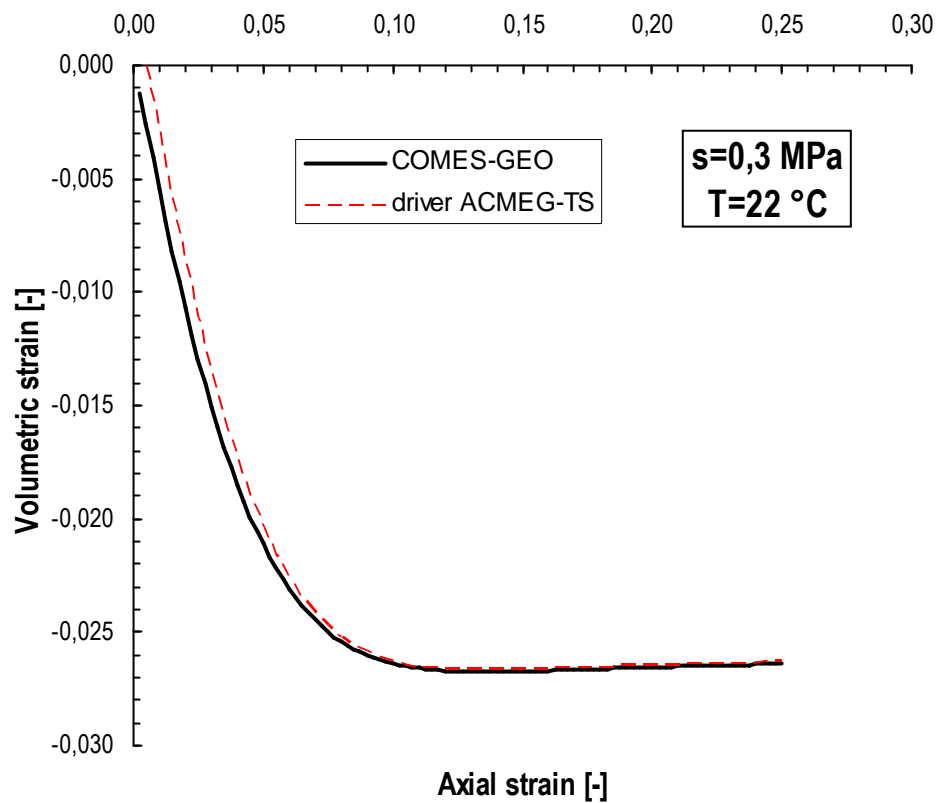


Figure 5.29: Axial strain versus Volumetric strain for $s=0.3 \text{ MPa}$ and $T=22 \text{ }^\circ\text{C}$

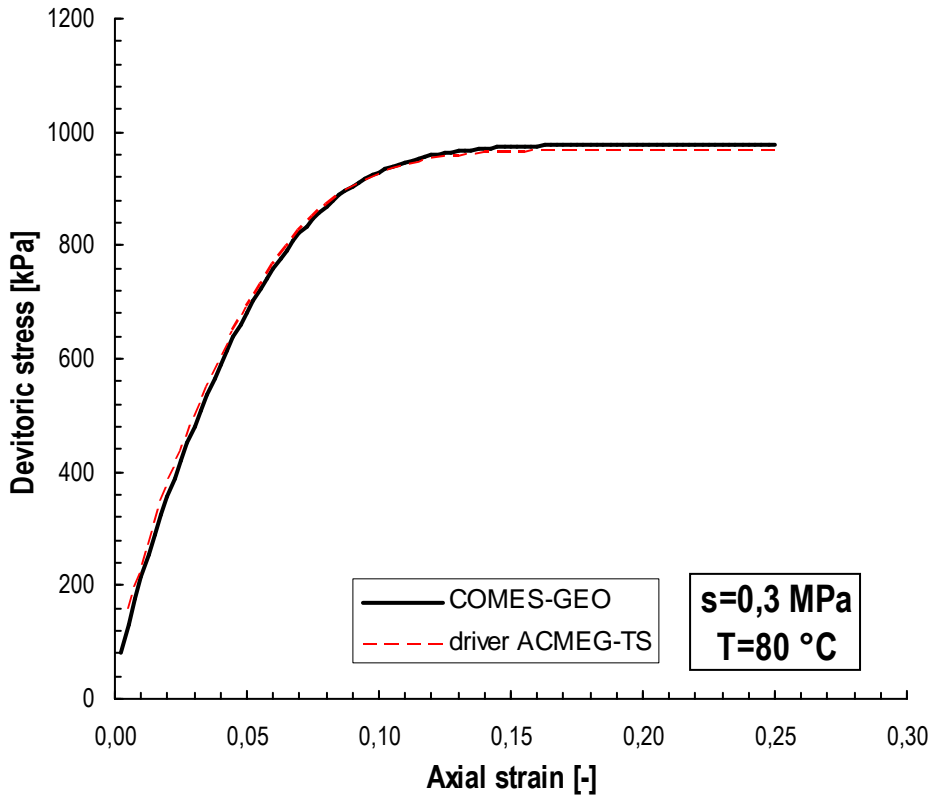


Figure 5.30: Axial strain versus Deviatoric Stress for $s=0.3$ MPa and $T=80$ °C

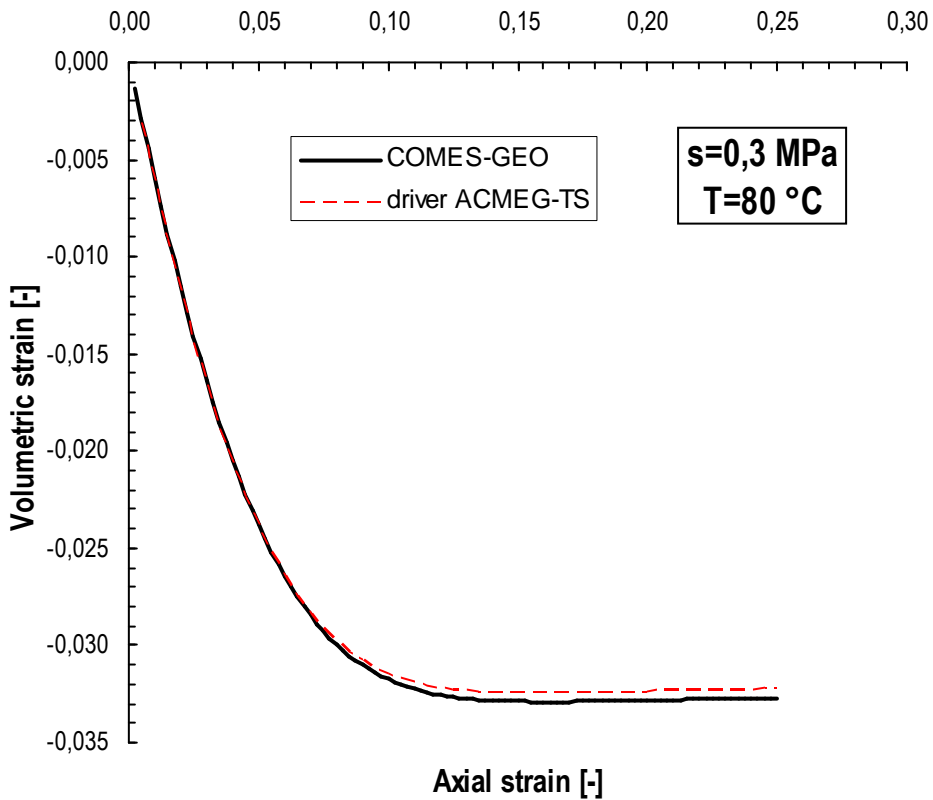
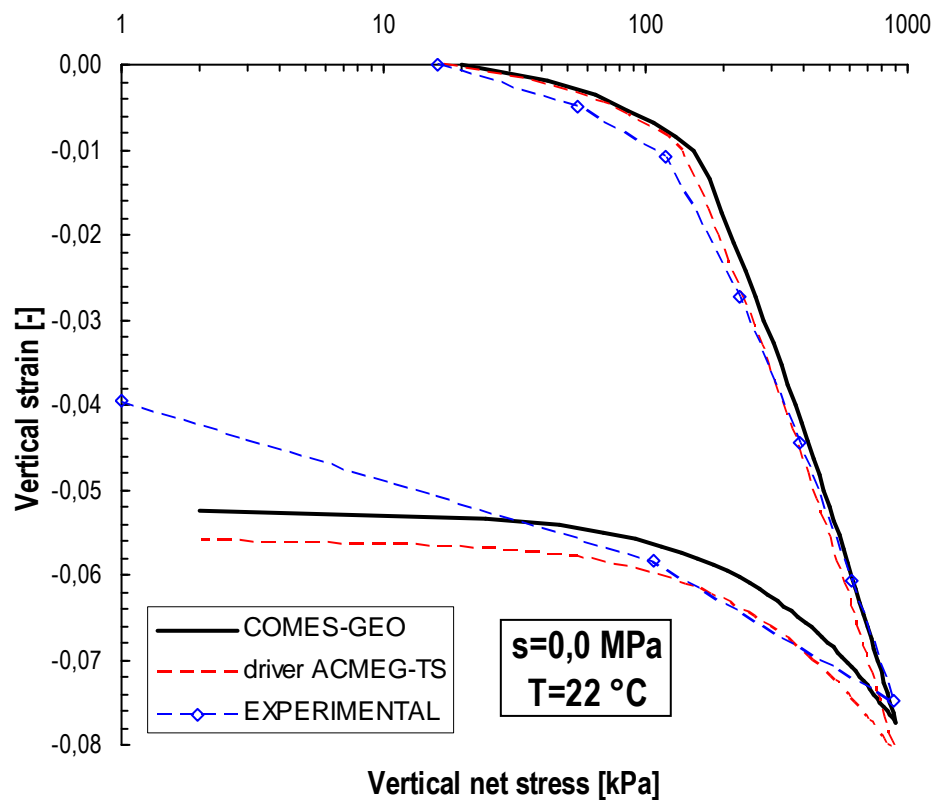
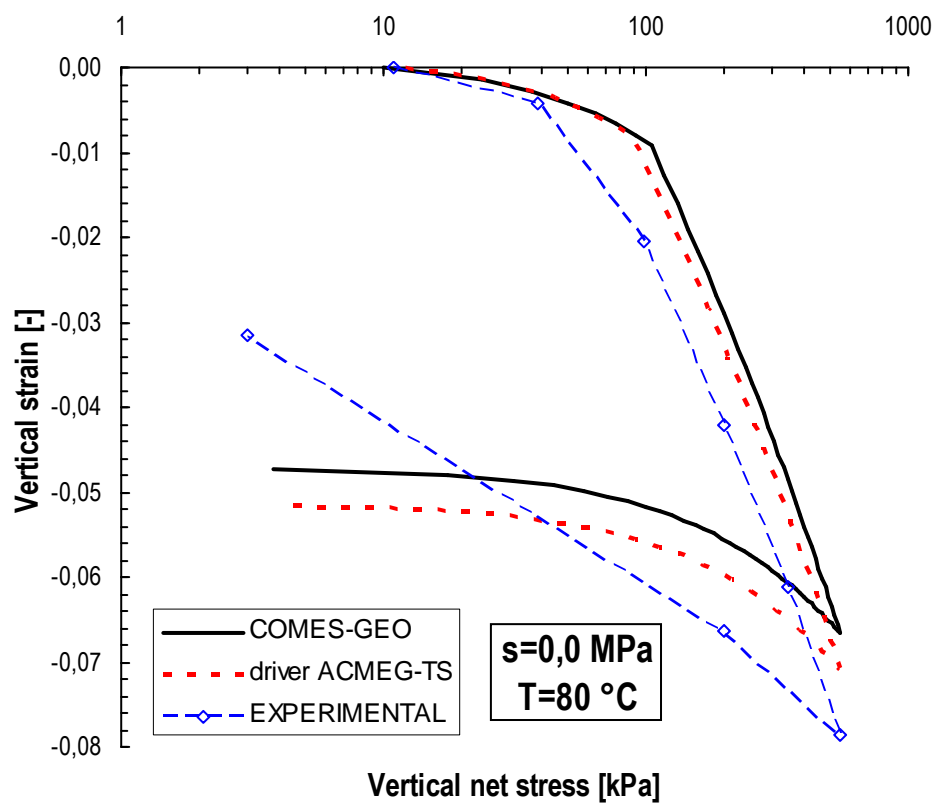


Figure 5.31: Axial strain versus Volumetric strain for $s=0.3$ MPa and $T=80$ °C

5.4.2.2 Oedometric tests

Figure 5.32: Vertical net Stress versus Axial strain for $s=0.0$ MPa and $T=22$ °CFigure 5.33: Vertical net Stress versus Axial strain for $s=0.0$ MPa and $T=80$ °C

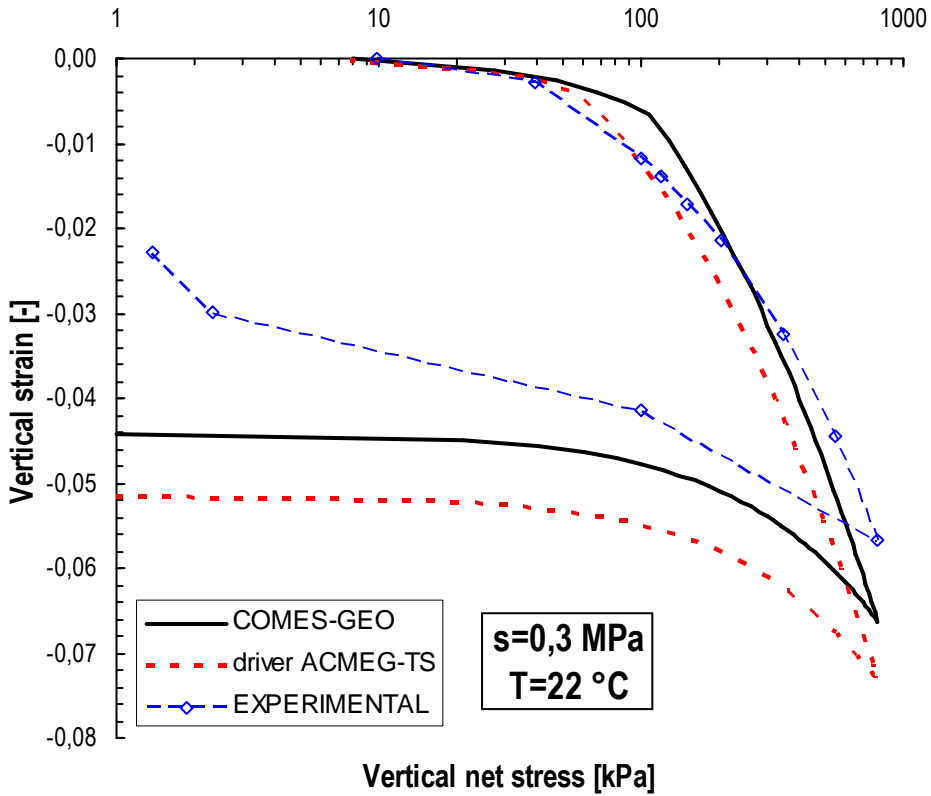


Figure 5.34: Vertical net Stress versus Axial strain for $s=0.3 \text{ MPa}$ and $T=22 \text{ }^\circ\text{C}$

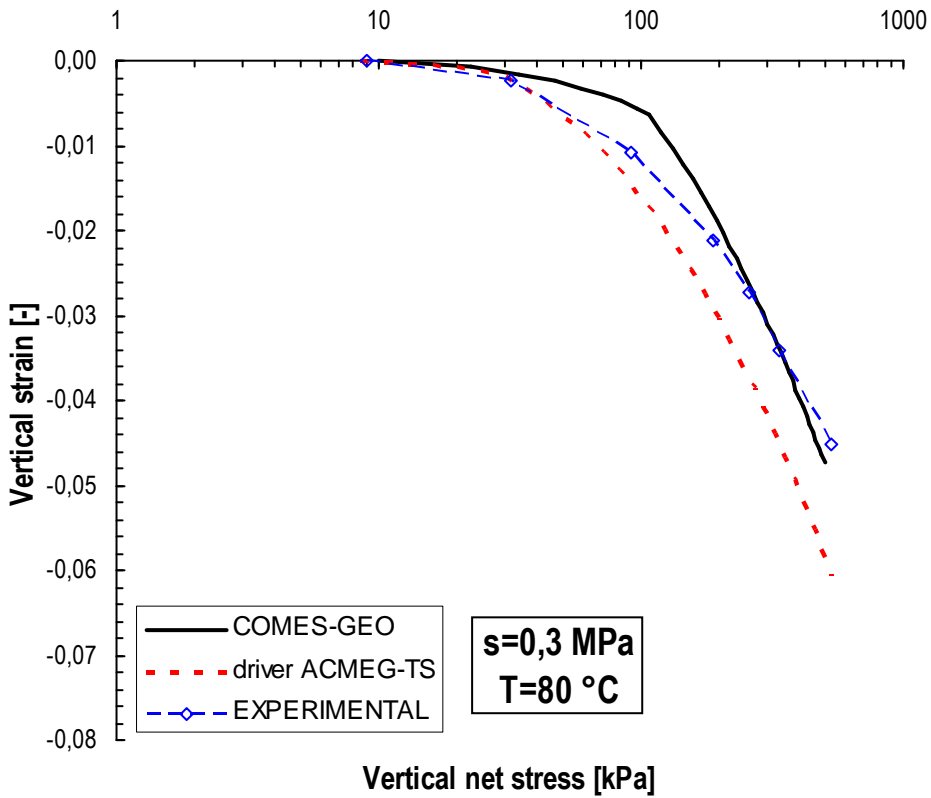


Figure 5.35: Vertical net Stress versus Axial strain for $s=0.3 \text{ MPa}$ and $T=80 \text{ }^\circ\text{C}$

A good agreement between the driver and the F.E.M results is shown for both the triaxial and oedometric tests.

The differences on Figure 5.32 to Figure 5.35 are due to the not accurate evaluation of the material parameters because of the initial slurry state of the samples.

References

- [Ait60] Aitchison G.D. (1960). Relationships of moisture stress and effective stress functions in unsaturated soils. Pore Pressure and Suction in Soils, London, Butterworths: 47-52.
- [B&C64] Brooks, R.J., and Corey, A.T., Hydraulic properties of porous media, Hydrology Papers 3, Colorado State University, Fort Collins, 1964.
- [Bor04] Borja R.I. (2004). Cam-Clay plasticity. Part V: A mathematical framework for three-phase deformation and strain localization analyses of partially saturated porous media. Computer Methods in Applied Mechanics and Engineering, 193: 5301-5338.
- [F&L08] François B. and Laloui L. (2008a). ACMEG-TS: A constitutive model for unsaturated soils under non-isothermal conditions. International Journal for Numerical and Analytical Methods in Geomechanics, 32: 1955-1988.
- [Fra08] François B. (2008). Thermo-Plasticity of Fine-Grained Soils at Various Saturation States: Application to Nuclear Waste Disposal. PhD Thesis. École Polytechnique Fédérale De Lausanne. Suisse.
- [Gei99] Geiser F. (1999). Comportement mécanique d'un limon non saturé: Etude expérimentale et modélisation constitutive. PhD Thesis, EPFL, Lausanne, Switzerland.
- [Huj79] Hujoux J.C. (1979). Calcul numérique de problèmes de consolidation élastoplastique. PhD Thesis, Ecole Centrale, Paris.
- [K&K98] Khalili N. and Khabbaz M.H. (1998). A unique relationship for x for the determination of the shear strength of unsaturated soils. Géotechnique, 48(5): 681-687.
- [L&C03] Laloui L. and Cekerevac C. (2003). Thermo-plasticity of clays: An isotropic yield mechanism, Computers and Geotechnics, 30(8): 649-660.
- [L&L04] Likos W.J. and Lu N. (2004). Hysteresis of capillary stress in unsaturated granular soil. Journal of Engineering Mechanics, ASCE, 130(6): 646-655.
- [L&S98] Lewis R.W. and Schrefler B.A. The Finite Element Method in the Static and Dynamic Deformation and Consolidation of Porous Media. J. Wiley, Chichester 1998.
- [N&L07] Nuth M. and Laloui L. (2007). New insight into the unified hydro-mechanical constitutive modeling of unsaturated soils. 3rd Asian Conference on Unsaturated Soils, Nanjing, China: 109-125.
- [N&L08] Nuth M. and Laloui L. (2008). Effective stress concept in unsaturated soils: clarification and validation of a unified framework. International Journal of Numerical and Analytical Methods in Geomechanics; 32(7): 771-801.
- [Rom99] Romero E. (1999). Characterisation and thermo-mechanical behaviour of unsaturated Boom clay: An experimental study. PhD Thesis, UPC, Barcelona.
- [S&P77] Nader M. Safai and George F. Pinder, Simulation of saturated-unsaturated deformable porous media, Water Resources Program, Department of Civil Engineering, Princeton University. Princeton, N. J. 08540
- [Sch84] Schrefler B.A. (1984). The finite element method in soil consolidation (with applications to surface subsidence). PhD Thesis. University College of Swansea, C/Ph/76/84.
- [Tan08] Tang A.M., Cui Y.J and Barnel N. (2008). Thermo-mechanical behaviour of a compacted swelling clay. Géotechnique, 58(1). 45-54.

-
- [Ter36] Terzaghi K. (1936). The shearing resistance of saturated soils and the angle between the planes of shear. 1st International Conference on Soil Mechanics and Foundations Engineering, Cambridge 1: 54-56.
- [Zer91] Zerhouni M.I. (1991). Rôle de la pression interstitielle négative dans le comportement des sols - application au calcul des routes. PhD Thesis. Ecole Centrale Paris.

6 THE GENERALIZED PLASTICITY MODEL FOR WATER SATURATED SANDS

The second class of constitutive laws, shown in this chapter and the following, is based on the generalised plasticity theory by Zienkiewicz and Morz [Z&M84] [M&Z84].

In this chapter the Pastor-Zienkiewicz model for sand under monotonic and cyclic loading is presented [Zie85] [Pas85] [P&Z86] following [Pas90]. This model can be applied also for clay [Pas90]. Then the validation of the implementation of this constitutive model is presented.

This model was developed to reproduce phenomena as liquefaction, cycling mobility or densification under cyclic loading. After the PZ model other models have been proposed during years to study the above mentioned phenomena but in any case they are more complex than the generalized plasticity.

The main advantage of the proposed model is that no plastic potential or yield surface are needed to be explicitly defined and hence neither the consistency rule need to be applied.

6.1 GENERALIZED PLASTICITY

The incremental non-linear constitutive relationship between strain and stress can be written as

$$d\boldsymbol{\sigma}' = \mathbf{D} : d\boldsymbol{\varepsilon} \quad [6.1]$$

where $\boldsymbol{\sigma}'$ is the stress tensor

\mathbf{D} is the elastoplastic constitutive tensor

$\boldsymbol{\varepsilon}$ is the strain tensor

The inverse relation of [6.1] is

$$d\boldsymbol{\varepsilon} = \mathbf{C} : d\boldsymbol{\sigma}' \quad [6.2]$$

Both the tensor \mathbf{D} and \mathbf{C} depend on the current state variables and on the directions of loading. If we indicate with λ the direction of loading and with α the state variables, then we can write

$$\mathbf{D} = \mathbf{D}(\lambda, \boldsymbol{\sigma}', \alpha) \quad [6.3]$$

$$\mathbf{C} = \mathbf{C}(\lambda, \boldsymbol{\sigma}', \alpha) \quad [6.4]$$

with

$$\lambda = \frac{d\boldsymbol{\sigma}'}{(\boldsymbol{\sigma}' : d\boldsymbol{\sigma}')^{\frac{1}{2}}} \quad [6.5]$$

Constitutive tensors should be such that all materials symmetries are preserved. This model further assume that deformation of the material can be considered as the result of deformations produced by M separate mechanism, all of these subjected to the same state of stress (series models).

The strain increment can be written as

$$d\boldsymbol{\epsilon} = \sum_{m=1}^M d\boldsymbol{\epsilon}^{(m)} \quad [6.6]$$

And, from [6.2] follows that

$$d\boldsymbol{\epsilon} = \sum_{m=1}^M \mathbf{C}^{(m)} : d\boldsymbol{\sigma}' \quad [6.7]$$

$$\mathbf{C} = \sum_{m=1}^M \mathbf{C}^{(m)} \quad [6.8]$$

If irreversible strain are to be produced, the constitutive tensor has to be dependent on the increment of stress direction, otherwise application of $d\boldsymbol{\sigma}'$ followed by $-d\boldsymbol{\sigma}'$ will produce an increment of strain

$$\mathbf{C} : d\boldsymbol{\sigma}' + \mathbf{C} : (-d\boldsymbol{\sigma}') = 0 \quad [6.9]$$

and hence no plastic permanent deformation can be induced.

For practical purposes, two directions of $d\boldsymbol{\sigma}'$ provide a sufficiently accurate description of the material behaviour during loading and unloading.

To this end, a direction vector $\mathbf{n}^{(m)}$ in the stress space discriminating between loading and unloading, that depends on $\boldsymbol{\sigma}'$ and α , is thus postulated for each mechanism.

This of course defines a set of surfaces which are equivalent to those used in classical plasticity but these surfaces need never be explicitly defined.

Loading and unloading are defined by

$$d\boldsymbol{\sigma}' : \mathbf{n}^m > 0 \quad [6.10]$$

$$d\boldsymbol{\sigma}' : \mathbf{n}^m < 0 \quad [6.11]$$

There is a limit case of neutral loading which is defined as

$$d\boldsymbol{\sigma}' : \mathbf{n}^m = 0 \quad [6.12]$$

The above definitions hold for hardening and perfecting plastic materials and will be generalized to account for softening later. Incremental stress-strain relations for a single mechanism (m) thus have the form

$$d\boldsymbol{\epsilon}^{(m)} = \mathbf{C}^{L(m)} : d\boldsymbol{\sigma}' \quad \text{loading} \quad [6.13]$$

$$d\boldsymbol{\epsilon}^{(m)} = \mathbf{C}^{U(m)} : d\boldsymbol{\sigma}' \quad \text{unloading} \quad [6.14]$$

Continuity between loading and unloading processes requires that constitutive tensors $\mathbf{C}^{L(m)}$ and $\mathbf{C}^{U(m)}$ are of the form [Z&M84]

$$\mathbf{C}^{L(m)} = \mathbf{C}^{e(m)} + \frac{1}{H_L} \mathbf{n}_{gL}^{(m)} \otimes \mathbf{n}^{(m)} \quad [6.15]$$

$$\mathbf{C}^{U(m)} = \mathbf{C}^{e(m)} + \frac{1}{H_U} \mathbf{n}_{gU}^{(m)} \otimes \mathbf{n}^{(m)} \quad [6.16]$$

where $\mathbf{n}_{gL/U}$, are arbitrary unit tensors and $H_{L/U}$, are plastic moduli corresponding to loading and unloading.

It can be verified that both laws predict the same strain increment under neutral loading in which both expressions are valid and hence non-uniqueness is avoided.

Material behaviour under neutral loading is reversible and it can therefore be regarded as elastic, as, given an infinitesimal cycle $+d\boldsymbol{\sigma} \rightarrow -d\boldsymbol{\sigma}$, we will have

$$d\boldsymbol{\varepsilon}^{(m)} = \mathbf{C}^{L(m)} : d\boldsymbol{\sigma}' + \mathbf{C}^{U(m)} : (-d\boldsymbol{\sigma}') = 0 \quad [6.17]$$

In small strains, the increment of strain caused by the mechanism (m) due to $d\boldsymbol{\sigma}'$ can thus be assumed to have two components, elastic and plastic, and

$$d\boldsymbol{\varepsilon}^{(m)} = d\boldsymbol{\varepsilon}^{e(m)} + d\boldsymbol{\varepsilon}^{p(m)} \quad [6.18]$$

where

$$d\boldsymbol{\varepsilon}^{e(m)} = \mathbf{C}^{e(m)} : d\boldsymbol{\sigma}' \quad [6.19]$$

$$d\boldsymbol{\varepsilon}^{p(m)} = \frac{1}{H_{L/U}} [\mathbf{n}_{gL/U}^{(m)} \otimes \mathbf{n}^{(m)}] : d\boldsymbol{\sigma}' \quad [6.20]$$

We note that irreversible plastic deformations have been introduced without the need for specifying any yield or plastic potential surfaces, nor hardening rules. All that is necessary to specify the behaviour for mechanism (m) are two scalar functions $H_{L/U}$ and three directions, $\mathbf{n}_{gL/U}$ and \mathbf{n} .

To account for softening behaviour of material, i.e. when H_L is negative, definitions of loading and unloading haven to be modified. We can now write

$$\mathbf{n}^{(m)} : d\boldsymbol{\sigma}'^{e(m)} > 0 \quad \text{loading} \quad [6.21]$$

$$\mathbf{n}^{(m)} : d\boldsymbol{\sigma}'^{e(m)} = 0 \quad \text{neutral loading} \quad [6.22]$$

$$\mathbf{n}^{(m)} : d\boldsymbol{\sigma}'^{e(m)} < 0 \quad \text{unloading} \quad [6.23]$$

where

$$d\boldsymbol{\sigma}'^{e(m)} = \mathbf{C}^{e(m)-1} : d\boldsymbol{\varepsilon}^{(m)} \quad [6.24]$$

It is easily verified that for positive definite $\mathbf{C}^{e(m)}$ the two definitions are identical when no softening exists.

Finally, total increment of strain is given by the summation of all mechanism

$$d\boldsymbol{\varepsilon} = \sum_{m=1}^M \mathbf{C}^{e(m)} : d\boldsymbol{\sigma}' + \sum_{m=1}^M \frac{1}{H_{L/U}} [\mathbf{n}_{gL/U}^{(m)} \otimes \mathbf{n}^{(m)}] : d\boldsymbol{\sigma}' \quad [6.25]$$

or, the equivalent

$$d\boldsymbol{\varepsilon} = \mathbf{C}_{L/U}^{ep} : d\boldsymbol{\sigma}' \quad [6.26]$$

Inversion of \mathbf{C}^{ep} will give \mathbf{D}^{ep} as

$$\mathbf{D}^{ep} = \mathbf{D}^e - \mathbf{D}^e \mathbf{n}_{gL/U} \mathbf{B}^{-1} \mathbf{D}^e \quad [6.27]$$

where $\mathbf{n} = \{ \mathbf{n}^m \}$

$$\mathbf{n}_{gL/U} = \{ \mathbf{n}_{gL/U}^m \}$$

and matrix \mathbf{B} is [Pas90]

$$\mathbf{B} = \mathbf{H} + \mathbf{n}^T \mathbf{D}^e \mathbf{n}_{gL/U} \quad [6.28]$$

where $\mathbf{H}_{ij} = \delta_{ij} \mathbf{H}_i^{(m)}$

It is possible to prove that the classical plasticity theory and the bounding surface models are a particular case of the theory outlined above [Pas90].

6.2 PASTOR-ZIENKIEWICZ MODEL FOR SAND

The behaviour of sands is considerably different, in fact under drained monotonic loading, dense and loose sands exhibit different characteristic stress-strain curves, which reach a common residual asymptotic state.

However, while very loose sands behaviour can be reproduced by critical state models, dense sands show a peak in deviatoric stress after which the material softens and local effects such as shear band development begin, making it difficult to analyse the experimental results.

Even if such phenomena obscure the test results, it seems logical to believe that a peak should exist, although less pronounced than the ones shown by standard experiments. This pattern could only be qualitatively reproduced by critical state models if the sand were to be assumed heavily overconsolidated (Figure 6.1).

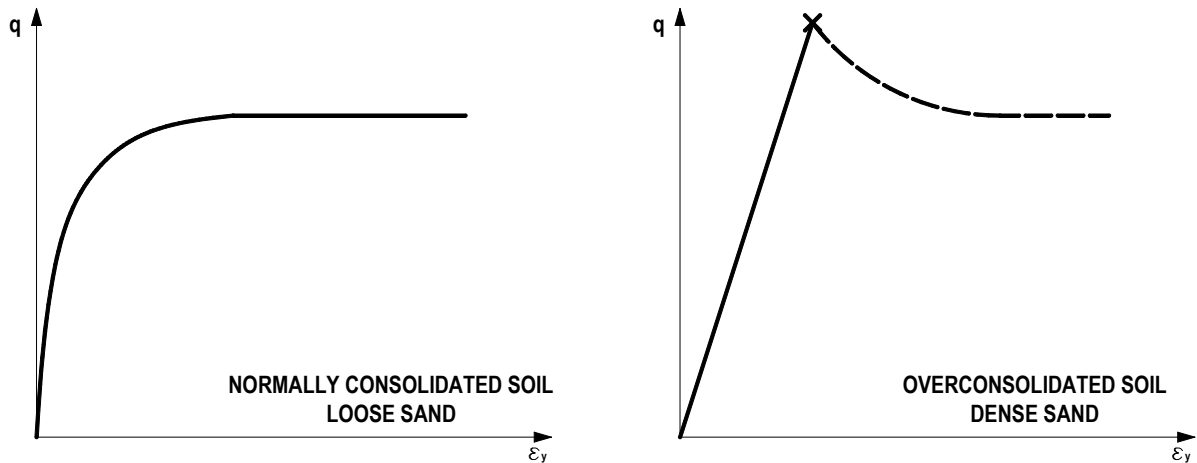


Figure 6.1: Predictions of a Classical Plasticity Model for NC and OC soils and loose and dense sands

However, with such a model, if the confining pressure is raised, a change from dense to loose behaviour for a dense sand is predicted and accuracy decreases.

A more suitable form of plastic potential can be derived from the analysis of plastic deformations under shearing. If crushing of sand grains is neglected, particle rearrangement under shear produces volumetric and shear strains related by dilatancy rules.

Following the experimental results obtained by Frossard [Fro83] in drained triaxial tests it may be observed that dilatancy d_g can be approached by a linear function of the stress ratio η

$$d_g = (1 + \alpha_g)(M_g - \eta) \tag{6.29}$$

where α_g and M_g are material parameters

and where η is defined as

$$\eta = \frac{q}{p'} \tag{6.30}$$

q and p' are two of the three stress invariant that are defined as

$$p' = \frac{1}{3} J_1 = \frac{1}{3} (\sigma'_x + \sigma'_y + \sigma'_z) \quad [6.31]$$

$$q = \sqrt{3J_2'} = \sqrt{\frac{3}{2} [(\sigma'_x - p')^2 + (\sigma'_y - p')^2 + (\sigma'_z - p')^2 + 2(\tau_{xy}^2 + \tau_{yz}^2 + \tau_{zx}^2)]} \quad [6.32]$$

$$\vartheta = \frac{1}{3} \sin^{-1} \left(-\frac{3\sqrt{3}}{2} \frac{J_3'}{J_2'^{\frac{3}{2}}} \right) \quad [6.33]$$

where

$$J_1 = \text{tr}(\boldsymbol{\sigma}') = \sigma'_x + \sigma'_y + \sigma'_z \quad [6.34]$$

$$J_2 = \sigma'_x \sigma'_y + \sigma'_y \sigma'_z + \sigma'_z \sigma'_x - \tau_{xy} \tau_{yx} - \tau_{yz} \tau_{zy} - \tau_{xz} \tau_{zx} \quad [6.35]$$

$$J_3 = \det(\boldsymbol{\sigma}') \quad [6.36]$$

$$J_2' = \frac{1}{3} (J_1^2 - 3J_2) \quad [6.37]$$

$$J_3' = \frac{1}{27} (2J_1^3 - 9J_1 J_2 + 27J_3) \quad [6.38]$$

It may be seen that dilatancy is zero at the line

$$(M_g = \eta) \Rightarrow d_g = 0 \quad [6.39]$$

which coincides with the projection on the p' - q plane of the critical state line. Also, note that the flow is non-associated and the dilatancy serves only in determining the strain vector η .

Once again the zero dilatancy line M_g represents all residual stress states as continuing yield can only be sustained without volume changes without creating (or destroying) material.

The plastic flow directions \mathbf{n}_{gLU} that from now we call \mathbf{m} to simplify the following relations [Mir09], and the loading direction \mathbf{n} , are expressed as

$$\mathbf{m} = m_v \cdot \mathbf{u}_1 + m_s \cdot \mathbf{u}_2 + m_\vartheta \cdot \mathbf{u}_3 \quad [6.40]$$

$$\mathbf{n} = n_v \cdot \mathbf{u}_1 + n_s \cdot \mathbf{u}_2 + n_\vartheta \cdot \mathbf{u}_3 \quad [6.41]$$

where the base vectors \mathbf{u}_1 , \mathbf{u}_2 and \mathbf{u}_3 are the derivatives of the stress invariants p' , q , ϑ with respect to the stress $\boldsymbol{\sigma}'$.

$$\mathbf{u}_1 = \begin{bmatrix} 1 \\ \frac{1}{3} \\ \frac{1}{3} \\ \frac{1}{3} \\ 0 \end{bmatrix} \quad [6.42]$$

$$\mathbf{u}_2 = \begin{bmatrix} \frac{S_1}{2\sqrt{\frac{J'_2}{3}}} \\ \frac{S_2}{2\sqrt{\frac{J'_2}{3}}} \\ \frac{S_3}{2\sqrt{\frac{J'_2}{3}}} \\ \frac{S_4}{2\sqrt{\frac{J'_2}{3}}} \end{bmatrix} \quad [6.43]$$

$$\mathbf{u}_3 = \begin{bmatrix} \frac{1}{3} \operatorname{tg}(3\psi) \left[\frac{1}{3} \frac{J'_2}{J'_3} + \frac{S_2 S_3}{J'_3} - \frac{3 S_1}{2 J'_2} \right] \\ \frac{1}{3} \operatorname{tg}(3\psi) \left[\frac{1}{3} \frac{J'_2}{J'_3} + \frac{S_1 S_3}{J'_3} - \frac{3 S_2}{2 J'_2} \right] \\ \frac{1}{3} \operatorname{tg}(3\psi) \left[\frac{1}{3} \frac{J'_2}{J'_3} + \frac{S_1 S_2 - S_4^2}{J'_3} - \frac{3 S_3}{2 J'_2} \right] \\ \frac{1}{3} \operatorname{tg}(3\psi) \left[-\frac{S_3 S_4}{J'_3} - \frac{3 S_4}{2 J'_2} \right] \end{bmatrix} \quad [6.44]$$

where $S_i = \sigma'_i - p'$ $i=1,2,3$

$$S_4 = \sigma'_4$$

For loading stress increments, the \mathbf{m}_L components are given by [N&W79]

$$\mathbf{m}_{L,v} = \frac{d_g}{\sqrt{1+d_g^2}} \quad [6.45]$$

$$\mathbf{m}_{L,s} = \frac{1}{\sqrt{1+d_g^2}} \quad [6.46]$$

$$\mathbf{m}_{L,\psi} = \frac{-qM_g \cos(3\psi)}{2\sqrt{1+d_g^2}} \quad [6.47]$$

In unloading conditions irreversible strains are contractive. Hence the \mathbf{m}_U components change as follows:

$$\mathbf{m}_{U,v} = -|\mathbf{m}_{L,v}| \quad [6.48]$$

$$\mathbf{m}_{U,s} = \mathbf{m}_{L,s} \quad [6.49]$$

$$\mathbf{m}_{U,\psi} = \mathbf{m}_{L,\psi} \quad [6.50]$$

The model assumes a non-associated flow rule; thus, the loading direction \mathbf{n} is different from \mathbf{m} , but with similar expressions for its components $\mathbf{n}_v, \mathbf{n}_s, \mathbf{n}_\psi$ that are given by

$$\mathbf{n}_v = \frac{d_f}{\sqrt{1+d_f^2}} \quad [6.51]$$

$$\mathbf{n}_s = \frac{1}{\sqrt{1+d_f^2}} \quad [6.52]$$

$$\mathbf{n}_\vartheta = \frac{-qM_f \cos(3\vartheta)}{2\sqrt{1+d_f^2}} \quad [6.53]$$

where

$$d_f = (1 + \alpha_f)(M_f - \eta) \quad [6.54]$$

with α_f and M_f material parameters

The PZ model assumes a non-linear elastic response of the soils. As in a large number of constitutive models, the non-linear reversible behaviour is described by Pastor et al. [Pas90] through a hypoelastic approach, in which the tangent bulk modulus K and shear modulus G only depend on the hydrostatic part of the effective stress tensor, according to the following relationships

$$K = K_{ref} \left(\frac{p'}{p'_{ref}} \right)^{n_e} \quad [6.55]$$

$$G = G_{ref} \left(\frac{p'}{p'_{ref}} \right)^{n_e} \quad [6.56]$$

where K_{ref} is the bulk modulus at the reference mean effective stress p'_{ref}

G_{ref} is the bulk modulus at the reference mean effective stress p'_{ref}

n_e is a material parameters that in PZ model is assumed $n_e=1$

hence

$$K = K_{ref} \frac{p'}{p'_{ref}} \quad [6.57]$$

$$G = G_{ref} \frac{p'}{p'_{ref}} \quad [6.58]$$

Although widely used, one of the major shortcomings of such hypoelastic formulation is that it results in a non-conservative elastic response and energy dissipation over closed stress paths [Zyt78].

In recent years attempts (e.i. [Lor85] [L&N87] [Mol88]) have been made to describe the elastic response of soils within a conservative framework and a number of energy-conserving elastic models have been proposed in the literature.

6.2.1 PZ in loading conditions

As suggested in [Z&P77] M_{gf} is assumed to depend on lode's angle ϑ . The model define a smoothed version of Mohr's criterion widely used in practice

$$M_g = \frac{18M_g^c}{18 + 3(1 - \sin(3\vartheta))} \quad [6.59]$$

$$M_f = \frac{18M_f^c}{18 + 3(1 - \sin(3\vartheta))} \tag{6.60}$$

where $M_{g/f}$ are the critical state line slope

It has to be remarked that both directions have been defined without reference to any yield or potential surfaces, though of course these can be established a posteriori.

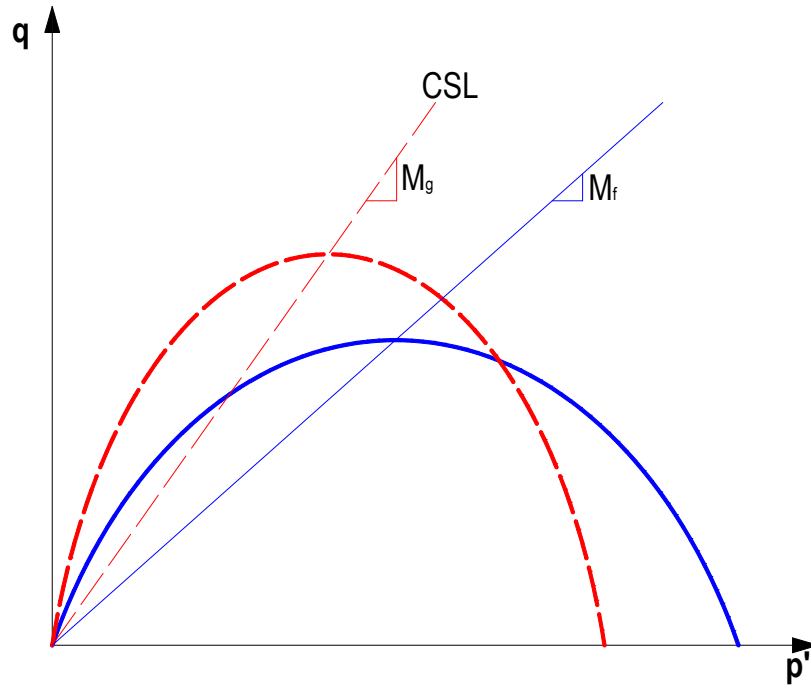


Figure 6.2: Theoretical yield surface (Equations [6.57] [6.58])

A classical plasticity model would require obtaining those surfaces from m_L and n by integration arriving at

$$f = \left\{ q - M_f p' \left(1 + \frac{1}{\alpha} \right) \left[1 - \left(\frac{p'}{p_c} \right)^\alpha \right] \right\} \tag{6.61}$$

$$g = \left\{ q - M_g p' \left(1 + \frac{1}{\alpha} \right) \left[1 - \left(\frac{p'}{p_g} \right)^\alpha \right] \right\} \tag{6.62}$$

A relative position of yield and flow surfaces indicates the possibility of material densification occurring in most of the loading region which coincides with observed facts.

If we now consider the behaviour under undrained conditions a critical state model with modified surfaces such as given by expression [6.48] can perform correctly for very loose to medium loose states in monotonic triaxial loading.

Modelling of the behaviour of very dense sands still causes difficulties as failure occurs as soon as the critical state line is reached.

As proposed by Pastor et al. [Pas85], the relative density of sands can be expressed by

$$D_R = \frac{M_f}{M_g} \tag{6.63}$$

D_R values for the various types of sand are given in Table 6.1.

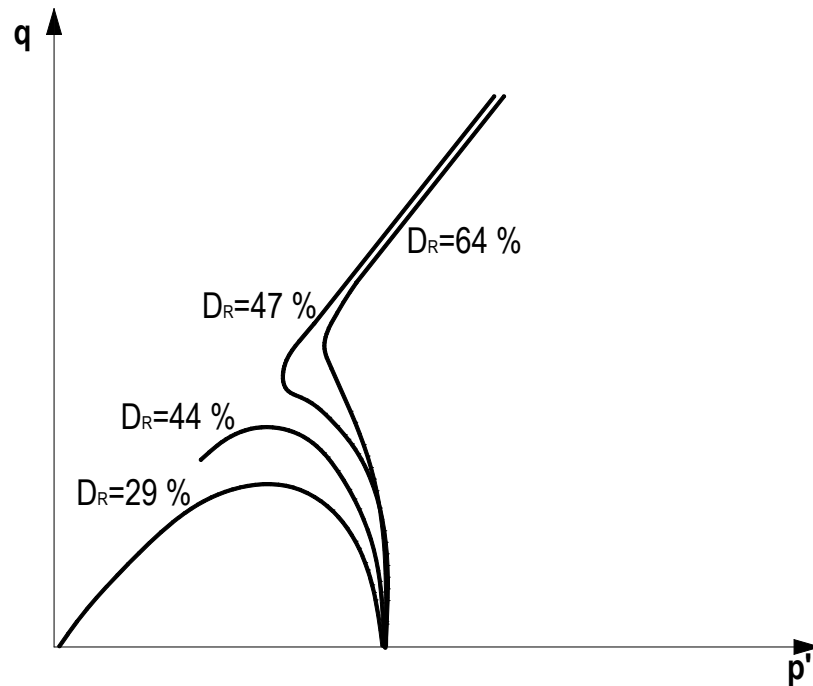


Figure 6.3: Schematic behaviour of undrained sand (from [Cas69]) for different D_R of material

D_R [%]	Type
0-20	Very loose
20-40	Loose
40-60	Medium
60-80	Dense
80-100	Very dense

Table 6.1: Classification of sands for different D_R

A solution for the difficulties in the modelling of very dense sands is to introduce deviatoric strain hardening as suggested by Wilde [Wil77] and indeed incorporated earlier in equation, that we will see later, that give the hardening modulus H_L .

For this reasons, we now can make the surface size parameter p_c such that

$$\frac{\partial p_c}{\partial \varepsilon_v^p} = \frac{1+e}{\lambda-\kappa} p_c \quad [6.64]$$

and then define

$$\frac{\partial p_c}{\partial \xi} = \beta_0 \beta_1 e^{-\beta_0 \xi} \quad [6.65]$$

where ξ is the accumulated deviatoric plastic strain

λ is the slope of virgin loading in isotropic compression

κ is the slope of virgin reloading in isotropic compression

The parameter λ is strongly dependent on the confining pressure [L&S67], this only accounts for densification caused by crushing of sand grains, which is of secondary importance to the densification actually occurring owing to rearrangement under shear.

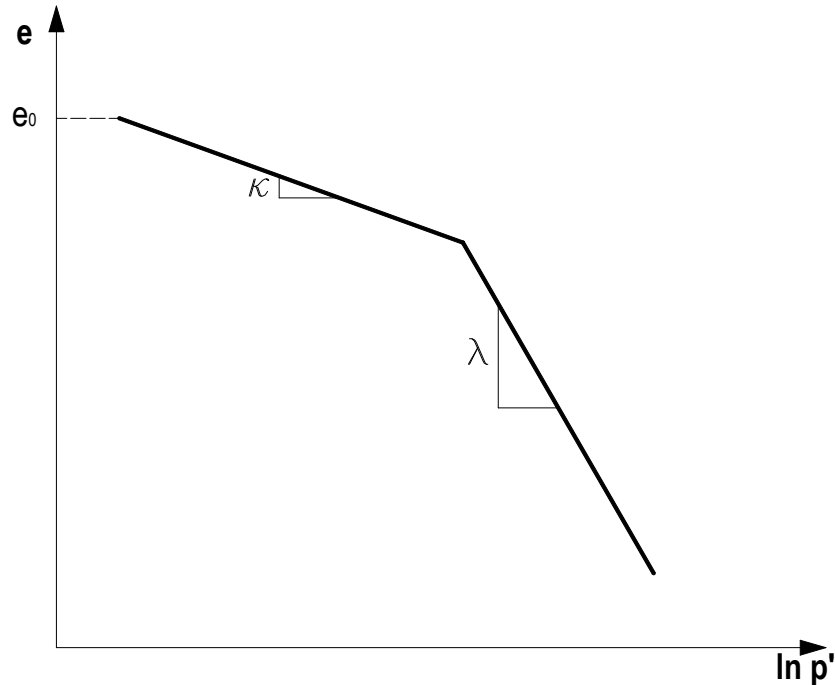


Figure 6.4: Graphical identification of κ and λ

It thus appears more logical to define the hardening modulus without reference to any consistency condition on the yield surface based on non realistic hardening laws and to return to the generalized plasticity forms without reference to any surfaces. With m and n_g defined previously, a suitable model can be directly constructed.

An expression for plastic modulus H_L has to take into account several well established experimental facts:

1. Residual conditions take place at the critical state line $\eta = M_g$.
2. Failure does not necessarily occur when this line is first crossed.
3. The frictional nature of material response requires the establishment of a boundary separating impossible exterior states from those which are permissible.

As suggested from [P&Z86] and [Pas90], a suitable expression accounting for the stiffness decrease as the shear plastic deformation increases and the material state get closer to the critical state for the plastic modulus in loading H_L is

$$H_L = H_0 \cdot p' \cdot H_f \cdot (H_v + H_s) \tag{6.66}$$

where

$$H_0 = \frac{1 + e_0}{\lambda - \kappa} \tag{6.67}$$

$$H_f = \left(1 - \frac{\eta}{\eta_f} \right)^4 \tag{6.68}$$

$$\eta_f = \left(1 + \frac{1}{\alpha_f}\right) M_f \quad [6.69]$$

$$H_v = 1 - \frac{\eta}{M_g} \quad [6.70]$$

$$H_s = \beta_0 \beta_1 e^{-\beta_0 \xi} \quad [6.71]$$

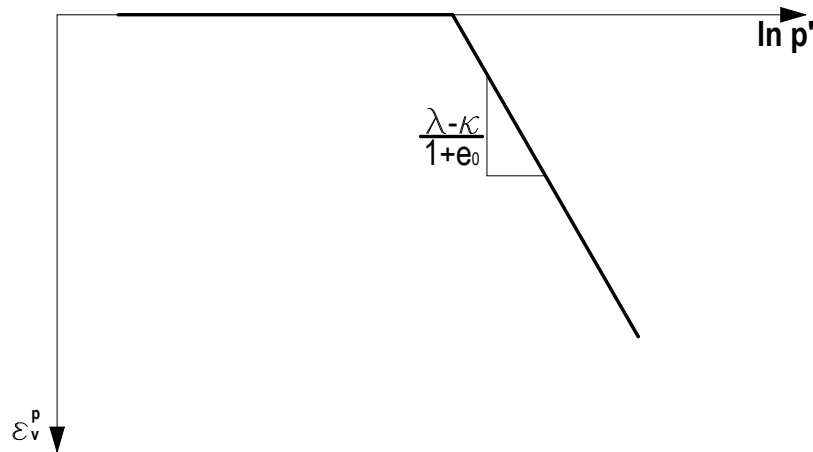


Figure 6.5: Graphical identification of H_0

6.2.1.1 Very loose sand liquefaction under undrained shearing

This case exhibits a peak in the deviatoric stress after which the strength is reduced to zero while the pore pressure increases continuously. In this case the stress path approaches the origin, and the soil loses its resistance to shear, reaching a liquefied state.

It must be emphasized that sand contracts or 'densifies' during the whole process which is shown by a continuous increase in pore pressure, suggesting in turn that hardening is taking place. This seems to be in contradiction to the fact that a peak exists and the material can be thought of as being softening, but in a frictional material strength has to be analysed in terms of stress ratios, and no peak is presented by this parameter.

This behaviour can be considered unstable in the sense of Drucker [Dru56] [Dru59]

$$d\sigma'^T d\epsilon^p < 0 \quad [6.72]$$

having thus

$$d\sigma'^T \left(\frac{1}{H} \mathbf{n}_g \mathbf{n}^T \right) d\sigma' < 0 \quad [6.73]$$

If such a feature is to be modelled with a positive plastic modulus, associated plasticity has to be abandoned by choosing

$$\mathbf{n}_g \neq \mathbf{n} \quad [6.74]$$

The modification introduced in the definition of equation [6.64] altering the critical state model described earlier is enough to deal with liquefaction under monotonic loading.

6.2.1.2 Deviatoric stress during drained shear of very dense sands

At the other end of the density range, peak exists in deviatoric stress during drained shear of very dense sand, this effect developing progressively as density is increased.

The factor H_s , is introduced in the expression [6.66] for the plastic modulus to account for

1. crossing of the critical state line ($\gamma = M_g$) without immediately producing failure;
2. reproduction of softening;
3. residual conditions taking place at CSL.

Deviatoric stress can be increased from zero in drained tests while H_v , and H_s decrease. Infact H_v reaches zero when CSL is crossed, taking negative values afterwards. A moment arrives at which

$$H_v + H_s = 0 \quad [6.75]$$

$$\gamma_p > M_g \quad [6.76]$$

If the test is run under strain control, at this point

$$dp' = dq = 0 \quad [6.77]$$

Immediately after the peak is reached, H_s , decreases while H_v does not, resulting in

$$H_v + H_s < 0 \quad [6.78]$$

and

$$H_L < 0 \quad [6.79]$$

From this moment, softening of the material will take place, producing a descending branch in deviatoric stress against axial strain plot.

Deviatoric strain hardening function H_s will vanish as deformations progress, reaching a final asymptotic value of zero. Residual conditions will then take place at CSL.

During the softening

$$d\sigma'^T d\epsilon^P < 0 \quad [6.80]$$

and

$$d\sigma'^T \left(\frac{1}{H} \mathbf{n}_g \mathbf{n}_g^T \right) d\sigma' < 0 \quad [6.81]$$

It can be seen that there is no need on this occasion for non associativeness to ensure the existence of peaks as H_L is negative, and, in fact, very dense sands exhibit the limiting associative behaviour with

$$M_g = M_f \quad [6.82]$$

6.2.1.3 Undrained shearing of medium loose to dense sands

The critical state line is reached and an upturn in the stress path produced as soil changes from contractive to dilative behaviour.

Determination of CSL position can easily be performed from a point at which the undrained stress path has a vertical tangent in p' - q space, as then

$$\begin{aligned}
 d\varepsilon_v^p &= 0 \\
 d\varepsilon_v^e &= 0 \\
 dp' &= 0
 \end{aligned}
 \tag{6.83}$$

Figure 6.3 shows how relative density influences the undrained behaviour of sand together with predictions of the proposed model.

6.2.1.4 Conclusion

At this point, a model has been developed such that

1. it reproduces the most salient features of sand under monotonic shearing;
2. no surfaces are involved and consistency conditions do not have to be fulfilled;
3. it is computationally efficient in FE codes, as the stress point does not have to be brought back to the yield surface and tangent moduli are easily established.

6.2.2 PZ in unloading conditions

A very important feature of sand behaviour is that plastic strains develop during unloading of the material, their importance increasing with the stress ratio from which unloading takes place, which is referred to the unloading stress ratio

$$\eta_u = \left(\frac{q}{p'} \right)_u
 \tag{6.84}$$

Elastic behaviour during undrained shearing is characterized by vertical stress path because the undrained nature of the test prevents volumetric strains from developing. It can be seen that unloading from a higher stress ratio results in higher plastic volumetric strain.

A simple expression for a plastic modulus fulfilling these requirements was proposed by Pastor et al. [Pas85]

$$\begin{aligned}
 H_u &= H_{u0} \left(\frac{M_g}{\eta_u} \right)^{\gamma_u} & \text{for } \left| \frac{M_g}{\eta_u} \right| > 1 \\
 H_u &= H_{u0} & \text{for } \left| \frac{M_g}{\eta_u} \right| \leq 1
 \end{aligned}
 \tag{6.85}$$

and extends the range of the model so far proposed hierarchically.

To determine the direction of plastic flow produced upon unloading Pastor et al. [Pas90] noted that irreversible strains are of contractive (densifying) nature.

Direction n_g are those described at [6.48], [6.49] and [6.50].

6.2.3 Liquefaction and cyclic mobility phenomena

When subject to drained cyclic loading of moderate amplitude, sand is observed to exhibit an overall densifying character. Under undrained conditions this mechanism causes progressive pore pressure buildup leading to failure.

In the case of very loose sands, liquefaction takes place following a series of cycles in which the stress path migrates towards lower confining pressures.

Denser sands do not exhibit liquefaction but cyclic mobility. Failure is progressive since the stress path approaches the CSL by its shift caused by the pore pressure buildup. Deformation during unloading causes the stress path to check towards the origin, and strains produced during the next loading branch are of higher amplitude.

Effects of the stress-strain history can be incorporated in the model with the largest intensity events superseding the memory of preceding ones.

Although the model so far developed predicts liquefaction satisfactorily, a further extension is necessary to account more accurately for cyclic loading phenomena.

This can be introduced by means of a new discrete memory factor H_{dm} multiplying the plastic modulus

$$H_L = H_0 \cdot p' \cdot H_f \cdot (H_v + H_s) \cdot H_{dm} \quad [6.86]$$

where

$$H_{dm} = \left(\frac{\zeta_{MAX}}{\zeta} \right)^\gamma \quad [6.87]$$

where ζ is a mobilized stress function defined as

$$\zeta = p' \left[1 - \left(\frac{1 + \alpha_f}{\alpha_f} \right) \frac{\eta}{M_f} \right]^{-\frac{1}{\alpha_f}} \quad [6.88]$$

Discrete memory factor is thus simply unity during virgin loading. After unloading, however, reloading takes place with a higher plastic modulus.

6.3 VALIDATION OF THE IMPLEMENTATION OF PZ MODEL IN COMES-GEO

Here experimental tests have been simulated with three different sands : Banding sand (section 6.3.1), Adige sand (section 6.3.2) and a dense sand (section 6.3.3). The results of the simulation with COMES-GEO have been compared with the experimental results (for Banding and Adige sands) and with the results obtained with the driver of the PZ model (for all the three simulations).

6.3.1 Banding sand

The first case simulated with the PZ model implemented in COMES-GEO is the one with $D_R=29\%$ shown in Figure 6.3 where a series of tests in sands at different relative density are simulated. These tests are triaxial compressions performed by Castro [Cas69] in undrained condition on Banding sand.

The material parameters are

Material parameters								
K_{ref} [MPa]	G_{ref} [MPa]	M_f	M_g	α_f	α_g	H_0	β_0	β_1
35.00	52.50	0.40	1.50	0.45	0.45	350	4.20	0.20

Table 6.2: Material parameters of the undrained tests performed by Castro [Cas69]

from which the Young's modulus E and the Poisson coefficient ν can be calculated

$$\nu = \frac{3K_{ref} - 2G_{ref}}{6K_{ref} + 2G_{ref}} = \frac{3 \cdot 35 - 2 \cdot 52.5}{6 \cdot 35 + 2 \cdot 52.5} = 0 \quad [6.89]$$

$$E = 2G(1 + \nu) = 2 \cdot 52.5(1 + 0) = 105 \text{ MPa} \quad [6.90]$$

For this reason, the value zero of ν , the load apply is a vertical and horizontal impress displacements. The two displacement are not equal and they are $\Delta y=0.048 \cdot l_y$ and $\Delta x=0.024 \cdot l_x$.

The finite element results are plotted in the p' - q and ε_v - q plane and compare with experimental data and the results obtained by the PZ driver.

Constant temperature (room temperature $T=293.15$ °K), constant gas pressure (atmospheric pressure $p^g=101325$ Pa) and constant capillary pressure (fully saturated condition $p^c=0$ Pa) are assumed during the f.e. simulation.

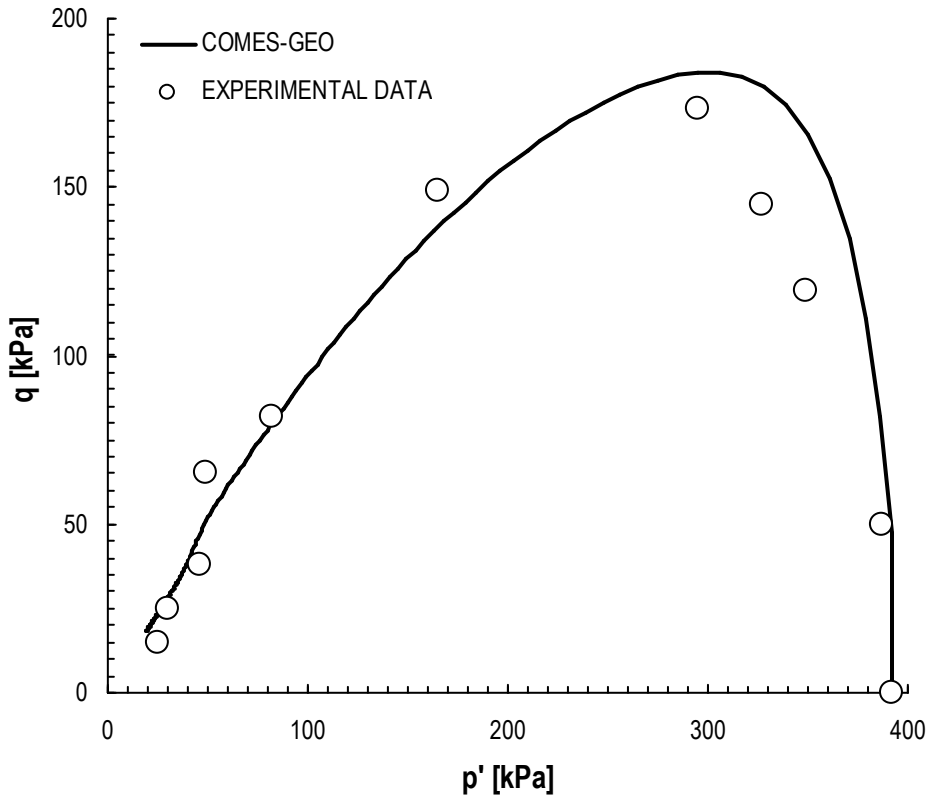


Figure 6.6: Comparison between COMES-GEO and experimental results [Cas69] in p' - q plane

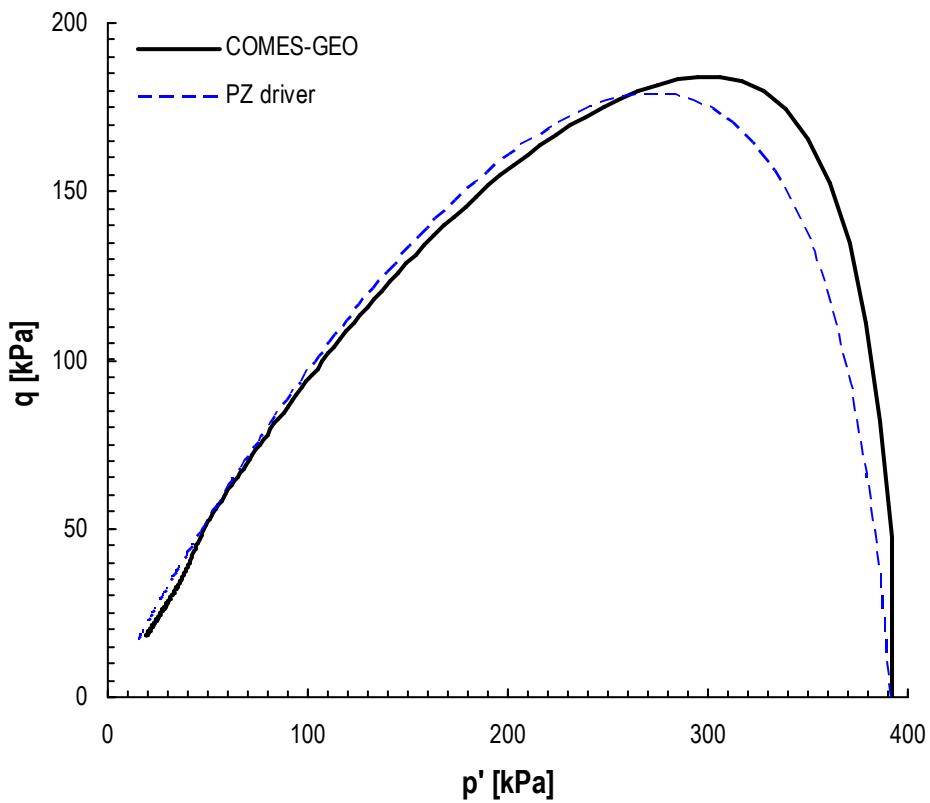


Figure 6.7: Comparison between COMES-GEO and PZ driver in p' - q plane

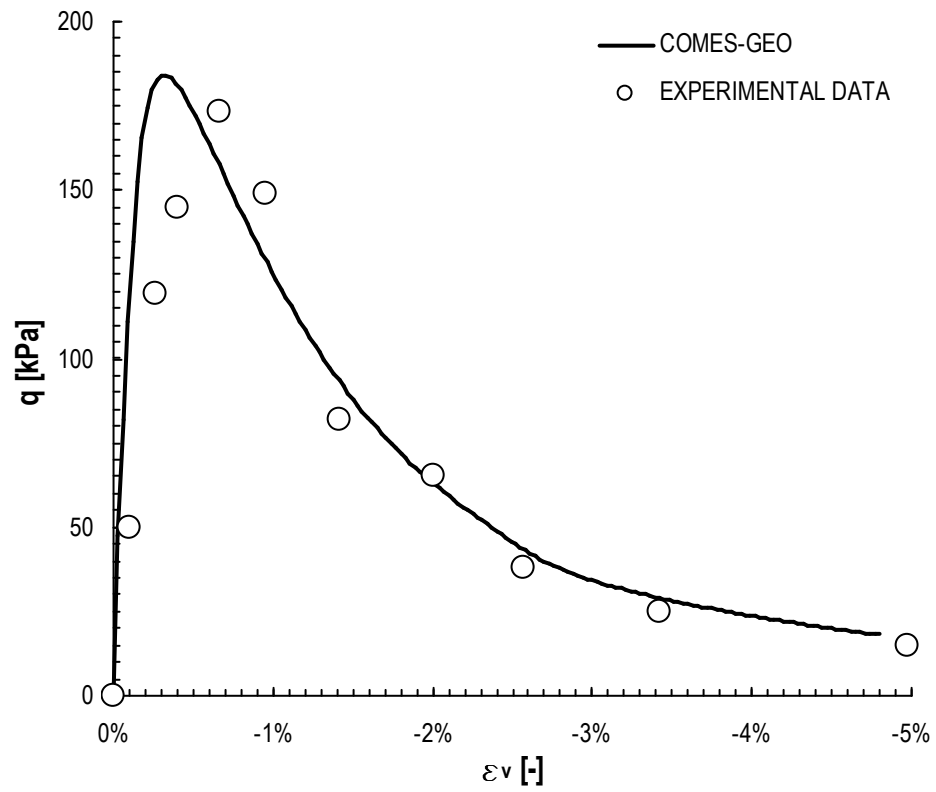


Figure 6.8: Comparison between COMES-GEO and experimental results [Cas69] in ε_v - q plane

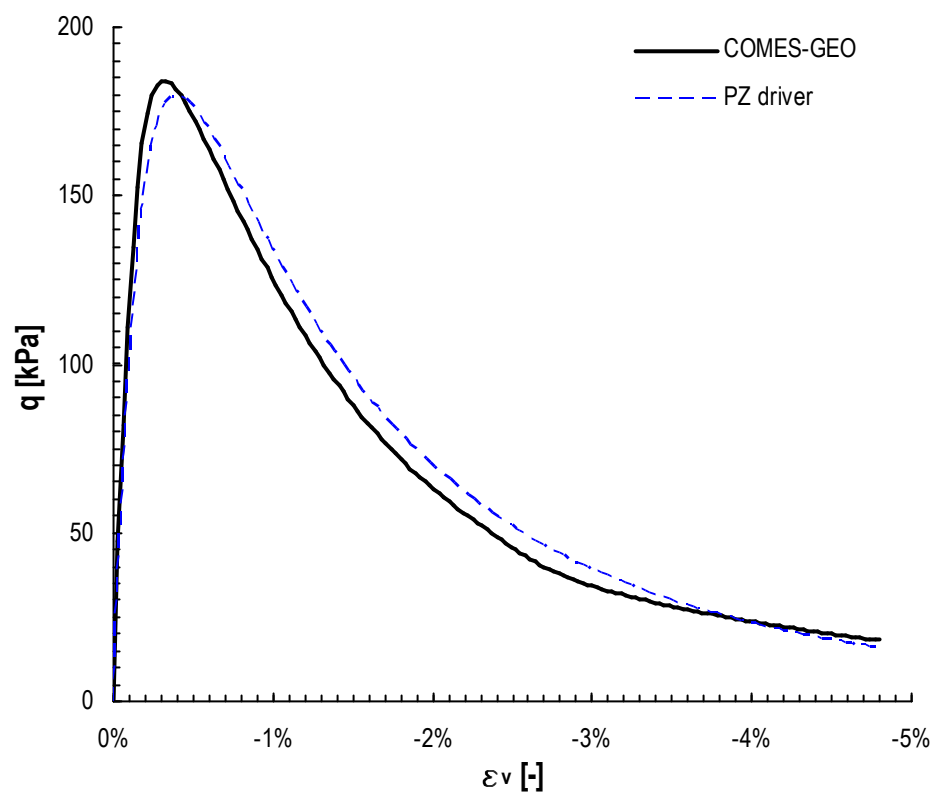


Figure 6.9: Comparison between COMES-GEO and PZ driver in ε_v - q plane

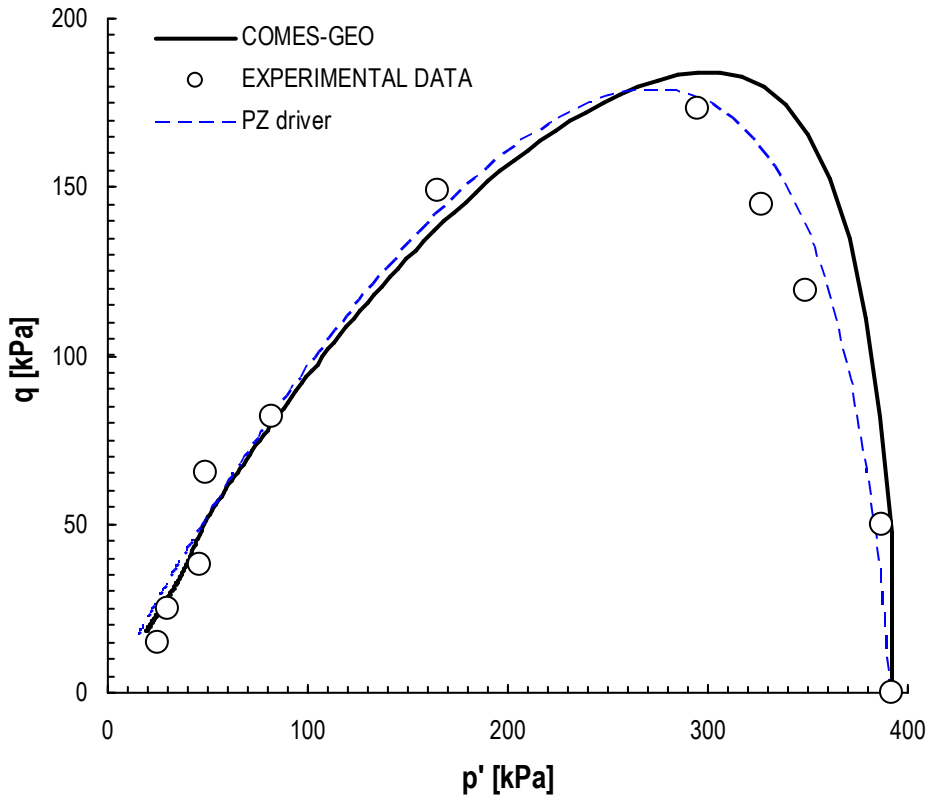


Figure 6.10: Comparison between COMES-GEO, experimental results [Cas69] and PZ driver in p' - q plane

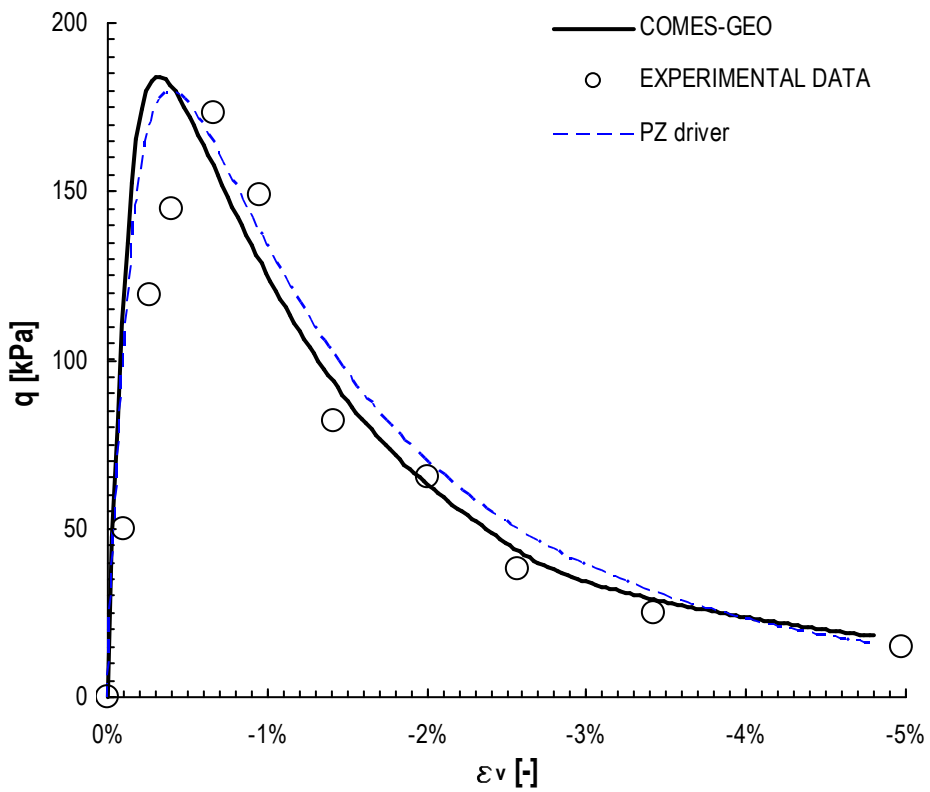


Figure 6.11: Comparison between COMES-GEO, experimental results [Cas69] and PZ driver in ϵ_v - q plane

6.3.2 Adige sand

This case consist in a series of triaxial compression test performed a three different isotropic compression pressure ($p'_c=50$ kPa, $p'_c=100$ kPa and $p'_c=200$ kPa) on a sample of Adige sand [Mir09]. The Adige sand is a very dense ($D_R=87$ %) sand taken from the mouth of the river Adige in Veneto, Italy.

Starting from the initial isotropic compression mentioned above, a compressive axial displacement is applied until a deformation of $\varepsilon_y=15$ % is reached.

Material parameters $p'_c=50$ kPa								
K_{ref} [MPa]	G_{ref} [MPa]	M_f	M_g	α_f	α_g	H_0	β_0	β_1
40.00	10.00	1.10	1.33	0.45	0.45	1100	2.0	0.18

Table 6.3: Material parameters of Adige sand for $p'_c=50$ kPa [Mir09]

Material parameters $p'_c=100$ kPa								
K_{ref} [MPa]	G_{ref} [MPa]	M_f	M_g	α_f	α_g	H_0	β_0	β_1
50.00	15.00	1.10	1.33	0.45	0.45	800	2.0	0.18

Table 6.4: Material parameters of Adige sand for $p'_c=100$ kPa [Mir09]

Material parameters $p'_c=200$ kPa								
K_{ref} [MPa]	G_{ref} [MPa]	M_f	M_g	α_f	α_g	H_0	β_0	β_1
55.00	20.00	1.10	1.33	0.45	0.45	550	2.0	0.18

Table 6.5: Material parameters of Adige sand for $p'_c=200$ kPa [Mir09]

The finite element results are plotted in the ε_y - q and ε_y - ε_v plane and compare with experimental data and the results obtained by the PZ driver.

Constant temperature (room temperature $T=293.15$ °K), constant gas pressure (atmospheric pressure $p^g=101325$ Pa) and constant capillary pressure (fully saturated condition $p^c=0$ Pa) are assumed during the f.e. simulation.

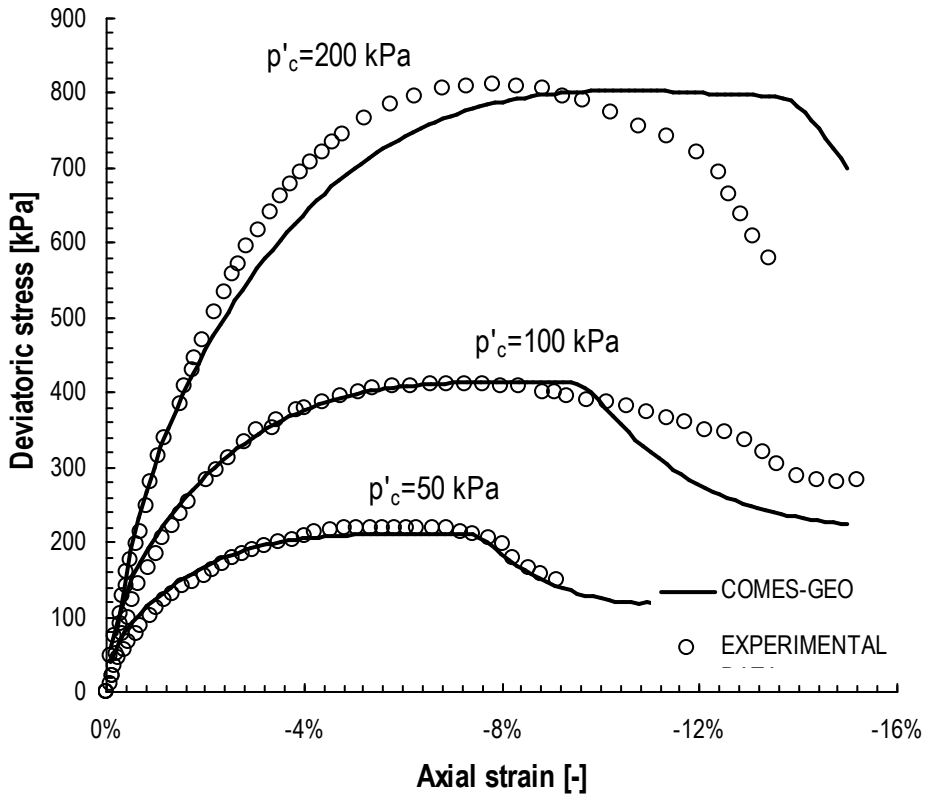


Figure 6.12: Comparison between COMES-GEO and experimental results [Mir09] in ϵ_γ - q plane

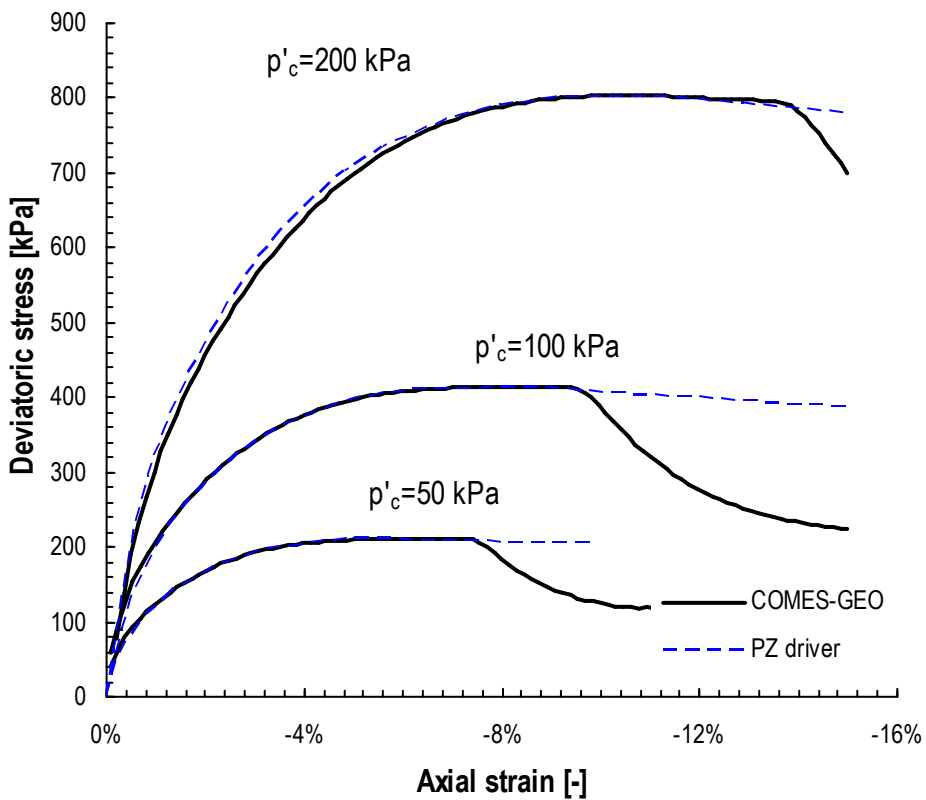


Figure 6.13: Comparison between COMES-GEO and PZ driver in ϵ_γ - q plane

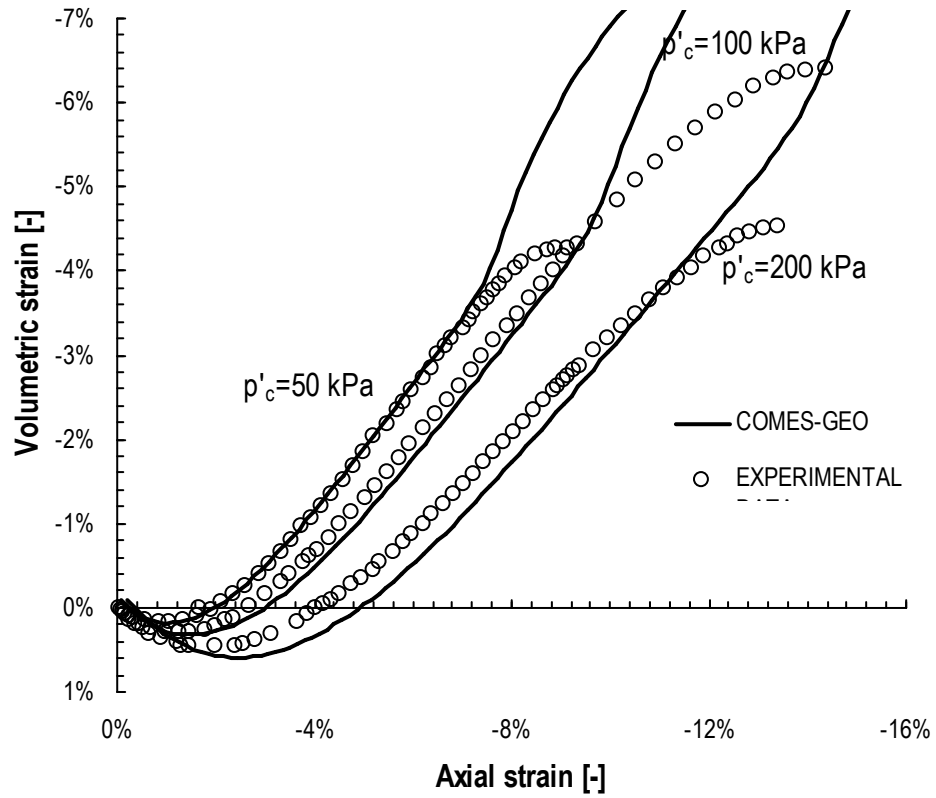


Figure 6.14: Comparison between COMES-GEO and experimental results [Mir09] in ε_γ - ε_v plane

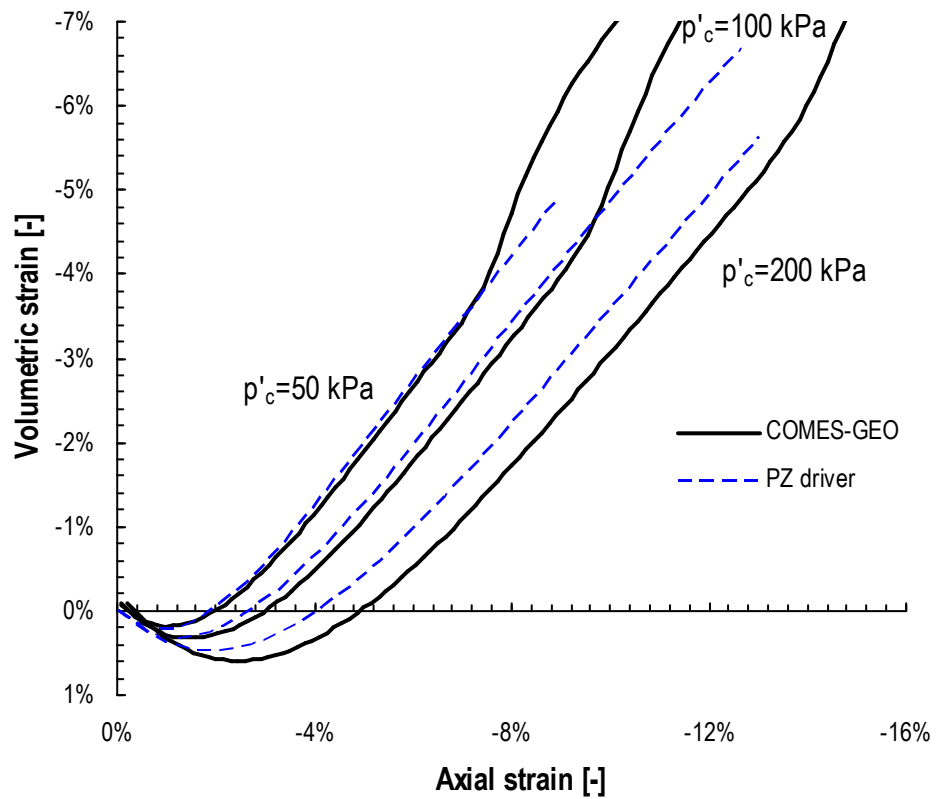


Figure 6.15: Comparison between COMES-GEO and PZ driver in ε_γ - ε_v plane

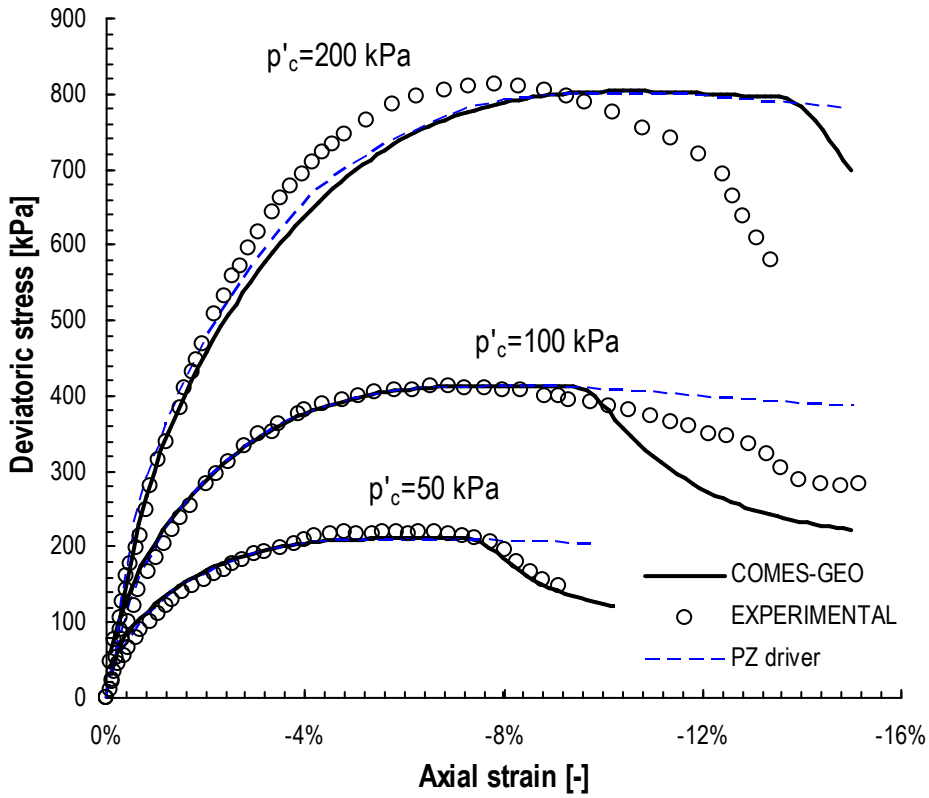


Figure 6.16: Comparison between COMES-GEO, experimental results [Mir09] and PZ driver in ϵ_γ - q plane

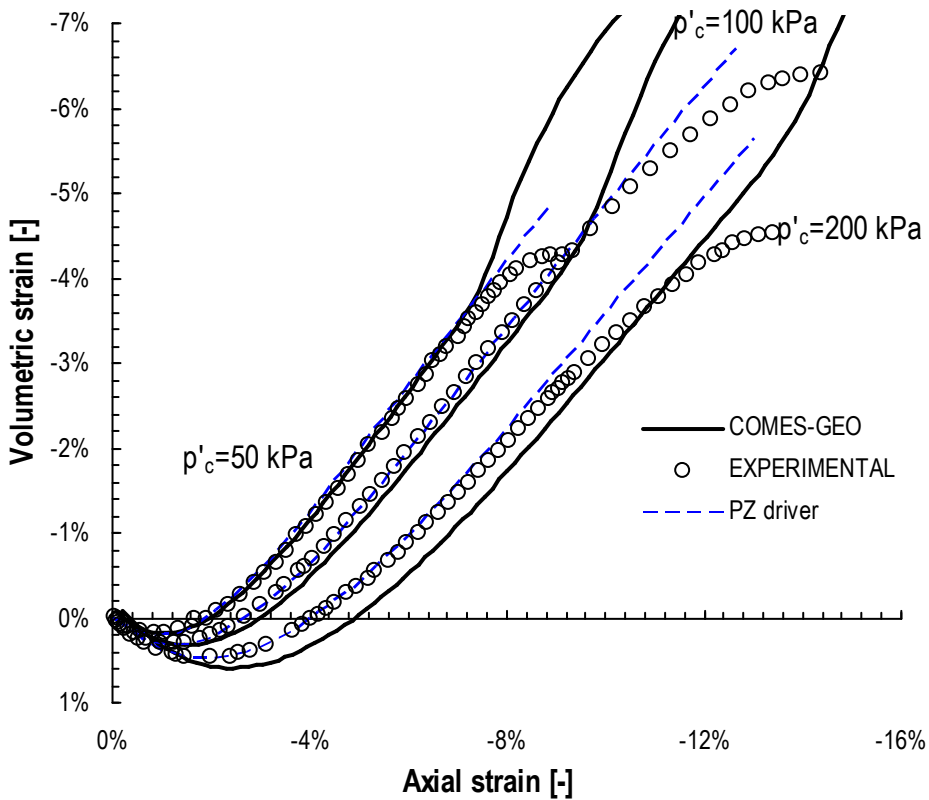


Figure 6.17: Comparison between COMES-GEO, experimental results [Mir09] and PZ driver in ϵ_γ - ϵ_v plane

6.3.3 Dense sand

This case consist in a triaxial compression test performed with COMES-GEO and PZ driver for a dense sand [Ton03].

In fact, from Table 6.6, the value of M_f and M_g are $M_f=0.95$ and $M_g=1.41$ and then

$$D_R = \frac{M_f}{M_g} = \frac{0.95}{1.41} 100 = 67.4 \% \quad [6.91]$$

The isotropic compression pressure is $p'_c=124$ kPa, and the loading path is compressive axial displacement applied until a deformation of $\varepsilon_v=15\%$ is reached.

Material parameters $p'_c=50$ kPa								
K_{ref} [MPa]	G_{ref} [MPa]	M_f	M_g	α_f	α_g	H_0	β_0	β_1
20.71	19.00	0.95	1.41	0.45	0.45	1000	2.2	0.12

Table 6.6: Material parameters of dense sand

The finite element results are plotted in the ε_v - q plane and compare with the results obtained by the PZ driver.

Constant temperature (room temperature $T=293.15$ °K), constant gas pressure (atmospheric pressure $p^g=101325$ Pa) and constant capillary pressure (fully saturated condition $p^c=0$ Pa) are assumed during the f.e. simulation.

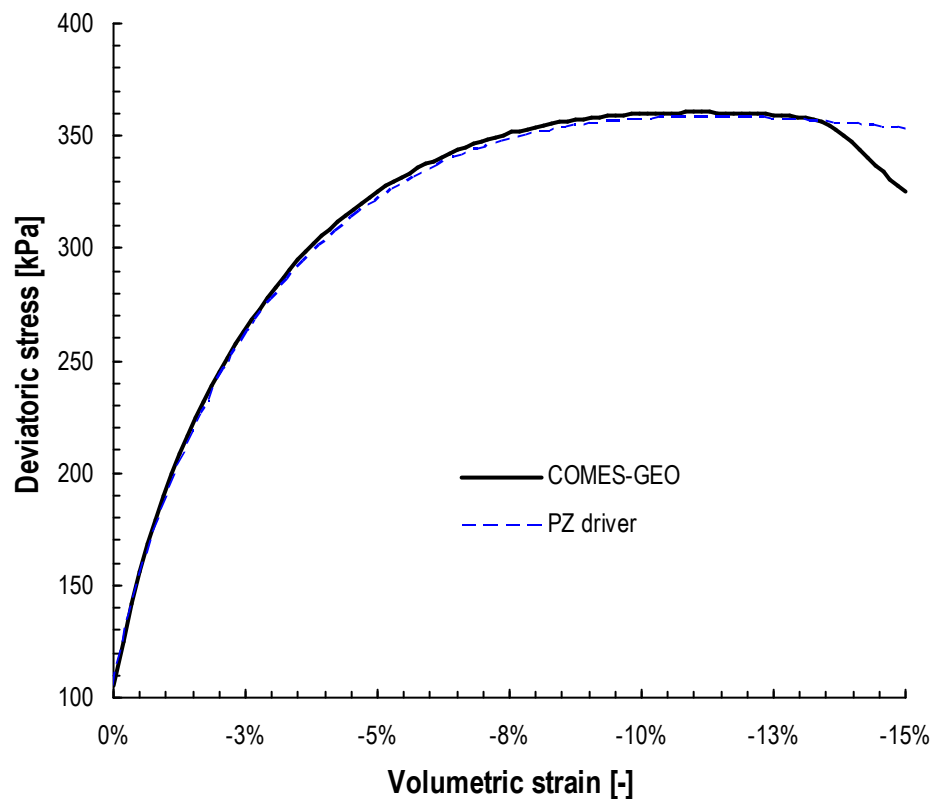


Figure 6.18: Comparison between COMES-GEO and PZ driver in ε_v - q plane

References

- [Cas69] Castro, G. (1969). Liquefaction of sands. Ph.D. thesis, Harvard Soil Mechanics Series No. 81, Harvard University, Cambridge, Massachusetts.
- [Dru56] D.C. Drucker, 1956. On uniqueness in theory of plasticity. *Quart. Appl. Mech.* 14, pp. 35–42.
- [Dru59] D.C. Drucker, 1959. A definition of stable inelastic material. *J. Appl. Mech.* 26, pp. 101–106.
- [Fro83] E. Frossard, Une équation d'écoulement simple pour les matériaux granulaires, *Géotechnique*, 33, 21-29, 1983.
- [L&N87] Lade PV, Nelson RB. Modelling the elastic behaviour of granular materials. *International Journal for Numerical and Analytical Methods in Geomechanics* 1987; 11:521–542.
- [L&S67] Lee K.L. e H.B. Seed (1967) Drained strength characteristics of sands *ASCE J. Geotech. Engrg.* Vol.93 No.6, 117-141
- [Lor85] Loret. The choice of elastic parameters for sand. *International Journal for Numerical and Analytical Methods in Geomechanics* 1985; 9(3):285–292.
- [M&Z84] Mroz. Z. and Zienkiewicz. O. C. (1984) Uniform formulation of constitutive equations for clays and sands. *Mechanics of Engineering Materials*. C. S. Desai and R. H. Gallagher (eds). Wiley, Chichester. Ch. 22, pp. 415-449.
- [Mir09] P. Mira, L. Tonni, M. Pastor and J. A. Fernandez Merodo. A generalized midpoint algorithm for the integration of a generalized plasticity model for sands. *International journal for numerical methods in engineering*. 2009; 77:1201–1223. DOI: 10.1002/nme.2445.
- [Mol88] Molenkamp F. A simple model for isotropic non-linear elasticity of frictional materials. *International Journal for Numerical and Analytical Methods in Geomechanics* 1988; 12:467–475.
- [N&W79] Nova R, Wood DM. A constitutive model for sand in triaxial compression. *International Journal for Numerical and Analytical Methods in Geomechanics* 1979; 3:255–278.
- [P&Z86] Pastor, M. & Zienkiewicz, O.C. 1986. A generalized plasticity, hierarchical model for sand under monotonic and cyclic loading. In G.N. Pande & W.F. Van Impe (eds), *Proc. 2nd Int. Symp. on Numerical Models in Geomechanics*, Ghent, Belgium: 131–150. M. Jackson and Son Pub.
- [Pas85] Pastor M, Zienkiewicz OC, Leung KH. Simple model for transient soil loading in earthquake analysis. II: Non-associative models for sands. *International Journal for Numerical and Analytical Methods in Geomechanics* 1985; 9:477–498.
- [Pas90] Pastor, M., Zienkiewicz, O.C. & Chan, A.H.C. 1990. Generalized plasticity and the modelling of soil behaviour. *Int. J. Numer. and Anal. Methods in Geomechanics* 14: 151–190.
- [Ton03] Tonni, L., Gottardi, G., Cola, S., Simonini, P., Pastor, M. & Mira, P. (2003). Use of Generalized Plasticity to describe the behaviour of a wide class of non-active natural soils. *Proc. 3rd International Symposium on Deformation Characteristics of Geomaterials*, Lyon, 22 – 24 September 2003, Di Benedetto, H., Doanh, T., Geoffroy, H. & Sauzéat, C. (eds), pp. 1145-1153. Balkema Publishers, The Netherlands.
- [Wil77] Wilde P. 1977 Two invariants dependent model of granular media, *Arch. of Mechanics*, 29, 799–809.

-
- [Z&M84] Zienkiewicz. O. C. and Mroz. Z. (1984) Generalized plasticity formulation and applications to geomechanics. *Mechanics of Engineering Materials*. C. S. Desai and R. H. Gallagher (eds). Wiley, Chichester. Ch. 33, pp. 655-679.
- [Z&P77] O.C. Zienkiewicz and G.N. Pande, Some useful forms of isotropic yield surfaces for soil and rock mechanics. In: G. Godehus Editor, *Finite elements in geomechanics* Wiley, New York (1977), pp. 179–190.
- [Zie85] Zienkiewicz OC, Leung KH, Pastor M. A simple model for transient soil loading in earthquake analysis. *International Journal for Numerical and Analytical Methods in Geomechanics* 1985; 9:953–976.
- [Zyt78] Zytynski M, Randolph MF, Nova R, Wroth CP. On modelling the unloading–reloading behaviour of soils. *International Journal for Numerical and Analytical Methods in Geomechanics* 1978; 2:87–94.

7 THE GENERALIZED PLASTICITY MODEL FOR UNSATURATED SANDS

7.1 INTRODUCTION

Starting from the Pastor-Zienkiewicz model [Pas90] developed within the generalized plasticity theory for water saturated soils, Bolzon et al. [Bol96] have proposed a model taking into account the conditions in partially saturated ($S_w < 1$). This new model is called here as BSZ model, results to be an extension of PZ model for partially saturated materials.

Since it was impossible to reproduce the behaviour of a soil in partial saturation only with the introduction of the Bishop's stress (see 2.6.1) in PZ model because the increase of soil compressibility with suction is not reproduced, the largest amount of volumetric collapse appears always for fully saturated conditions for varying net mean stress, and the isotropic yield limit decreases with increasing suction and this is in contrast with experimental observations, the authors of [Bol96], proposed the BSZ model where a proper enhancement of the hierarchical PZ model allows to overcome these drawbacks and that experimentally observed behaviour can be reproduced.

Hence the BSZ model gives advantages in partially saturated problems and where there is a transition from saturated to unsaturated conditions. This is in particular the case when modelling dynamic behaviour of fully saturated and partially saturated zones, as for instance in embankments, earth dams and slopes.

In literature other mathematical models were presented as for instance the one proposed by Wheeler and Sivakumar [W&S95] where the BBM (Basic Barcelona Model) was improved, the bitensorial elastoplastic model HiSS- δ_1 -unsat proposed by Geiser [Gei99] or the model proposed by Jommi and Di Prisco [J&D94] where the degree of saturation was introduced as a second independent state variable in the hardening rule, and the ACMEG-S model [Fra08], which can be derived by the already presented in chapter 5.

A further development of the BSZ model to non isothermal conditions has been proposed by Bolzon and Schrefler (BS model) [B&S05] and will be presented at the end of this chapter.

Both these models have been implemented in COMES-GEO but only the implementation of the BSZ model has been validated because of lack of material parameters for the non isothermal BS model.

For these reasons, the BSZ model can be considered validated although other tests were searching for a next future work to have further evidence of predictive ability of the model, and the same is in progress for the BS model.

7.2 BSZ MODEL

From section 6.2.1, and from Figure 6.4, we can write for a fully saturated soil

$$d\varepsilon_v = d\varepsilon_v^e = \frac{\kappa}{v_0} \frac{dp'}{\rho'} \quad [7.1]$$

in case of elastic loading and

$$d\varepsilon_v = d\varepsilon_v^e + d\varepsilon_v^p = \frac{\lambda}{v_0} \frac{dp'}{\rho'} \quad [7.2]$$

In case of plastic loading, where

$$\varepsilon_v = \frac{v - v_0}{v_0} = \frac{e - e_0}{1 + e_0} \quad [7.3]$$

$$d\varepsilon_v^p = \frac{1}{H_0} \frac{dp'}{\rho'} \quad [7.4]$$

Substitution of Bishop's definition [2.157] for partially saturated soil in terms of mean stress ρ'

$$\rho' = \rho_{net} + S_w s \quad [7.5]$$

where $\rho_{net} = \rho - \rho^g$

and s is the suction

in [7.1], [7.2] and [7.4], it would introduce a dependence of water content on volumetric strains.

Under monotonic loading, equation [7.4], can be integrated to give:

$$\varepsilon_v^p = \frac{1}{H_0} \ln \frac{\rho'}{\rho'_0} \quad [7.6]$$

and if a rigid plastic behaviour is assumed ($\varepsilon_{vp} = \varepsilon_v$)

$$v = v_0 - \frac{v_0}{H_0} \ln \frac{\rho'}{\rho'_0} \quad [7.7]$$

Introducing the Bishop's stress [7.5] in [7.6] and [7.7] we obtain

$$\varepsilon_v^p = \frac{1}{H_0} \ln \frac{\rho_{net} + S_w s}{\rho_{0,net} + S_w s} \quad [7.8]$$

$$v = v_0 - \frac{v_0}{H_0} \ln \frac{\rho_{net} + S_w s}{\rho_{0,net} + S_w s} \quad [7.9]$$

As far as suction is kept constant, equations [7.6], [7.7], [7.8] and [7.9] give relationships between pressure and volume changes which are similar to those of saturated soils, in accordance with experimental results (for instance [Kar86]) but it is clear that the generally observed increase of soil compressibility with suction (for instance [Jos88]) is not taken into account.

The yield function [6.63] begin now

$$f = q - 2M_f \left[\rho_{net} + S_w s - \frac{(\rho_{net} + S_w s)^2}{\rho_c} \right] \quad [7.10]$$

Because BSZ model does not consider explicitly the yield function, it is assumed to changing the plastic modulus H [6.66].

This is done by introducing the multiplicative function H_w , which is linearly related to suction through the relationship proposed in [Bol96]

$$H_w = 1 + as \quad [7.11]$$

where a is a material parameters expressed in MPa^{-1} if s is expressed in MPa .

The plastic modulus under isotropic compression is now

$$H = H_0 \cdot p' \cdot H_w \quad [7.12]$$

Since in fully saturated condition (see equation [6.67])

$$H_0 = \frac{1 + e_0}{\lambda - \kappa} \quad [7.13]$$

we can write the compressibility as

$$\lambda(s) = \frac{1 + e_0}{H_0 H_w} + \kappa = \frac{1 + e_0}{H_0 (1 + as)} + \kappa \quad [7.14]$$

From some experimental observation on compacted kaolin [Jos88], $\lambda(s)$ can be considered constant for a sufficiently high applied pressure.

Function H_w can be computed to fit different experimental data. As suggested by Alonso et al. [Alo90], a two parameter exponential function has been proposed

$$H_w = \frac{1}{1 + b_1 (e^{-b_2 s} - 1)} \quad [7.15]$$

where b_1 is a material parameter

b_2 is a material parameter [MPa^{-1}]

In some cases, a dependence of H_w on p' has to be assumed, to describe the behaviour of soils which exhibits a maximum collapse at some value of the mean effective stress. This feature can be dealt with in the above formulation by assuming the dependence of the parameter a introduced in [7.11] on the effective mean stress p' through the function

$$a = a_1 e^{-p'} - a_2 \quad [7.16]$$

Hence the plastic modulus H becomes:

$$H = H_0 \cdot p' \cdot [1 + (a_1 e^{-p'} - a_2) s] \quad [7.17]$$

where a_1 is a material parameter [MPa^{-1}]

a_2 is a material parameter [MPa^{-1}]

In this way, the original formulation for fully saturated soils is still recovered when suction is equal to zero (also with [7.11]).

Integration of the following relationship

$$dv = \frac{v_0}{H_0 [1 + (a_1 e^{-p'} - a_2) s]} \frac{dp'}{p'} \quad [7.18]$$

and introducing the [7.5]

it can be shown that the maximum collapse is obtained at

$$p'_{|\Delta v_{MAX}} = \ln \frac{a_1}{a_2} \quad [7.19]$$

The ratio between the material constants a_1 , and a_2 hence gives the critical value of the effective mean stress, at which the maximum collapse is detected. On the other hand, the total amount of the collapse depends on the absolute value of these parameters. The choice of assuming the material function a [7.11] a polynomial of p' , would lead to undesired singularities of the material behaviour, and has then been discarded.

Further refinements of the function H_w will require the determination of new material parameters, which may be troublesome. This is out of the main purpose of the authors of BSZ model [Bol96], which is to give a simple and handy, although reliable model of the behaviour of partially saturated soils.

As far as yield limits are concerned, a dependence of the hardening parameter p_c on suction must be hypothesized to find correspondence between simulations and experimental observations. Once experiments give the initial yield limit p'_{y0} for saturated condition, and value of $p'_y(s)$ at different suction values, a linear regression of data may often be considered satisfactory

$$p'(s) = p'_{y0} + is \quad [7.20]$$

whence

$$p_{y,net} = p'_{y0} + (i - S_w)s \quad [7.21]$$

Since $S_w < 1$, the condition $i > 1$ is sufficient (not necessary) for $p_{y,net}(s)$ to be an increasing function of suction.

The evolution of the yield surface during the plastic process will be then governed by the development of plastic strains. Due to this assumption, one could introduce the reference value p'_c of Bishop's pressure, characterizing the limit situation where no plastic strains develop as a consequence of suction changes. Then it must result that

$$\varepsilon_v^p = \frac{1}{H_0} \ln \frac{p'_{y0}}{p'_c} = \frac{1}{H_0 H_w} \ln \frac{p'_y(s)}{p'_c} \quad [7.22]$$

As a consequence, the evolution of the yield surface will be governed by the following relationship:

$$\frac{p'_y(s)}{p'_c} = \left[\frac{p'_{y0}}{p'_c} \right]^{H_w} = \left[\frac{p'_{y0}}{p'_c} \right]^{\frac{\lambda_0 - \lambda}{\lambda(s) - \lambda_0}} \quad [7.23]$$

7.3 BS MODEL

This model [B&S05], has been developed from the BSZ model with the aim to model the behaviour of soils under temperature changes. In particular, functions describing the yield surface and the compressibility modulus are modified to account for the shrinking of the elastic domain and for the increase of irreversible volumetric strain with heating.

The behaviour of soils in non isothermal conditions was already describes in Chapters 4 and 5. Here we would like to remark only a controversial aspect related to the effect of temperature upon compressibility with respect to loading. According to most experimental observations, compressibility is slightly affected by temperature changes, especially in fully saturated or nearly saturated conditions (see references [C&M68], [C&L04], [Sul02], [M&L97], [S&J90], [Sai91], [Bur00] and [Del00]).

On the contrary, the experimental results obtained by Romero [Rom99] testing clay samples with different water content and saturation degree, show a marked influence of the temperature on the virgin consolidation line as suction decreases, i.e. toward fully saturated condition.

A mentioned before, in the BS model, starting from BSZ model, some enhancements are proposed, taking advantage of the hierarchical structure of the original formulation. The resulting constitutive model can be introduced into general coupled thermo-hydraulic-mechanical frameworks recently put forward (see references [Sch01], [W&S03] and [Tho03]).

The presented BS model is alternative to that proposed by Wu et al. [Wuw04].

7.3.1 BS Model for saturated soils

The hardening rule can be obtained by integration of the relationship [7.4], where equations [7.13] and [7.3] have been introduced, during continuous plastic flow [B&S05], to give

$$p'_{c0}(\varepsilon_v^p) = p'_0 e^{H_0 \varepsilon_v^p} = p'_0 e^{\left(\frac{\lambda_0}{\lambda_0 - \kappa}\right) \varepsilon_v^p} \quad [7.24]$$

where p'_0 is the initial elastic limit at the reference temperature

λ_0 is the slope of the virgin consolidation line at $s=0$

p'_{c0} is p' during plastic flow

Temperature variations influence the elastic strains, which develop at constant effective pressure; this dependence can be analytically described as follows

$$d\varepsilon_v^e(T) = 3\beta'_s dT \quad [7.25]$$

where β'_s is the isotropic thermal expansion coefficient of the solid skeleton [K^{-1}] (see 4.3.1)

The coefficient β'_s varies with temperature and, slightly, with pressure [Bal88], [HBa90] and [C&L04], however, this constitutive model assumed that β'_s is almost constant and relatively small.

In equation [7.25] reversible thermal strains are disregarded, because it is assumed that inelastic phenomena prevail. Irreversible volumetric thermal strains are observed upon heating of clay soils, which usually undergo compaction as in standard consolidation test.

Thermal consolidation can be ascribed to a variation of the pre-consolidation pressure, namely to shrinking of the yield surface in the $p'-T$ space, as suggested by Hueckel and Borsetto [HBo90]. This contraction can be described by the following expression, proposed by Picard [Pic94] and experimentally verified by Sultan et al. [Sul02]

$$p'_{cT} = p'_{c0} e^{-\beta \Delta T} \quad [7.26]$$

where p'_{cT} is the consolidation pressure at temperature T

$\Delta T = T - T_0$

T_0 is the reference temperature

β is a material parameter, possibly depending on T

A good fit of experimental data is usually obtained by assuming

$$\beta = 3 \frac{1 + e_0}{\lambda_0 - \kappa} \alpha^p = 3 \alpha^p H_0 \quad [7.27]$$

where α^p is a positive scalar (function) [K^{-1}]

so that $3 \alpha^p \Delta T$ represents the equivalent unrecoverable volumetric strain.

Relationship [7.27] is equivalent to that proposed by Modaressi and Laloui [M&L97] when

$$3 \alpha^p = \frac{1}{a_T \Delta T + b_T} \quad [7.28]$$

A different analytical expression has been considered by Cekerevac and Laloui [C&L04], but the essential features of the above-modelled material response to heating are maintained unaltered (see chapter 4).

Combination of [7.24], [7.26] and [7.27] returns

$$p'_{cT}(\varepsilon_v^p, \Delta T) = p'_0 e^{H_0(\varepsilon_v^p - 3 \alpha^p \Delta T)} \quad [7.29]$$

The influence of temperature on both elastic and post-yield compressibility parameters (κ and λ_0 , and henceforth H_0) is somewhat controversial, but in most materials in saturated or nearly saturated condition, consolidation curves remain substantially parallel at different temperature (see references [C&M68], [Rob96], [HBa90], [C&L04], [Sul02], [M&L97] and [Bur00]).

The capability of this model to reproduce the peculiar features of fully saturated soil behaviour under temperature changes is visualized in [B&S05].

Some clays tested in oedometric conditions at nearly saturated states [Rom99], show a peculiar behaviour characterized by an increase of both the compression modulus λ and the amount of irreversible volumetric strain with temperature, which develops for a given effective pressure change under isothermal conditions.

These correlated effects are easily accounted for in the present model, by introducing a suitable dependence of the hardening modulus H_0 on temperature, as proposed in [B&S05]

$$H_0(T) = \frac{1}{h_0 + h_T \Delta T} \quad [7.30]$$

Relationship [7.30] returns the simplest approximation for $\lambda_0(T)$ which thus increases linearly with temperature.

The evolution of the yield surface, and its consequences on the amount of irreversible collapse developed by a material sample loaded at different temperature, are shown in [B&S05].

7.3.2 BS Model for partially saturated soils

Available experimental results show that the behaviour of partially saturated soils is substantially similar at room and at high temperature. Main differences may concern the amount of irreversible volumetric strain which develops upon wetting. Shrinkage upon drying is also enhanced at high temperature [Rom03] but this aspect is not included in the BS model.

Following some results published by Saix and Jouanna [S&J90], Saix [Sai91], Recordon [Rec93] and Romero [Rom99] [Rom03], the authors of [B&S05] have outlined the following main features of the thermal behaviour of partially saturated soils on which base the developed model:

1. water content at higher temperature is smaller than at reference (ambient) temperature, but the shape of water retention curve is almost insensitive to heating (differently from that proposed in ACMEG-TS);
2. suction versus saturation relationship is even less affected by temperature changes;
3. the amount of irreversible strains which develop during wetting may increase with temperature for those soils which exhibit, as peculiar features, irreversible swelling with suction decrease (even at reference temperature) and thermal dependence of the hardening moduli.

The water content and the saturation degree of soils were described in 5.3.

As seen for the family of ACMEG models, partially saturated soils develop unrecoverable volumetric strains with heating in normally consolidated conditions, while thermal strains are mainly reversible in overconsolidated states, exactly as in the case of full saturation. The amount of thermal deformation can be quantified by the relationships [7.4], [7.25], [7.26] and [7.27].

As already observed for BSZ model, in most instances preconsolidation stress reduces with heating, while temperature changes do not affect significantly the elastic and plastic material compressibility. Therefore, yield surface can be described as follows in the p' - s - T space

$$p'_{csT}(s, \Delta T) = p'_r \left(\frac{p'_{cT}(\varepsilon_v^p, \Delta T)}{p'_r} \right)^{H_w(s)} \quad [7.31]$$

Writing the relation [7.11] in terms of λ and κ changing with s

$$H_w(s) = \frac{\lambda_0 - \kappa}{\lambda(s) - \kappa} \quad [7.32]$$

and then introducing equations [7.32] and [7.29] into [7.31], the yield surface is obtained as

$$p'_{csT}(s, \Delta T) = p'_r \left(\frac{p'_0}{p'_r} \right)^{\frac{\lambda_0 - \kappa}{\lambda(s) - \kappa}} e^{\frac{\nu_0}{\lambda(s) - \kappa} (\varepsilon_v^p - 3a^p \Delta T)} \quad [7.33]$$

Equation [7.33] is validated in [B&S05].

A compaction process usually takes place during soil wetting. The corresponding unrecoverable strain can be evaluated through relation

$$d\varepsilon_v^p = \frac{1}{H_0 H_w(s)} \frac{dp'}{p'} \quad [7.34]$$

being $p' = p'_{csT}$, account taken of the fact that plastic compatibility implies the evolution of the consolidation stress with suction changes. The amount of irreversible strain which develops upon wetting is substantially similar at room and high temperature, consistently with the results of some available experimental investigation [Rom99] and [Rom03].

In the same references [Rom99] and [Rom03], is shown that by some soils irreversible swelling upon wetting occurs even at reference temperature. Contemporarily both of the slopes of the virgin compression line and of the unrecoverable volumetric strain increasing with temperature is observed during oedometric tests.

Irreversible swelling can be described by a proper choice of the hardening function; for instance, expression [7.16] foresees volume increments corresponding to suction reduction for some pressure ranges and suitably chosen parameters a_1 and a_2 [Bol96].

The possible increase of irreversible strain with temperature during the soil wetting is instead easily accounted for even by the simplest version of the present constitutive model, account taken of the contemporarily observed variation of the compressibility modulus.

7.4 VALIDATION OF THE IMPLEMENTATION OF THE BSZ MODEL IN THE F.E. CODE COMES-GEO

As mentioned in section 7.1, the validation of the implementation in the finite element code COME-GEO has been done only for the BSZ model. BS model has been only implemented and the numerical implementation will be validated in the near future.

For the numerical validation of the BSZ model, a series of triaxial compression test in saturated state served to calibrate the model, and then, some predictive triaxial compression tests were made in unsaturated conditions. The tests were taken from the extensive experimental investigation conducted by Geiser [Gei99] and [S&S05]. The soil used is a slime of the Sion region in Switzerland composed by slime (72%), clay (8%) and sand (20%).

The tests performed by Geiser were made for different preconsolidation pressure. For validation of the BSZ model it was considered the cases with $p'_c=600$ kPa, $p'_c=400$ kPa and $p'_c=100$ kPa.

Material parameters (Geiser)							
E_{ref} [MPa]	ν	K_{ref} [MPa]	G_{ref} [MPa]	n_e	p_{ref} [MPa]	M_{g0}	n (porosity)
110.00	0.35	122.22	40.74	0.5	0.40	1.18	0.4286
Material parameters (calibrated)							
M_{f0}	α_f	α_g	H_0	β_0	β_1	a [MPa ⁻¹]	
1.18	0.45	0.45	235	1.70	0.25	5.00	
Hydraulic parameters (modified Safai and Pinder)							
S_{irr}	β [cm ⁻¹]	γ	r'				
0.086	6.50	2.20	1.00				

Table 7.1: Material parameters of Sion silt tested by Geiser

The material parameters were found through the calibration of the model with the triaxial tests at fully saturated state. Therefore, before moving on to the analysis in partially saturation conditions, a comparison was made, with other triaxial test with different p'_c having the same parameters.

For the elastic modulus, Geiser suggest to use a relationship similar to [4.6] and [4.7]

$$E = E_{ref} \left(\frac{p'}{p'_{ref}} \right)^{n_e} \tag{7.35}$$

where $E_{ref}=110$ MPa

$$n_e=0.5$$

$$p_{ref}=0.4 \text{ MPa}$$

Being $\nu=0.35$, K_{ref} and G_{ref} are computed according to [4.6] and [4.7].

The material parameters are shown in Table 7.1.

Temperature and gas pressure are constant at $T=20 \text{ }^\circ\text{C}$ and $p^g=101325 \text{ Pa}$.

The water retention constitutive law chosen for this test is the one proposed from Safai and Pinder (see Figure 7.1) where at three suctions (in add at the saturated case $s=0 \text{ MPa}$) correspond the following degree of saturation

$$s=50 \text{ kPa} \quad S_w=0.930$$

$$s=100 \text{ kPa} \quad S_w=0.740$$

$$s=200 \text{ kPa} \quad S_w=0.410$$

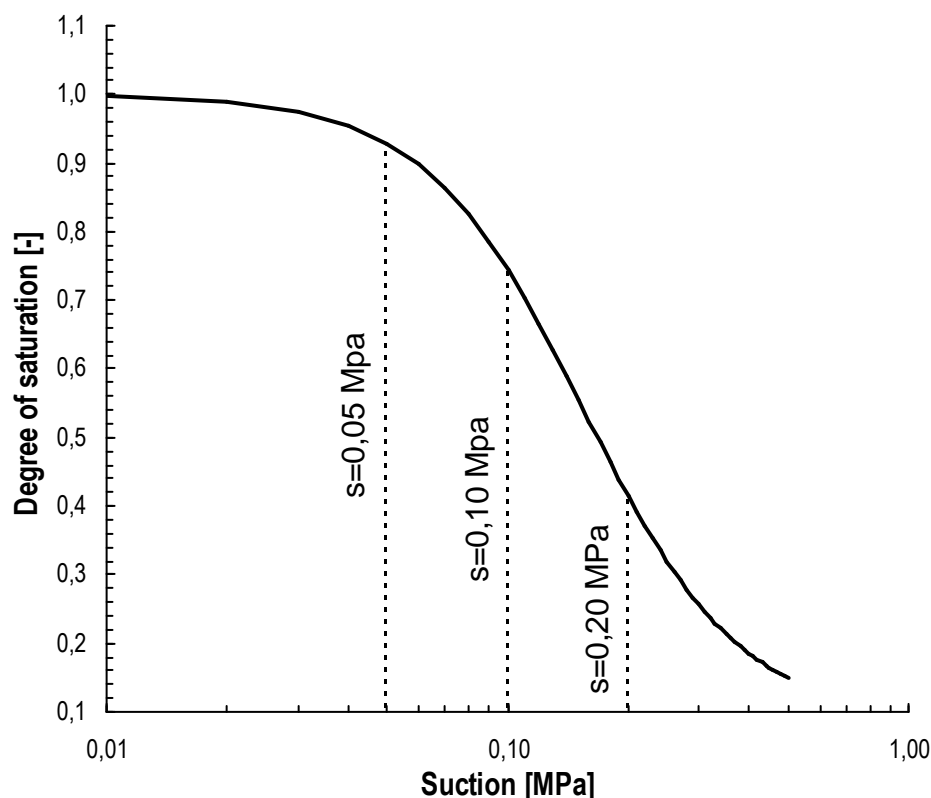


Figure 7.1: Water retention constitutive law Safai and Pinder for Sion silt

In the next graphs (Figure 7.2 and Figure 7.3) are shown first the comparison between the experimental data [Gei99] and the simulation of the triaxial compression test with a confining pressure $p'_c=600 \text{ kPa}$ and in fully saturated state and then the comparison with the tests performed with $p'_c=100 \text{ kPa}$ and $p'_c=400 \text{ kPa}$.

The simulation referred to the Figure 7.2 served, as mentioned above, for the calibration of the model through the fitting experimental data for the parameters that are properly only of the BSZ model.

In the Figure 7.3 instead the results was predicted and then compared with the experimental one.

Until this point, the BSZ model coincide with the PZ (because $s=0$).

At the same mode, the parameter a for the extension of the PZ model to BSZ model is obtained with a calibration for the triaxial compression at $s=0.10 \text{ MPa}$ for the two confining pressure $p'_c=400 \text{ kPa}$ and $p'_c=600 \text{ kPa}$.

The simulation with the predicted results are the two triaxial tests at $p'_c=600$ kPa at two different suction $s=0.05$ MPa and $s=0.20$ Mpa.

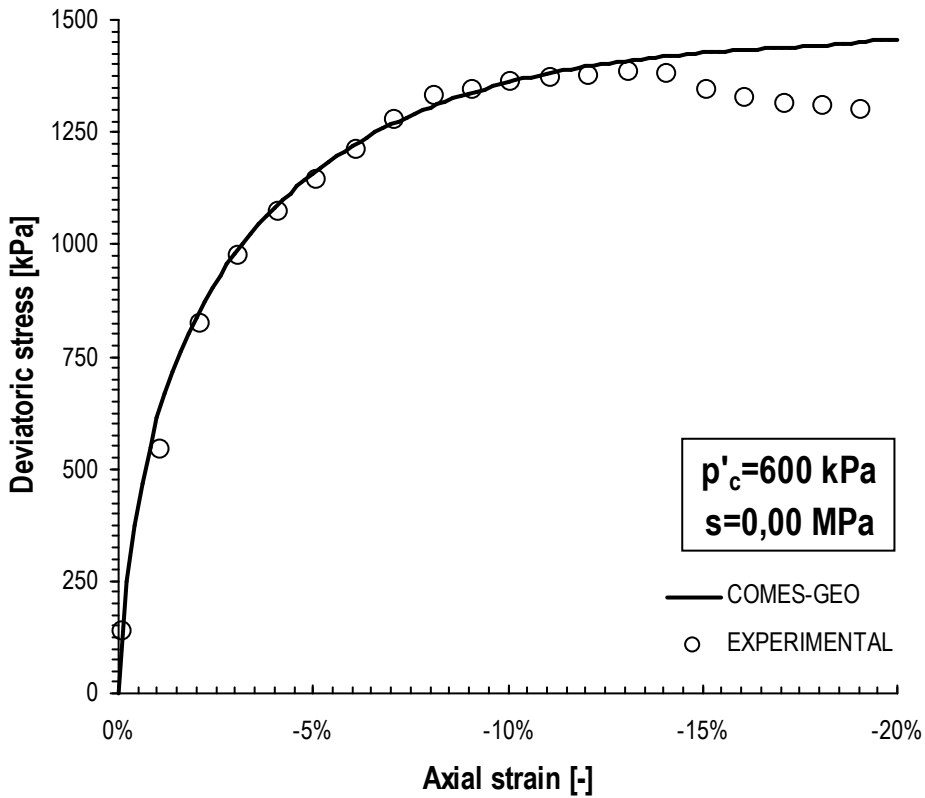


Figure 7.2: Triaxial test for the calibration of the model $p'_c=600$ kPa and $s=0.00$ MPa

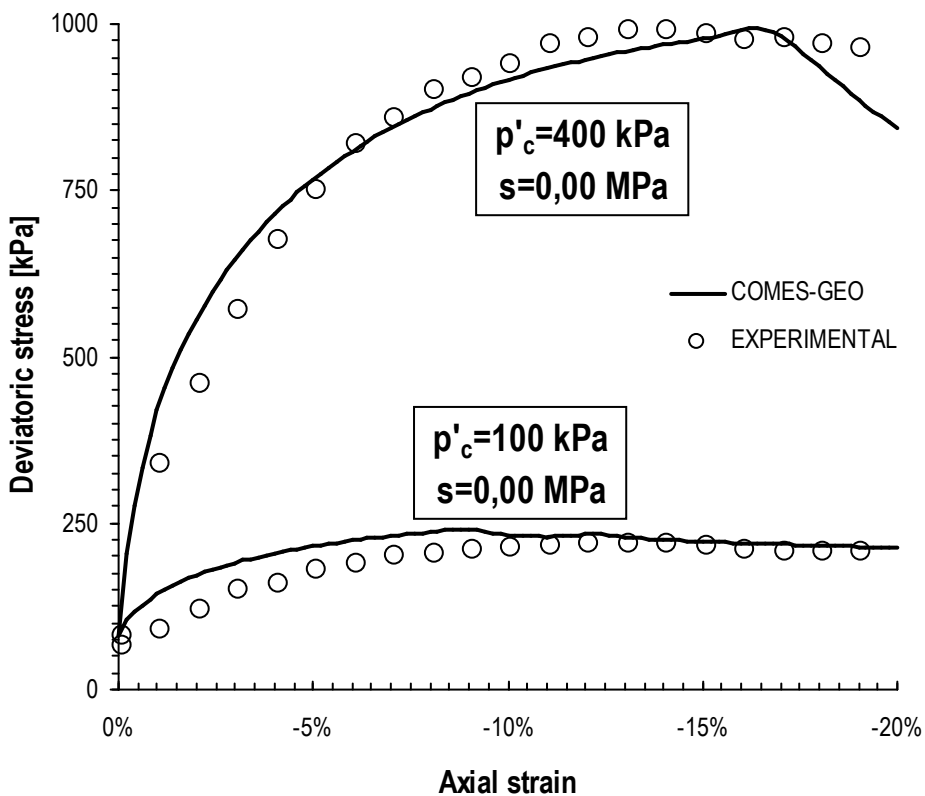


Figure 7.3: Comparison between experimental data [Gei99] and BSZ model in COMES-GEO after calibration of material parameter (Figure 7.2) $p'_c=100$ kPa and $p'_c=400$ kPa and $s=0.00$ MPa

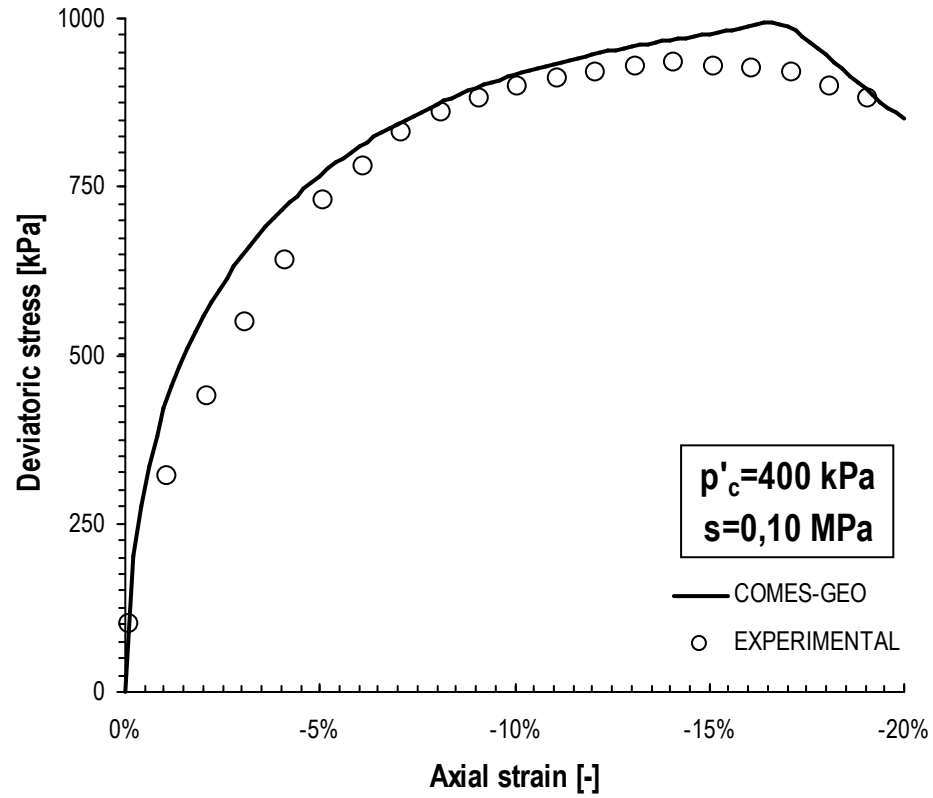


Figure 7.4: Triaxial test for the calibration of the parameter a $p'_c=400$ kPa and $s=0.10$ MPa

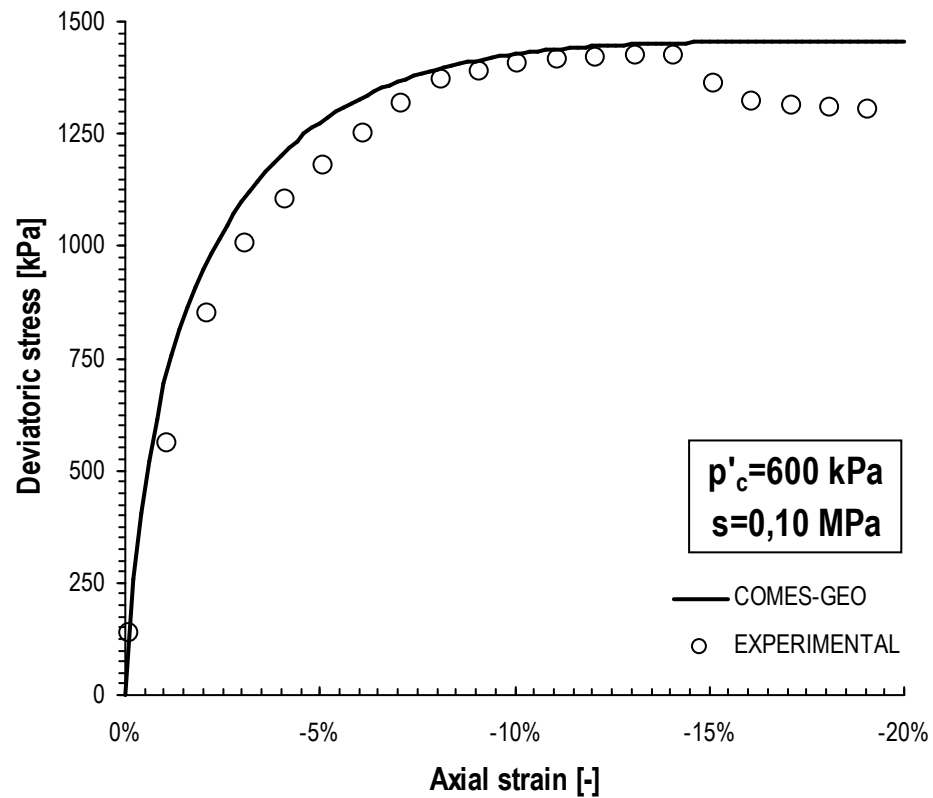


Figure 7.5: Triaxial test for the calibration of the parameter a $p'_c=600$ kPa and $s=0.10$ MPa

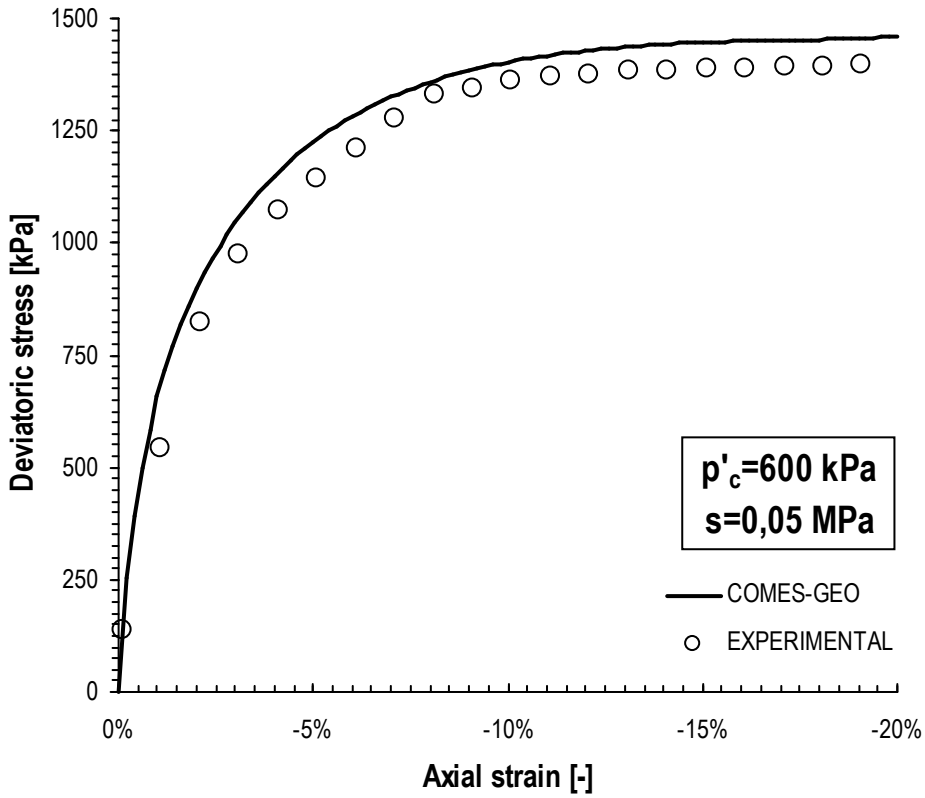


Figure 7.6: Comparison between experimental data [Gei99] and BSZ model in COMES-GEO after calibration of material parameter a $p'_c=600$ kPa and $s=0.05$ MPa

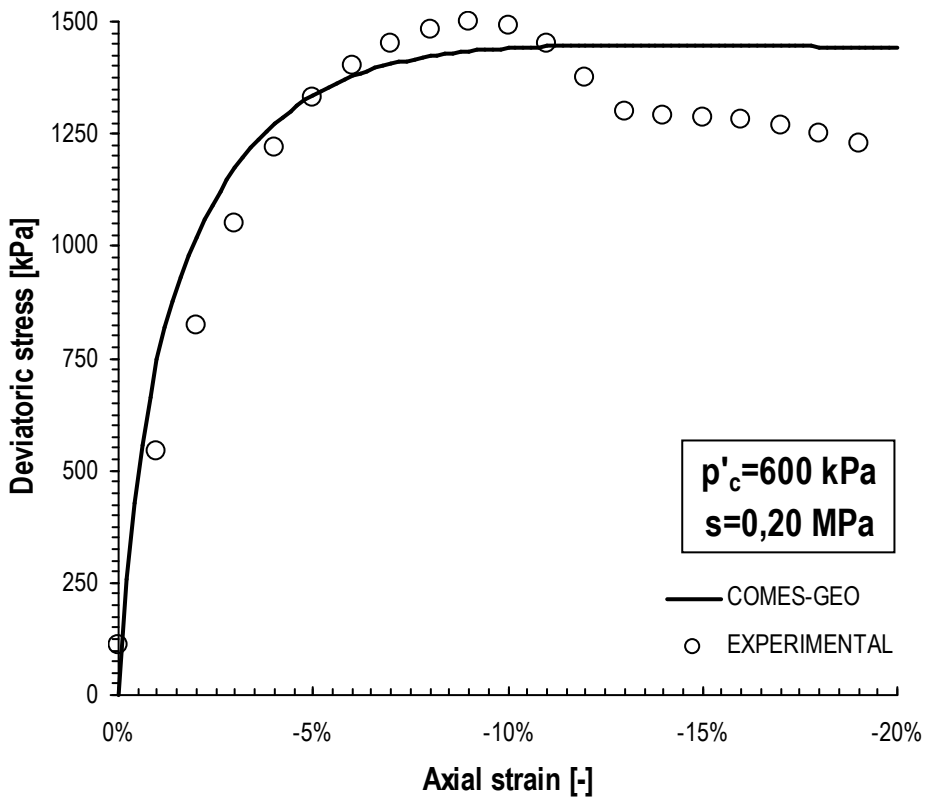


Figure 7.7: Comparison between experimental data [Gei99] and BSZ model in COMES-GEO after calibration of material parameter a $p'_c=600$ kPa and $s=0.20$ MPa

7.5 REMARKS

1. Numerical validation of the BSZ and BS models need of further investigations once the complete set of material parameters of these models could be determined or identified.
2. An enhanced BSZ constitutive model was developed by Santagiuliana and Schrefler [S&S06] based on the constitutive model proposed by Jommi and Di Prisco [J&D94] for partially saturated soils.
3. A future development of this Phd thesis will be the implementation of the eBSZ (enhanced Bolzon-Schrefler-Zienkiewicz constitutive model).

References

- [Alo90] Alonso EE, Gens A, Josa A. A constitutive model for partially saturated soils. *Géotechnique* 1990; 40:405–430.
- [B&S05] Bolzon G. and Schrefler B.A. (2005). Thermal effects in partially saturated soils: a constitutive model. *International Journal for Numerical and Analytical Methods in Geomechanics*, 29(9): 861-877.
- [Bal88] Baldi G, Hueckel T, Pellegrini R. Thermal volume changes of mineral-water system in low porosity clay soils. *Canadian Geotechnical Journal* 1988; 25:807–825.
- [Bo196] Bolzon G, Schrefler BA, Zienkiewicz OC. Elastoplastic soil constitutive law generalized to partially saturated states. *Géotechnique* 1996; 46:279–289.
- [Bur00] Burghignoli A, Desideri A, Miliziano S. A laboratory study on the thermomechanical behaviour of clayey soils. *Canadian Geotechnical Journal* 2000; 37:764–780.
- [C&L04] Cekerevac C. and Laloui L. (2004). Experimental study of thermal effects on the mechanical behaviour of a clay. *International Journal for Numerical and Analytical Methods in Geomechanics*, 28(3): 209-228.
- [C&M68] Campanella R.G. and Mitchell J.K. (1968). Influence of temperature variations on soil behaviour. *Journal of the Soil Mechanics and Foundation Division, ASCE*, 94: 709-734.
- [Del00] Delage P, Cui YJ, Sultan N. On the thermal consolidation of Boom clay. *Canadian Geotechnical Journal* 2000; 37:343–354.
- [Fra08] François B. (2008). Thermo-Plasticity of Fine-Grained Soils at Various Saturation States: Application to Nuclear Waste Disposal. PhD Thesis. École Polytechnique Fédérale De Lausanne. Suisse.
- [Gei99] Geiser F. (1999). Comportement mécanique d'un limon non saturé: Etude expérimentale et modélisation constitutive. PhD Thesis, EPFL, Lausanne, Switzerland.
- [HBa90] Hueckel T, Baldi G. Thermo-plasticity of saturated clays: experimental constitutive study. *ASCE Journal of Geotechnical Engineering* 1990; 116(12):1778–1796.
- [HBo90] Hueckel T, Borsetto M. Thermo-plasticity of saturated soils and shales: Constitutive equations. *ASCE Journal of Geotechnical Engineering* 1990; 116(12):1765–1776.
- [J&D94] Jommi C., di Prisco C. (1994). Un semplice approccio teorico per la modellazione del comportamento meccanico di terreni granulari parzialmente saturi. Il ruolo dei fluidi nei problemi di ingegneria geotecnica, *Mondovì, Vol.1, II*: 167,188.
- [Jos88] Josa, A. (1988). Un modelo elastoplástico para suelos no saturados. Tesis Doctoral. Universitat Politècnica de Catalunya, Barcelona.
- [Kar86] Karube, D. (1986). New concept of effective stress in unsaturated soil and its proving tests. *ASTM Symp. on Advanced Triaxial Testing of Soil and Rock, ST 977*,539-552. Philadelphia: American Society for Testing and Materials.
- [M&L97] Modaressi H. and Laloui L. (1997). A thermo-viscoplastic constitutive model for clays. *International Journal for Numerical and Analytical Methods in Geomechanics*, 21(5): 313–315.
- [Pas90] Pastor, M., Zienkiewicz, O.C. & Chan, A.H.C. 1990. Generalized plasticity and the modelling of soil behaviour. *Int. J. Numer. and Anal. Methods in Geomechanics* 14: 151–190.

-
- [Pic94] Picard J. Ecrouissage thermique des argiles saturées: application au stockage des déchets radioactifs. Doctoral Thesis. Ecole Nationale de Ponts et Chaussées, 1994.
- [Rec93] Recordon E. Déformabilité des sols non saturés à diverses températures. *Revue Française de Géotechnique* 1993; 65:37–56.
- [Rob96] Robinet J-C, Rahbaoui A, Plas F, Lebon P. A constitutive thermomechanical model for saturated clays. *Engineering Geology* 1996; 41:145–169.
- [Rom03] Romero E, Gens A, Lloret A. Suction effects on a compacted clay under non-isothermal conditions. *Géotechnique* 2003; 53(1):65–81.
- [Rom99] Romero E. (1999). Characterisation and thermo-mechanical behaviour of unsaturated Boom clay: An experimental study. PhD Thesis, UPC, Barcelona.
- [S&J90] Saix C, Jouanna P. Appareil triaxial pour l'étude du comportement thermique de sols non saturés. *Canadian Geotechnical Journal* 1990; 27:119–128.
- [S&S06] Santagiuliana R., Schrefler B.A. :2006, Enhancing The Bolzon-Schrefler-Zienkiewicz Constitutive Model For Partially Saturated Soil, *Transport in porous media*, 65:1-30.
- [Sai91] Saix C. Consolidation thermique par chaleur d'un sol non saturé. *Canadian Geotechnical Journal* 1991; 28:42–50.
- [Sch01] B.A. Schrefler. *Environmental Geomechanics*. CISM Courses and Lectures No 417, Springer Verlag Wien, New York, 2001.
- [Sul02] Sultan N, Delage P, Cui YJ. Temperature effects on the volume change behaviour of Boom clay. *Engineering Geology* 2002; 64:135–145.
- [Tho03] Thomas HR, Yang HT, He Y, Cleall PJ. A multi-level parallelized substructuring-frontal solution for coupled thermo/hydro/mechanical problems in unsaturated soils. *International Journal for Numerical and Analytical Methods in Geomechanics* 2003; 27:951–976.
- [W&S03] Wang Z, Schrefler BA. Fully coupled thermo-hydro-mechanical analysis by an algebraic multigrid method. *Engineering Computations* 2003; 20:211–229.
- [W&S95] Wheeler, S.J. & Sivakumar, V. (1995). An elasto-plastic critical state framework for unsaturated soil. *Géotechnique*, 45, No. 1, 35-53.
- [Wuw04] Wu W, Li X, Charlier R, Collin E. A thermo-hydro-mechanical constitutive model and its numerical modelling for unsaturated soils. *Computers and Geotechnics* 2004; 31:155–167.

8 APPLICATION TO GEO-ENVIRONMENTAL ENGINEERING PROBLEMS

As reported in the first chapter of this work, the implementation and the numerical validation of advanced constitutive models for soils, is needed to study the complex THM nature of several geo-environmental engineering problems. In this chapter two works in progress are shown: the simulation of the long-term behaviour of a deep nuclear waste disposal and of land subsidence due to gas production. Both the cases are complex and it is difficult to completely define their study because of the multitude of uncertainties and variables. For each case, it will be shown a description of the problem, the finite element discretization with the boundary conditions and, the most significant preliminary results. Furthermore, future developments will be suggested.

8.1 DEEP NUCLEAR WASTE DISPOSAL

8.1.1 Introduction

This work is the results of collaboration with the research group of Prof. L. Laloui.

The exercise proposed from the *Agence nationale pour la gestion des déchets radioactifs* [BRGM91] has been simulated with the aim to analyze the THM interaction of a theoretical storage system for radioactive waste of and many steps of type B and C (i.e. intermediate and high level waste). The results described in the following summarize those reported in [Lui06], [Pas08], [Pas09] and [San10].

The storage system consists of three horizontal tunnels 80 distant with a vertical section 6 m high and 5 m large. In each tunnel, a series of vertical wells are drilled with a diameter of 50 cm and an high of 55 m (of which 40 m are filled with the radioactive waste and the last 5 to form a clay stopper).

Two wheelbases between the wells, 10 m or 20 m, and two depths of the tunnels, 400 m or 750 m, have been analyzed.

In particular the following analyses have been performed:

1. Case 1-A: tunnels' dept of 400 m and wells' wheelbase of 20 m
2. Case 1-B: tunnels' dept of 400 m and wells' wheelbase of 10 m
3. Case 2-A: tunnels' dept of 750 m and wells' wheelbase of 20 m
4. Case 2-B: tunnels' dept of 750 m and wells' wheelbase of 10 m

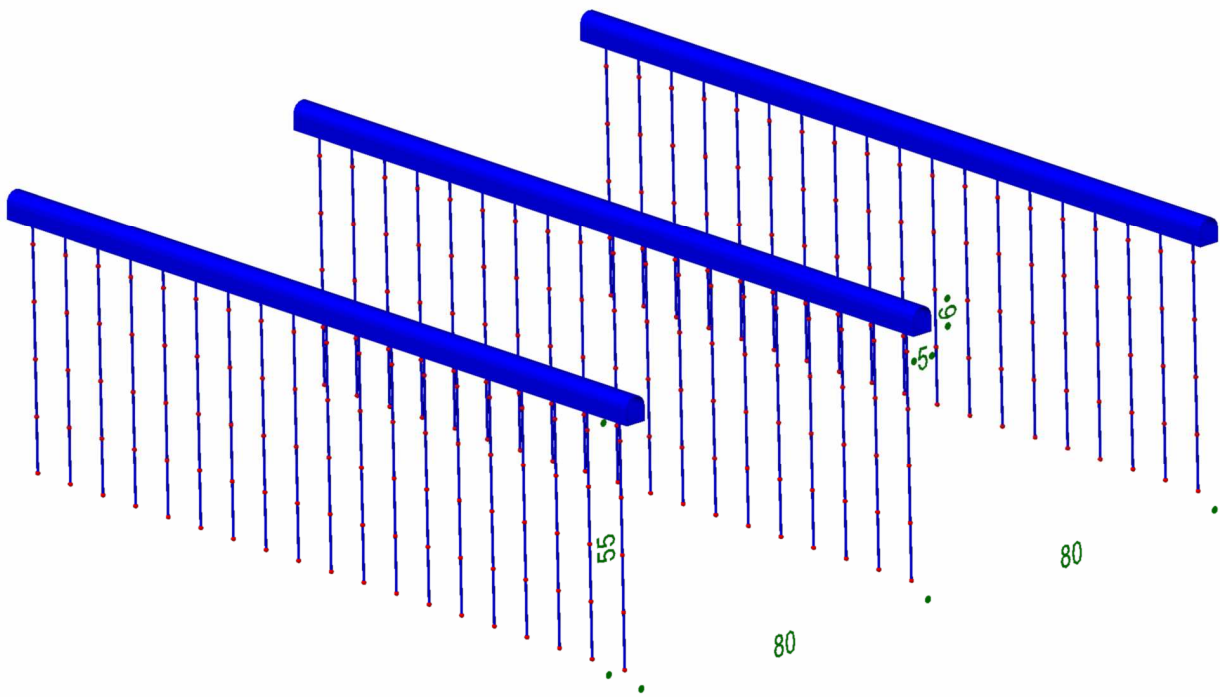
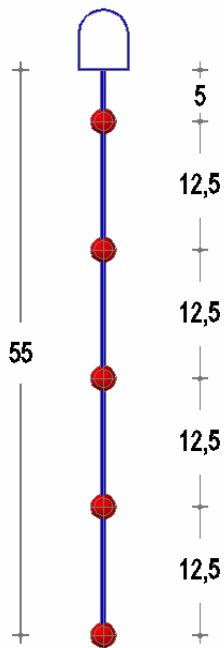


Figure 8.1: Tunnels and wells scheme

8.1.2 Source of temperature



Here a nuclear waste of type C for a period of about 200 years starting from the storage of the containers into the wells is considered. Each container has the same releases of heat described from the power law depicted in Figure 8.3.

This release has been transformed in five equivalent heat sources applied in five specific points at a constant distance of 12.5 m (see Figure 8.2) that are considered to be direct in contact with the host rock. This temperature history increases, from 30 °C to 98 °C in the first 30 years and then a slowly decreases in the next 180 years (Figure 8.4).

Figure 8.2: Distribution of temperature source

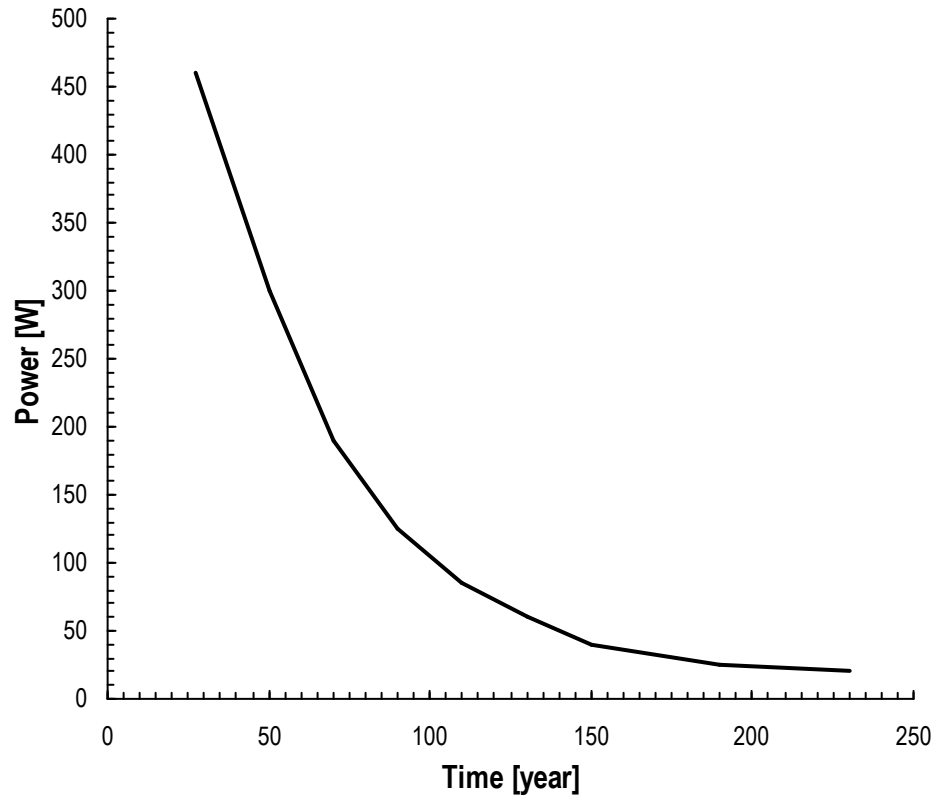


Figure 8.3: Power released on time from each container

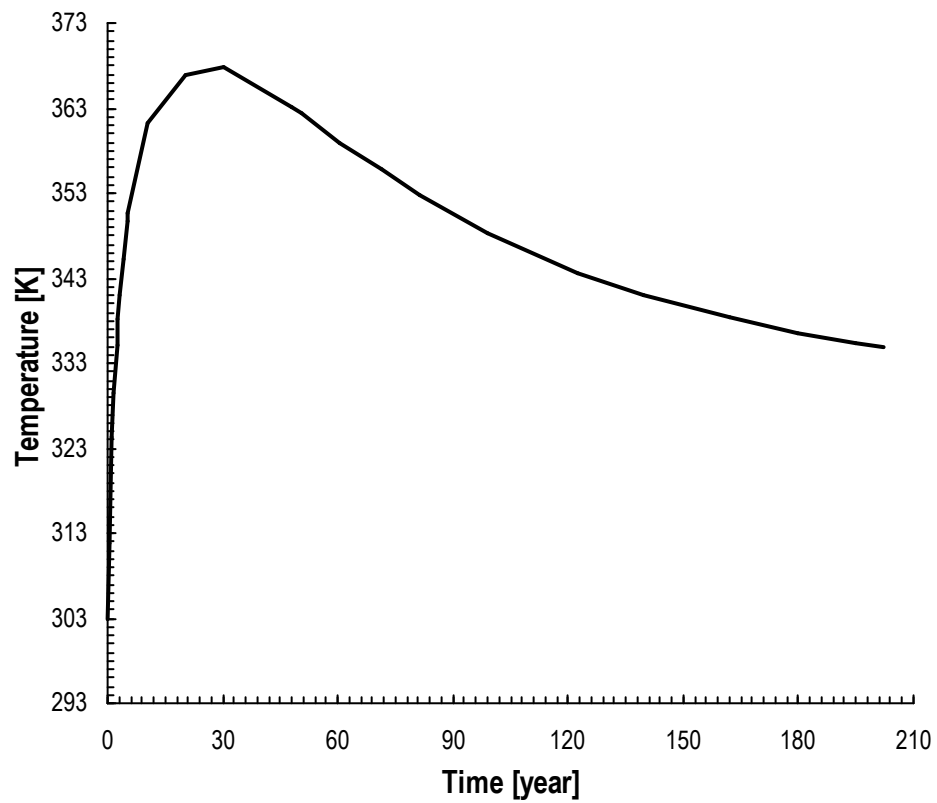


Figure 8.4: Temperature released on time from each source

8.1.3 Material parameters

The material parameters are obtained from a series of triaxial compression tests made by the B.R.G.M. geotechnical laboratory of Orleans on samples of clay of Montcornet [BRGM91] and are listed in Table 8.1 and Table 8.2 for Case 1 and Case 2 respectively. The tests were performed in drained and undrained conditions, monotonic or cyclical load conditions and with different confining pressure and load speed.

CASE 1						
sample name	sample deep [m]	confining [MPa]	γ_s [kg/m ³]	n	k [m/s]	
A 1950	437.7-438.0	5.30-10.60	2070	0.37	10 ⁻¹²	
Elastic parameters						
K_{ref} [MPa]	G_{ref} [MPa]	n_e	β'_s [°C ⁻¹]			
200.0	120.0	0.70	3.0 · 10 ⁻⁵			
Isotropic plastic parameters						
β	c	r_{iso}^e	p'_c [MPa]	γ_T		
12.0	0.002	0.005	15.00	0.4		
Deviatoric plastic parameters						
b	d	\varnothing'_0 [°]	r_{dev}^e	a	g	α
1.0	1.5	15	0.005	0.001	4.5 · 10 ⁻⁵	1.0

Table 8.1: Material parameters for Case 1

CASE 2						
sample name	sample deep [m]	confining [MPa]	γ_s [kg/m ³]	n	k [m/s]	
A 2149	779.7-780.0	12.00-19.80	2320	0.22	10 ⁻¹³	
Elastic parameters						
K_{ref} [MPa]	G_{ref} [MPa]	n_e	β'_s [°C ⁻¹]			
250.0	130.0	0.70	3.0 · 10 ⁻⁵			
Isotropic plastic parameters						
β	c	r_{iso}^e	p'_c [MPa]	γ_T		
12.0	0.002	0.005	36.00	0.4		
Deviatoric plastic parameters						
b	d	\varnothing'_0 [°]	r_{dev}^e	a	g	α
1.0	1.5	28	0.005	0.007	4.5 · 10 ⁻⁵	1.0

Table 8.2: Material parameters for Case 2

Not all the parameters necessary for ACMEG-T model were found in the B.R.G.M. report [BRGM91], in particular for the missing parameter those relative to Boom clay have been selected.

8.1.4 Initial and boundary conditions

The problem can be analyzed in plane strain conditions and hence two different bi-dimensional problems are solved: a vertical section surrounding the central tunnel and containing a well (Figure 8.5) and an horizontal section containing three wells (Figure 8.6).

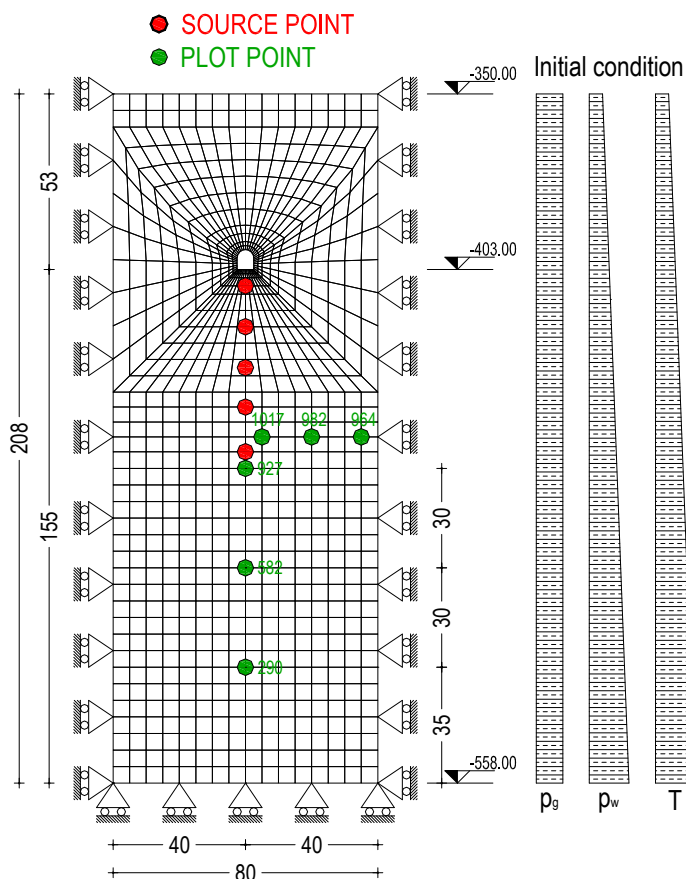


Figure 8.5: Boundary and initial condition of vertical section

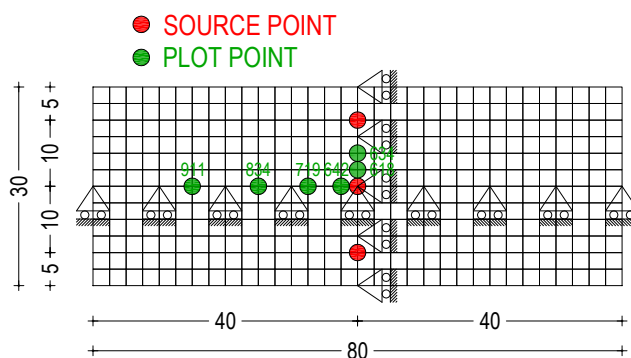


Figure 8.6: Boundary conditions of horizontal section

The initial and boundary conditions are described now.

8.1.4.1 Gas pressure

Because the host rock is initially water saturated, the gas pressure is assumed constant and equal to the atmospheric pressure $p^{atm}=101325$ Pa for all the nodes of the spatial discretization.

8.1.4.2 Capillary pressure

Similarly the water pressure presents the hydrostatic distribution. From the relation

$$p^c = p^g - p^w = p^g - (p^{atm} + \gamma_w h) = -\gamma_w h \quad [8.1]$$

where h is the deep from the top surface

it is possible to calculate the capillary pressure (negative) to be imposed on the boundaries.

8.1.4.3 Temperature

A temperature gradient of 30 K/100 m starting from the ambient temperature of 15 °C at the surface in contact with the atmosphere has been assumed. Hence the following relationship has been used to compute the temperature distribution on the lateral boundaries:

$$T_y = T_{amb} + 0.03 \cdot h \quad [8.2]$$

where h is the deep from the top (positive quantities)

$$T_{amb}=15 \text{ °C}$$

For the two cases the initial conditions are the following

	Case 1	Case 2
y_0 [m]	-400.00	-750.00
y_{sup} [m]	-350.00	-700.00
y_{inf} [m]	-550.00	-900.00
T_0 [°C]	27.00	37.50
T_{sup} [°C]	25.00	36.00
T_{inf} [°C]	31.50	42.00

Table 8.3: Summary of initial condition of temperature

8.1.4.4 Displacement

For symmetry (see Figure 8.1) the boundary conditions for the horizontal displacement are those shown in Figure 8.5.

Vertical displacements are constrained on the bottom surface (see Figure 8.5).

At the top of the mesh a total vertical stress is applied to simulate the weight of 350 m of water saturated soil for Case 1 and 700 m for Case 2.

For the calculation of the soil load the following relation was used

$$q_y = [\gamma_s(1-n) + \gamma_w \cdot n]h \cdot g \quad [8.3]$$

where γ_s [kg/m³] is the solid grain density

$\gamma_w=1000$ kg/m³ is the water density

n is the porosity

$g=9.81$ m/s² is the gravity acceleration

h [m] is the high of soil from the surface in contact with the atmosphere.

For Case 1 we have from Table 8.1 that $q_y=5'748'022,35$ Pa (because $\gamma_s=2070$ kg/m³ and $n=0.37$).

For Case 2 we have from Table 8.2 that $q_y=13'937'263,20$ Pa (because $\gamma_s=2320$ kg/m³ and $n=0.22$).

8.1.5 Mesh

The mesh for both the horizontal and vertical sections is composed by eight node quadrilateral elements, as shown in Figure 8.5 and Figure 8.6.

The vertical section is discretized with 896 elements and 2836 nodes (14180 dof), while the horizontal one with 384 elements and 1241 nodes (6205 dof).

8.1.6 Simulations

As reported in the following Table 8.4, seven different analysis have been performed. The early three present different peak value T_{max} of the temperature law of Figure 8.4, see Figure 8.7.

In particular, the third case simulates a failure condition of the canisters.

N° simulations	Deep [m]	Well's wheelbase [m]	Time analysis [Year]	T_{max} [K]
1	400	10	210	95
2	400	10	210	178
3	400	10	210	300
4	400	10	400	95
5	400	20	210	95
6	400	10	210	95
7	400	20	210	95

Table 8.4: Summary of simulations

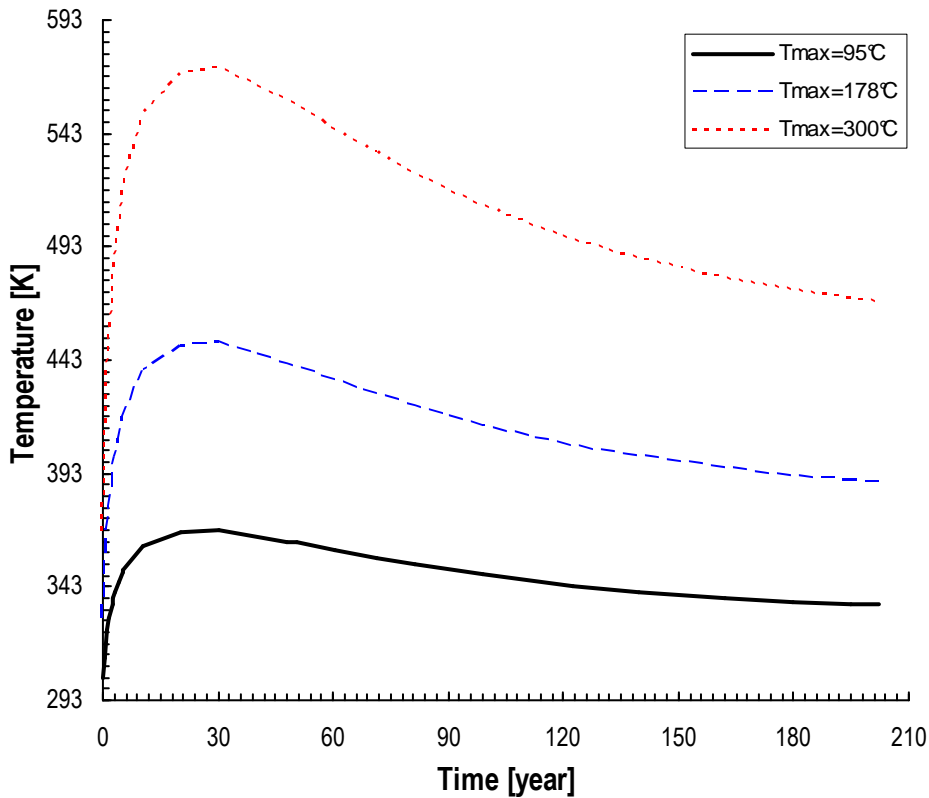


Figure 8.7: Temperature of simulations

8.1.7 Results

The finite element analysis is performed first by computing the initial mechanical conditions in equilibrium with the given boundary conditions and the gravity load. To this end two different elastic analysis have been performed. The first one is an analysis that considers the material as linear elastic while the second one considers the material as non-linear elastic. Then the transient analysis is applied by considering the temperature loading function plotted in Figure 8.7.

In particular a comparison between the node 290, 582 and 927 (see Figure 8.5) of vertical section are shown for Case 1 (with dept 400 m) and Case 2 (with dept 750 m).

Then, the results of horizontal section are shown for nodes 618 and 634 (see Figure 8.6) for Case A (with wheelbase of 20 m) and Case B (with wheelbase of 10 m).

From the time histories plotted in Figure 8.8 to Figure 8.13 it could be concluded that the results in terms of T , ε_v and ε_p is similar for the two selected tunnel depth. The only difference is in the initial temperature due to different initial and boundary conditions. An opposite conclusion should be done when analyzing the effect of different wheelbase. The deformation due to the thermal gradient is bigger in the case with wheelbase of 10 m (about twice).

However the amount of the deformation is negligible because the high confining pressure, and therefore both the wheelbase can be adopted.

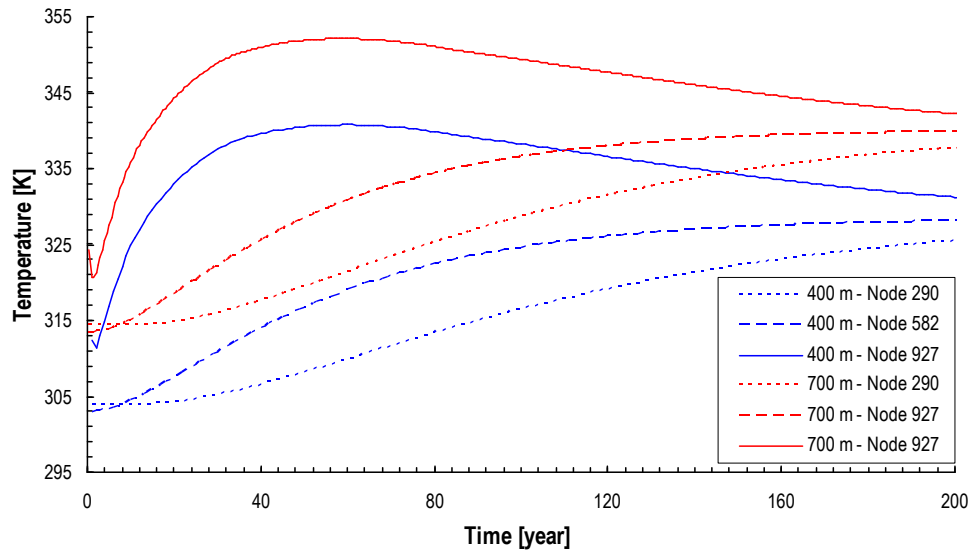


Figure 8.8: Vertical section – Temperature T

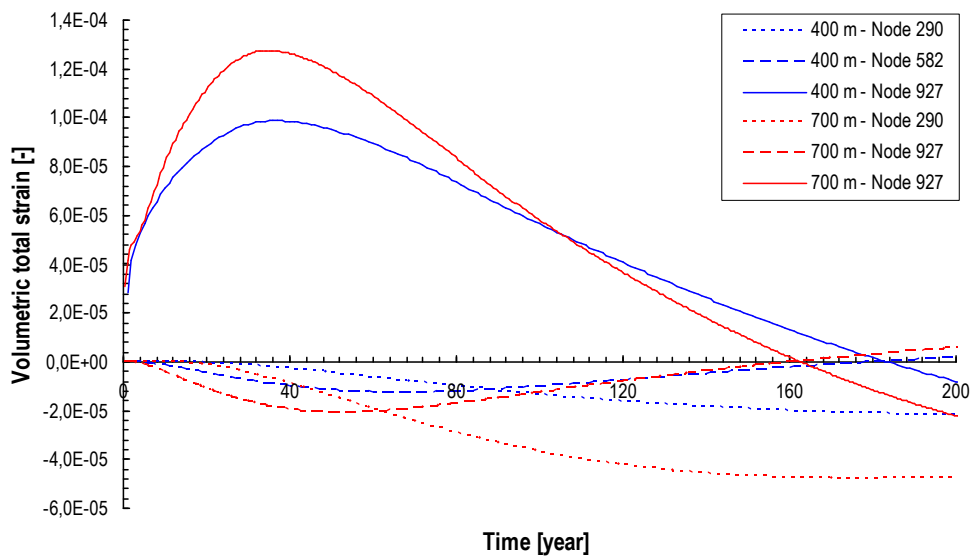


Figure 8.9: Vertical section – Volumetric total strain ε_v^T

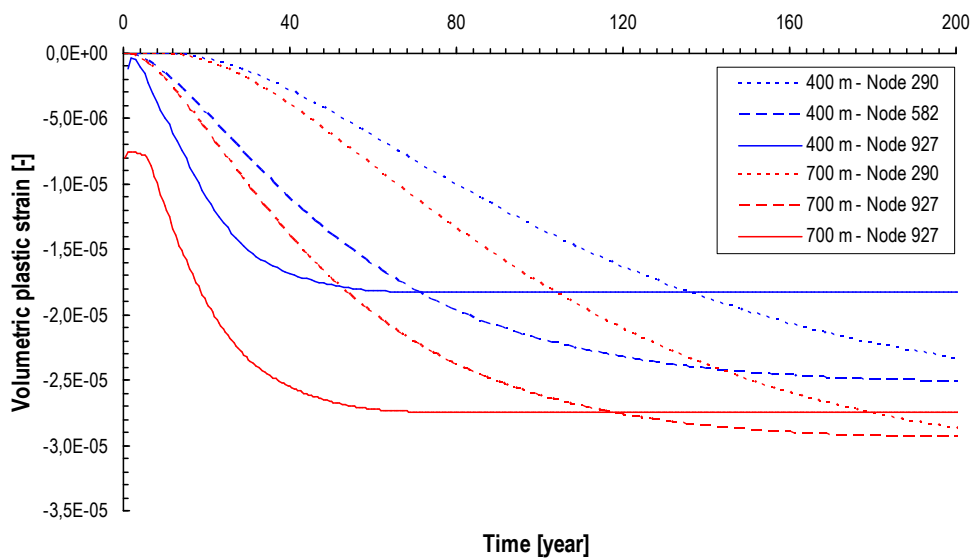


Figure 8.10: Vertical section – Volumetric plastic strain ε_v^p

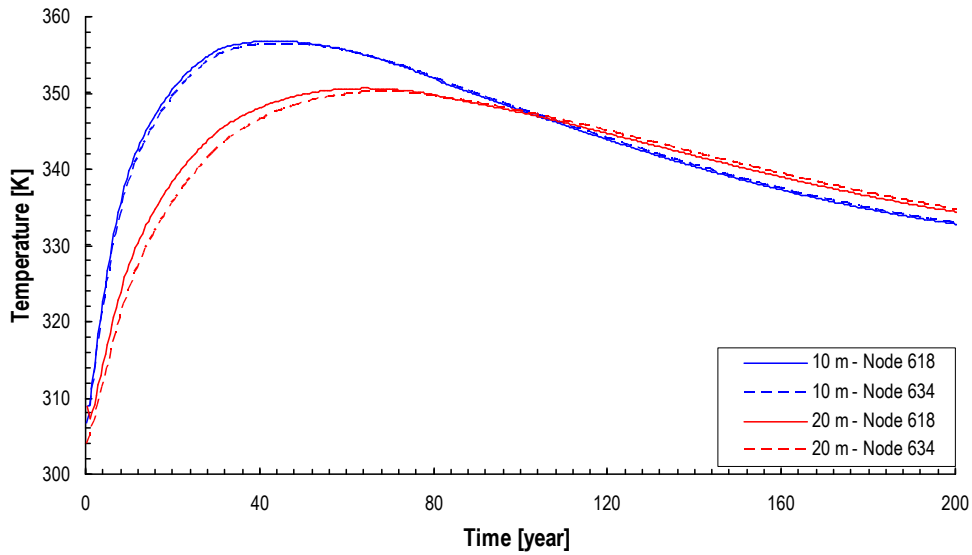


Figure 8.11: Horizontal section – Temperature T

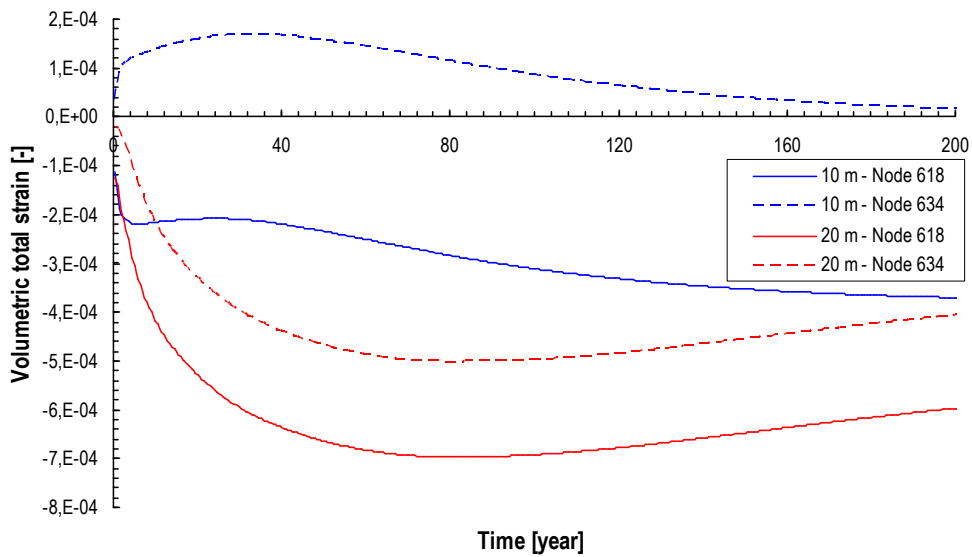


Figure 8.12: Horizontal section – Volumetric total strain ϵ_v^T

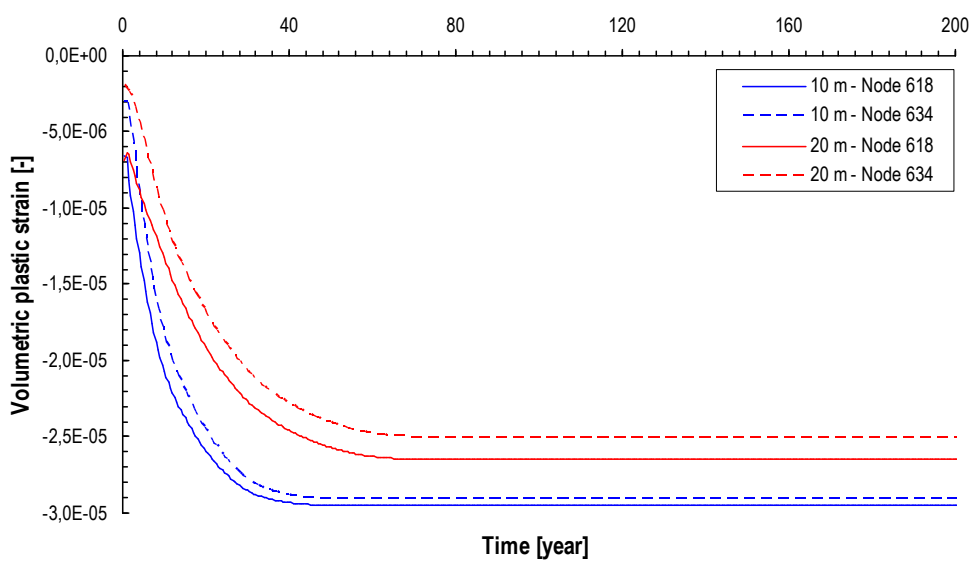


Figure 8.13: Horizontal section – Volumetric plastic strain ϵ_v^p

Now the contours of the volumetric total strain ε_v in the time are shown for the vertical section (Case 1: tunnels' dept of 400 m).

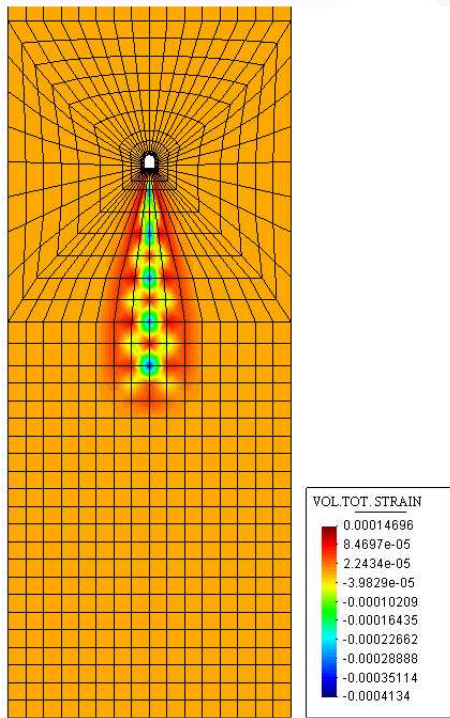


Figure 8.14: t=2 years

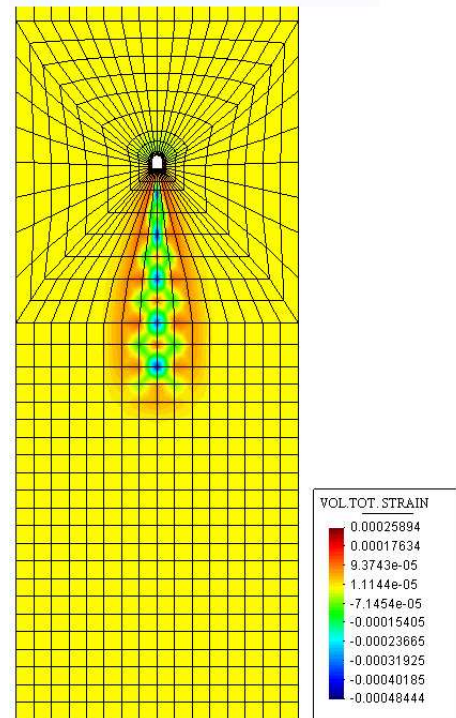


Figure 8.15: t=7,5 years

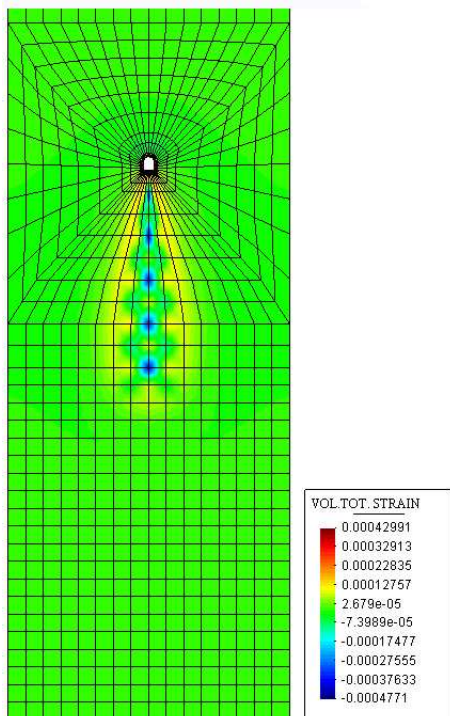


Figure 8.16: t=15 years

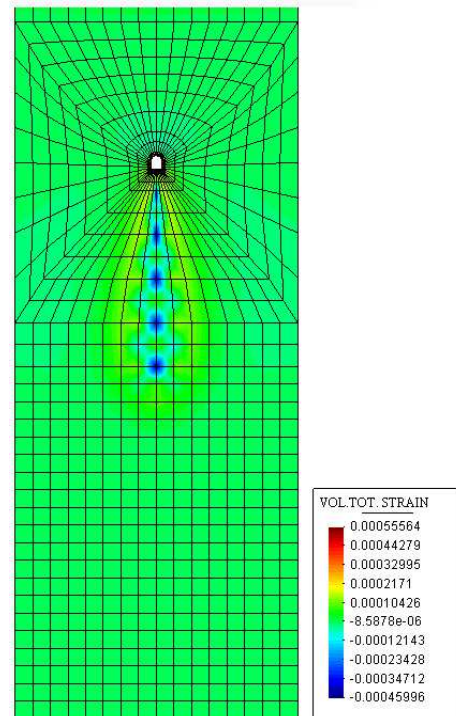


Figure 8.17: t=22,5 years

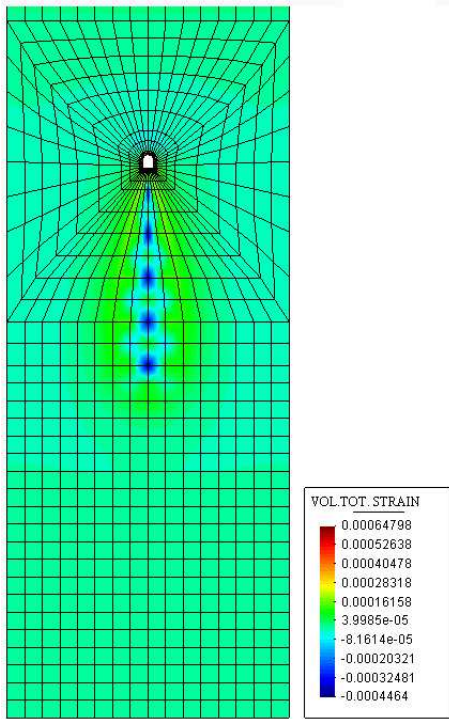


Figure 8.18: t=30 years

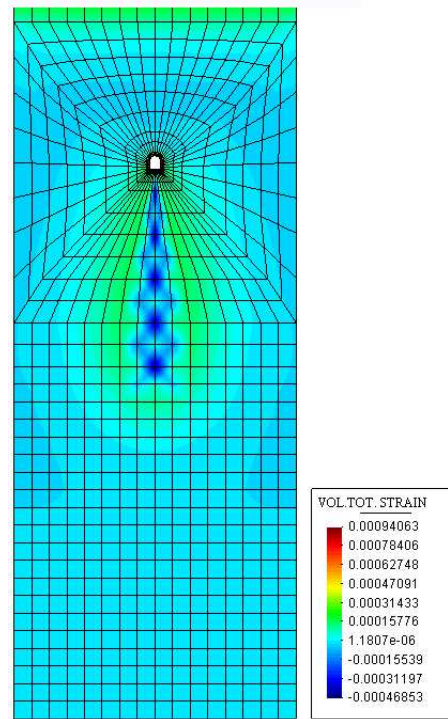


Figure 8.19: t=45 years

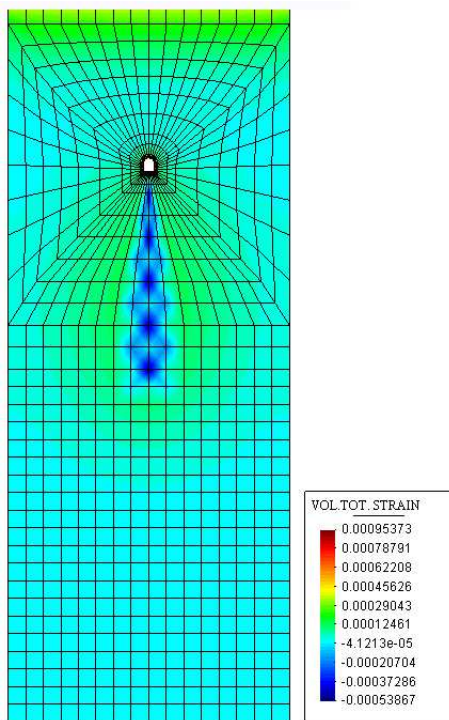


Figure 8.20: t=145 years

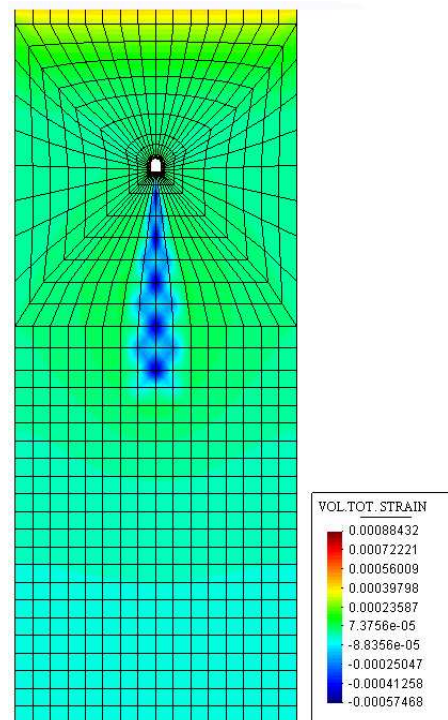


Figure 8.21: t=200 years

8.1.8 Failure conditions

As mentioned in 8.1.6 a nuclear accident due to the failure of the containers in a well is simulated by the temperature law reaching the 300 °C. At this temperature the liquid water in the soil close the heat source starts to evaporate and causes desaturation of the near host rock (Figure 8.22).

At the same time, a quite large volumetric plastic bulb surrounding the well is described, as depicted in Figure 8.22.

For this simulation, ACMEG-TS model should be used to model correctly the occurrence of the partially saturated condition. This will be performed in the near future.

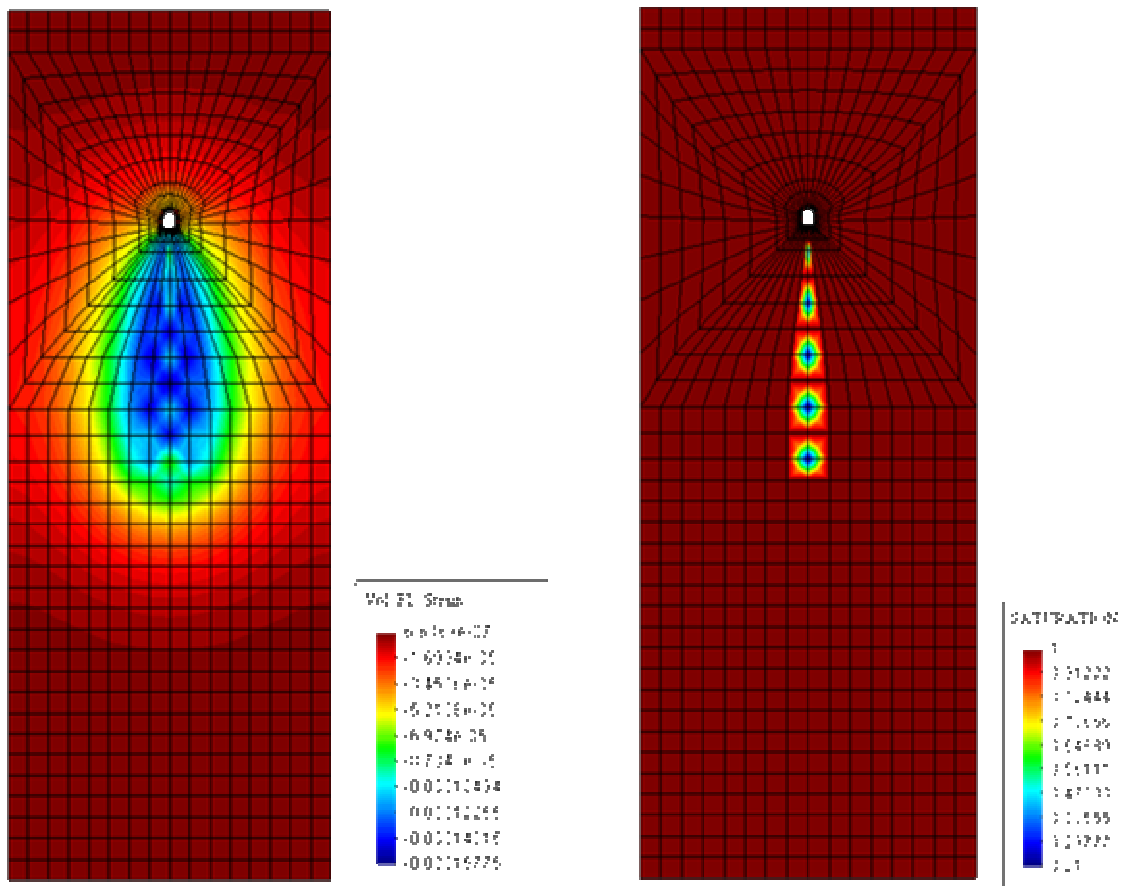


Figure 8.22: Volumetric plastic strain and Degree of saturation state for the reached temperature of 300 °C.

8.2 SUBSIDENCE DUE TO GAS PRODUCTION

8.2.1 Introduction

In this section the problem described by Zhang et al. [Zha01] has been simulated. A gas reservoir of the type investigated in this section contains gaseous and liquid phases at the same time and within it pressure gradients are possible. As a consequence, the pressure measurements usually performed cannot represent what happens in the whole reservoir. Moreover the reservoirs are in hydraulic continuity with confining aquifers and aquitards. A complete mathematical model to simulate the mechanical behaviour of such a multiphase system needs therefore a mass balance equation for all present fluids together with momentum balance equations for fluids and the mixture. All these equations are coupled owing to the interactions between the fluids and the solid.

In this case the constitutive law BSZ is used because the reservoir is in partially saturated conditions.

Part of the material parameters are taken from Papamichos and Schei: "Characterization of Adriatic soft weak sediments for subsidence" [P&S98], the others are taken from the parameter identification of Simoni and Schrefler [S&S01] or extrapolated as illustrated in section 8.2.2.

8.2.2 Identification of parameters

8.2.2.1 Parameter from test

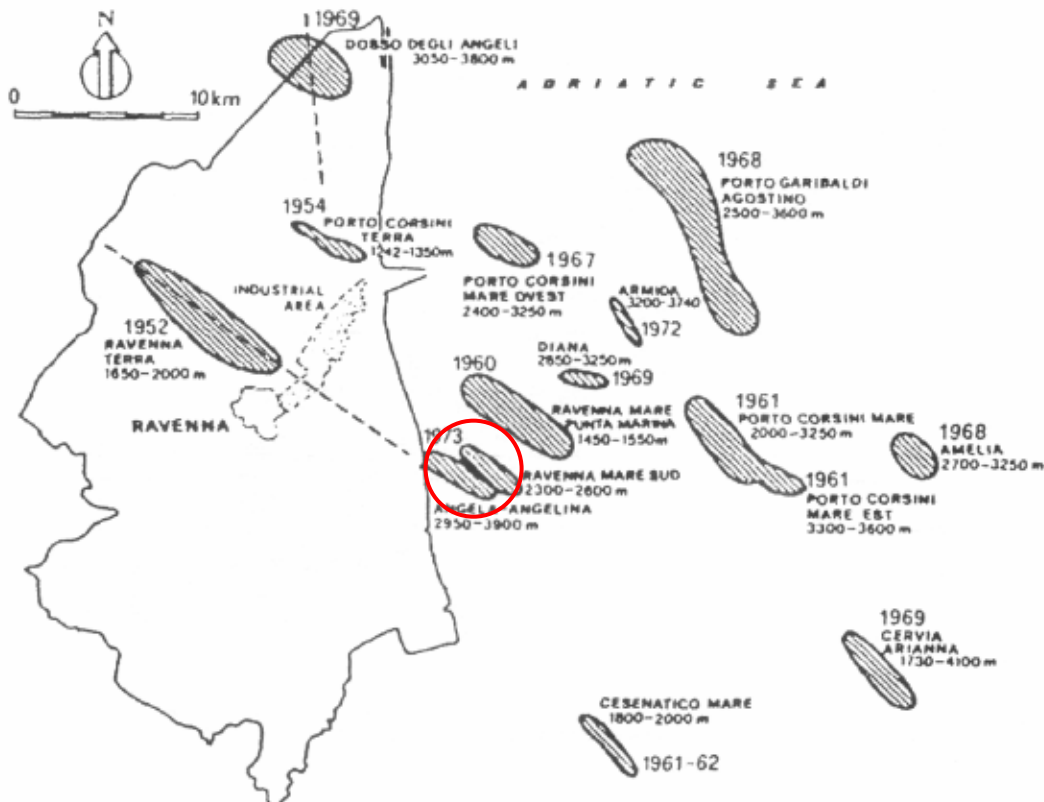


Figure 8.23: Location of the Ravenna Terra gas field and wells (Redrawn from [Men08]). Into the red circle there is the Angela reservoir from which Core 1305 comes.

In the following table the parameters given from Papamichos and Schei for "Core 1305", which is one of the tests performed by the authors (Figure 8.23), are reported. This is a laboratory experiment performed at IKU Petroleum Research, Trondheim [P&S98] on behalf of AGIP (Italian National Petroleum Company). The problem deals with a silty consolidated sandstone sample extracted from a gas bearing formation in the Northern Adriatic basin at a depth of 3400 m.

As mentioned in the previous chapter, the parameters for the BSZ model are not so easy to be determined, hence part of the parameters missing in [P&S98] for the Core 1305 are taken from the parameter identification of Simoni and Schrefler [S&S01]. The other parameters are extrapolated by the comparison between the F.E.M. results obtained with COMES-GEO and the experimental one obtained by [P&S98] in an oedometric test performed on Core 1305.

N° Test	Deep [m]	ID Core	Height [mm]	Diameter [mm]	Material description
Core 1305	3401.4 3401.5	Angela 14 Core 13	61.5	37.3	Silty (68%), consolidated sandstone (18%) with some clay/shale layers (14%)

Table 8.5: Identification of sample

N° Test	Porosity	In situ water saturation	Irreducible water saturation
Core 1305	0.21	0.38-0.45	0.22-0.34

Table 8.6: Parameter from Papamichos and Schei

8.2.2.2 Test on Core 1305

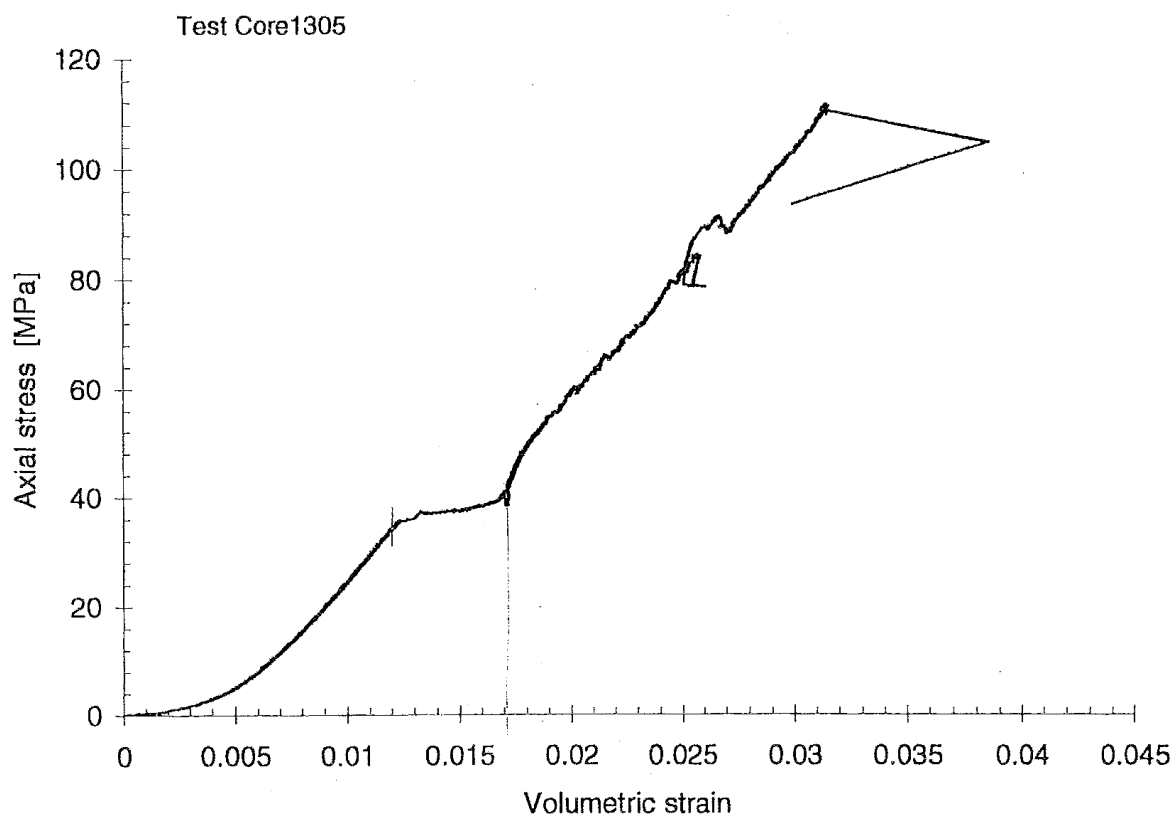


Figure 8.24: Results in terms of volumetric strain and axial stress from Papamichos and Schei [P&S98]

The loading process was scheduled as follows: the sample at in situ saturation (0.38-0.45) is firstly stressed with an initial hydrostatic phase presenting σ_h -rate equal to 0.01 MPa/s until $\sigma_h=0.5$ MPa. This is followed by a uniaxial phase with σ -rate of 0.004 MPa/s until σ reaches 35M Pa; the sample is then held at constant stress level and water is injected for 25 hours until full saturation is attained. This procedure is simulated through the specification of change of saturation (suction) from 0.38 to 1.0. During this period of time, volumetric changes of the specimen are recorded, as during the phases of stress changes. Once full saturation is reached, a second uniaxial phase, at constant water content, with stress rate of 0.004 MPa/s till about 110 MPa is performed.

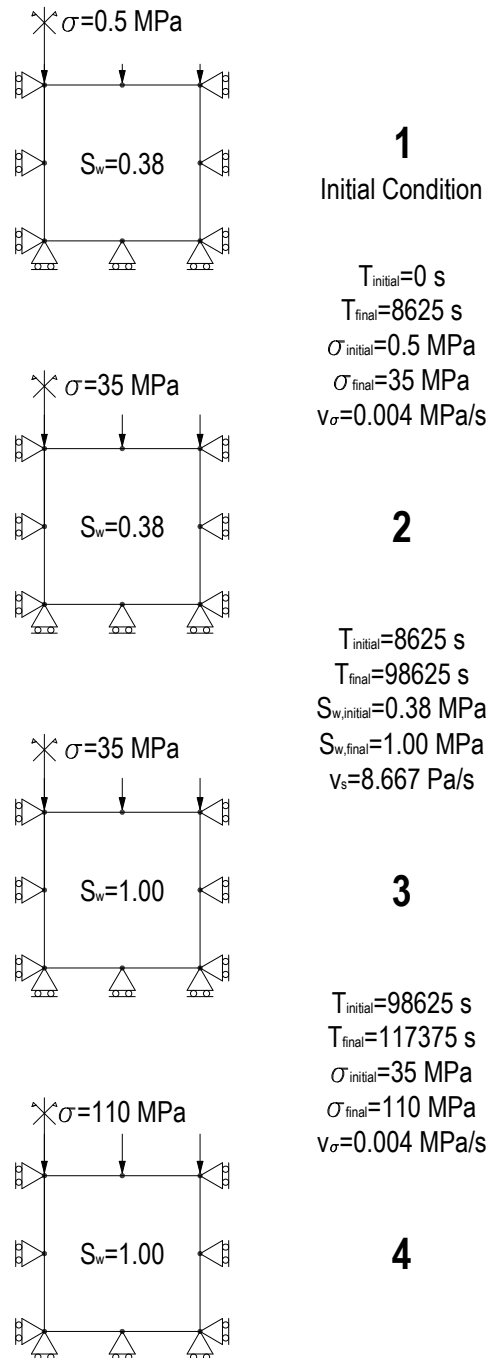


Figure 8.25: Phases of mechanical and hydraulic loading for Core 1305

The test includes also unloading cycles to determine the elastic behaviour and recoverable deformation. The water injection test (hydric-path) simulates the behaviour of the gas reservoir rock during artificial water injection or during the flooding associated with gas extraction. For this reason the axial stress level at which the sample is injected is representative of the vertical stress in reservoir conditions. In the absence of other information, we assume that gas pressure during the test maintains the same value (atmospheric pressure).

In the scheme of Figure 8.25 the test is illustrated with the different time length and load speed for each phase.

The total time necessary to perform the test is 117375 s, that is equal to 32 hours, 36 minutes and 15 seconds.

The results of this test are reported from Papamichos and Schei in terms of volumetric strain and axial stress (Figure 8.24).

It is important to note that there is a further decrease in volume during the injection but the reason is not so clear, it can be due to the rearrangement of the soil (saturation under high confining pressure) or to the viscous behaviour of the soil, but without a creep test on Core 1305 it is impossible to say how much of this volumetric deformation is due to the first or the second aspect.

8.2.2.3 Pore size distribution

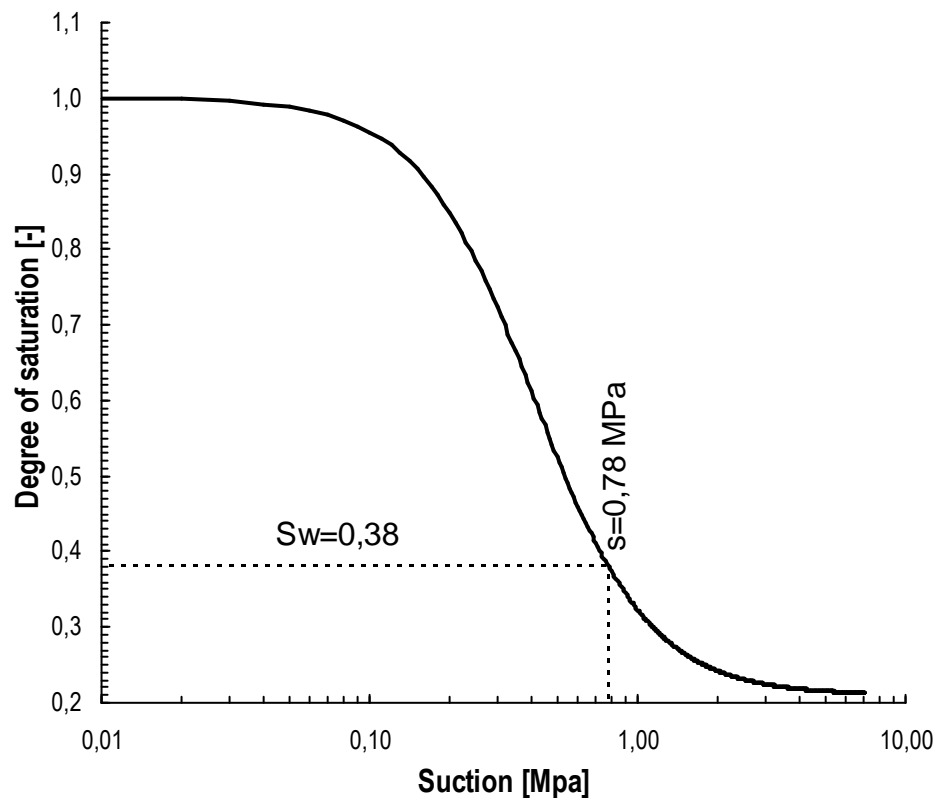


Figure 8.26: Suction vs Degree of saturation for Core 1305

The retention curve is taken accordingly to Zhang et al. [Zha01] adjusting the Safai and Pinder law see in 5.3.2.

$$S_w = S_w(s) = \frac{\Theta'_r}{\Theta'_s} + \frac{1 - \frac{\Theta'_r}{\Theta'_s}}{\left[1 + (\beta s)^\gamma\right]^{1/\gamma}} = 0.22 + \frac{1 - 0.22}{1 + (2.448s)^2} \quad [8.4]$$

where $\frac{\Theta'_r}{\Theta'_s} = 0.22$

$$\beta = 2.448 \text{ cm}^{-1}$$

$$\gamma = 2$$

$$r' = 1$$

The relation [8.4] is plotted in Figure 8.26.

8.2.2.4 Identification of parameters

In the Figure 8.27 the comparison between the experimental results and those obtained by the numerical simulation performed with COMES-GEO are shown. The material parameters used in the simulation are listed in the Table 8.7.

For the elastic moduli the law proposed for the ACMEG-T model

$$K = K_{ref} \left(\frac{p'}{p'_{ref}} \right)^{n_e} \quad [8.5]$$

$$G = G_{ref} \left(\frac{p'}{p'_{ref}} \right)^{n_e} \quad [8.6]$$

are used.

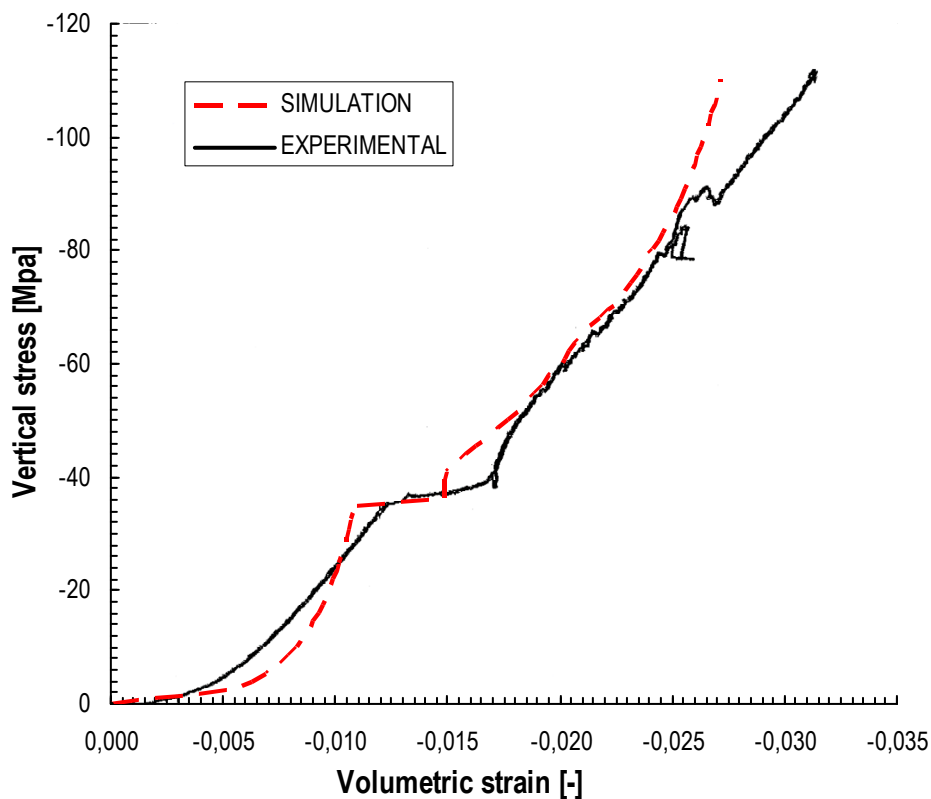


Figure 8.27: Comparison between experimental results [P&S98] and simulation

Elastic material parameters identifier							
K_{ref} [MPa]	G_{ref} [MPa]	ρ_{ref} [MPa]	n_e				
570.00	220.00	0.50	0.97				
BSZ material parameters identifier							
M_{f0}	M_{g0}	α_f	α_g	H_0	β_0	β_1	a [MPa ⁻¹]
1.20	1.00	0.45	0.45	180	0.80	0.90	0.9604
Hydraulic parameters (Safai and Pinder)							
S_{irr}	β [cm ⁻¹]	γ	r'				
0.22	2.448	2.00	1.00				

Table 8.7: Material parameters identified

The comparison between the numerical and the experimental results (Figure 8.27) shows a good agreement. The difference between the results can be attributed to several aspects: the retention curve which is supposed by [Zha01] and not obtained with experimental tests, the need of other tests to determine correctly all the parameters and the need of a careful study on the behaviour of the soils under high confining pressure for the BSZ model.

8.2.3 Reservoir analysis

A gas (methane) reservoir of the type investigated in this section contains gaseous and liquid phases at the same time. Moreover the reservoir is in hydraulic continuity with confining aquifers. Obviously, for this geo-environmental engineering problem, a complete mathematical model to simulate the mechanical behaviour of such a multiphase system needs therefore a mass balance equation for all the fluids together with momentum balance equations for fluids and the mixture.

This numerical simulation has already been studied from Evangelisti and Poggi [E&P70] and, with an additional clay layer, in [L&S98].

8.2.3.1 Boundary conditions

The reservoir is studied in axialsymmetric conditions and its dimensions are:

R=14000 m Radius

Z=1080 m Height

As shown in Figure 8.28, the reservoir (cell number 1) is bounded by two layers of clay (cell number 3) and by a zone of sand in fully saturated state (cell number 2).

The capillary pressure is imposed equal to the hydrostatic pressure along all the sides of the mesh, except for the left boundary of the reservoir (note that the problem is axialsymmetric) where the capillary pressure is assumed $p_c=4 \cdot 10^5$ Pa.

The gas pressure is assumed equal to the atmospheric pressure $p_g=101325$ Pa for all the mesh except for the reservoir where the gas pressure is $p_g=11$ MPa.

The temperature is assumed to be constant at every point and equal to $T=320\text{ K}$ (hence about $47\text{ }^\circ\text{C}$). Vertical displacements are constrained at the bottom and horizontal displacements are constrained along the lateral surfaces.

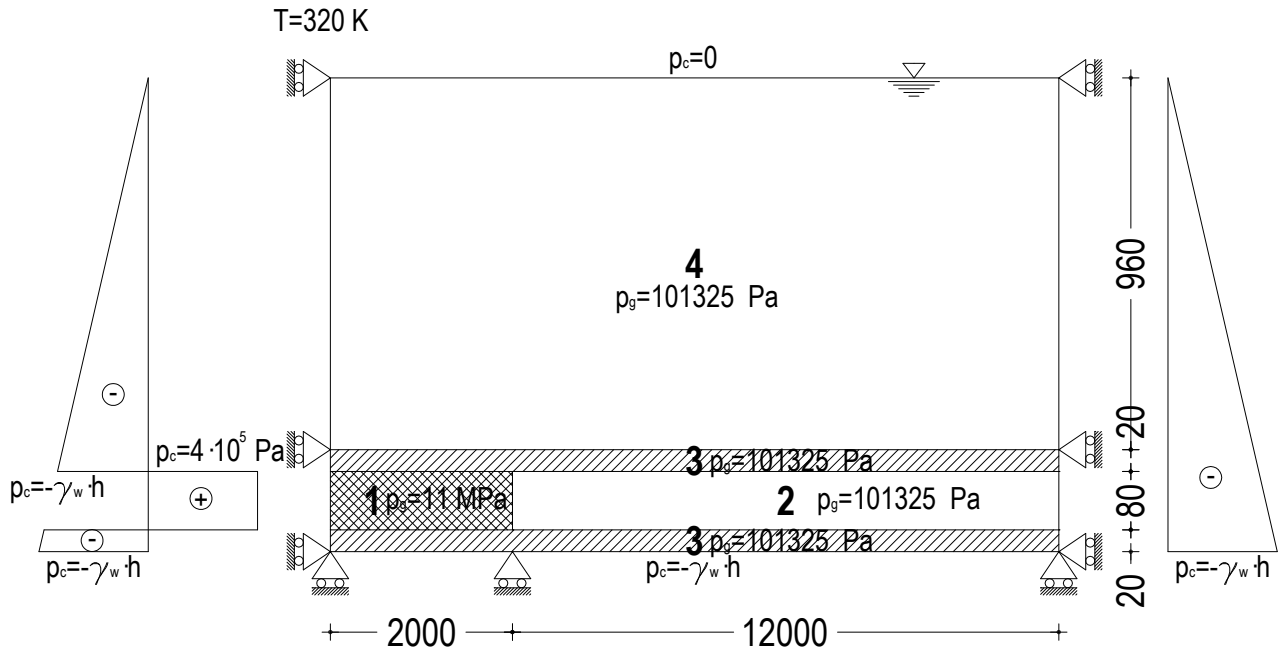


Figure 8.28: Boundary Conditions

The loading function is represented by an outflow of gas coming out from the reservoir, the basic idea is to simulate the gas production history of a real reservoir (see Figure 8.29).

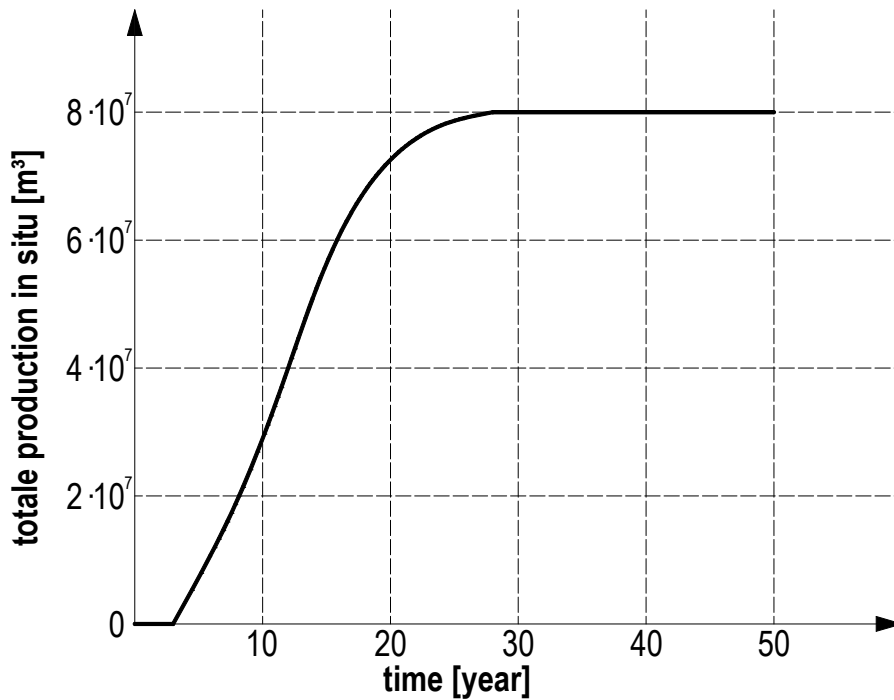


Figure 8.29: Gas production history for numerical simulation

From the graph of the gas production history, is possible to see that the extraction starts after 3 years and continues for 25 years, and then the simulation continues without extraction for a total of 50 years.

8.2.3.2 Results

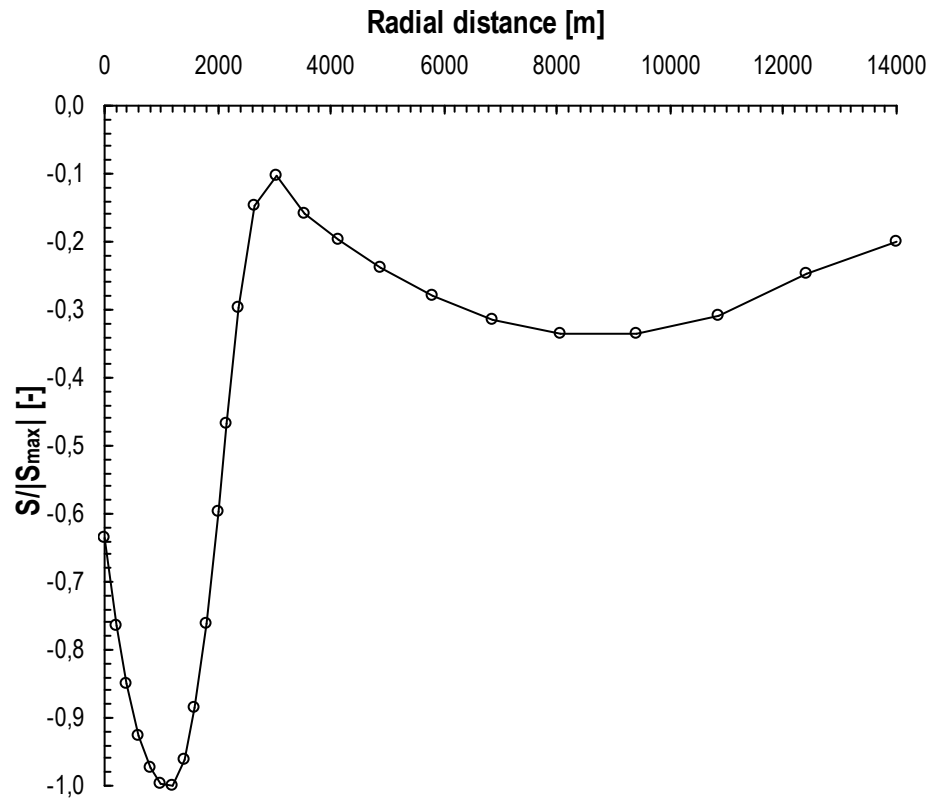


Figure 8.30: Displacement of the top of surface

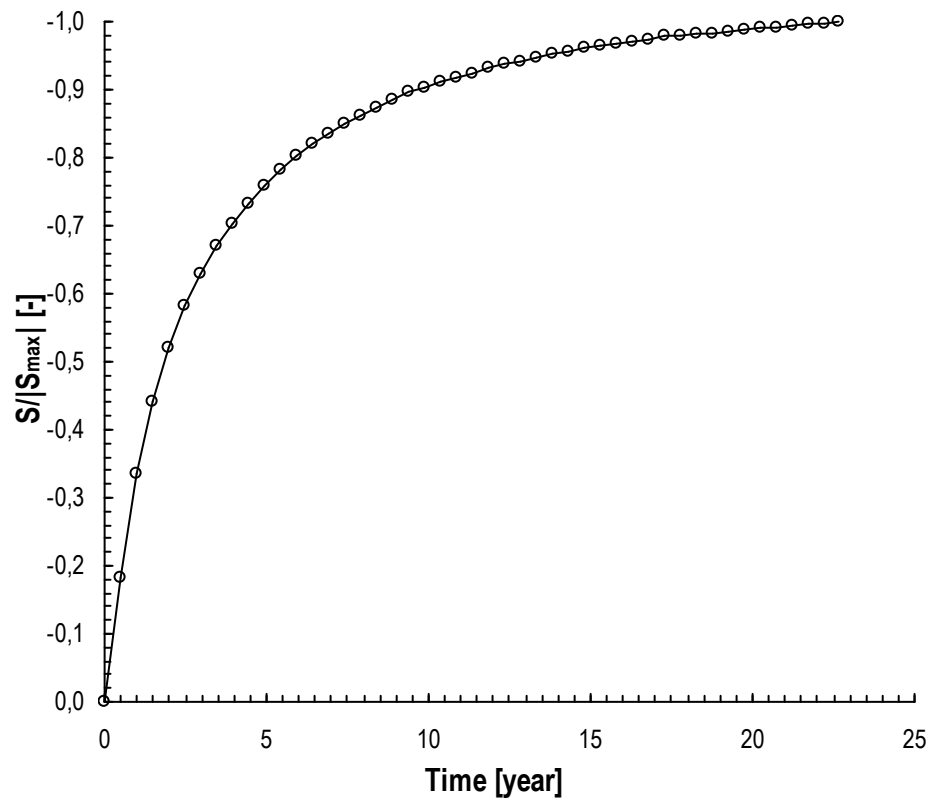


Figure 8.31: Displacement at radial distance of 1200 m

The results shown in Figure 8.30 and Figure 8.31 are relative to the early 23 years of extraction. The rest of the analysis is still in progress. However, from the first results, is possible to see that the qualitative behaviour predicted from the model is correct. In fact, as it is possible to see in Figure 8.30, there is the maximum vertical displacement, measured at the top of the surface about in the middle of the reservoir (between 1000 m and 1200 m). Part of this deformation is recovered near to the end of the reservoir (little farther than the 2000 m). This zone in fact is in expansion for the water flux that enters in the reservoir (see Figure 8.32 and Figure 8.33).

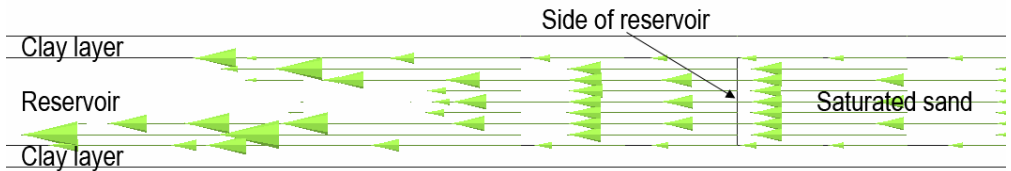


Figure 8.32: Water flow vectors

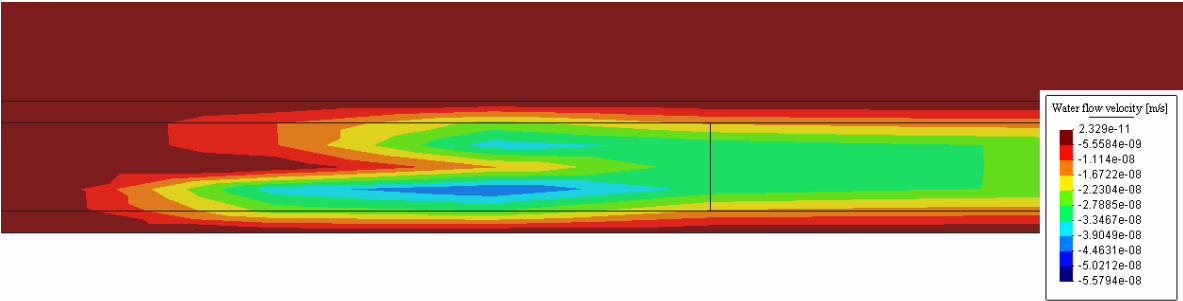


Figure 8.33: Contour of water flow velocity

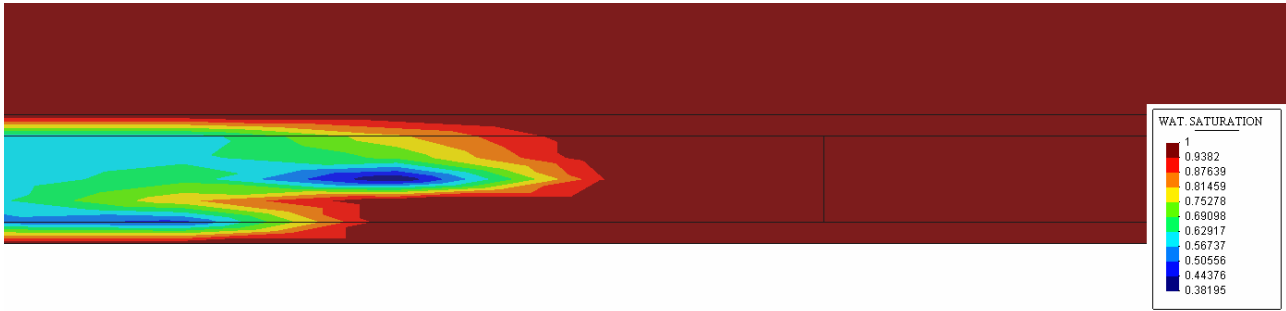


Figure 8.34: Degree of saturation

Figure 8.32, Figure 8.33 and Figure 8.34 show that the water flux goes from the saturated sand zone into the reservoir. This cause an advancement of the saturated front that is, for the time of about 23 years, of more than 200 m. Figure 8.35 shows the equivalent plastic strain distribution for the zone of the reservoir close to the aquifer.

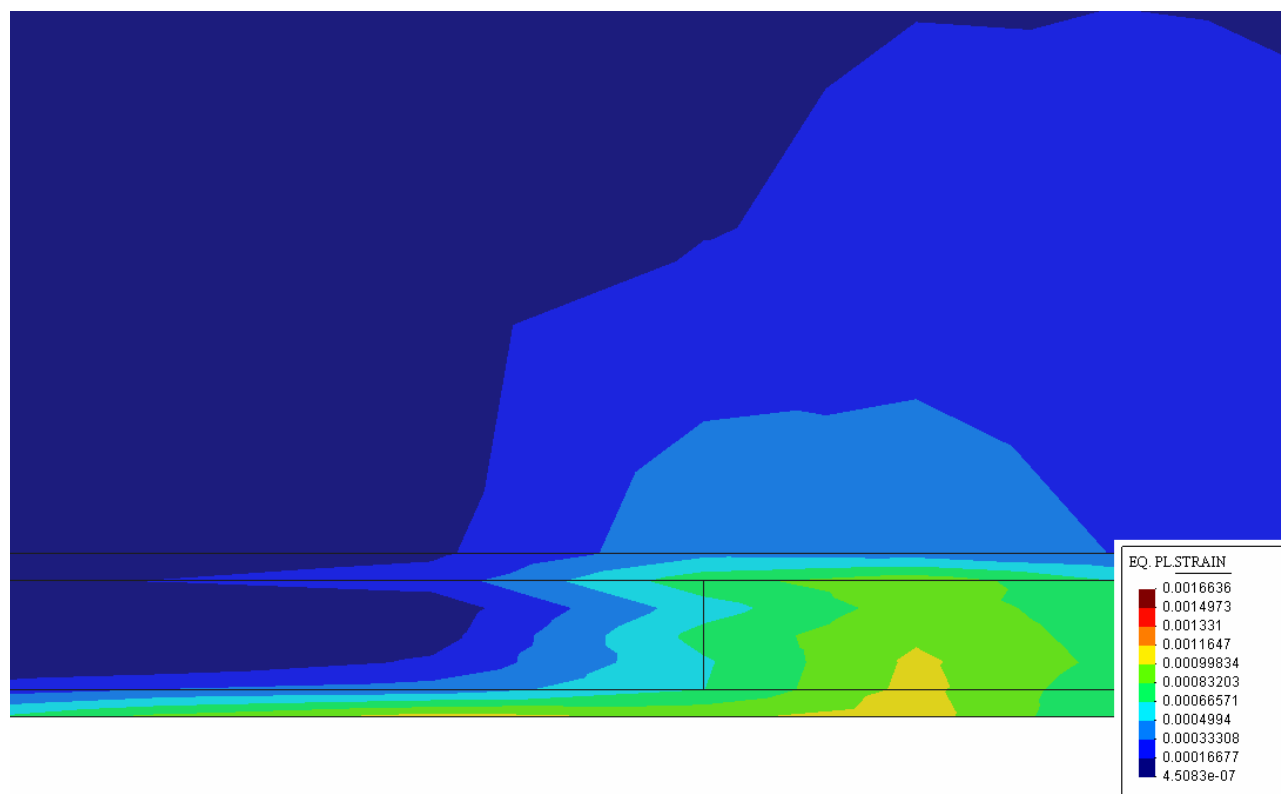


Figure 8.35: Equivalent plastic strain

8.2.3.3 Conclusion

The results shown for this hypothetical case of subsidence can be considered just qualitative because the deformation compute on the ground surface is smaller than expected. This is due to the uncertainly of the parameters assumed for the simulation in particular for the material outside the reservoir.

However, the qualitative behaviour of the reservoir during the gas extraction seems reasonable.

A thorough investigation will be performed in the near future too.

References

- [BRGM91] Bouilleau M., H. Modaressi, C. Perrin, D. Aubry, A. Modaressi, L. Laloui & I. Benzenati. "Exercice de calcul de stabilité des ouvrages de stockage des déchets de type B et C en couche d'argile". Report to the French Atomic Energy Commission (CEA) – The French National Radioactive Waste Management Agency (ANDRA), 1991.
- [Lui06] L. Luison (2006). Implementazione di un modello termo-elasto-plastico in un codice agli elementi finiti per mezzi porosi multifase. Tesi di laurea. Università degli studi di Padova. Italia.
- [Pas08] M. Passarotto (2008). Analisi accoppiata termo-idro-meccanica di depositi profondi di scorie radioattive. Tesi di laurea. Università degli studi di Padova. Italia.
- [Pas09] M. Passarotto, L. Luison, L. Sanavia, L. Laloui, B. François. ALERT Workshop 2009 – Poster session "Coupled hydro-thermo-mechanical analysis of a deep radioactive waste disposal based on porous media mechanics".
- [Zha01] Zhang HW, Heeres OM, de Borst R, Schrefler BA. : 2001, Implicit integration of a generalized plasticity constitutive model for partially saturated soil, *Eng. Comput.*, 18:314-36.
- [P&S98] Papamichos E, Schei G.: 1998, Characterization of Adriatic soft weak sediments for subsidence studies. IKU Petroleum Research, Trondheim, Norway, Report Nr. 33.0693.00/01/01/98.
- [Men08] A. Menin, V.A. Salomoni, R. Santagiuliana, L. Simoni, A. Gens, B.A. Schrefler, A mechanism contributing to subsidence above gas reservoirs and its application to a case study, *International Journal for Computational Methods in Engineering Science & Mechanics*, 9(5), 270-287, 2008 (ISSN: 1550-2287, DOI:10.1080/15502280802225234)
- [E&P70] Evangelisti G., Poggi B.: 1970, Sopra i fenomeni di deformazione dei terreni da variazione della pressione di stato, *Atti Acc. Sc. Ist. Bologna, Mem.*, s. II, n. 6, Bologna.
- [L&S98] Lewis R.W. and Schrefler B.A. *The Finite Element Method in the Static and Dynamic Deformation and Consolidation of Porous Media*. J. Wiley, Chichester 1998.
- [S&S01] Simoni L., Schrefler, B.A: 2001, An accelerated algorithm for parameter identification in a hierarchical plasticity model accounting for material constraints, *Int. J. Numer. Anal. Meth. Geomech.*, 25, 263-272.
- [San10] L. Sanavia, L. Laloui, M. Passarotto, L. Luison, "Coupled hydro-thermo-mechanical analysis of a deep radioactive waste disposal" (paper in preparation)

9 CONCLUSIONS AND FUTURE DEVELOPMENTS

This thesis contributed to develop a general framework for the computational analysis of geo-environmental engineering problems analysed as coupled multi-physics processes.

Advanced constitutive models for isothermal and non-isothermal water saturated or unsaturated soils have been implemented and numerically validated in the finite element code COMES-GEO based on an existing fully coupled Thermo-Hydro-Mechanical (THM) model developed during years at the University of Padua.

Summarizing, the following advanced constitutive models for soil have been implemented with the collaboration of the research group of Prof. Lyesse Laloui and of the research group of the Prof. Manolo Pastor:

1. ACMEG-T for water saturated clays in non isothermal condition;
2. ACMEG-TS for water saturated and partially saturated clays in non isothermal condition;
3. Pastor-Zienkiewicz for water saturated sands in isothermal condition;
4. Bolzon-Schrefler-Zienkiewicz for partially saturated sands in isothermal condition;
5. Bolzon-Schrefler for partially saturated sands in non isothermal condition.

As further numerical validation, a linear thermo elastic consolidation in fully saturated condition was analyzed and preliminary results concerning typical geo-environmental problems such as the thermo-hydro-mechanical behaviour of deep nuclear waste disposal in a geological clay formation and the simulation of the subsidence above gas reservoirs due to gas production, close this present work.

Obviously, speaking about soils, the word *complete* can never be used because of the inhomogeneity typical of this material and because of the many phenomena that play a role in the behaviour of soils (i.e. creep).

For this reason, the future developments following this works can be infinite.

In this moment, there are two works in progress and are the continuation of the geo-environmental problems illustrate in the chapter 8: nuclear waste disposal and subsidence.

Future developments in the field of the applications will be the simulation of other case of nuclear waste disposal and subsidence different from the two presented, and the simulation of the onset of flowslides and catastrophic landslides.

Several developments will concern the extension to 3D cases for which multiprocessing calculation is needed.

Further development in terms of constitutive models will be a further enhanced model for the Generalized Plasticity proposed by Jommi and Di Prisco (Reference [J&D95] of chapter 7).

LORIS LUISON

date of birth: 21 september 1980
place of birth: Cittadella (PD) – Italy
citizenship: Italian

e-mail

loris.luison@unipd.it

address

Dipartimento di Costruzioni e Trasporti
Università degli studi di Padova
via Marzolo 9
35131 – Padova (Italy)
tel. +39 049.8275605
fax. +39 049.8275604
www.dic.unipd.it